FACOLTA' DI INGEGNERIA

Dottorato di ricerca
in
Ingegneria delle Strutture

AEROELASTICITY OF SUSPENSION BRIDGES

USING NONLINEAR AERODYNAMICS

AND GEOMETRICALLY EXACT STRUCTURAL MODELS

PhD CANDIDATE
Andrea Arena

ADVISORS
Prof. Walter Lacarbonara
Prof. Pier Marzocca

PhD COORDINATOR
Prof. Giuseppe Rega

Rome
December 10, 2012

Contents

Abstract

Wind-induced vibration in super-long-span bridges is a major concern for the designers. There is a need to enhance the structural design technology, through improved computational capabilities, a critical step for a better understanding of fluid-flow physics that induce vibration and fluid-structure dynamics of flexible bridges. The design of bridges with spans significantly longer than those existing today is quite challenging. To refine the computational tools required for such bridges, a multi-disciplinary research effort devoted to the advanced modeling of flexible long-span suspension bridges is proposed. These structures exhibit an aeroelastic behavior quite different from conventional bridges.

In the present work, a fully nonlinear model of suspension bridges parameterized by one single space coordinate is proposed to describe the overall three-dimensional motion. The nonlinear equations of motion are obtained via a direct Lagrangian formulation and the kinematics, for the deck-girder and the suspension cables, feature the finite displacements of the associated base lines and the flexural and torsional finite rotations of the deck cross sections. The strain-displacement relationships for the generalized strain parameters - the cable elongations, the deck elongation, and the three curvatures - retain the full geometric nonlinearities.

The nonlinear aerodynamic characteristics of the boxed sharp-edge cross section of the Danish Great Belt Bridge are investigated by using two state-of-the-art computational methods, the k-ϵ turbulence model implemented in FLUENT-ANSYS to solve the Reynolds Averaged Navier Stokes (RANS) equations and the Navier Stokes (NS) discrete-vortex method implemented in DVMFLOW-COWI. The computational fluid dynamics tools have been used to develop computationally efficient unsteady aerodynamic models taking into account viscous effects, including flow separation and boundary layer thickening, treated using Reduced-Order Models (ROMs). Frequency-domain representations of the aerodynamic loads in terms of flutter derivatives are obtained for selected values of the wind initial angle of attack. Consequently, nonlinear indicial functions are derived for these angles and incorporated into the proposed ROMs.

As a result, a fully nonlinear coupled fluid-structure model for suspension bridges is assembled to study the nonlinear static and dynamic behavior thus addressing problems of static aeroelastic stability, such as torsional divergence, and dynamic aeroelastic instabilities, such as flutter and post-flutter.

The geometrically exact formulation developed in this study lends itself naturally to parametric studies about the sensitivity of the static and dynamic limit states of the bridges with respect to variations of the characteristic structural parameters. In addition, the study addresses the dynamic response of the bridges under time- and space-dependent loading conditions due to time- and space-wise distributed gust excitations as well as the study of the effects of spatial nonuniform wind distributions on the critical *flutter* condition. Finally, the post-flutter behavior is studied by using a continuation method to highlight the post-critical bifurcation scenarios and emphasize the complex nonlinear response of slender self-excited suspended structures.

Sommario

Le vibrazioni indotte dall'azione del vento su ponti sospesi di grandissima luce rappresentano uno dei maggiori problemi per i progettisti di tali opere. Vi è pertanto la necessità di migliorare le attuali tecnologie progettuali, facendo uso delle più avanzate tecniche computazionali, poichè ciò è essenziale per una migliore comprensione della fluido dinamica che governa il problema e che è la causa dell'accopiamento fluido-strutturale in ponti così flessibili e dunque delle vibrazioni che ne conseguono. La progettazione di ponti aventi luci significativamente più lunghe di quelle tutt'ora esistenti rappresenta oggi una grande sfida. Per poter effettivamente migliorare gli strumenti computazionali necessari per la progettazione di ponti di grandissima luce, è proposto un contributo di ricerca multi disciplinare mirato alla modellazione avanzata di ponti sospesi di grande luce. Tali strutture hanno un comportamento aeroelastico alquanto differente da quello dei ponti convenzionali.

Nel presente lavoro di ricerca, è proposto un modello completamente nonlineare di ponte sospeso parametrizzato attraverso una singola coordinata spaziale al fine di descrivere la dinamica tri-dimensionale globale del sistema. Le equazioni del moto non lineari sono ottenute mediante una formulazione Lagrangiana diretta e la cinematica, per l'impalcato e per i cavi di sospensione, è basata sull'ipotesi di spostamenti finiti e di rotazioni flessionali e torsionali finite delle sezioni trasversali dell'impalcato. Le relazioni di congruenza interna, deformazione-spostamento, dei parametri generalizzati della deformazione - l'elogazione dei cavi, quella dell'impalcato e le tre curvature - conservano le non linearità geometriche complete, ovvero nessuno sviluppo in serie è stato condotto al fine di semplificare le loro espressioni.

Le caratteristiche aerodinamiche non lineari della sezione scatolare del Great Belt Bridge in Danimarca sono state investigate mediante l'uso di due metodi di analisi fluidodinamica computazionale tradizionali, il modello di turbolenza k-ϵ, implementato nel codice di calcolo FLUENT-ANSYS, che utilizza le equazioni Reynolds Averaged Navier Stokes (RANS) e il metodo *discrete vortex* per la soluzione delle equazioni di Navier Stokes (NS), implementato nel codice DVMFLOW-COWI. Tali strumenti di calcolo fluidodinamico sono stati utilizzati per la formulazione di una aerodinamica instazionaria che tenga in conto degli effetti viscosi, come la separazione del filetto fluido e l'accrescimento in spessore dello strato limite, attraverso modelli aerodinamici di ordine ridotto (ROMs). Le rappresentazioni nel dominio delle frequenze delle forzanti aerodinamiche in termini delle derivate aeroelastiche sono state ottenute per determinati valori di angolo d'attacco iniziale del vento. Di conseguenza, funzioni indiciali non lineari sono state derivate per tali angoli e incorporate nei ROMs proposti.

Infine, un modello completamente non lineare di accoppiamento fluido strutturale per ponti sospesi è stato messo a punto per analizzare il comportamento statico e dinamico di tali strutture e mirato allo studio di stabilità aeroelastica statica, tipo *divergenza torsionale*, e di instabilità dinamiche, tipo *flutter*, nonchè all'analisi della risposta dinamica in regime di post-flutter.

La formulazione geometricamente esatta sviluppata in questo lavoro si presta per natura a studi parametrici di sensitività degli stati limite dinamici e statici dei ponti rispetto alle variazioni dei parametri strutturali caratteristici. Ulteriori studi sono stati rivolti all'analisi della risposta dei ponti sotto l'azione di carichi aerodinamici con distribuzioni spaziali e temporali del vento non uniformi, come quelli indotti da raffiche, e alla valutazione degli effetti di distribuzioni spaziali non uniformi del vento sulla condizione critica di *flutter*. Infine, è stato studiato il comportamento in post-flutter mediante l'uso di metodi di continuazione con lo scopo di evidenziare gli scenari biforcativi post-critici ed enfatizzare la complessa risposta non lineare di strutture snelle soggette a carichi dinamici autoeccitanti.

Chapter 1
Introduction

Structures possessing high flexural-torsional flexibility when subjected to wind-induced excitations can be affected by elastic instability phenomena such as torsional divergence or flexural-torsional flutter. In long- and super-long-span suspension bridges, the geometric nonlinearities induced by the suspension cables and the high flexural-torsional slenderness of the deck-girder play an important role in the static and dynamic response of the bridge. Moreover, the nonlinear effective stiffness of the structure in its prestressed equilibrium configuration under dead loads can strongly influence the behavior under both autonomous forces (e.g., aeroelastic loads) and non-autonomous dynamic forces (e.g., traffic-induced excitations). These bridges show a characteristic nonlinear precritical behavior under quasi-static incremental loads and, depending on the direction of loading (downward or upward), the ensuing increase or loss of tension in the suspension cables causes an increase or a loss of stiffness as a result of the positive or negative geometric stiffness effects, respectively. Thus, to predict correctly any static or dynamic critical condition, it is necessary to describe accurately the overall precritical behavior as well as the mechanical asymmetry exhibited by these formidable suspended structures. Phenomena including static and dynamic aeroelastic instabilities induced by wind-structure interaction can be effectively investigated in the context of a parametric modeling and a continuum formulation of the elastostatic and elastodynamic problems.

Several numerical models of suspension bridges have been proposed in the technical literature and different studies have been conducted to investigate their static/dynamic response and the aeroelastic limit states. One of the first and most important contributions can be found in [1] where parametric formulations are adopted to describe the static and dynamic response of cables and suspended structures. Different studies on linearized models of suspension bridges can be found in [2, 3, 4, 5], whereas the first general theory and analysis of nonlinear vibrations of such structures were proposed in [6, 7] where the authors used the method of multiple scales to investigate nonlinear free flexural-torsional vibrations. By the same method, passive and active schemes were investigated to control nonlinear oscillations in suspension bridges [8, 9]. Most recent works can be found in [10] and in [11, 12] in which the nonlinear equations of motion are obtained by employing variational methods based on truncated geometric nonlinearities.

Studies on the static aeroelastic instability of long-span cable-stayed bridges were carried out in [13] to evaluate the critical wind velocity that will lead to a nonlinear lateral-torsional buckling instability using a Finite Element (FE) approach. Three-dimensional nonlinear FE analyses on a super-long-span suspension bridge were also performed in [14] to demonstrate the significant influence of the geometric nonlinearities on the static and dynamic behaviors of such slender structures under the action of aerodynamic loads. In [15, 16] a series method was proposed for the deterministic static aeroelastic stability analysis of suspension bridges; however, some conservative assumptions in the kinematic modeling and in the prestress contribution of the dead and wind-induced loads were made. In [17] numerical static aeroelastic stability analyses are performed on a three-dimensional FE model of a suspension bridge to

study the combined effects of geometric and material nonlinearities and the nonlinear modeling of the wind loads. A simplified method to analyze the lateral response of suspension bridges under wind loads was proposed in [18] deriving the analytical formulas of the aeroelastic response for a three-DOF model under some kinematic and mechanical assumptions. A continuum model of suspension bridges, that can undergo three-dimensional motions, was first proposed in [19, 20]. The model was formulated via a total Lagrangian approach within a geometrically exact framework. The torsional divergence condition was determined as the static bifurcation condition at a flow speed for which the tangent stiffness along the nonlinear equilibrium path becomes was singular.

The dynamic aeroelastic behavior of suspension bridges has also been widely investigated in the literature by different numerical strategies. The flutter instability, whose general theory is given in [21], is classically studied by the frequency- and time-domain approaches [22]. The importance of the structural nonlinearities on the aerodynamic response of suspension bridges is a well-known fact as shown in [23].

In [24] the concept of aeroelastic derivatives –see also [25] and [26]– was first proposed to evaluate the flutter wind speed by solving a complex-valued eigenvalue problem whose solution represents the bridge frequency at the flutter condition. A modal analysis technique was applied in [27], [28, 29], and more recently in [30] and [31] for the evaluation of the critical flutter speed of a suspension bridge by using a linear three-dimensional multi-dof framework. A numerical model that treats the bridge and flowing air as elements of a single dynamic system was proposed in [32] where the governing equations are integrated numerically, simultaneously, and interactively to predict the onset of flutter.

A fully nonlinear parametric model for the study of wind-induced excitation in arch bridges was first proposed in [33] and [34] where the flutter analysis of Ponte della Musica, recently erected in Rome, Italy, was carried out by solving the complex eigenvalue problem associated with the governing equations of motion linearized about the in-service prestressed bridge equilibrium under dead loads and wind-induced forces. The same approach was followed in [35] on a classical FE model. An interesting application of classical eigenvalue analysis for the critical flutter condition on a real bridge is given in [36] and [37] where an iterative procedure was employed to estimate the flutter velocity for different wind angles of attack and several suspension bridge configurations. In [38] a FE calculation of the aerodynamic flutter phenomenon is presented for a cable-stayed bridge by solving the eigenvalue problem delivered by the mode-by-mode method with the limitation that it neglects any a priori modal coupling. A multi-mode flutter analysis was performed in [39] by a FE model. To account for the wind loading spatial distribution, especially for long-span bridges, [40, 41] proposed a three-dimensional flutter analysis of a simply supported bridge girder by the so-called finite strip method which allows to consider distributed wind forces on different strips of the bridge girder. The wind spatial distribution can influence both the stability and the aeroelastic response of suspension bridges. In [37] the effects of nonuniform discrete wind spatial distribution are studied by adopting empirical coefficients that account for the horizontal (span-wise) and vertical variation of the wind speed. In [42] is proposed an iterative approach of non-Gaussian conditional simulation employing the spectral representation technique together with non-Gaussian mapping technique to simulate the wind speed profiles by using the speed data collected at different locations. It was found that the buffeting response evaluated using the non-Gaussian simulation scheme may be higher when compared with other simulation schemes. The aerodynamic forces acting on the bridge deck are usually modeled using the *aeroelastic derivatives*, which correspond to a set of functions evaluated through wind-tunnel tests on a sectional scaled model of the reference bridge [26, 43, 44].

An important aspect to be carefully considered in the study of the static and dynamic aeroelastic response of such structures is the proper definition of the aerodynamic properties of the bridge deck-girder cross section. The sharp edges and the corners characterizing their shape are in fact the reason of vortex shedding and the separation of the flow around the section at low wind speeds and small angles of attack. These phenomena represent a non-negligible source of nonlinearities in the aerodynamic

loads generated around the section. An analytical formulation of the aerodynamic loads acting on a rigid section is only available in the thin plate theory, where the description in the time and frequency domains of the aerodynamic loads is provided by the well known theories formulated by Wagner [45] first and then Theodorsen [21], Küssner [46], von Kármán [47] and Garrick [48, 49]. These methods all provide a closed-form solution, in the frequency and time domains, for the pressure distribution on the thin-airfoil lifting surface for generic forcing conditions and are valid for two-dimensional incompressible irrotational potential flow. Alternatively, numerical solutions or experimental data can be used in the development of semi-analytical or semi-empirical methods for the study of the aerodynamics of bluff bodies, such as the bridge deck sections. These methods are supplied by Computational Fluid Dynamics (CFD) tools or by performing experimental tests in wind tunnels.

The cross section of the Great Belt Bridge (GBB) deck was assumed as reference geometry in order to carry out the computational fluid dynamic (CFD) simulations necessary to develop the nonlinear aerodynamic tools. This particular section has been subject of various experimental measurements [50] and computational studies, such as in [51, 52] and more recently in [53, 54, 55], therefore it provides a significant data-base to be used for testing the simulations performed in the present work.

1.1 Objectives

The objectives of the present thesis are multifold:

- to develop a geometrically exact one-dimensional formulation of the static and dynamic aeroelastic problem for suspension bridges and validate the aeroelastic predictions based on this model
- to develop an unsteady aerodynamic formulation taking into account viscous effects, including flow separation and boundary layer thickening, in a reduced-order aerodynamic model based on nonlinear indicial functions
- to assemble a fully nonlinear coupled fluid-structure model for suspension bridges as to study their nonlinear static and dynamic behavior to address problems of static stability, including divergence, and dynamic instabilities including flutter. In addition the study addresses the dynamic response of the bridge under time and space dependent loading conditions due to a distributed gust excitation
- to perform parametric studies to evaluate the static and dynamic behavior of the bridge to selected structural characteristic parameters using the geometrically exact formulation developed in this study
- to study the post-flutter bifurcation behavior of the bridge using a continuation tool to emphasize the complex nonlinear response of flexible slender structures

1.2 Chapters Overview

In Chapter 2, aeroelastic modeling aspects are discussed and the fluid-structure interaction (FSI) phenomena treated in this work are described. In particular, the geometric descriptors and associated forces generated by the flow are presented together with a discussion related to static and dynamic aeroelastic instabilities. The analytical approaches employed to study these phenomena and the formulation of the aerodynamic loads, both in the frequency and time domains, are proposed.

Chapter 3 presents the aerodynamic modeling of bridge deck cross sections. The background theory concerning the fluid-dynamic modeling for incompressible viscous flows is briefly described and computational fluid dynamic (CFD) simulations for sharp-edge bluff-sections are proposed to investigate the aerodynamic response of the GBB bridge deck cross section. Two different approaches and CFD solvers are

used to perform the simulations and the results obtained are compared with the results from the available literature. The static curves of the aerodynamic coefficients and the frequency- and time-domain expressions of the aerodynamic loads, accounting for the nonlinearities related to the viscous effects, the flow separation and high angle of attack, are defined.

In Chapter 4, a fully nonlinear parametric model of suspension bridges, taking into account accurately any nonuniform stiffness and mass properties as well as all other nonuniform data (e.g., the wind force distribution) is proposed. The structural model accounts for the elastic characteristics of the suspension hangers, modeled as a continuum elastic (membrane-type) distribution along the bridge span while the Cosserat theory is employed to describe the mechanics of the deck-girder. No restrictions are placed on the geometry of deformation besides the rigidity of the cross sections. A 3D kinematic theory accounting for large displacements and finite rotations is first derived and the equilibrium equations and the equations of motion are thus derived via a Lagrangian formulation which allows to include in a straightforward manner nonconservative loads such as aeroelastic forces. A finite element (FE) approach is chosen to solve the nonlinear partial differential equations (PDEs) governing the bridge statics and dynamics, and the solver Comsol Multiphysics® [56] was chosen to implement and integrate the PDEs system. Two cases-studies are proposed in order to validate the model and modal analyses and nonlinear precritical equilibrium paths are performed.

In Chapter 5, the static aeroelastic stability of these two suspension bridges is investigated by performing nonlinear incremental analyses and evaluating torsional-divergence. The flutter analysis is then performed for one case study and a comparison between two modal techniques is proposed; the study is in fact conducted by solving a complex-valued eigenvalue problem and a classical, iterative, eigenvalue problem by considering the pre-stressed configurations induced by the bridge dead loads and the in-service loads as well as the static components of the wind loads. A few sensitivity analyses are then carried out in order to demonstrate the wide applicability of the model.

The nonlinear aerodynamics characterizing the geometry of the GBB section and generated in the first part of this work (Chapter 3) are then applied to the proposed structural nonlinear model and, in Chapter 6, studies on the dynamic aeroelastic response at pre- and post-critical wind speed regime are performed. Linear and nonlinear flutter is evaluated and the post-critical response is studied in the context of a quasi-steady nonlinear aerodynamics as well as by accounting for a nonlinear unsteady formulation of the self-excited aerodynamic loads and the limit cycle oscillations occurring in the post-critical condition are investigated. The effects in the critical flutter condition of nonuniform wind speed spatial distributions are studied and the modeling of a non uniformly distributed wind gust is then proposed and the pre-critical aeroelastic response of suspension bridges under its action is presented and commented.

Chapter 2
Aeroelastic Phenomena

2.1 Introduction

Critical aeroelastic instabilities can occur in flexible structures when subjected to the action of aerodynamic loads, generated by the motion of air flow around them and strictly dependent on the self-excited motion of the structure. In suspension bridges, in particular in long- and super-long-span bridges, the effect of the wind-structure interaction is emphasized by the high slenderness of the deck and the associated low bending-torsional stiffness. Moreover, these structures are mostly erected on flat, wide areas like river beds, canyons or over the sea, where the air flow, not dammed by any natural or artificial obstacles, can reach high values of speed that can be of critical magnitude for the stability of the bridge. The air flows in which such structures are immersed are usually turbulent, that is, the velocity vector $\boldsymbol{U}$ has non uniform component both in space $\boldsymbol{x}$ and in time t

$$\boldsymbol{U}(\boldsymbol{x}, t) = \boldsymbol{U}_{\infty}(\boldsymbol{x}) + \boldsymbol{U}_{\mathrm{T}}(t) \tag{2.1.1}$$

where, $\boldsymbol{U}_{\infty}(\boldsymbol{x})$ is the static space-dependent free-stream component, whereas $\boldsymbol{U}_{\mathrm{T}}(t)$ represents its dynamic component, due to time-dependent gust or turbulence. The main interest of this work is referred to the aeroelastic phenomena induced by the static mean component $\boldsymbol{U}_{\infty}(\boldsymbol{x})$ of the wind speed and the response to a space- and time-dependent wind gust, while the effects associated to the turbulent part will not be treated in these studies. In particular, the loss of stability due to torsional divergence and the dynamic instability associated to the flutter phenomenon will be investigated.

The aerodynamic loads do not depend only on the magnitude of the wind speed but, because of their self-exciting character, they are also function of the effective wind angle of attack α^{E} that is varying with the motion of the structure. The *drag* force D, acting in the direction of the flow, the *lift* force L, orthogonal to that, and the *aerodynamic moment* M of axis normal to the section's plane are defined as

$$D(\alpha^{\mathrm{E}}) = \frac{1}{2}\rho U^2 B\, C_{\mathrm{D}}(\alpha^{\mathrm{E}}), \ L(\alpha^{\mathrm{E}}) = \frac{1}{2}\rho U^2 B\, C_{\mathrm{L}}(\alpha^{\mathrm{E}}), \ M(\alpha^{\mathrm{E}}) = \frac{1}{2}\rho U^2 B^2\, C_{\mathrm{M}}(\alpha^{\mathrm{E}}) \tag{2.1.2}$$

where ρ is the air density, U is the intensity of the wind speed ($U = ||\boldsymbol{U}_{\infty}||$), B is the deck width and C_{D}, C_{L} and C_{M} are the drag, the lift, and the aerodynamic moment coefficients, respectively.

By referring to an orthonormal fixed frame $\{\boldsymbol{e}_1, \boldsymbol{e}_2, \boldsymbol{e}_3\}$, where $\boldsymbol{e}_1$ is collinear with the section width, $\boldsymbol{e}_2$ lays in the section plane and $\boldsymbol{e}_3$ is along the bridge span direction, the static component $\boldsymbol{U}_{\infty}$ of the flow velocity is defined as $\boldsymbol{U}_{\infty} = -U\cos\bar{\alpha}\,\boldsymbol{e}_1 + U\sin\bar{\alpha}\,\boldsymbol{e}_2$, where $\bar{\alpha}$ is the angle between the direction $\boldsymbol{e}_1$ and the vector of the absolute wind velocity $\boldsymbol{U}_{\infty}(\boldsymbol{x})$ (see Fig. 2.1). The angle α^{E} can be defined as the sum of the three contributions $\alpha^{\mathrm{E}} = \bar{\alpha} + \phi_3 + \phi_3^{\mathrm{R}}$ where ϕ_3 is the pure torsional rotation of the section and ϕ_3^{R} is the relative angle due to the motion of the section and defined as:

$$\phi_3^{\mathrm{R}} = \tan^{-1}\left(\frac{(\boldsymbol{U}_\infty \times \boldsymbol{U}_{\mathrm{R}})\cdot \boldsymbol{e}_3}{\boldsymbol{U}_\infty \cdot \boldsymbol{U}_{\mathrm{R}}}\right) \tag{2.1.3}$$

where $\boldsymbol{U}_{\mathrm{R}}$ is the vector of the relative wind velocity

$$\boldsymbol{U}_{\mathrm{R}} = \boldsymbol{U}_\infty - \boldsymbol{w} \tag{2.1.4}$$

where $\boldsymbol{w}$ is the velocity of the section quarter-chord point

$$\boldsymbol{w} = \dot{u}_1\,\boldsymbol{e}_1 + \left(\dot{u}_2 + \frac{B}{4}\,\dot{\phi}_3\right)\boldsymbol{e}_2 \tag{2.1.5}$$

u_2 and u_1 are respectively the wind speed magnitude, the vertical (heave) and the horizontal (sway) section displacements referred to the elastic center of the section and the dot indicates the time derivative.

$$\boldsymbol{U}_{\mathrm{R}} = -\left(U\cos\bar{\alpha} + \dot{u}_1\right)\boldsymbol{e}_1 + \left(U\sin\bar{\alpha} - \dot{u}_2 - \frac{B}{4}\,\dot{\phi}_3\right)\boldsymbol{e}_2 \tag{2.1.6}$$

The adopted positive sign convention is proposed in Figure 2.1, note that $\bar{\alpha}$ is assumed positive in the opposite direction of ϕ_3. The definition of the velocity vector $\boldsymbol{w}$ is critical since it is related to the contribution of $\dot{\phi}_3$ to the effective angle of incidence α^{E}. In the classical aeronautical convention, in the airfoil theory, its vertical component is assumed as $\dot{u}_2 - \frac{B}{4}\,\dot{\phi}_3$ indicating that the velocity at the three-quarter-chord point is selected for the calculation of α^{E}. However, this is inconsistent with the airfoil theory and the wind tunnel derived data concerning bluff bridge sections [57, 58]. Alternatively, the expression $\dot{u}_2 + \frac{B}{4}\,\dot{\phi}_3$ can be assumed corresponding to the velocity at the quarter-chord point.
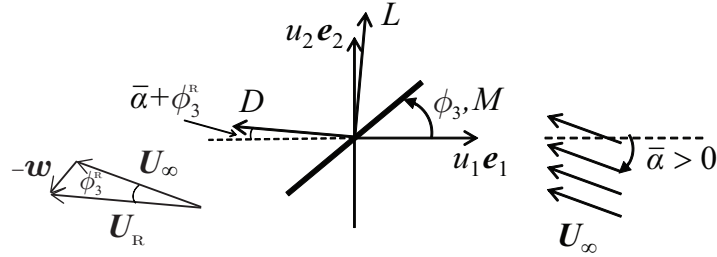
Fig. 2.1: *Positive aerodynamic convention.*

$$\phi_3^{\mathrm{R}} = \tan^{-1}\left[-\frac{\dot{u}_1\sin\bar{\alpha} + \left(\dot{u}_2 + \frac{B}{4}\,\dot{\phi}_3\right)\cos\bar{\alpha}}{U + \dot{u}_1\cos\bar{\alpha} - \left(\dot{u}_2 + \frac{B}{4}\,\dot{\phi}_3\right)\sin\bar{\alpha}}\right] \tag{2.1.7}$$

by assuming small initial angles of attack $\bar{\alpha} \approx 0$, expression (2.1.7) can be linearized and approximated as

$$\phi_3^{\mathrm{R}} \approx -\frac{\dot{u}_2 + \frac{B}{4}\,\dot{\phi}_3}{U + \dot{u}_1} \tag{2.1.8}$$

thus the effective angle of attack is given by the following expression

$$\alpha^{\mathrm{E}} = \bar{\alpha} + \phi_3 - \frac{\dot{u}_2 + \frac{B}{4}\,\dot{\phi}_3}{U + \dot{u}_1} \tag{2.1.9}$$

that, when no motion is induced in the section, becomes

$$\alpha^{\text{E}} = \bar{\alpha} + \phi_3 \tag{2.1.10}$$

2.2 Static Aeroelastic Loads and Torsional Divergence

The static drag, lift, and aerodynamic moment can be expressed in a form equivalent to (2.1.2), where the effective angle of attack is given by (2.1.10) and the static coefficients can be obtained via experimental or numerical simulations. These loads, functions of the angle ϕ_3, introduce an aerodynamic torsional stiffness term, proportional to the square of the wind speed, and usually of opposite sign of the elasto-geometric stiffness of the structure; thus, by increasing the velocity of the flow, the torsional divergence occurs when the global stiffness, combination of the aerodynamic and elastogeometric stiffness, becomes zero. By referring to the case of a single degree-of-freedom (SDOF) sectional model, the equilibrium of the section under the action of the aeroelastic loads can be reduced to the linear equilibrium equation involving the equivalent torsional stiffness of the structure (accounting for the contribution of the deck elastic stiffness and the cables geometric stiffness) and the aerodynamic moment

$$K_\phi \, \phi_3 = \frac{1}{2} \rho \, U^2 B^2 C_{\text{M}}(\alpha^{\text{E}}) \tag{2.2.1}$$

In the hypothesis of small angle of attack and small rotation and assuming $\bar{\alpha} = 0$, that is $\alpha^{\text{E}} = \phi_3$, the aerodynamic moment coefficient can be linearized around $\phi_3 = 0$ as

$$C_{\text{M}}(\phi_3) = C_{\text{M}}^0 + \phi_3 \left. \frac{dC_{\text{M}}}{d\phi_3} \right|_{\phi_3=0} \tag{2.2.2}$$

and the equilibrium Eq. (2.2.1) can be written in the form

$$K_\phi \, \phi_3 = \frac{1}{2} \rho \, U^2 B^2 \left(C_{\text{M}}^0 + C_{\text{M}}' \phi_3 \right) \tag{2.2.3}$$

where C_{M}^0 is the value of the moment coefficient at $\phi_3 = 0$ and $C_{\text{M}}' = \left. \frac{dC_{\text{M}}}{d\phi_3} \right|_{\phi_3=0}$ represents the slope of the static moment coefficient curve evaluated at $\phi_3 = 0$. By defining the strictly positive parameter $\sigma^2 = \frac{1}{2} \rho \, U^2 B^2$, Eq. (2.2.3) can be written as

$$\left(K_\phi - \sigma^2 C_{\text{M}}' \right) \phi_3 = \sigma^2 C_{\text{M}}^0 \tag{2.2.4}$$

from Eq. (2.2.4) it is easy to notice that the bifurcation of the equilibrium state occurs when

$$K_\phi - \sigma^2 C_{\text{M}}' = 0 \tag{2.2.5}$$

and the velocity at the onset of the torsional divergence can be calculated as:

$$U^{\text{cr}} = \sqrt{\frac{2K_\phi}{\rho \, B^2 C_{\text{M}}'}} \tag{2.2.6}$$

When a continuous model is employed to describe the aeroelastic response of a structure, the velocity at the onset of the torsional divergence can be still evaluated by solving an eigenvalue problem, equivalent

to the one shown in (2.2.4) for the case of an SDOF system, where the critical condition is identified when the first eigenvalue becomes purely real.

2.3 Dynamic Aeroelastic Loads and Flutter

Flutter is a dynamic aeroelastic instability that arises when the aerodynamic loads are such that the global damping of the mechanical system vanishes, hence, a perturbation of the equilibrium state can lead to unbounded oscillations of the structure. Differently from the case of the torsional divergence earlier discussed, this dynamic instability involves the torsional rotation ϕ_3 of the section and it arises as a flexural-torsional periodic oscillation where, in the case of suspension bridges, the torsional rotation is coupled with the vertical motion. The critical flutter velocity can be evaluated either as the solution of a linear (or nonlinear) eigenvalue problem or by time-dependent simulations.

One important parameter used in the description of the unsteady aerodynamics is the reduced frequency K adopted to determine the degree of unsteadiness of the system. In aircraft aerodynamics, this parameter is usually defined in terms of the airfoil (streamlined lifting surface) semi-chord $c/2$, while in bridges aerodynamics applications, is commonly expressed in terms of the section width B

$$K := \frac{2\pi f B}{U} \tag{2.3.1}$$

where f is the section dimensional frequency of oscillation in the flow. Another important parameter is represented by the reduced time (or nondimensional time) s representing the relative distance measured in width length B (or, in alternative, semi-chord $c/2$) traveled by the section through the flow in the time t:

$$s := \frac{1}{B} \int_0^t U \, dt \tag{2.3.2}$$

2.3.1 The Frequency-Domain Approach in the Flutter Analysis

Analytical frequency-domain closed-form expressions of the aerodynamic lift and moment acting on a lifting surface oscillating in an incompressible flow were developed by Theodorsen in 1935 [21]

$$L(K) = \pi \frac{1}{2}\rho \, U^2 B \left[\frac{B}{2U^2}\ddot{h} + \frac{B}{2U}\dot{\alpha} - \left(\frac{B}{2V}\right)^2 a\,\ddot{\alpha} \right] + $$
$$+ 2\pi \frac{1}{2}\rho \, U^2 B \left[\frac{\dot{h}}{U} + \alpha + \frac{B\dot{\alpha}}{2U}\left(\frac{1}{2} - a\right) \right] C(K) \tag{2.3.3}$$

$$M(K) = -\rho \frac{B^2}{8} \left[\pi \left(\frac{1}{2} - a\right) U B\dot{\alpha} + \pi \frac{B^2}{2}\left(\frac{1}{8} + a^2\right)\ddot{\alpha} - a\,\pi B\,\ddot{h} \right] + $$
$$+ 2\rho U \frac{B^2}{4}\pi\left(a + \frac{1}{2}\right)\left[U\,\alpha + \dot{h} + \frac{B}{2}\left(\frac{1}{2} - a\right)\dot{\alpha} \right] C(K) \tag{2.3.4}$$

where a is the distance of the pitch axis (elastic axis) measured from the mid-chord $B/2$, whereas the reduced frequency-dependent function $C(K) = F(K) + i\,G(K)$ is the complex-valued *Theodorsen function* accounting for wake effects on the unsteady aerodynamic loads.

However, these expressions are only valid for thin airfoil assuming fully attached flow and small oscillations and, unfortunately, as already mentioned, in the case of bridge deck cross section analytical closed-form expressions for the aerodynamic loads are not available. The most common description in the frequency-domain of the aerodynamic loads acting on a sharp-edge bluff section, such as bridge cross sections, was first given by Scanlan [24] as

$$D(K) = \tfrac{1}{2}\rho B\, U^2\Big(\frac{K}{U}P_1\dot{h} + \frac{KB}{U}P_2\dot{\alpha} + K^2P_3\alpha + \frac{K^2}{B}P_4h + \frac{K}{U}P_5\dot{p} + \frac{K^2}{B}P_6p\Big)$$

$$L(K) = \tfrac{1}{2}\rho B\, U^2\Big(\frac{K}{U}H_1\dot{h} + \frac{KB}{U}H_2\dot{\alpha} + K^2H_3\alpha + \frac{K^2}{B}H_4h + \frac{K}{U}H_5\dot{p} + \frac{K^2}{B}H_6p\Big) \qquad (2.3.5)$$

$$M(K) = \tfrac{1}{2}\rho B^2U^2\Big(\frac{K}{U}A_1\dot{h} + \frac{KB}{U}A_2\dot{\alpha} + K^2A_3\alpha + \frac{K^2}{B}A_4h + \frac{K}{U}A_5\dot{p} + \frac{K^2}{B}A_6p\Big)$$

The eigenvalue approach is thus based on the knowledge of the so-called *flutter* (or *aeroelastic*) *derivatives*, P_i, H_i, and A_i $i = 1,...6$, that is, coefficients depending on the reduced frequency K and obtained via experimental or numerical simulations by imposing a forced sinusoidal motion to the section. The motion of the structure is described by the heave h, the sway p, and the pitch α accordingly to the original definition given by Scanlan and assuming the sign convention shown in Figure 2.2. Further details on the procedure to evaluate the aeroelastic derivatives will be given in Chapter 3. The eigenvalue problem is then solved by linearizing the bridge equations of motion around the configuration induced by the action of static component of the aeroelastic forces. The critical condition is obtained at the value of the wind
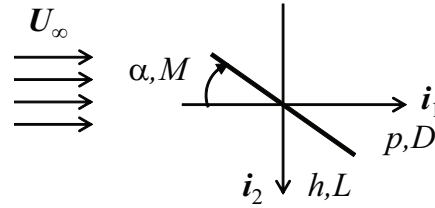
Fig. 2.2: *Scanlan positive aerodynamic convention.*

speed where the first complex eigenvalue describes an undamped vibrational mode. The full description of the eigenvalue procedures developed to investigate the flutter phenomenon in suspension bridges is provided in Section 5.2.

2.3.2 The Time-Domain Approach in the Flutter Analysis

Differently from the eigenvalue analysis, the time-dependent approach allows to account for all the nonlinearities modeled in the system, geometrical and constitutive, and evaluate the flutter condition by analyzing the time histories at different wind speeds and estimating the critical velocity when an undamped periodic oscillation is reached. In this case, the aerodynamic loads can be suitably defined in the time domain by employing the *indicial theory*. Within this theory, the time evolution of the aerodynamic forces is described by the convolution integral of particular functions representing the response of the bridge section to the step-change (instantaneous variation) of an aerodynamic input.

This more general theory for the formulation of the unsteady aerodynamic loads in the time domain was first developed by Wagner in 1925 [45], for thin airfoil in incompressible flow as a solution for the indicial lift by imposing a step-change in the airfoil angle of attack. In particular, the resulting variation

in the lift coefficient for an instantaneous change of the angle of attack can be written as:

$$C_{\mathrm{L}}(t) = \frac{\pi c}{2U}\,\delta(t) + 2\pi\alpha\,\phi(s) \tag{2.3.6}$$

where $\delta(t)$ is the Dirac-δ function, $\phi(s)$ is the Wagner function, $s = (2U/c)\,t$ (with the assumption of being U constant) and c the airfoil chord length; $2\pi\alpha$ is the steady-state value of the lift coefficient for 2D thin airfoil. Usually, the most complicated exact analytical form of the Wagner function $\phi(s)$ is replaced by a simpler linear combination of exponential terms

$$\phi(s) \approx 1 - \sum_{i=1}^{N} a_i\,e^{-b_i s} \tag{2.3.7}$$

where, according to the Wagner exact solution, $b_i > 0$ and $\sum_{i=1}^{N} a_i = 0.5$. One of the most employed approximation of the function $\phi(s)$ is due to Jones [59] and defined as

$$\phi(s) \approx 1 - \left(0.165\,e^{-0.0455s} + 0.335\,e^{-0.3s}\right) \tag{2.3.8}$$

An algebraic, less accurate, approximation of the Wagner function was proposed by Garrick [48]

$$\phi(s) \approx \frac{s+2}{s+4} \tag{2.3.9}$$
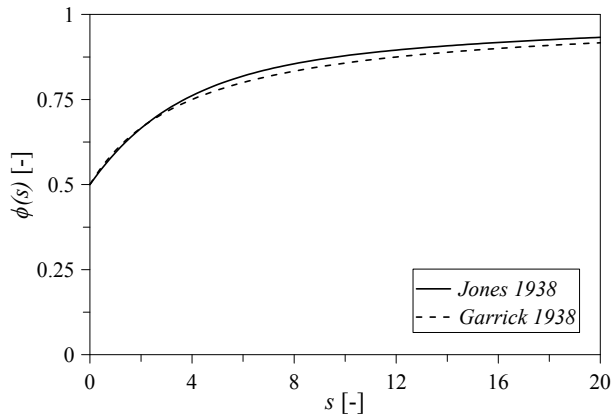
Fig. 2.3: *Wagner function approximations.*

The main advantage of the method is that, when the response to this particular variation of the aerodynamic input ξ is determined, then the unsteady response to an arbitrary change in the effective angle of attack can be obtained by means of Duhamel integral, that is the superposition of the indicial responses.

$$F(t) = \xi(0)\phi(t) + \int_0^t \frac{d\xi}{dt}\,\phi(t-\tau)\,d\tau \tag{2.3.10}$$

2.3.3 Unsteady Aerodynamics of Bridges cross sections in the Linear Indicial Theory

As previously described, the linear indicial method is based on the fundamental principle that the motion of the section develops in regime of small oscillations and assuming a fully attached flow around the lifting surface. Even if a closed form expression of the indicial function for bridges cross sections cannot be determined, computational fluid dynamics (CFD) simulations can be employed to derive numerically the indicial response of such sections.

Based on the assumptions made, the aerodynamic loads, which are in general nonlinear functions of the effective angle of attack α^{E}, can be linearized about the mean value α^0, and the generic unsteady aerodynamic coefficient $C_{\mathrm{AE}}(\alpha^{\mathrm{E}}, t)$ can then be expressed as

$$C_{\mathrm{AE}}(\alpha^{\mathrm{E}}, t) = C_{\mathrm{AE}}(\alpha^0, t = 0) + \left.\frac{\partial C_{\mathrm{AE}}}{\partial \alpha^{\mathrm{E}}}\right|_{\alpha^0} \Delta\alpha^{\mathrm{E}} \tag{2.3.11}$$

If $\partial C_{\mathrm{AE}}/\partial\alpha^{\mathrm{E}}$ does not depend on α^{E} but it only depends on the time after the instantaneous change of the aerodynamic input is applied, then the coefficient can be written as

$$C_{\mathrm{AE}}(t) = C_{\mathrm{AE}}(\alpha^0, t = 0) + \Phi_{\mathrm{AE}}(t)\Delta\alpha^{\mathrm{E}} \tag{2.3.12}$$

where the function $\Phi_{\mathrm{AE}}(t)$ represents the indicial response of the section due to a step-change of the angle α^{E}. At the time $t = 0$, when the instantaneous change in the effective angle of attack is applied, there is no circulation in the flow around the section. As time progresses the non-circulatory part of the aerodynamic loads decays quickly as the pressure waves propagate away at the local speed of sound, and the circulatory part of the loads simultaneously begins to build up. By referring to the linearized expression of (2.1.7), the unsteady part of the effective angle of attack α^{E} can be decomposed in the contribution given by the pitch, the heave, and the sway motions, and the response in terms of the aerodynamic coefficients can be generalized by the indicial theory as follow

$$C_{\mathrm{AE}}(t) = \frac{dC_{\mathrm{AE}}}{d\xi}\left[\xi(0)\Phi_{\mathrm{AE}}(t) + \int_0^t \frac{d\xi}{dt}(\tau)\Phi_{\mathrm{AE}}(t - \tau)\,d\tau\right] \tag{2.3.13}$$

where $\xi = \alpha,\ \dot{p}/U,\ \dot{h}/U$ represents the aerodynamic input. The evaluation of the convolution integral (2.3.13) contains all the prior time history information of what has happened to the aerodynamic response since the initial time.

Differently from the case of the determination of the aeroelastic derivatives, experimental procedures to obtain the indicial functions for bridges deck cross sections are not yet well established, thus numerical CFD simulations are typically employed to this purpose. The indicial functions $\Phi_{\mathrm{AE}}(s)$ are then typically represented by a series of N exponential terms whose coefficients can be obtained by least-square approximations of the aerodynamic response curves calculated numerically. In this approach, the main issue is related to the instantaneous step-change of the aerodynamic input that has to be assigned to obtain the indicial response. The numerical procedures adopted to bypass this inconvenience is to simulate the instantaneous step-change via an equivalent smooth ramp variation of the input. One could also assume the temporal dynamics of the section configuration right after the first time step. Alternatively to the step-change simulations, it is also possible to derive the analytical approximation of the indicial functions from the aeroelastic derivatives obtained, also in this case, either by experimental procedures or CFD calculations. Further details on these procedures are given in Chapter 3.

2.3.4 Aerodynamic Added State Formulation

Once the functions $\Phi_{\mathrm{AE}}(s)$ are evaluated, the main issue related to the indicial method is the calculation of the convolution integral (2.3.13) in order to evaluate the aeroelastic response of the section and integrate the aeroelastic governing equations. The most interesting strategy to bypass the calculation of the Duhamel integral consists in the use of the state-space representation of the unsteady aerodynamics. In particular, the unsteady loads are defined as a combination of further aerodynamic states whose time evolution is described by a set of first-order differential equations coupled with the motion of the section.

Let now derive the expressions of the aerodynamic forces and moment by the superposition of the indicial responses obtained for a step change in the wind angles of attack α, $\dot{h}/U$, and $\dot{p}/U$. By assuming respectively $j = $ Lift, Drag, and Moment and $\xi = \alpha$, $\dot{p}/U$, $\dot{h}/U$, the indicial function for the generic aerodynamic load due to a step change of the input ξ, can be generalized with the exponential series of N_j^ξ terms

$$\Phi_j^\xi(s) = 1 - \sum_{k=1}^{N_j^\xi} a_{j,k}^\xi \, e^{-b_{j,k}^\xi s} \tag{2.3.14}$$

where s is the nondimensional time defined as $s = \frac{2U}{B}t$. By the use of the Duhamel superposition integral, the aerodynamic load $F_j(t)$ due to the generic variation of all the aerodynamic inputs $\xi(t)$ can be written as

$$F_j(t) = G_j \sum_\xi c_j^\xi \int_{-\infty}^{t} \Phi_j^\xi(t - \tau)\dot{\xi}(\tau) \, d\tau \tag{2.3.15}$$

where the dot is the derivative with respect to time t and G_j is a coefficient representing the mean kinetic force or moment per unit length of the air, and it is defined as

$$G_j = \begin{cases} \frac{1}{2}\rho U^2 B & j = \text{ Lift and Drag} \\[2mm] \frac{1}{2}\rho U^2 B^2 & j = \text{Moment} \end{cases} \tag{2.3.16}$$

By assuming the origin of the time at $t = 0$, Eq. (2.3.15) can be written in the form

$$F_j(t) = G_j \sum_\xi^\xi c_j^\xi \left[\Phi_j^\xi(t)\xi(0) + \int_0^t \Phi_j^\xi(t - \tau)\dot{\xi}(\tau) \, d\tau \right] \tag{2.3.17}$$

and integrating by part the convolution integral in (2.3.17), the aerodynamic load can be expressed as

$$F_j(t) = G_j \sum_\xi c_j^\xi \left[\Phi_j^\xi(t)\xi(0) + \left(\Phi_j^\xi(0)\xi(t) - \Phi_j^\xi(t)\xi(0) \right) + \int_0^t \dot{\Phi}_j^\xi(t - \tau)\xi(\tau) \, d\tau \right]$$

$$= G_j \sum_\xi c_j^\xi \left[\Phi_j^\xi(0)\xi(t) + \int_0^t \dot{\Phi}_j^\xi(t - \tau)\xi(\tau) \, d\tau \right] \tag{2.3.18}$$

By referring to the indicial function Φ_j^ξ as in Eq. (2.3.14), its derivative with respect to time t is given by:

$$\dot{\Phi}_j^\xi(t - \tau) = \sum_{k=1}^{N_j^\xi} \hat{b}_{j,k}^\xi a_{j,k}^\xi \, e^{-\hat{b}_{j,k}^\xi(t - \tau)} \tag{2.3.19}$$

where, from the linear relation between the dimensionless time s and the time t, the coefficient $\hat{b}_{j,k}^\xi$ is defined as $\hat{b}_{j,k}^\xi = (2U/B)\, b_{j,k}^\xi$. For the sake of notation, it is useful to introduce the function

$$\varphi_{j,k}^{\xi}\left(t-\tau\right) := e^{-\hat{b}_{j,k}^{\xi}\left(t-\tau\right)} \tag{2.3.20}$$

and rewrite Eq.(2.3.19) in term of $\varphi_{j,k}^{\xi}\left(t-\tau\right)$ as

$$\dot{\Phi}_{j}^{\xi}\left(t-\tau\right) = \sum_{k=1}^{N_{j}^{\xi}} \hat{b}_{j,k}^{\xi} a_{j,k}^{\xi} \varphi_{j,k}^{\xi}\left(t-\tau\right) \tag{2.3.21}$$

thus, the convolution integral in (2.3.18) accordingly to (2.3.21) can be written as

$$\int_{0}^{t} \dot{\Phi}_{j}^{\xi}(t-\tau)\xi(\tau)\,d\tau = \sum_{k=1}^{N_{j}^{\xi}} \hat{b}_{j,k}^{\xi} a_{j,k}^{\xi} \int_{0}^{t} \varphi_{j,k}^{\xi}\left(t-\tau\right)\xi(\tau)\,d\tau \tag{2.3.22}$$

By denoting now with $W_{j,k}^{\xi}$ the new generic state variable governing the aerodynamics of the section and defined as

$$W_{j,k}^{\xi}(t) := \int_{0}^{t} \varphi_{j,k}^{\xi}\left(t-\tau\right)\xi(\tau)\,d\tau \tag{2.3.23}$$

Eq. (2.3.22) becomes

$$\int_{0}^{t} \dot{\Phi}_{j}^{\xi}(t-\tau)\xi(\tau)\,d\tau = \sum_{k=1}^{N_{j}^{\xi}} \hat{b}_{j,k}^{\xi} a_{j,k}^{\xi} W_{j,k}^{\xi}(t) \tag{2.3.24}$$

By enforcing the differentiation properties of the convolution integral, the time derivative, counterpart of (2.3.23), can be written as

$$\dot{W}_{j,k}^{\xi}(t) = \xi(t)\varphi_{j,k}^{\xi}(0) + \int_{0}^{t} \dot{\varphi}_{j,k}^{\xi}\left(t-\tau\right)\xi(\tau)\,d\tau \tag{2.3.25}$$

where it is worth notice that $\frac{d}{dt}\left[\varphi_{j,k}^{\xi}\left(t-\tau\right)\right] = -\hat{b}_{j,k}^{\xi}\varphi_{j,k}^{\xi}\left(t-\tau\right)$ and that $\varphi_{j,k}^{\xi}(0) = 1$. Consequently, Eq. (2.3.25) can be manipulated and cast in the form

$$\dot{W}_{j,k}^{\xi}(t) = \xi(t) - \hat{b}_{j,k}^{\xi} \int_{0}^{t} \varphi_{j,k}^{\xi}\left(t-\tau\right)\xi(\tau)\,d\tau \tag{2.3.26}$$

Finally, according to the definition (2.3.23) the time evolution of the generic added aerodynamic state $W_{j,k}^{\xi}(t)$ is governed by the following differential equation

$$\dot{W}_{j,k}^{\xi}(t) = \xi(t) - \hat{b}_{j,k}^{\xi} W_{j,k}^{\xi}(t) \tag{2.3.27}$$

The first-order differential Eq. (2.3.27) represents one of the $\sum_{j=1}^{3}\sum_{\xi} N_{j}^{\xi}$ additional state equations describing the time evolution of the $j_{max} = 3$ unsteady aerodynamic loads (the lift, the drag and the aerodynamic moment), with N_{j}^{ξ} exponential terms (for each indicial function) due to the generic variation of the aerodynamic inputs $\xi(t)$.

2.3.5 Nonlinear Indicial Formulation

Differently from the linear case, nonlinear indicial functions can depend on the motion of the section and not only on time delay $t - \tau$ since the application of the instantaneous step-change of the aerodynamic state variable $\xi(t)$ such as the angle of attack α, $\dot{h}/U$, etc. The bases of the nonlinear indicial theory were first formalized by [60, 61] and [62], and more recently in [63, 64] and [65] where interesting applications in the aerodynamics of helicopter blades sections in subsonic and supersonic flow regimes can be found.

In the nonlinear indicial formulation, a more general expression of the aerodynamic coefficient given in (2.3.13) can be defined as

$$C_{\mathrm{AE}}(t) = C_{\mathrm{AE}}\left(t, \xi(0)\right) + \int_0^t \left.\frac{\partial C_{\mathrm{AE}}}{\partial \xi}\right|_\tau \frac{d\xi}{dt}(\tau)\Phi_{\mathrm{AE}}(\xi; t - \tau) \, d\tau \qquad (2.3.28)$$

where the nonlinear indicial function Φ_{AE} depends not only on the time interval $t - \tau$ but also on the time evolution of the aerodynamic state $\xi(t)$. Since the fluid-dynamics of sharp-edge bluff-sections, like those considered in this work, is characterized by flow separation at any value of the mean angle of attack, and the aerodynamic loads generated at different angles may vary significantly because of the separation effects, the assumption of linear indicial response may not be sufficient to describe the aeroelastic response of bridge deck sections.

The exponential series approximation can still be adopted to describe the indicial response at a generic input ξ

$$\Phi_{\mathrm{AE}}(\xi; t - \tau) = 1 - \sum_{i=1}^N A_i(\xi)\, e^{-B_i(\xi)s} \qquad (2.3.29)$$

where, differently from expression (2.3.7), the coefficients A_i and B_i of the series expansion now depend on the aerodynamic state ξ itself. Thus, these coefficients must be first determined for each instantaneous change in ξ and then expressed by an appropriate analytical approximation determined via least square minimization of the coefficients evaluated at each discrete values $\bar{\xi}$. In this sense, a low-order polynomial approximation can be adopted:

$$A_i(\bar{\xi}) = \sum_{j=0}^M p_j\, \bar{\xi}_j\,, \ \ B_i(\bar{\xi}) = \sum_{j=0}^M p_j\, \bar{\xi}_j \qquad (2.3.30)$$

The use of nonlinear indicial functions in the study of the aeroelastic response of suspension bridges, turns out to be not straightforward as in the linear case. In fact, the added state formulation adopted to bypass the evaluation of the convolutional integral is not possible anymore because of the functional nature of the integral (2.3.28). Therefore, a step-by-step time integration of the aeroelastic equations might be considered for evaluating the dynamic response of the bridge. In Chapter 3, the formulation of the nonlinear indicial functions for a bridge deck cross section is proposed and the nonlinear dependence to the angle of attack of the indicial coefficients is derived. However, the fully nonlinear aerodynamic formulation was not implemented in the aeroelastic modeling and analysis of suspension bridge performed in the following chapters.

Nevertheless, as to retain the effect of nonlinear unsteady aerodynamic contributions, at least at the first order, nonlinearities are retained within the coefficients c_j^ξ in Eq. (2.3.15) representing the static drag, lift, and moment coefficients curve slopes. Within this representation, the aerodynamic loads are calculated at the effective angle of attack α^{E}, defined in Eq. (2.1.9), and only the instantaneous variation from the dynamic configuration, is assumed to be linear and described through the indicial formulation derived in Section 2.3.4.

Chapter 3
Aerodynamics of Bridge Deck Cross Sections

Long-span bridges have remarkably low natural frequencies with an associated low ratio between the fundamental torsional and vertical modes. This makes long-span bridges very susceptible to the actions of strong wind and may experience, among others, vortex-induced vibration, turbulence-induced buffeting and motion-induced flutter instability. While the computationally efficient mode-by-mode approach used in the prediction of flutter and buffeting is valid for the large majority of bridges currently built, the aerodynamic performance of very long-span bridges requires studies at very low frequencies and associated higher reduced velocities. In those circumstances aerodynamic coupling needs to be properly considered. In this sense aerodynamic coupling in terms of the contribution of the aerodynamic forces on the bridge system damping can lead to a multi-mode coupled flutter behavior.

Flutter and buffeting aeroelastic responses of bridges are usually computed using aerodynamic forces linearized about statically deformed configurations. This approach based on linear aerodynamic forces model is quite useful and has been proved to work in most designs, however, particularly for long-span bridges, this model is incapable of accounting for complex issues such as aerodynamic nonlinearities and turbulence effects, increasingly important when the aerodynamic characteristics of bridge decks exhibit significant sensitivity with respect to the effective angle of incidence and as the bridges span increases.

In this respect, the author of this thesis is proposing a novel nonlinear aerodynamic model and associated time-domain analysis framework where the aeroelastic response of bridges under turbulent winds in pre- and post-flutter condition is predicted using an efficient reduced-order model for the nonlinear aerodynamics based on novel nonlinear indicial functions. The aerodynamic forces model includes the frequency-dependent unsteady aerodynamic characteristics that are nonlinear functions of the effective angle of incidence, and is based on a nonlinear functional form accounting for viscous flow, thickness effect, large flow separation at varying angles of incidence. The proposed aerodynamic framework provides a novel tool to study the influence of aerodynamic nonlinearities and turbulence on aeroelastic response of bridges.

Before plunging into the description of the proposed procedure developed to evaluate the aerodynamic indicial functions, a short overview of the aerodynamic modeling aspects along with pertinent assumptions used in the computational tools employed in this work are presented.

3.1 The Equations of Viscous Flows

A brief overview describing the equations governing the physics of the problems is presented. Most comprehensive and detailed interpretations of the fluid dynamics theories and the derivation and application of the Navier-Stokes equations can be found in the wide available literature, among which the

book of F.M. White [66] represents, according to the author of this thesis, one of the most interesting contribution.

The symbolism adopted to define the physical parameters governing the motion of viscous fluids are presented next. Let consider an infinitesimal fluid control volume $d\mathcal{V} = dx\,dy\,dz$, this volume can be assumed fixed in the space with the fluid moving through it or, alternatively moving into the stream with a certain velocity $\boldsymbol{U}$. At the time t, the velocity vector describing the motion of the fluid volume in the fixed inertial frame $(\boldsymbol{e}_1, \boldsymbol{e}_2, \boldsymbol{e}_3)$ can be expressed as:

$$\boldsymbol{U}(\boldsymbol{x}, t) = u(\boldsymbol{x}, t)\,\boldsymbol{e}_1 + v(\boldsymbol{x}, t)\,\boldsymbol{e}_2 + w(\boldsymbol{x}, t)\,\boldsymbol{e}_3$$

where $\boldsymbol{x} = \boldsymbol{x}(t)$ is the volume position vector at time step t. By introducing the fluid density $\rho = \rho(\boldsymbol{x}, t)$, the instantaneous time rate of change in density of the fluid element as it moves from position $\boldsymbol{x}(t_0)$ to $\boldsymbol{x}(t)$ is given by the *substantial derivative* of ρ:

$$\frac{D\rho}{Dt} = \frac{\partial\rho}{\partial t} + \boldsymbol{U} \cdot \nabla(\rho) \tag{3.1.1}$$

where $\partial\rho/\partial t$ is the *local derivative* of ρ, with the physical meaning of average time rate of change of fluid density at the initial position $\boldsymbol{x}(t_0)$, whereas $\boldsymbol{U} \cdot \nabla(\rho)$ is the *convective derivative* and represents the time rate of change of ρ due to the fluid motion from position $\boldsymbol{x}(t_0)$ to $\boldsymbol{x}(t)$. $\nabla(\cdot)$ is the gradient operator defined as:

$$\nabla(\cdot) = \frac{\partial(\cdot)}{\partial x_1}\boldsymbol{e}_1 + \frac{\partial(\cdot)}{\partial x_2}\boldsymbol{e}_2 + \frac{\partial(\cdot)}{\partial x_3}\boldsymbol{e}_3$$

The internal stress state in the infinitesimal fluid elements is described by the stress tensor $\boldsymbol{T}$

$$\boldsymbol{T} = \begin{bmatrix} \sigma_1 & \tau_{12} & \tau_{13} \\ \tau_{21} & \sigma_2 & \tau_{23} \\ \tau_{31} & \tau_{32} & \sigma_3 \end{bmatrix} \tag{3.1.2}$$

whereas the forces acting on the generic volume can be summarized as follow:

a) The surface forces, such as the pressure, at the interface $d\boldsymbol{S}$ between two adjacent fluid elements.
b) The volume forces $\boldsymbol{f} = (f_1\boldsymbol{e}_1 + f_2\boldsymbol{e}_2 + f_3\boldsymbol{e}_3)$, such as the gravitational force.

On the generic fluid control volume, the rate of work due to volume and surface forces can be written as:

$$\mathcal{L}^I = \rho\,(\boldsymbol{f} \cdot \boldsymbol{U})\,d\mathcal{V} + [\nabla \cdot (\boldsymbol{T} \cdot \boldsymbol{U}) - \nabla \cdot (\rho\boldsymbol{U})]\,d\mathcal{V} \tag{3.1.3}$$

where

$$\boldsymbol{T} \cdot \boldsymbol{U} = \begin{bmatrix} u\sigma_1 + v\tau_{12} + w\tau_{13} \\ u\tau_{21} + v\sigma_2 + w\tau_{23} \\ u\tau_{31} + v\tau_{32} + w\sigma_3 \end{bmatrix} \tag{3.1.4}$$

The net flux of heat into the element is given by two different contributions: the volumetric heating, such as absorbtion or emission of radiation, and the heat transfer across the surface due to temperature gradients (thermal conduction).

$$\mathcal{L}^{II} = [\rho\dot{q} + \nabla \cdot (k\nabla\mathcal{T})]\,d\mathcal{V} \tag{3.1.5}$$

where $\dot{q}$ represents the rate of volumetric heat added per unit mass, therefore $\rho\dot{q}\,d\mathcal{V}$ is the volumetric heating of element, with $q = ||\boldsymbol{q}(\boldsymbol{x}, t)||$. The Fourier law of heat conduction has been employed, such that the temperature $\mathcal{T}$ and the thermal conductivity k lead to: $\dot{\boldsymbol{q}} = -k\nabla\mathcal{T}$. The rate of energy exchange inside the fluid volume, can be written as:

$$\mathcal{L}^{III} = \left\{ \frac{\partial}{\partial t}\left[\rho\left(e + \frac{U^2}{2}\right)\right] + \nabla \cdot \left[\rho\left(e + \frac{U^2}{2}\right)\boldsymbol{U}\right]\right\} d\mathcal{V} \tag{3.1.6}$$

where e is the element's internal energy per unit mass and $\rho U^2/2$ its kinetic energy; this expression has to be equal to the sum of the two works $\mathcal{L}^I$ and $\mathcal{L}^{II}$. The equations governing the motion of viscous flow are derived in their differential form, assuming that the fluid control volume is fixed in space and the field equations (i.e. the momentum, continuity and energy equations) are written in their conservation form. The governing equations for an unsteady three-dimensional, compressible, viscous flow are defined as follows:

1. The continuity equation (e.g. the conservation of mass equation)

$$\frac{\partial \rho}{\partial t} + \nabla \cdot (\rho \boldsymbol{U}) = 0 \tag{3.1.7}$$

2. The momentum equations (e.g. the Navier-Stokes equations)

$$\frac{\partial (\rho u)}{\partial t} + \nabla \cdot (\rho u \boldsymbol{U}) = -\frac{\partial p}{\partial x_1} + \frac{\partial \sigma_1}{\partial x_1} + \frac{\partial \tau_{12}}{\partial x_2} + \frac{\partial \tau_{13}}{\partial x_3} + \rho f_1$$

$$\frac{\partial (\rho v)}{\partial t} + \nabla \cdot (\rho v \boldsymbol{U}) = -\frac{\partial p}{\partial x_2} + \frac{\partial \tau_{21}}{\partial x_1} + \frac{\partial \sigma_2}{\partial x_2} + \frac{\partial \tau_{23}}{\partial x_3} + \rho f_2$$

$$\frac{\partial (\rho w)}{\partial t} + \nabla \cdot (\rho w \boldsymbol{U}) = -\frac{\partial p}{\partial x_3} + \frac{\partial \tau_{31}}{\partial x_1} + \frac{\partial \tau_{32}}{\partial x_2} + \frac{\partial \sigma_3}{\partial x_3} + \rho f_3 \tag{3.1.8}$$

3. The energy equation (e.g. the conservation of energy equation)

$$\frac{\partial}{\partial t}\left[\rho\left(e + \frac{U^2}{2}\right)\right] + \nabla \cdot \left[\rho\left(e + \frac{U^2}{2}\right)\boldsymbol{U}\right] = \rho\dot{q} + \nabla \cdot (k\nabla\mathcal{T}) - \nabla \cdot (p\boldsymbol{U}) + \nabla \cdot (\boldsymbol{T} \cdot \boldsymbol{U}) + \rho\boldsymbol{f} \cdot \boldsymbol{U} \tag{3.1.9}$$

Most of the CFD codes commercially available solve the Reynolds-averaged Navier-Stokes equations (or RANS equations). These are time-averaged equations of motion for the fluid flow, based on the Reynolds decomposition, whereby an instantaneous quantity is decomposed into its time-averaged and fluctuating quantities. These equations are primarily used to describe turbulent flows, and can be used with approximations based on knowledge of the properties of flow turbulence to give approximate time-averaged solutions to the Navier-Stokes equations.

For a stationary, incompressible Newtonian fluid, these equations can be written in Einstein notation as:

$$\rho\frac{D\overline{\boldsymbol{U}}}{Dt} + \rho\frac{\partial\overline{u_i' u_j'}}{\partial x_j} = \rho\boldsymbol{f} - \nabla\overline{p} + \mu\nabla^2\overline{\boldsymbol{U}} \tag{3.1.10}$$

where overline refers to the mean value of the time dependent variables and the prime refers to their fluctuation. An ensemble version of the governing equations is solved by introducing the apparent Reynolds stresses. This adds a second order tensor of unknowns for which various models can provide different levels of closure.

It is worth remarking that RANS equations do apply to flows with a time-varying mean flow. Statistically unsteady or non-stationary flows can be treated, but the turbulence models used to close the equations are valid only as long as the time over which these changes in the mean occur are large compared to the time scales of the turbulent motion containing most of the energy.

3.1.1 Boundary Conditions

Two particular types of boundary conditions are considered in this work

a) Solid surface (not porous, the so called *wall*) .
b) Inlet or outlet boundary.

Other boundary conditions, such as a free liquid surface condition, a liquid-vapor interface, and a liquid-liquid interface might be required depending on the fluid dynamic problems at hand. Details related to these boundary conditions can be found in [66].

Considering a stationary solid surface with the flow moving past it, the boundary condition assumes zero relative velocity between the surface and the fluid, that is

$$\boldsymbol{U} = \boldsymbol{0} \tag{3.1.11}$$

a *no-slip* condition at the wall. The analogous *no-slip* condition in term of the temperature $\mathcal{T}$ at the surface, can be written simply as $\mathcal{T} = \mathcal{T}_w$, where $\mathcal{T}_w$ is the temperature at the wall. If the temperature $\mathcal{T}_w$ is not known, by enforcing the Fourier law, one can write the boundary condition on the temperature gradient at the wall as

$$\left(\frac{\partial \mathcal{T}}{\partial \boldsymbol{n}}\right)_w = -\frac{\dot{q}_w}{k} \tag{3.1.12}$$

and in the case of adiabatic wall condition

$$\left(\frac{\partial \mathcal{T}}{\partial \boldsymbol{n}}\right)_w = 0 \tag{3.1.13}$$

where $\boldsymbol{n}$ denotes the direction normal to the wall. At every generic position $\boldsymbol{x}$ of the inlet or outlet boundary section of the fluid domain, it is then necessary to know the velocity field $\boldsymbol{U}$, the pressure p, and the temperature T, defined as:

$$\boldsymbol{U}(\boldsymbol{x},t) = \boldsymbol{U}_0\,,\ \ p(\boldsymbol{x},t) = p_0\,,\ \ T(\boldsymbol{x},t) = T_0 \tag{3.1.14}$$

3.1.2 Turbulent Boundary Layer on a Flat Plate

The average velocity of a turbulent flow at a specific point is proportional to the logarithm of the distance from that point to the wall, a boundary of the fluid region. The law of the wall is attributed to Theodore von Kármán in 1930. The logarithmic law of the wall is valid for flows at high Reynolds numbers, that is in a region with constant shear stress, and far enough from the wall, to be able to neglect direct viscous effects.

In the log-law region, the velocity profile can be estimated using the well known law

$$
\begin{aligned}
u^+ &= \frac{1}{k}\ln\left(y^+\right) + C \quad &\forall \quad 30 \leq y^+ \leq 300 \\
u^+ &= y^+ \quad &\forall \quad y^+ \leq 5
\end{aligned}
\tag{3.1.15}
$$

where u^+ is the nondimensional fluid velocity defined as $u^+ = U/u^*$, with U the local fluid dimensional velocity and u^* the friction velocity at wall:

$$u^* = \sqrt{\frac{\tau_w}{\rho}} \tag{3.1.16}$$

where ρ is the fluid density (for air at sea level it is $\rho = 1.225$ kg/m^3) and τ_w is the wall shear stress. The nondimensional wall distance y^+ is defined as

$$y^+ = \frac{u^* y_w}{\nu} \tag{3.1.17}$$
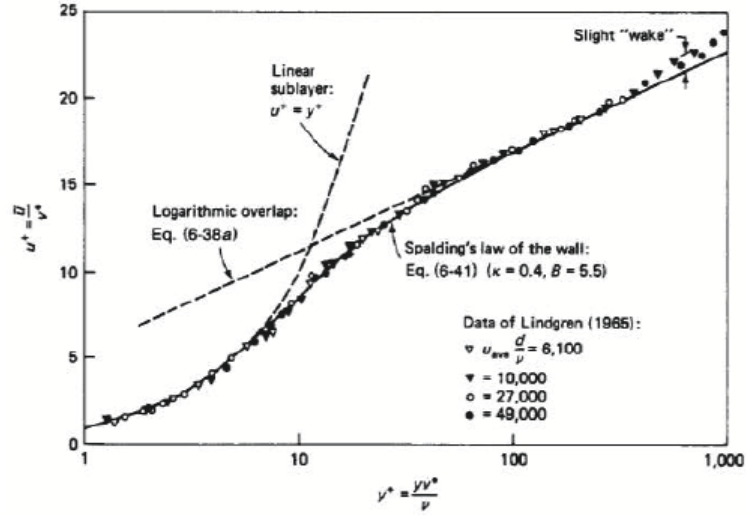
Fig. 3.1: *Law of the wall [66].*

Herein y_w represents the dimensional distance from the wall and when the y^+ values are assigned, can be found as:

$$y_w = \frac{y^+ \nu}{U}\left[\frac{1}{k}\ln\left(y^+\right) + C\right] \quad \forall \quad 30 \leq y^+ \leq 300$$
$$y_w = \frac{\nu}{U}\left(y^+\right)^2 \qquad\qquad \forall \quad y^+ \leq 5 \tag{3.1.18}$$

where ν is the air kinematic viscosity, assumed to be $\nu = 1.45 \cdot 10^{-5}$ m^2/s, whereas k is the von Kármán constant $k = 0.41$ and $C = 5.1$ is a constant [67].

3.2 Computational Fluid Dynamic Modeling, a Case Study: the GBB Suspension Bridge

The main section of the Great Belt suspension Bridge (GBB) deck was assumed as reference geometry in order to study the aerodynamic response of bluff-sharped edge sections typical of many bridge decks. This particular bridge cross section, has been widely studied in the past and a large amount of data, from experimental and numerical investigations, are today available and useful for comparison and validation purpose. Initial analyses were performed to evaluate the aerodynamic loads of this section in terms of the static coefficients at several mean angles of attack, and to calibrate the parameters of the computational tool used for the simulations. In this work, two different softwares were tested and their efficiency, in terms of accuracy in the results and computational effort, was evaluated. In particular it was determined

which commercial CFD software would be used for further studies, including the development of the indicial functions, required in the aeroelastic modeling and dynamic analysis of the bridge section. The two softwares employed are FLUENT® by ANSYS and DVMFLOW® by COWI, respectively.

3.2.1 ANSYS FLUENT®

FLUENT®, was employed first for the prediction of the aerodynamic loads around the bluff body bridge cross section. This is a robust CFD program that can solve the Reynolds-Averaged Navier-Stokes (RANS) Equations using a finite volume approach. In addition, FLUENT® has a wide range of applications and features several well-know turbulence models, including the $k - \epsilon$ selected for this work. This general purpose CFD code is able to treat many different fluid-dynamic problems, however it is not specifically developed for the study of the aerodynamics of bridge sections. Because of its wide range of application, the software implements various numerical methods for solving the equations described in Section 3.1, and consequently requires a wise choice of a number of variables, specific for the particular problem at hand.

In the following Sections, the geometry adopted, the meshing procedures, and the numerical methods selected by pertinent assumptions along with their justification are presented. In addition, the results and the comparisons with archival literature are shown as a validation of the studies carried out.

3.2.1.1 Computational Domain

The computational two dimensional (2-D) domain used in the carried out CFD simulations is proposed in Fig. 3.2. Four different subdomains have been defined in order to properly define the mesh size in each particular zone. The elliptical shape for subdomain Ω_1 has been chosen to easier fit the mesh in the leading and trailing edges regions of the bridge section. Ω_2 represents the wake zone, where vortex shedding develops when the range of velocities is such that the turbulence phenomena can generate eddies detachment. Subdomains Ω_3 and Ω_4 allow to quickly reduce the cells number in the zones far away from the bridge section. The domain is meshed by using paved triangular elements.

This *ad hoc* domain partition was selected in order to evaluate the indicial response of the cross section in terms of the step-change of the wind angle of attack. More precisely, subdomain Ω_1 is a moving zone, that moves together with the wall boundaries defined by the bridge section as a rigid body with respect to the other three domains that are fixed. Subdomains Ω_2 and Ω_3 are characterized by a deforming mesh structure whereas in subdomain Ω_4 a stationary undeformable mesh is used. In this study, four different mesh sizes are proposed and used to validate the results of the employed turbulence model in term of mesh independency. Table 3.1 shows, for each considered mesh, the number of cells generated in the subdomains Ω_i. The partition generated in the four cases, was obtained by varying the number of cells around the bridge section (subdomain Ω_1) and in the wake zone (subdomain Ω_2), that is, in the zones affected by large turbulence production. It is worth mentioning that the 4 meshes were derived accordingly with the boundary layer sensitivity analysis shown in Table 3.2, and, in particular, the first cell thickness y_w was assumed to be such that $y_w/B \approx 1.29 \cdot 10^{-4}$ (see Fig. 3.3).

Table 3.2, shows the number of triangular cells contained in each subdomain Ω_i and the value of the nondimensional wall cell thickness y_w/B adopted (Fig. 3.4). More precisely, boundary layers among the various mesh sizes, differ by the value of the first cell thickness y_w in order to have a y^+ value in the appropriate range required when using the standard wall treatment, as proposed by Launder and Spalding [68] and evaluated by the classic log-law valid for flat plates, the first expression of (3.1.15).
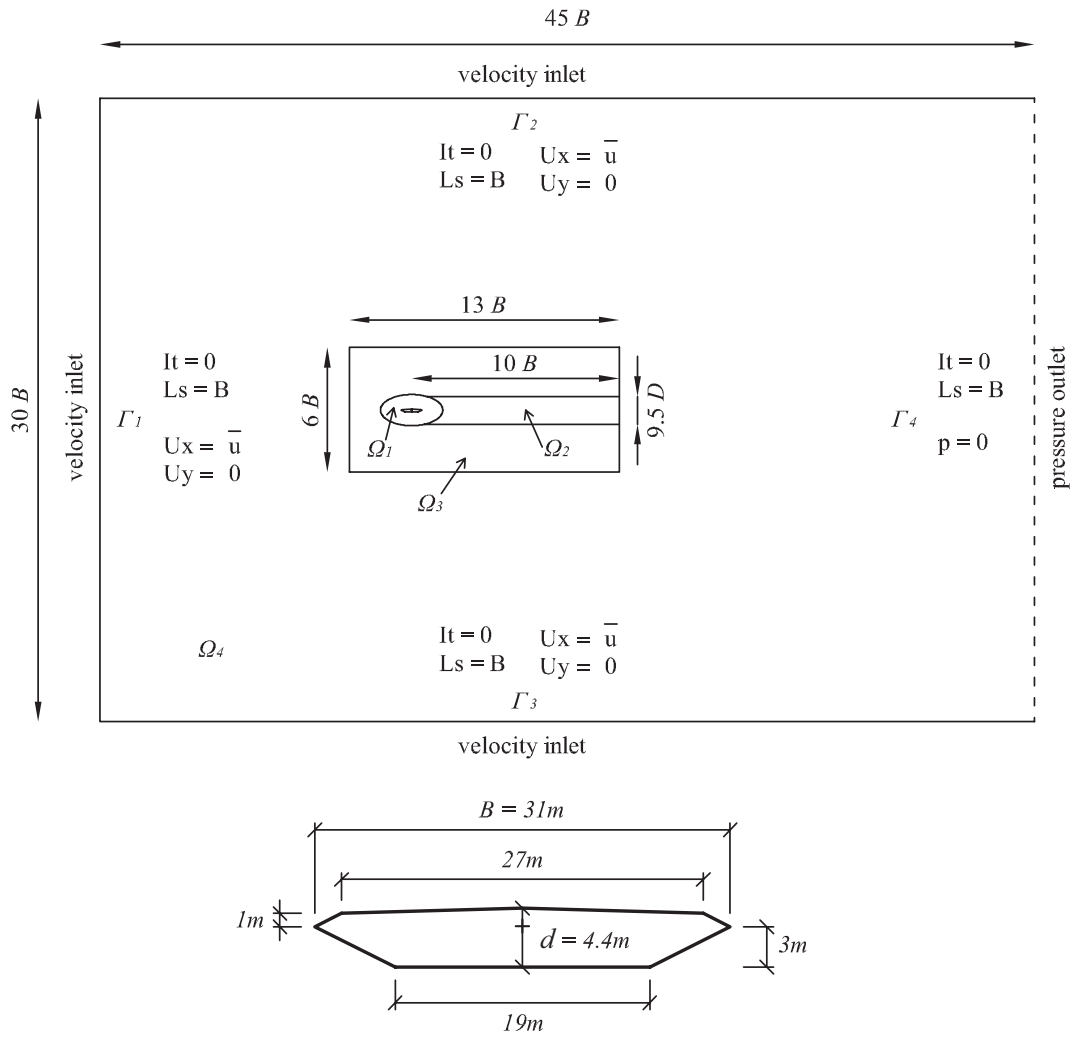
Fig. 3.2: *Computational domain and geometry of the GBB deck section.*
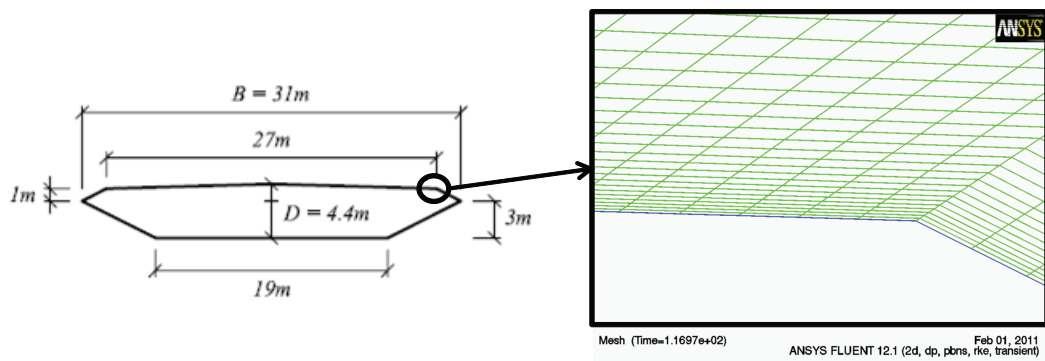
Fig. 3.3: *GBB deck section: boundary layer discretization.*

Mesh fitting has been performed to upgrade the mesh resolution closer to the bridge section boundary and in the zone where vortex shedding might develop, thus domains Ω_3 and Ω_4 have not been modified in terms of number of cells. To resolve the boundary layer close to the wall, the value of the y^+ has been

	Ω_1	Ω_2	Ω_3	Ω_4	Tot.	$\Delta[\%]$
Mesh 1	211105	33437	22144	15302	281988	−
Mesh 2	150787	22253	22144	15302	210486	−25.35%
Mesh 3	284043	48963	22144	15302	370452	+31.37%
Mesh 4	55775	831	3602	5110	65318	−76.84%

Table 3.1: *Boundary Layer 2, first cell thickness $y_w = 4$ mm, $y_w/B \approx 1.29 \cdot 10^{-4}$.*

|	Ω_1	Ω_2	Ω_3	Ω_4	Tot.	y_w/B
		Mesh 1				
Boundary Layer 1	211401	33437	22144	15302	282284	$6.45 \cdot 10^{-5}$
Boundary Layer 2	211105	33437	22144	15302	281988	$1.29 \cdot 10^{-4}$
Boundary Layer 3	213483	33437	22144	15302	284366	$1.935 \cdot 10^{-4}$
		Mesh 4				
Boundary Layer 2	55775	831	3602	5110	65318	$1.29 \cdot 10^{-4}$
Boundary Layer 4	54273	831	3602	5110	63816	$3.23 \cdot 10^{-4}$
Boundary Layer 5	51093	831	3602	5110	60636	$6.45 \cdot 10^{-4}$

Table 3.2: *Mesh partitioning: boundary layer sizes.*
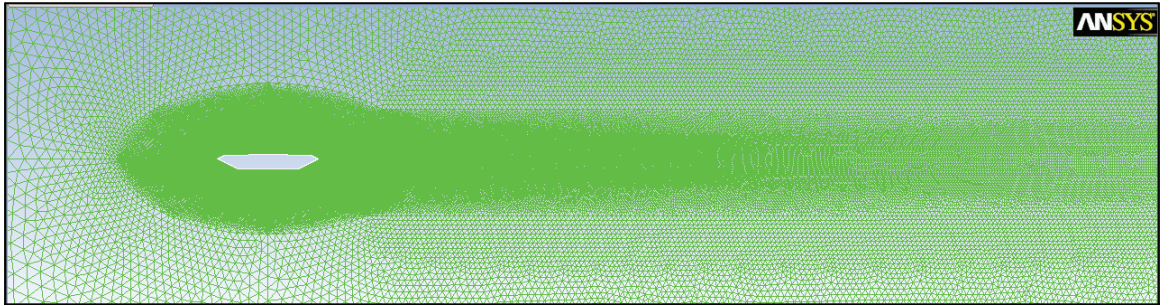
(a) *Mesh* 1
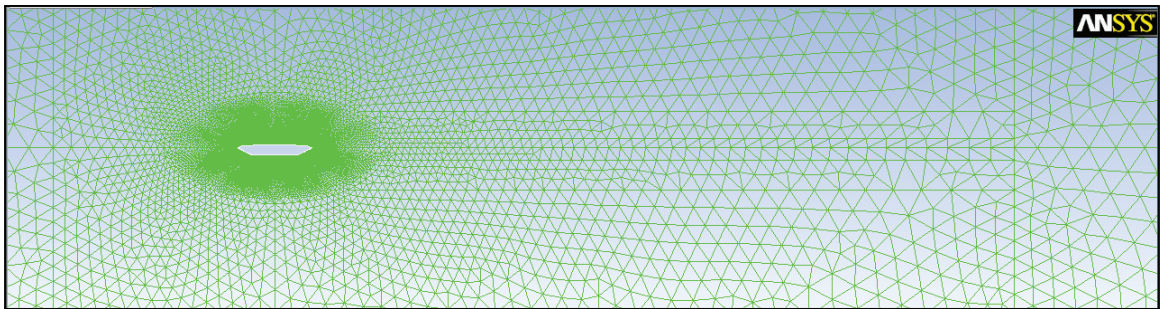
(b) *Mesh* 4

Fig. 3.4: *Example of mesh used in the analyses:* (a) *Mesh* 1 *and* (b) *Mesh* 4.

evaluated for each of the selected mesh and the value y_w of the cell thickness nearest to the wall is also presented in Table 3.2.

Since the main vortical structure is located on the lower surface of the bridge deck near the wake, a refined mesh is required in this region to properly capture the wake phenomena. In this respect boundary layer separation occurs at every corner of the bridge deck. On the other end, on the lower surface of the deck, advected vortices are traveling from the front far-wake side to the rear near-wake side of the section.

Vortices generated in the far-wake during advected procession coalesce with vortices in the near-wake side and shed into the wake, generating the vortex shedding phenomenon. This complex phenomenon can be captured at the right frequency by properly sizing the mesh and performing its refinement as needed.

3.2.1.2 The $k - \epsilon$ Model

For fluid flow problems with high Reynolds numbers it is important to choose an appropriate turbulence model capable of capturing the flow characteristics and associated aerodynamic loads acting on the object of interest. Since no turbulence model is accepted as better than another, it is important to choose a model that is specific to the problem at hand, sufficiently accurate within the available computational recourses. Among the various turbulence models currently available $k-\epsilon$ as been widely used and accepted, particularly for free-shear layer flows and for wall-bounded and internal flows, when there are relatively small mean pressure gradients, while accuracy has been shown experimentally to be reduced for flows containing large adverse pressure gradients, and becomes inappropriate for problems such as inlets and compressors.

Turbulence models are associated to the Reynolds Average Navier-Stokes (RANS) equations to compute the Reynolds stresses, which can be done by three main categories of RANS-based turbulence models, i) the linear eddy viscosity models, ii) the nonlinear eddy viscosity models, and iii) Reynolds stress model (RSM).

Among the two equations linear eddy viscosity models, one of the most used types in a variety of engineering and industry problems, the k-eps turbulent model, has been selected for its less computational time and resources requirement to achieve high degree of accuracy. This is a two equations model including two extra transport equations to represent the turbulent properties of the flow and to account for history effects like convection and diffusion of turbulent energy. Two transported variable are used in this model, the turbulent kinetic energy, k, and the turbulent dissipation, ϵ. While k determines the energy in the turbulence, ϵ determines the scale of the turbulence. The standard $k - \epsilon$ model is based on the two equations, for turbulent kinetic energy k

$$\frac{\partial}{\partial t}(\rho k) + \frac{\partial}{\partial x_i}(\rho k u_i) = \frac{\partial}{\partial x_j}\left[\left(\mu + \frac{\mu_t}{\sigma_k}\right)\frac{\partial k}{\partial x_j}\right] + P_k + P_b - \rho\epsilon - Y_M + S_k \tag{3.2.1}$$

and for dissipation ϵ

$$\frac{\partial}{\partial t}(\rho\epsilon) + \frac{\partial}{\partial x_i}(\rho\epsilon u_i) = \frac{\partial}{\partial x_j}\left[\left(\mu + \frac{\mu_t}{\sigma_\epsilon}\right)\frac{\partial \epsilon}{\partial x_j}\right] + C_{1\epsilon}\frac{\epsilon}{k}\left(P_k + C_{3\epsilon}P_b\right) - C_{2\epsilon}\rho\frac{\epsilon^2}{k} + S_\epsilon \tag{3.2.2}$$

The turbulent viscosity is modeled as:

$$\mu_t = \rho C_\mu \frac{k^2}{\epsilon} \tag{3.2.3}$$

while the production of k is modeled as

$$P_k = -\rho\overline{u_i' u_j'}\frac{\partial u_j}{\partial x_i} \tag{3.2.4}$$

$$P_k = \mu_t S^2 \tag{3.2.5}$$

Herein S is the modulus of the mean rate-of-strain tensor, defined as :

$$S \equiv \sqrt{2S_{ij}S_{ij}} \tag{3.2.6}$$

and the effect of buoyancy is modeled as

$$P_b = \beta g_i \frac{\mu_t}{\mathrm{Pr}_t} \frac{\partial T}{\partial x_i} \tag{3.2.7}$$

In addition, Pr_t is the turbulent energy (Prandtl number) and g_i is the component of the gravitational vector in the ith direction. For the standard and realizable models, the default value of Pr_t is 0.85. The coefficient of thermal expansion, β , is defined as

$$\beta = -\frac{1}{\rho} \left(\frac{\partial \rho}{\partial T} \right)_p \tag{3.2.8}$$

furthermore, the constants used in the turbulent model are:

$$C_{1\epsilon} = 1.44, \;\; C_{2\epsilon} = 1.92, \;\; C_\mu = 0.09, \;\; \sigma_k = 1.0, \;\; \sigma_\epsilon = 1.3 \tag{3.2.9}$$

There exist variants of the standard $k - \epsilon$ model. The one considered in this study is the realizable $k - \epsilon$ model, usually used when predicting the flow effects in flows with large amount of energy producing eddies that are unpredictable in the spread rate by the standard $k - \epsilon$ model. The following values of the parameters governing the $k - \epsilon$ viscous turbulence model are assumed:

a) Realizable $k - \varepsilon$ model accounting for standard wall functions, since this selection of wall functions give reasonably accurate predictions for the majority of high-Reynolds-number, wall-bounded flows. The transport equation for the realizable $k - \epsilon$ model is

$$\frac{\partial}{\partial t}(\rho k) + \frac{\partial}{\partial x_j}(\rho k u_j) = \frac{\partial}{\partial x_j} \left[\left(\mu + \frac{\mu_t}{\sigma_k} \right) \frac{\partial k}{\partial x_j} \right] + P_k + P_b - \rho \epsilon - Y_M + S_k \tag{3.2.10}$$

$$\frac{\partial}{\partial t}(\rho \epsilon) + \frac{\partial}{\partial x_j}(\rho \epsilon u_j) = \frac{\partial}{\partial x_j} \left[\left(\mu + \frac{\mu_t}{\sigma_\epsilon} \right) \frac{\partial \epsilon}{\partial x_j} \right] + \rho C_1 S\epsilon - \rho C_2 \frac{\epsilon^2}{k + \sqrt{\nu \epsilon}} + C_{1\epsilon} \frac{\epsilon}{k} C_{3\epsilon} P_b + S_\epsilon \tag{3.2.11}$$

where

$$C_1 = \max \left[0.43, \frac{\eta}{\eta + 5} \right], \quad \eta = S\frac{k}{\epsilon}, \quad S = \sqrt{2 S_{ij} S_{ij}} \tag{3.2.12}$$

in these equations, P_k represents the generation of turbulence kinetic energy.

b) Turbulence parameters at the inflow boundaries: turbulence intensity $It = 0$, turbulence length scale $l_t = 31$ (in [m], represents the section width B)

c) Integration scheme: SIMPLE (Semi-Implicit Method for Pressure-Linked Equations). As the pressure appears in all three momentum equations while the velocity field also has to satisfy the continuity equation. While there is no explicit equation for pressure, to solve the four equations in the four variables, a pressure-velocity coupling algorithms is used to derive an equation for the pressure from the momentum and the continuity equations. The SIMPLE algorithm, a default algorithm in most commercial finite volume codes, uses an algebraic equation for the pressure correction in a form similar to the equations derived for the convection-diffusion equations.

The momentum equations were solved using second-order upwind spatial discretization, and a least square cell based gradient option. Since a pressure-based solver is used, PREssure STaggering Option (PRESTO!) for pressure interpolation scheme was also selected. In addition, second order upwind was also selected to spatially discretize both the turbulent kinetic energy and dissipation rate equations.

3.2.1.3 Numerical Results

The simulations were carried out for a turbulent flow regime, in particular assuming a free-stream velocity $U = 8$ m/s, corresponding to a Reynolds number $Re = 1.71 \times 10^7$. The unsteady analyses were run by adopting a time step size $\Delta t = 1 \times 10^{-3}$ sec, nevertheless studies on the Δt convergence were previously performed and an example of that is given in Table 3.5. The geometry of the section is described in Fig. 3.2 where a deck with $B = 31$ m and depth $d = 4.4$ m represent the main parameters. The aerodynamic drag, lift, and moment coefficients (C_D, C_L and C_M) evaluated by the CFD analyses, are here defined according to the following convention:

$$C_D := \frac{D}{\frac{1}{2}\rho U^2 B} \,, \ C_L := \frac{L}{\frac{1}{2}\rho U^2 B} \,, \ C_M := \frac{M}{\frac{1}{2}\rho U^2 B^2} \tag{3.2.13}$$

where D, L are the drag and lift forces, respectively, and M is the aerodynamic moment computed with respect to the elastic center of the section. It is important to note that the drag coefficient appears in the literature also in an alternative form, evaluated in terms of deck depth d as $C_D^* := \frac{D}{\frac{1}{2}\rho U^2 d}$. Moreover, the aerodynamic moment is assumed positive accordingly to the *nose-up* positive convention for the rotation α of the section. The dimensionless Strouhal number, describing the oscillating flow mechanism for fixed aerodynamic sections, is also computed. It is defined as $St = \frac{fd}{U}$, where f is the vortex shedding frequency in [Hz] of the calculated unsteady aerodynamic loads extracted from the Fourier spectrum of their time histories.

Simulations at a mean angle of attack $\alpha = 0°$ were first carried in order to evaluate the influence of the computational domain discretization in the calculation of the aerodynamic coefficients. In Table 3.3 the results obtained by using the 4 meshes previously described in this Section (see an example of them in Figure 3.4), show how also with the minimum discretization adopted (*Mesh* 4) the estimation of the aerodynamic loads is very close to the values calculated with smaller mesh size. Nevertheless, the mesh resolution strongly affects the vorticity dissipation in the wake, as shown in Figure 3.5b where the generated eddies vanish after less than one chord length. Higher variations were instead found by adopting the different boundary layers described in Table 3.2.

Finally, in Table 3.5, the comparison between the analyses performed assuming different time steps is proposed and the best compromise, in terms of computational effort and accuracy of results, was found to be corresponding to the adoption of the *Mesh* 4 and the *Boundary Layer* 2.

Boundary Layer 2			
Mesh 1	*Mesh* 2	*Mesh* 3	*Mesh* 4
C_L	0.0786	0.0790	0.0778	0.0756
C_D	0.03518	0.03525	0.03521	0.03368
C_D^*	0.2479	0.2484	0.2480	0.2373
C_M	0.02970	0.02976	0.02965	0.02915

Table 3.3: *Mean value of the aerodynamic coefficients, $Re = 1.71 \times 10^7$ and $\alpha = 0°$, $\Delta t = 0.001$ sec.*

In Figure 3.6, the velocity and vorticity fields generated by the flow around the section and in the wake are shown when adopting the best mesh resolution implemented in this study, that is *Mesh* 1. Figure 3.7 finally shows the time histories of the aerodynamic coefficients and their frequency spectrum and the main frequency of oscillation, corresponding to the Strouhal number reported in Table 3.5, is highlighted.

Although not of a major interest for the content of this thesis, it is worth presenting a note about the flow pattern around the bridge deck at the Reynolds numbers at which the computations have been

	Mesh 1			Mesh 4	
	B-L 1	B-L 2	B-L 3	B-L 4	B-L 5
C_L	0.0663	0.0786	0.0912	0.0970	0.1248
C_D	0.0360	0.03518	0.03458	0.03099	N.A.
C_D^*	0.2537	0.2479	0.24365	0.21834	N.A.
C_M	0.03031	0.02970	0.02928	0.02798	0.02718

Table 3.4: *Mean aerodynamic coefficients, $Re = 1.71 \cdot 10^7$ and $\alpha = 0°$, integration time step $\Delta t = 0.001$ sec.*

	Mesh 4 - Boundary Layer 2	
	$\Delta t = 1 \times 10^{-3}$ sec	$\Delta t = 0.5 \times 10^{-4}$ sec
C_L	0.0756	0.0755
C_D	0.03368	0.03366
C_D^*	0.2373	0.2372
C_M	0.02915	0.02916
St	≈ 0.36	≈ 0.356

Table 3.5: *Aerodynamic coefficients and Strouhal number, $Re = 1.71 \times 10^7$ and $\alpha = 0°$, boundary layer $y_w = 4$ mm, Mesh 4.*
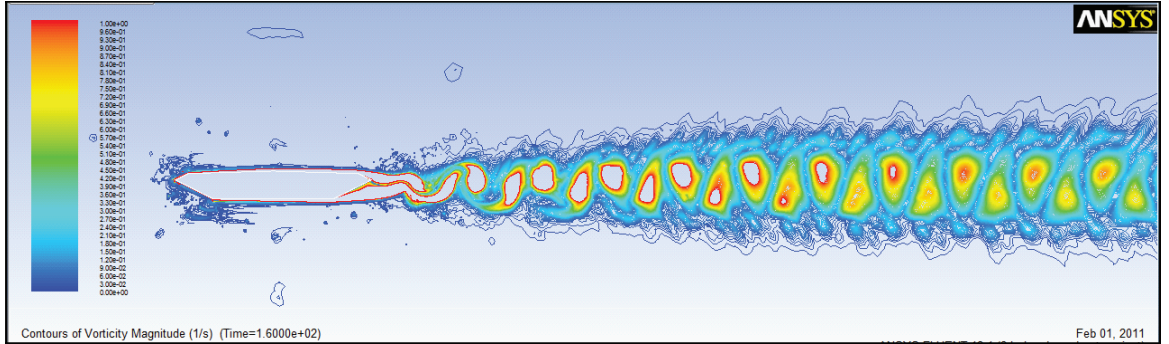
(a)
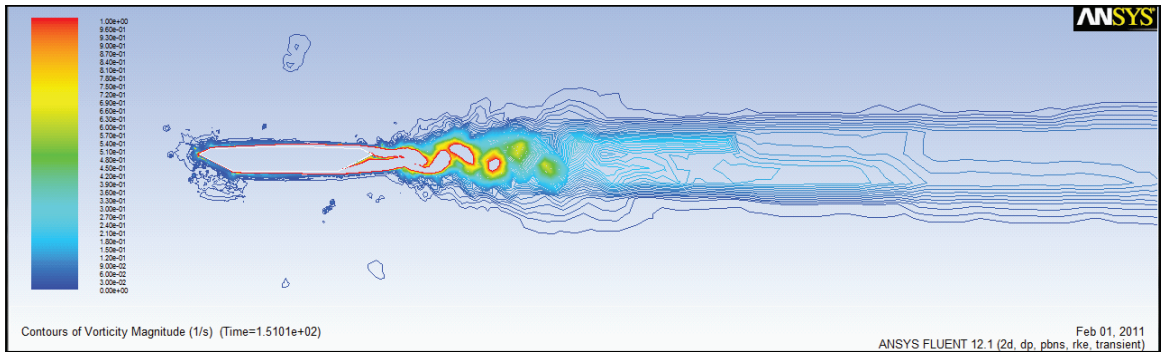
(b) *Mesh 4*

Fig. 3.5: *Vorticity around the GBB deck section, at $Re = 1.71 \times 10^7$ and $\alpha = 0°$, assuming different meshes.*

performed. It is particularly important to infer about the effect of the vortices generated on the upper and lower surface of the bridge deck. From the study of the flow pattern and vortices motion one can conclude that there is a strong interaction between vortices that are generated on the upper and on the
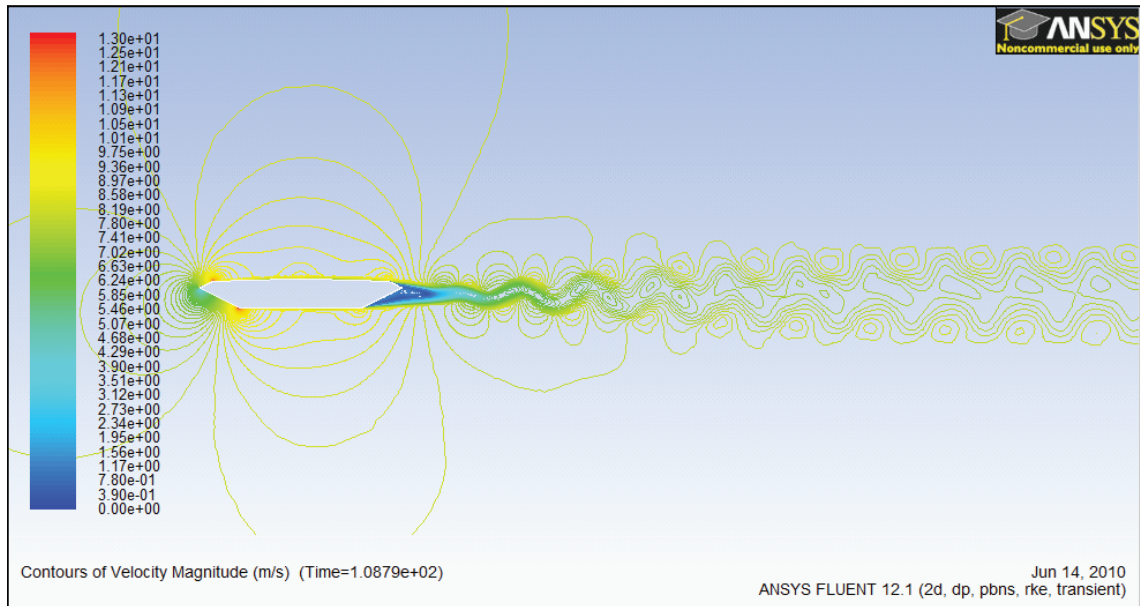
(a) *Velocity magnitude*
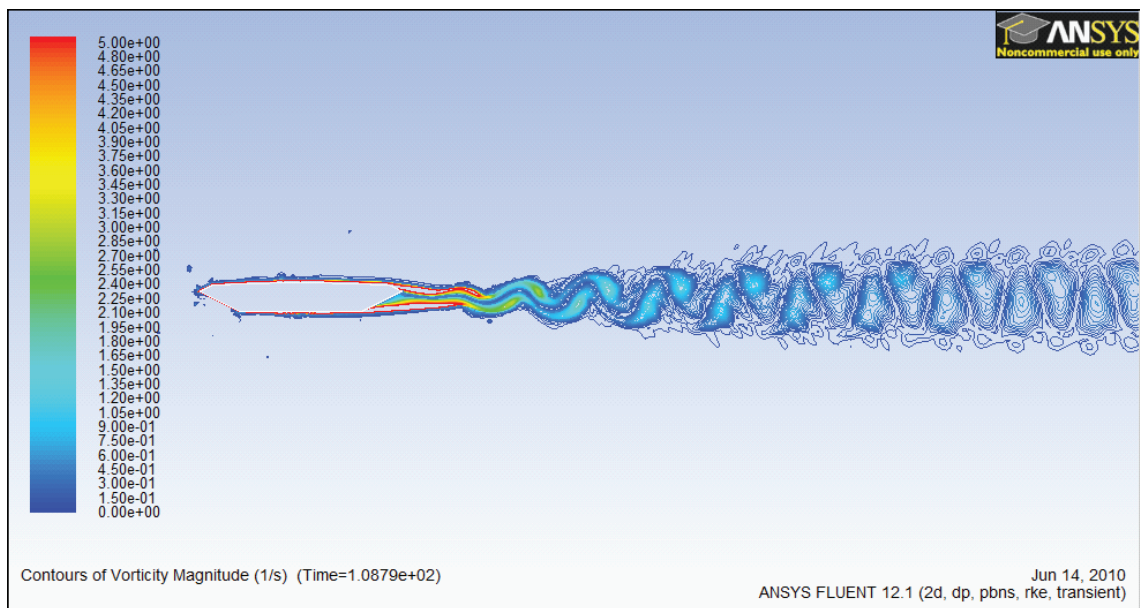
(b) *Vorticity magnitude*

Fig. 3.6: *Velocity and vorticity profiles around the GBB deck section, at $Re = 1.71 \times 10^7$ and $\alpha = 0°$.*

lower surface of the bridge deck as they are traveling downstream. The size and strength of the vortices affect the shedding frequency between the vortices that are migrating into the wake.

In Table 3.6, reported from the work of Bruno and Khris [55], are summarized the experimental and numerical results carried out for the GBB section at an angle of attack $\bar{\alpha} = 0°$ by the most relevant studies available in literature. It is worth pointing out the wide range of variation of the aerodynamic coefficients and the Strouhal number calculated by the different simulations. None of the numerical results shown in the table is obtained by employing the k-ϵ turbulence model which was employed in this thesis. In spite of the large variability in results presented in Table 3.6, by comparing the values calculated in the
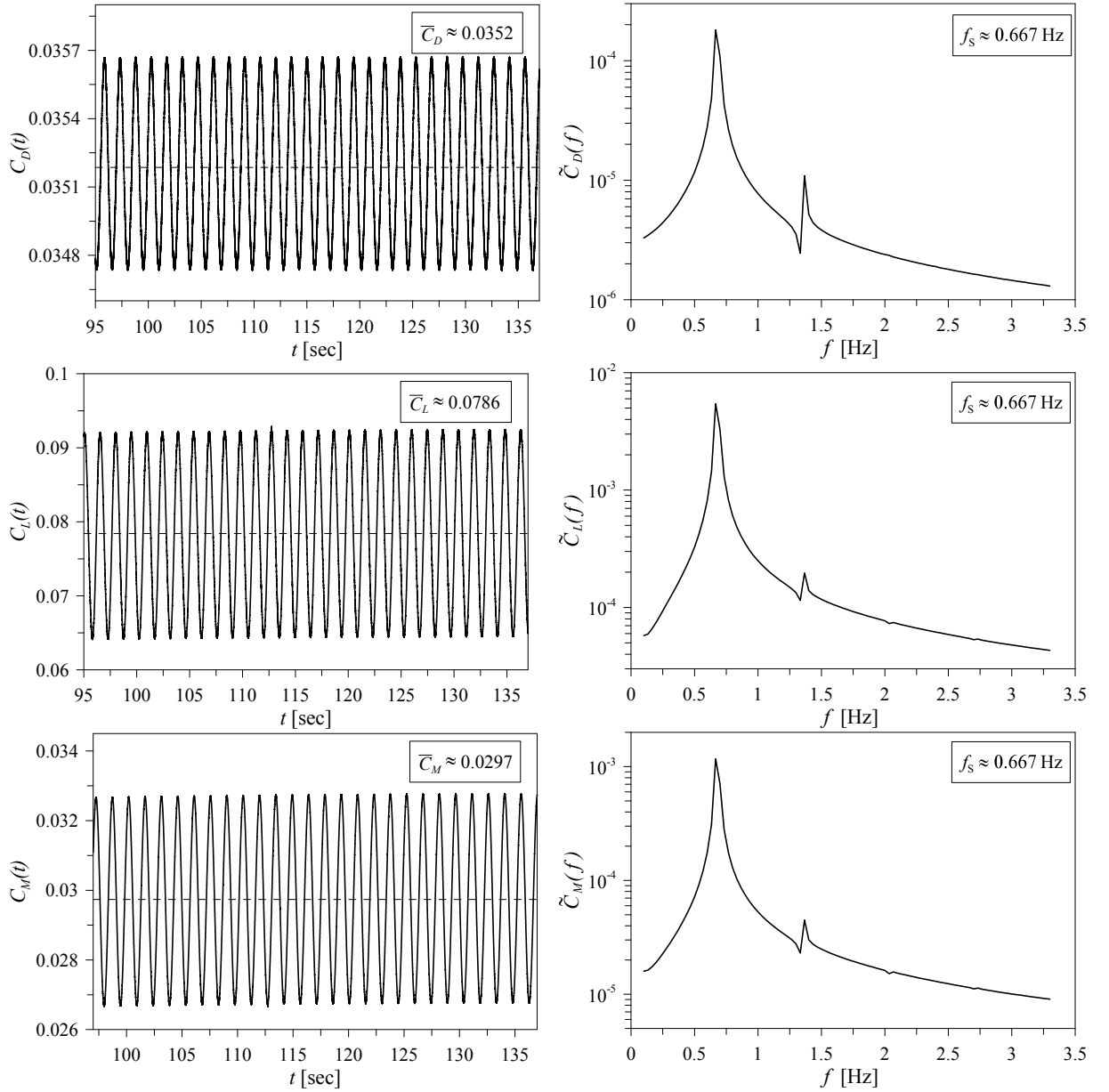
Fig. 3.7: *Aerodynamic drag, lift and moment coefficients at $Re = 1.71 \times 10^7$ and $\alpha = 0°$: time histories and FFT.*

present work, reported in Table 3.5, a good agreement is achieved in terms of lift coefficient whereas the estimation of C_D appears to underestimate the effect of the drag force. It is likely that the underestimate prediction of the drag coefficient can be attributed to the fact that the numerical simulations performed did not include barriers, and the incoming flow to the bridge section was much smoother than the one realized during the experimental and other numerical investigations.

In Table 3.7 are reported the values of the mean aerodynamic coefficients evaluated at different values of the angle of attack $\bar{\alpha}$ for $Re = 1.71 \times 10^7$, by adopting the *Mesh* 4, *Boundary Layer* 2 and $\Delta t = 1 \times 10^{-3}$ s.

Author	Method	Model	Geom.	Re	$\bar{C}_D$	$\bar{C}_L$	St
Reinhold	Exp.	Section	det	$1 \cdot 10^5$	0.08	+0.01	0.109-0.158
Larose	Exp.	Taut-strip	det	$7 \cdot 10^4$	0.10	-0.08	0.11
Frandsen	Exp.	Full scale	det	$1.7 \cdot 10^7$	-	-	0.08-0.15
Larsen	DVM	pot. ω	2Dbas	$1 \cdot 10^5$	0.06	+0.06	0.1-0.168
Taylor	DVM	pot. ω	2Dbas	$1 \cdot 10^5$	0.05	+0.07	0.16-0.18
Frandsen	DVM	pot. ω	2Dbas	$1.6 \cdot 10^7$	0.08	+0.06	0.09
	FEM	NSE lam	2Dbas	$1.6 \cdot 10^7$	0.06	-0.09	0.25
Kuroda	FDM	NSE lam	2Dbas	$3 \cdot 10^5$	0.07	-0.19	0.101-0.168
Selvam	FEM	NSE les	2Dbas	$1 \cdot 10^5$	0.06	-0.34	0.168
Jenssen	FVM	NSE les	3Ddet	$4.5 \cdot 10^4$	0.06	+0.04	0.16
Enevoldsen	FEM	NSE les	2Ddet	$7 \cdot 10^4$	0.07	+0.08	0.17

Table 3.6: *Mean value of the lift and drag coefficients and Strouhal number, for $\alpha = 0°$ and different Reynolds number: literature results [55] for GBB section.*

α [deg]	C_D	C_L	C_M
0	0.0337	0.0756	0.0291
1	0.0327	0.1647	0.0538
5	0.0177	0.5820	0.1523
10	0.0863	0.4291	0.1121

Table 3.7: *FLUENT® results: mean coefficients at different angle of attack α.*

3.2.2 DVMFLOW®

In addition to the simulations performed in FLUENT®, a mesh-less Discrete Vortex Method (DVM) is also employed to characterize the aerodynamics of the GBB deck section. In particular, the software DVMFLOW® by COWI, was used to perform the analyses. This CFD software was specifically developed to study the aerodynamics of bluff-bodies, and sharped-edge sections such as bridge deck cross sections, and it showed to provide aerodynamic and aeroelastic (static/dynamic) loads in agreement with experimental and literature results for the tested sections [53, 54, 55], with a relatively low computational time. Computational efficiency is obtained thank to fast adaptive multipole algorithm.

DVMFLOW® handles viscous two-dimensional single and multiple bodies undergoing prescribed and arbitrary motion. Using a boundary element method, DVMFLOW® enforces the velocity boundary condition as to determine the surface vorticity while the random walk algorithm is used to handle diffusion. The value of the vorticity at the solid boundary is obtained from the Biot-Savart (B-S) relation, in which only the contribution from the surface vorticity is unknown while volume and surface integrals are known, e.g.:

$$\int_{\mathcal{D}} \frac{\omega_0 \times (r_0 - r)}{|r_0 - r|^d} \, d\mathcal{D} = I(r_{\mathcal{B}}) - A\left[v(r_{\mathcal{B}}) - U\right] \tag{3.2.14}$$

$$I(r_{\mathcal{B}}) = \oint_{\mathcal{B}} \frac{(v_0 \cdot n_0)(r_0 - r)}{|r_0 - r|^d} \, d\mathcal{B} + \oint_{\mathcal{B}} \frac{(v_0 \times n_0) \times (r_0 - r)}{|r_0 - r|^d} \, d\mathcal{B} - \int_{\mathcal{D}} \frac{\omega_0 \times (r_0 - r)}{|r_0 - r|^d} \, d\mathcal{D}$$

By introducing a vortex sheet, one can solve equations (3.2.14) for the no penetration velocity component. A detailed mathematical treatment of the DVMFLOW® code is provided in J. H. Walther PhD thesis, the interested reader is referred to [51]. One of the greatest advantages of this code as compared to other CFD codes, here-hence the numerical efficiency gained, is the fact that is mesh free, where the velocity boundary condition is handled according to the B-S relation, without referring to boundary layer approximation. Once the surface vorticity is computed, it is then converted into circulation and it is assigned to the nascent vortices on the surface of the body. Subsequently these vortices diffuses into the flow, and are subjected to diffusion and convection. The process of discretization of the boundary, the flow boundary conditions along with the vorticity boundary value and the process of vortex-vortex interaction and surface-vortex influence are well described in [51]. Detailed application of the code on bridge deck sections and several aerodynamic analyses are proposed in [52].

The parameters employed to perform the CFD simulations carried out in this work are thus based on those assumed by Walther [51] and optimized for the section considered here. The main parameters characterizing the specific fluid dynamic problem are: the dimensional free-stream wind velocity U, assumed by default to be 1 m/s, the width B of the section is scaled in order to have $B = 1$ m. Accordingly to the default settings, the user can select different free-stream velocities by varying the Reynolds number Re and providing the kinematic viscosity $\nu = UB/Re$. The simulation time t is also a dimensionless parameter representing the number of chord lengths $s = (U/B) \cdot t$ traveled by the fluid.

Mesh-convergence analyses were not needed using the DVM method, while only tests on the accuracy of the solution varying the integration time step size and analyses at two different Reynolds number were carried out to validate the results for the GBB section. As specified before, the internal code parameters optimized for the proposed deck section by Walther [51] were implemented as such for the simulations carried out in this work, hence, no further convergence tests were needed.

3.2.2.1 Static Coefficients

In the follow, the lift, drag and moment coefficients are evaluated at different values of the mean angle of attack α by performing time dependent simulations, and their steady-state value was calculated by averaging the response after a convenient calculation time. In particular, the total dimensionless simulation time assumed in the analyses was $s_{max} = 100$, that is 100 chord lengths traveled by the fluid, and the averaging process was performed for $s \in [50, 100]$. The step sizes used in the simulations were $\Delta s = 0.001$ and $\Delta s = 0.025$ (value set as *optimum* by the software developers [51, 52]) for two different Reynolds number, $Re = 1 \times 10^5$ and $Re = 1.71 \times 10^7$. The results obtained by the simulations performed at $Re = 1.71 \times 10^7$, were compared with those got by $k - \epsilon$ and LES methods.

The simulations were performed for selected angles of attack $\alpha = 0, 0.1, 1, 5, 10, 15$ degrees. Figure 3.8 shows small differences between the curves calculated at different Δs at value of the angle of attack $\alpha \geq 5°$, as also reported in Tab. 3.8.
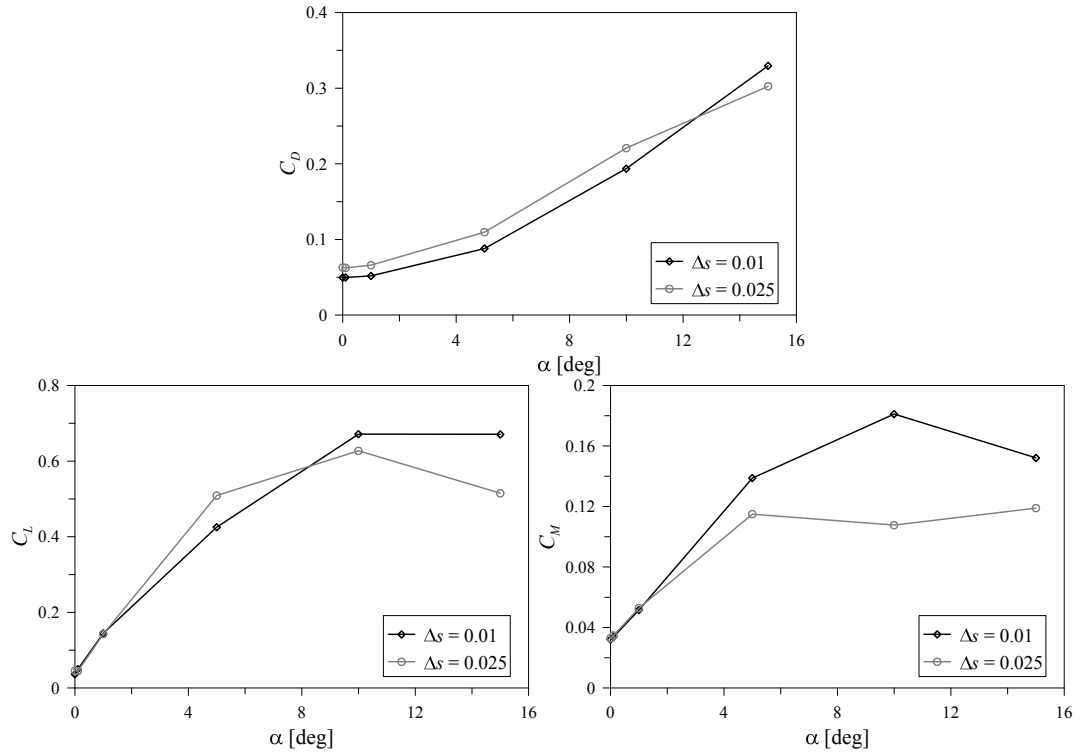
Fig. 3.8: *Static coefficients curves evaluated at different time step sizes for a Reynolds number of $Re = 1 \times 10^5$.*

A wider and more refined range of α values was employed to determine the static coefficients curves for the case studies $Re = 1 \times 10^5$ and $Re = 1.71 \times 10^7$. These curves, shown in Fig. 3.9, highlight the nonlinear behavior due to the stall phenomenon occurring at high angles of attack and characteristic of these sections for a turbulent wind flow regime. As expected, the steady state value of the aerodynamic coefficients turns out to be only slightly affected by the assumed Re at small angle of attack, and such difference becomes appreciable only at high angles of attack, when the stall phenomenon is governing the aerodynamics of the section.

α	Δs	C_L	C_D	C_M	α	Δs	C_L	C_D	C_M
0	0.01	0.03670	0.04954	0.03205	5	0.01	0.4255	0.08802	0.1388
0	0.025	0.04579	0.06307	0.03292	5	0.025	0.5091	0.1097	0.1149
0.1	0.01	0.04980	0.04977	0.03378	10	0.01	0.6714	0.1937	0.1811
0.1	0.025	0.04465	0.06244	0.03474	10	0.025	0.6272	0.2209	0.1077
1	0.01	0.1447	0.05187	0.05160	15	0.01	0.6710	0.3297	0.1522
1	0.025	0.1428	0.06610	0.05285	15	0.025	0.5152	0.3025	0.1189

Table 3.8: *Mean values of the aerodynamic coefficients at different value of the angle of attack α, for $Re = 1 \times 10^5$: convergence in time step size Δs.*
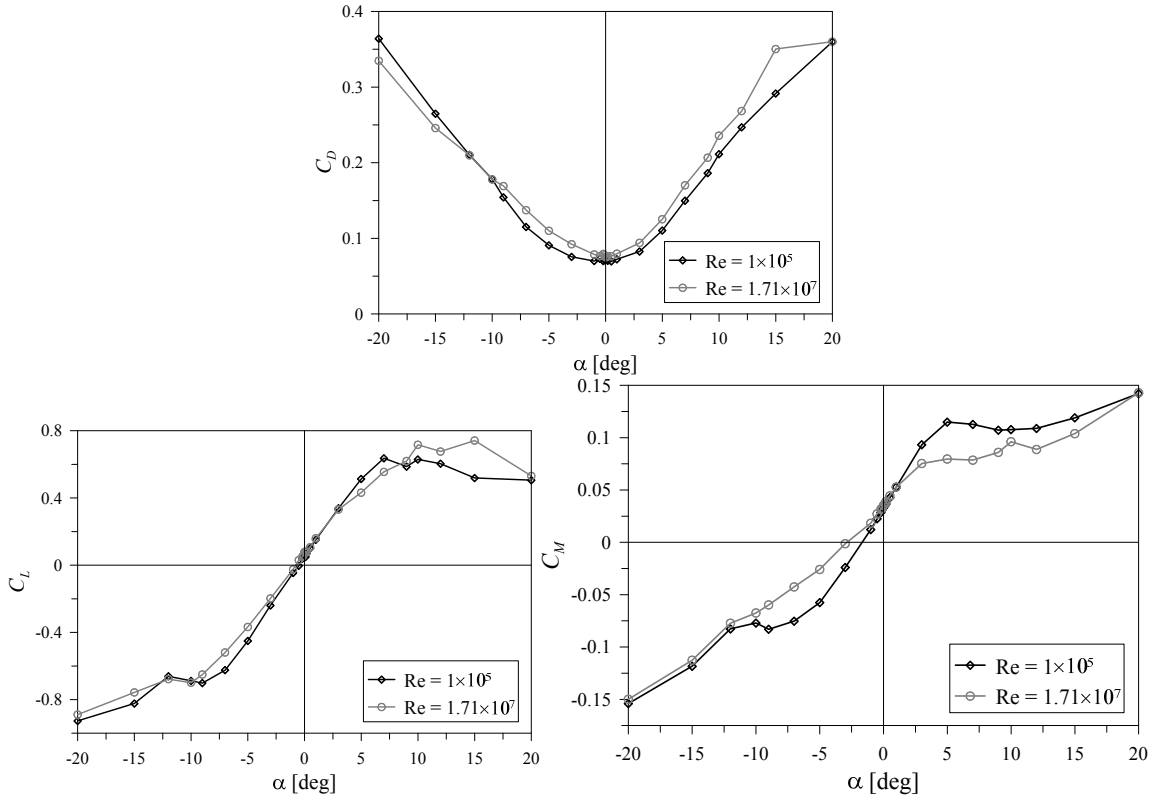

Fig. 3.9: *Static coefficients curves evaluated at different Reynolds numbers, $\Delta s = 0.025$.*

In Tab. 3.9 the calculated values of the aerodynamic coefficients are presented and a good agreement with the literature results for $\alpha = 0°$ is demonstrated by comparing them, for the corresponding Reynolds numbers, as reported in Tab. 3.10.

$Re = 1 \cdot 10^5$				$Re = 1.71 \cdot 10^7$			
α [deg]	C_L	C_D	C_M	α [deg]	C_L	C_D	C_M
-20	-0.9267	0.3641	-0.1540	-20	-0.8889	0.3349	-0.1499
-15	-0.8230	0.2648	-0.1182	-15	-0.7570	0.2459	-0.1126
-12	-0.6611	0.2104	-0.08262	-12	-0.6779	0.2098	-0.07723
-10	-0.6881	0.1783	-0.07699	-10	-0.6992	0.1780	-0.06744
-9	-0.7016	0.1542	-0.08300	-9	-0.6505	0.1692	-0.05972
-7	-0.6247	0.1151	-0.07520	-7	-0.5193	0.1374	-0.04249
-5	-0.4508	0.09085	-0.05751	-5	-0.3672	0.1101	-0.02585
-3	-0.2393	0.07557	-0.02400	-3	-0.1977	0.09232	-0.001255
-1	-0.04618	0.07007	0.01223	-1	-0.02519	0.07877	0.01833
-0.5	-0.003441	0.07312	0.02253	-0.5	0.03035	0.07646	0.02725
-0.2	0.03916	0.06989	0.02859	-0.2	0.04982	0.07946	0.03168
-0.1	0.04340	0.07150	0.03131	-0.1	0.05623	0.07764	0.03263
0	0.05292	0.07141	0.03292	0	0.07818	0.07515	0.03520
0.1	0.04921	0.07244	0.03474	0.1	0.08139	0.07540	0.03667
0.2	0.06910	0.07044	0.03679	0.2	0.07929	0.07632	0.03903
0.5	0.1003	0.06954	0.04260	0.5	0.1074	0.07631	0.04445
1	0.1515	0.07235	0.05285	1	0.1602	0.07972	0.05280
3	0.3390	0.08269	0.09328	3	0.3315	0.09411	0.07540
5	0.5131	0.1105	0.1149	5	0.4320	0.1253	0.07965
7	0.6360	0.1498	0.1127	7	0.5554	0.1701	0.07858
9	0.5865	0.1862	0.1072	9	0.6199	0.2067	0.08598
10	0.6293	0.2114	0.1077	10	0.7167	0.2359	0.09615
12	0.6039	0.2469	0.1089	12	0.6766	0.2683	0.08879
15	0.5190	0.2916	0.1189	15	0.7416	0.3504	0.1039
20	0.5059	0.3599	0.1422	20	0.5312	0.3601	0.1429

Table 3.9: *Mean coefficients at different angle of attack α, $\Delta s = 0.025$.*

In Tab. 3.10 is proposed the comparison between the values of the lift and drag coefficients evaluated for $\alpha = 0°$ at different turbulence regimes evaluated in the present work by the two CFD methods described in the previous sections (k-ϵ and DVM) and the corresponding results available in literature and shown in Tab. 3.6. The curves generated for $Re = 1 \times 10^5$ are assumed as baseline to define the nonlinear

$Re = 1 \cdot 10^5$	C_{L}	C_{D}	St
PW: DVMFLOW	0.053	0.071	0.084
Reinhold Exp.	0.01	0.08	0.109-0.158
Larsen DVM	0.06	0.06	0.1-0.168
Taylor DVM	0.07	0.05	0.16-0.18
Selvam FEM	-0.34	0.06	0.168
$Re = 1.71 \cdot 10^7$	C_{L}	C_{D}	St
PW: k-ϵ	0.076	0.034	0.36
PW: DVMFLOW	0.078	0.075	0.077
Frandsen DVM	0.06	0.08	0.09
Frandsen FEM	-0.09	0.06	0.25

Table 3.10: *Mean coefficients at $\alpha = 0°$, comparison between proposed work (PW) and literature results.*

static aerodynamic loads acting on the bridge section; in particular, a polynomial law is proposed using a least square minimization to fit the discrete data computed by DVMFLOW® . The analytical nonlinear expressions of the aerodynamic coefficients are given in (3.2.15), and the fitting of the CFD data is shown in Fig. 3.10.

$$C_L(\alpha) = 0.0496 + 6.3567\,\alpha - 2.5893\,\alpha^2 - 109.3908\,\alpha^3 - 2.6756\,\alpha^4 + 786.1796\,\alpha^5$$
$$C_D(\alpha) = 0.0695 + 0.1332\,\alpha + 4.7033\,\alpha^2 - 1.1667\,\alpha^3 - 24.1297\,\alpha^4 \qquad (3.2.15)$$
$$C_M(\alpha) = 0.0330 + 1.1379\,\alpha - 0.7673\,\alpha^2 - 27.0033\,\alpha^3 + 4.5606\,\alpha^4 + 249.0324\,\alpha^5$$
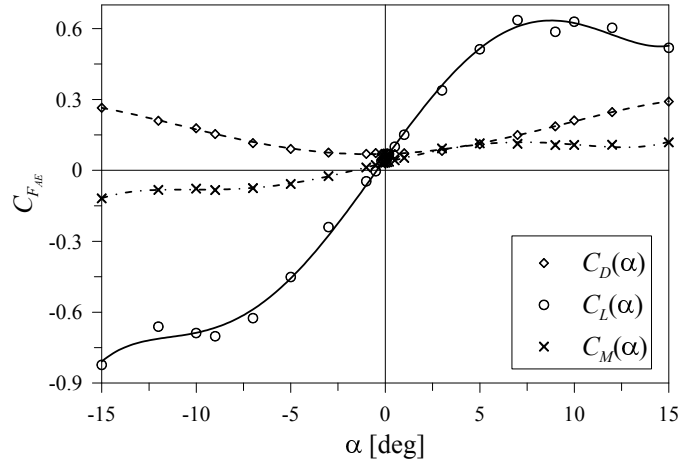

Fig. 3.10: *Static lift, drag and moment coefficients at $Re = 1 \times 10^5$: CFD data and polynomial fitting, lift (solid), drag (dashed) and moment (dash-dot).*

3.2.2.2 Aeroelastic Derivatives

In order to fully describe the aerodynamic response of the GBB section, an extensive set of CFD simulations was performed to define the aerodynamic loads acting on the section, both in the frequency- and in the time-domain. In particular, in the frequency-domain the aerodynamic forces and moment are defined, accordingly to the expressions provided by Simiu and Scanlan in [25], as

$$
\begin{aligned}
D(K) &= \tfrac{1}{2}\rho B\, U^2\Big(\frac{K}{U}P_1\dot{h} + \frac{KB}{U}P_2\dot{\alpha} + K^2 P_3\alpha + \frac{K^2}{B}P_4 h + \frac{K}{U}P_5\dot{p} + \frac{K^2}{B}P_6 p\Big) \\
L(K) &= \tfrac{1}{2}\rho B\, U^2\Big(\frac{K}{U}H_1\dot{h} + \frac{KB}{U}H_2\dot{\alpha} + K^2 H_3\alpha + \frac{K^2}{B}H_4 h + \frac{K}{U}H_5\dot{p} + \frac{K^2}{B}H_6 p\Big) \\
M(K) &= \tfrac{1}{2}\rho B^2 U^2\Big(\frac{K}{U}A_1\dot{h} + \frac{KB}{U}A_2\dot{\alpha} + K^2 A_3\alpha + \frac{K^2}{B}A_4 h + \frac{K}{U}A_5\dot{p} + \frac{K^2}{B}A_6 p\Big)
\end{aligned}
\tag{3.2.16}
$$

where the dot represents derivation with respect to time t, ρ is the air density, K is the reduced frequency of oscillation defined as $K = 2\pi f B/U$ (with f the dimensional frequency), h, α and p represent the heave, pitch, and sway degree of freedom, respectively, and H_i, A_i and P_i ($i = 1, ..., 6$) are the associated aeroelastic derivatives. It is worth mentioning that, in literature, expressions (3.2.16) are often given by neglecting the factor $1/2$ as well as switching the aeroelastic derivatives referred to heave and sway (i.e. P_1 and P_2 multiply $\dot{p}$ and p instead of $\dot{h}$ and h, respectively). In the following, only the aeroelastic derivatives covering an important role in the aeroelastic behavior of suspension bridges are considered, that is, H_i, A_i ($i = 1, 2, 3, 4$), P_5 and P_6.

The evaluation of the aeroelastic derivatives was performed according to the classical technique first proposed by Scanlan [24], that is, by forcing the section in a sinusoidal motion and extracting the values of the derivatives via a minimization procedure. In particular, pure pitch, heave, and sway oscillations are imposed by time, and the derivatives associated to the degree of freedom involved in the motion are extracted.

The procedure employed to calculate the flutter derivatives for a forced pure pitch motion is briefly illustrated next. Equivalent analyses are then performed also for heave and sway.

1. For a given reduced frequency K, a pure pitch sinusoidal motion $\alpha(s) = \alpha_{max}\sin(K\,s)$ is imposed to the section.
2. The time response in terms of the aerodynamic lift, drag and moment is evaluated by the CFD simulation: $\bar{L}(K)$, $\bar{D}(K)$ and $\bar{M}(K)$.
3. A nonlinear least square minimization of the error between the evaluated aerodynamic loads $\bar{L}(K)$, $\bar{D}(K)$, $\bar{M}(K)$ and the expressions suggested by Scanlan in terms of aeroelastic derivatives accounting for pure pitch motion

$$
\begin{aligned}
D(K) &= \tfrac{1}{2}\rho B\, U^2\Big(\frac{KB}{U}P_2\dot{\alpha} + K^2 P_3\alpha\Big) \\
L(K) &= \tfrac{1}{2}\rho B\, U^2\Big(\frac{KB}{U}H_2\dot{\alpha} + K^2 H_3\alpha\Big) \\
M(K) &= \tfrac{1}{2}\rho B^2 U^2\Big(\frac{KB}{U}A_2\dot{\alpha} + K^2 A_3\alpha\Big)
\end{aligned}
\tag{3.2.17}
$$

   is provided by the software (DVMFLOW®) and the coefficients P_2, P_3, H_2, H_3, A_2 and A_3, respectively, are calculated.
4. The procedure is repeated in the range of reduced frequencies K assumed.
5. Pure heave and sway sinusoidal motions, $h(s) = h_{max}\sin(K\,s)$ and $p(s) = p_{max}\sin(K\,s)$, are also applied in order to evaluate the remaining derivatives.

The amplitudes of the sinusoidal motion were assumed according to the suggestions of the DVMFLOW® developers [51, 52] and, in particular, $\alpha_{max} = 0.05236\,rad = 3°$ and $h_{max} = p_{max} = 0.04B$ were used in the computations. The analyses were then performed for a wind velocity corresponding to $Re = 1 \times 10^5$ and in a range of reduced velocities $U_r := 2\pi/K$ such that $U_r \in [1, 14]$; the results obtained assuming a mean wind angle of attack $\bar{\alpha} = 0°$ are shown in Fig. 3.11 and will be discussed in the next section. Further analyses were performed at different mean angles of attack $\bar{\alpha}$ and the corresponding flutter derivatives are reported in Fig. 3.12. The effect of the angle of attack is appreciable in the coefficients H_2 and A_2, representing the contribution in the lift force and pitching moment, respectively, in terms of aerodynamic torsional damping. Increasing the value of $\bar{\alpha}$ in fact, these two coefficients become positive, therefore they introduce a negative damping in the aeroelastic system (suspension bridge), at lower values of the reduced velocity U_r with the expecting effect of reducing the critical flutter velocity.
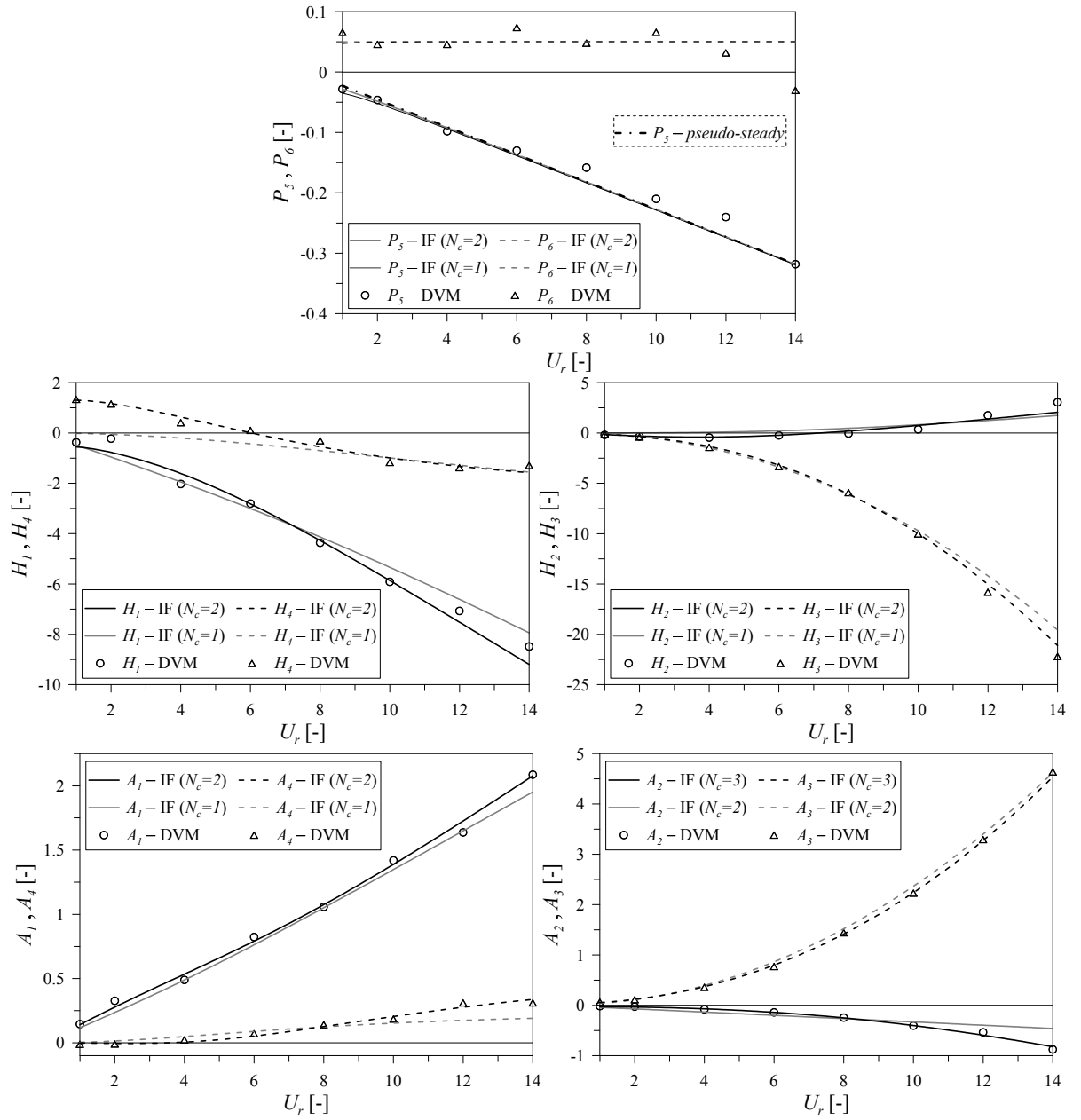
Fig. 3.11: *GBB deck section: aeroelastic derivatives calculated at a mean angle of attack $\bar{\alpha} = 0°$.*
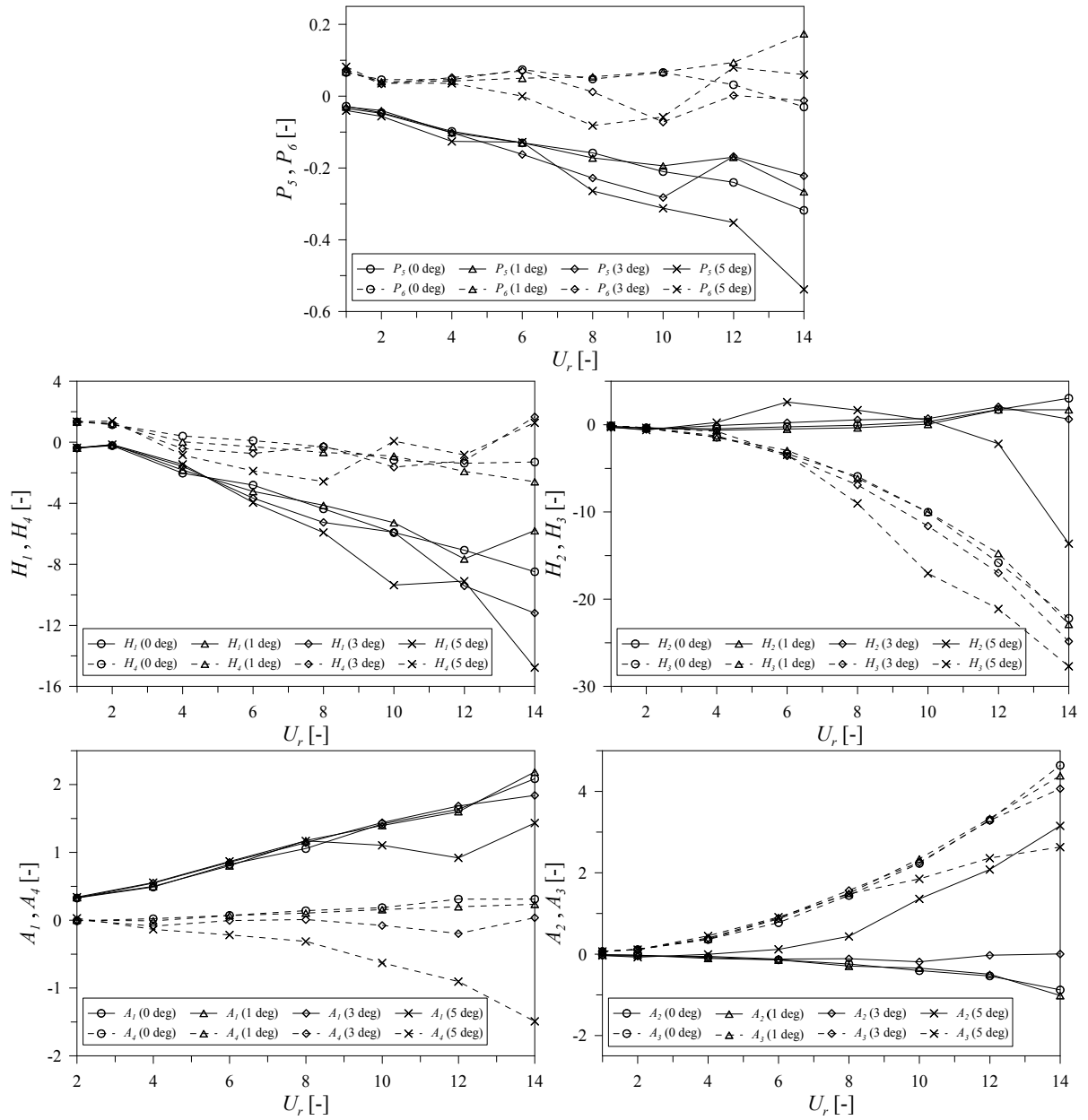
Fig. 3.12: *GBB deck section: aeroelastic derivatives calculated at different mean angles $\bar{\alpha}$.*

3.2.2.3 Indicial Functions from Frequency- and Time-Domain Analyses

As introduced in Section 2.3.2, an analogous formulation of the aerodynamic loads in the time domain can be provided by employing the indicial theory, that is, using the aerodynamic response to a step change of the aerodynamic state $\xi(t)$ (e.g. the indicial response $\Phi_j^\xi(t)$), to obtain the response to a generic variation in time of $\xi(t)$. For the ease of notation it is useful to define the state governing the aerodynamics of the section as $\xi(t) = \left\{ h(t), \alpha(t), p(t), \dot{h}(t), \dot{\alpha}(t), \dot{p}(t) \right\}$, thus, the expressions of the aerodynamic drag $D(t)$, lift $L(t)$ and moment $M(t)$, can be defined in the time domain as follows:

$$F_j = G_j \sum_\xi c_j^\xi \left(\Phi_j^\xi(0)\xi(t) + \int_0^t \dot{\Phi}_j^\xi(t - \tau)\xi(\tau)d\tau \right) \tag{3.2.18}$$

In expression (3.2.18), F_j represents the generic aerodynamic force and moment, where $j = D, L, M$ correspond to drag, lift and moment, respectively; $G_j = 0.5\rho U^2 B$ for drag and lift and $G_j = 0.5\rho U^2 B^2$ for the aerodynamic moment. The indicial function associated with the $j-$th aerodynamic load and the aerodynamic state $\xi(t)$ is defined as a linear combination of exponential functions as

$$\Phi_j^\xi(s) = 1 - \sum_{k=1}^{N_j^\xi} a_{j,k}^\xi e^{-b_{j,k}^\xi s} \tag{3.2.19}$$

where s is the nondimensional time $s = 2(U/B)\,t$ and N_j^ξ is the number of exponential terms adopted. Note that in this case, the time s represents the dimensionless distance measured in half deck width $B/2$ traveled by the fluid; this notation results in fact the most employed in the indicial theory, that finds most of its applications in the aeronautical field where the semi-chord $c/2$ is used to nondimensionalize the variables.

As first proposed in [49], and more recently in [58, 69, 22], the coefficients of the aerodynamic states in (3.2.16) can be derived from the coefficients $a_{j,k}^\xi$, $b_{j,k}^\xi$ and c_j^ξ in the time domain formulation (3.2.18) and vice-versa using the appropriate reciprocity relations:

$$D_j^\xi = c_j^\xi \left(1 - \pi^2 \sum_{k=1}^{N_j^\xi} \frac{a_{j,k}^\xi}{\pi^2 + \left(U_r b_{j,k}^\xi \right)^2} \right)$$
$$E_j^\xi = -c_j^\xi \frac{U_r^2}{2} \sum_{k=1}^{N_j^\xi} \frac{a_{j,k}^\xi b_{j,k}^\xi}{\pi^2 + \left(U_r b_{j,k}^\xi \right)^2} \tag{3.2.20}$$

In (3.2.20), the unsteady coefficients D_j^ξ and E_j^ξ are directly related to the aeroelastic derivatives and to the reduced frequency K, their expressions are provided, and fully described, in [22] and are summarized herewith:

$$\bar{D}_D^{\dot{h}} = K\bar{P}_1\,,\ \ \bar{D}_D^\alpha = K^2\bar{P}_3\,,\ \ \bar{D}_D^{\dot{p}} = K\bar{P}_5\,,\ \ \bar{E}_D^{\dot{h}} = -\bar{P}_4\,,\ \ \bar{E}_D^\alpha = K\bar{P}_2\,,\ \ \bar{E}_D^{\dot{p}} = -\bar{P}_6$$
$$\bar{D}_L^{\dot{h}} = K\bar{H}_1\,,\ \ \bar{D}_L^\alpha = K^2\bar{H}_3\,,\ \ \bar{D}_L^{\dot{p}} = K\bar{H}_5\,,\ \ \bar{E}_L^{\dot{h}} = -\bar{H}_4\,,\ \ \bar{E}_L^\alpha = K\bar{H}_2\,,\ \ \bar{E}_L^{\dot{p}} = -\bar{H}_6 \tag{3.2.21}$$
$$\bar{D}_M^{\dot{h}} = K\bar{A}_1\,,\ \ \bar{D}_M^\alpha = K^2\bar{A}_3\,,\ \ \bar{D}_M^{\dot{p}} = K\bar{A}_5\,,\ \ \bar{E}_M^{\dot{h}} = -\bar{A}_4\,,\ \ \bar{E}_M^\alpha = K\bar{A}_2\,,\ \ \bar{E}_M^{\dot{p}} = -\bar{A}_6$$

Thus, in order to evaluate the $\sum_j \sum_\xi (2\,N_j^\xi + 1)$ coefficients needed in the indicial formulation, it is useful to define error functions between the values of the unsteady coefficients $(\bar{D}_j^\xi, \bar{E}_j^\xi)$, derived from the aeroelastic derivatives calculated via CFD simulations (or experimentally), and their expressions

(D_j^ξ, E_j^ξ) in terms of the indicial coefficients. One possible choice for defining these error functions can be that proposed in [22] :

$$\epsilon_j^\xi = \sum_{i=1}^{M} \left[\left(D_j^\xi(K_i) - \bar{D}_j^\xi(K_i) \right)^2 + \left(E_j^\xi(K_i) - \bar{E}_j^\xi(K_i) \right)^2 \right] \qquad (3.2.22)$$

where M represents the total number of frequencies K_i for which the aeroelastic derivatives in the simulations have been evaluated. Finally, by minimizing the error (3.2.22) with respect to the unknown parameters $a_{j,k}^\xi$, $b_{j,k}^\xi$ and c_j^ξ, the values of the indicial coefficients can be estimated. This minimization procedure turns out to be represented by a high nonlinear algebraic system of equations which solution was performed by employing appropriate algorithms implemented in the code Mathematica® [70].

It is worth mentioning that, by analogy with the quasi-steady formulation of the aeroelastic forces, the unknowns c_j^ξ can be related to the values $\bar{C}_j(\bar{\alpha})$ of the aerodynamic coefficients and to the slope $\partial_\alpha C_j$ of the static curves at the mean value of the angle of attack $\bar{\alpha}$; by these relations, it turns out that only 6 of the 9 coefficients c_j^ξ are independent, as shown in recent works in [58] and [22], and the expressions (3.2.23) show the dependence of the remaining 3 coefficients:

$$c_D^{\dot{h}} = c_D^\alpha - \frac{c_L^{\dot{p}}}{2} \, , \; c_L^{\dot{h}} = c_L^\alpha + \frac{c_D^{\dot{p}}}{2} \, , \; c_M^{\dot{h}} = c_M^\alpha \qquad (3.2.23)$$

and the following relations are valid

$$\bar{C}_D(\bar{\alpha}) = \left(c_L^\alpha - c_L^{\dot{h}} \right) = -\frac{c_D^{\dot{p}}}{2} \, , \; \bar{C}_L(\bar{\alpha}) = \left(c_D^\alpha - c_D^{\dot{h}} \right) = \frac{c_L^{\dot{p}}}{2} \, , \; \bar{C}_M(\bar{\alpha}) = -\frac{c_M^{\dot{p}}}{2}$$
$$\partial_\alpha C_D|_{\bar{\alpha}} = c_D^\alpha \, , \; \partial_\alpha C_L|_{\bar{\alpha}} = -c_L^\alpha \, , \; \partial_\alpha C_M|_{\bar{\alpha}} = c_M^\alpha \qquad (3.2.24)$$

Accordingly to the choice of retaining only the contribution of the flutter derivatives H_i, A_i ($i = 1, 2, 3, 4$), P_5 and P_6 in the expressions of the aeroelastic loads, only $5N + 3$ are the total number of identified coefficients for the considered 5 indicial functions. Nevertheless, relating the unknowns c_j^ξ to the aerodynamic coefficients and the slope of the static curves it is not a prerequisite for determining the indicial functions from the aerodynamic derivatives. In Tables 3.11 and 3.12 one can appreciate the difference.

The expressions of the unsteady coefficients (3.2.20) satisfy the limit conditions (3.2.25)

$$\lim_{K \to \infty} D_j^\xi = c_j^\xi \left(1 - \sum_{k=1}^{N_j^\xi} a_{j,k}^\xi \right) \, , \; \lim_{K \to \infty} E_j^\xi = 0 \qquad (3.2.25)$$

whereas, the values of the numerically evaluated coefficients (3.2.21) depends on the aeroelastic derivatives. As specified before, the flutter derivatives are extracted within the range of reduced velocities $U_r = 2\pi/K \in [1, 14]$, in order to be able to represent also the behavior in the non-circulatory part of the aerodynamic response of the section. In order of limiting the description to a *finite* value of indicial coefficients, an additional constraint was introduced in the minimization of the error functions (3.2.22), that is:

$$\left(1 - \sum_{k=1}^{N_j^\xi} a_{j,k}^\xi \right) < \Phi_j^\xi(0) \qquad (3.2.26)$$

where $\Phi_j^\xi(0)$ represents the finite value of the indicial function at $t = 0^+$ assumed to be sufficiently large to correctly represent the non-circulatory part of the indicial response or, in other terms, it is capable of producing indicial functions that are able to correctly reproduce the aeroelastic derivatives (Eqs. (3.2.20)

and (3.2.21)) at the lowest values of U_r. The steady-state condition that $\Phi_j^\xi(t)$ must represent for $t \to \infty$, then imposes the additional constraint

$$b_{j,k}^\xi > 0 \tag{3.2.27}$$

The curves representing the aeroelastic derivatives in terms of the reduced velocity U_r, determined by the coefficients of the indicial functions with the discrete values calculated via CFD simulations, are compared in Fig. 3.11. A good agreement is also obtained at low values of U_r. The results obtained for different number N_j^ξ of exponential terms assumed to define the indicial function are presented in Fig. 3.11. The trial value for this number is usually chosen as lowest as possible and then increased in order to capture the aerodynamic response in the non-circulatory part and reproduce the asymptotic behavior of the circulatory part of the response (the latter is usually such that $\Phi_j^\xi(t) \approx 1$ for $s < 10$). According to these criteria, $N_j^\xi = 1$ turns out to be sufficient to represent the aerodynamic response in terms of the drag force, whereas the minimum number N_j^ξ for representing the indicial lift response due to the change in the states α and $\dot{h}$ and the indicial response of the moment due to the change in $\dot{h}$ appears to be $N_j^\xi = 2$; finally, $N_j^\xi = 3$ was necessary for Φ_M^α, as evident in Fig. 3.11. In Fig. 3.13 the indicial functions evaluated for selected values of the number of the exponential terms for a mean value of the wind angle of attack of $\bar{\alpha} = 0°$ are compared. Fig. 3.14, shows the indicial functions derived from the aeroelastic derivatives calculated for selected values of $\bar{\alpha}$ and reported in Fig. 3.12. The effect of the leading edge separation is evident at high angle of attack. The good agreement between the numerical results obtained in the evaluation of the aeroelastic derivatives P_5 and its theoretical estimation based on the pseudo-steady formulations commonly used in the flutter analyses (see [71]) in the absence of numerical or experimental values is presented in Fig. 3.11.

$$P_5 = -\frac{U_r}{\pi} C_D \tag{3.2.28}$$
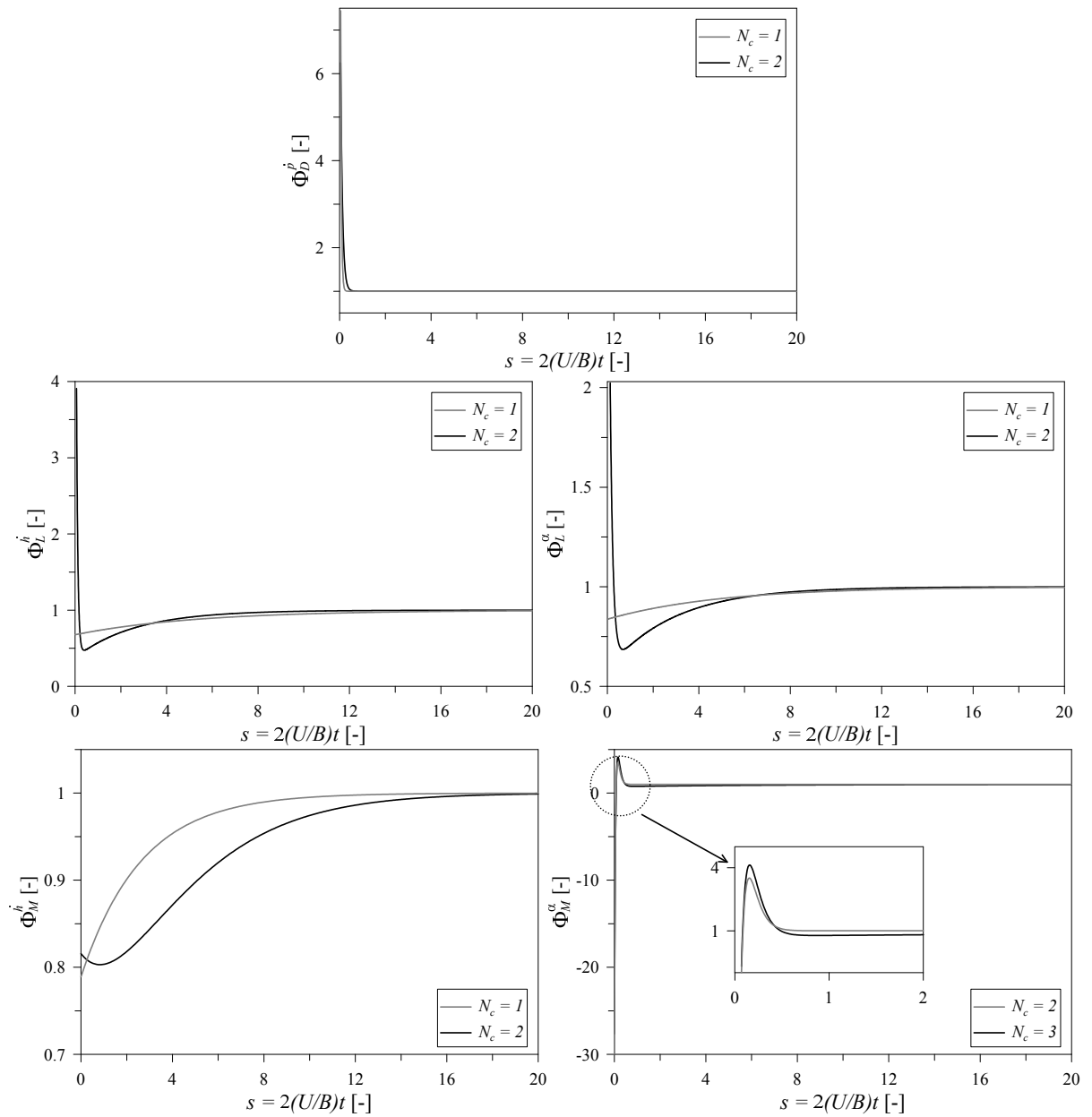
Fig. 3.13: *GBB deck section: indicial functions evaluated from the aeroelastic derivatives at $\bar{\alpha} = 0°$.*
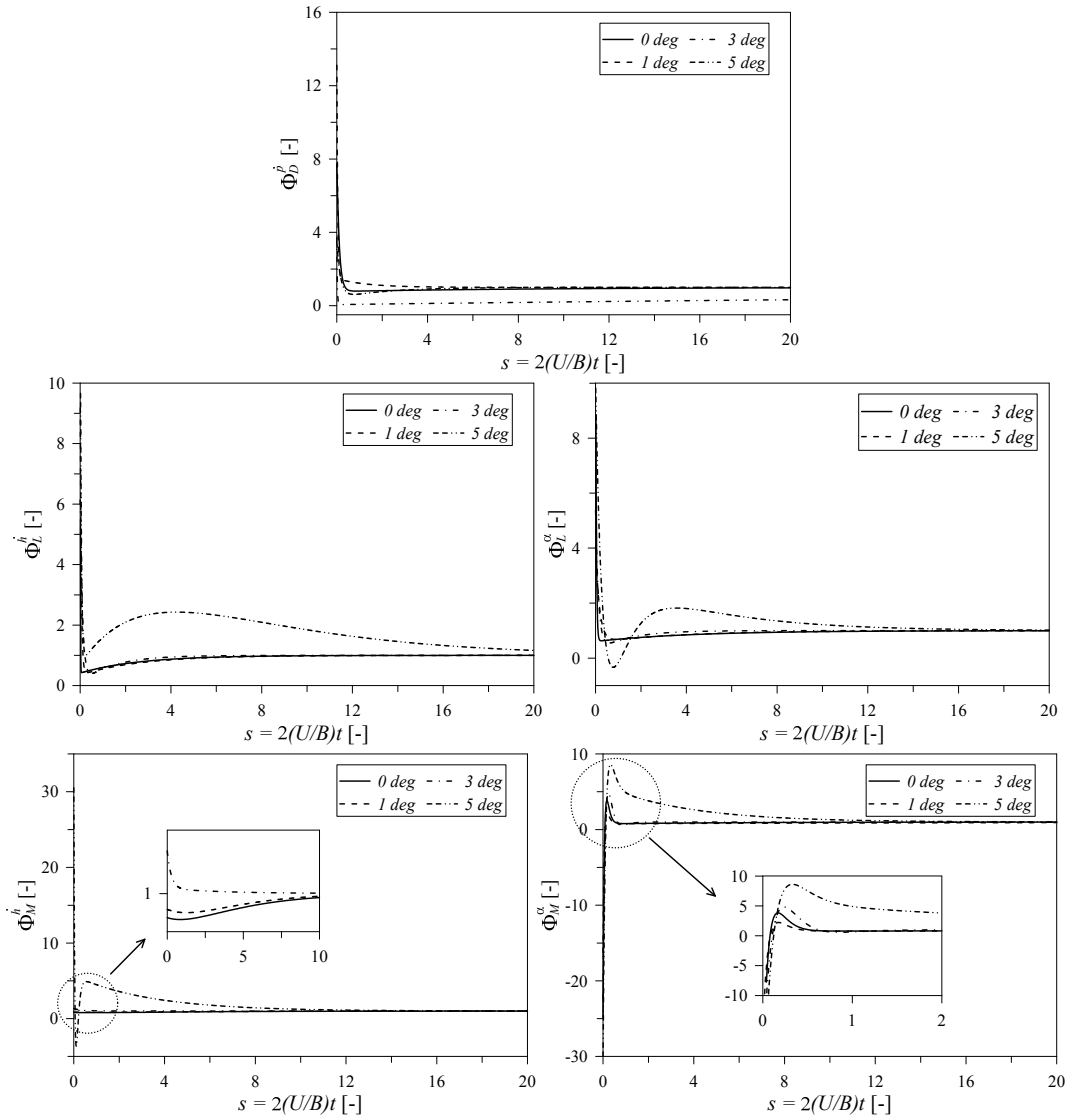
Fig. 3.14: *GBB deck section: indicial functions evaluated from the aeroelastic derivatives at different values of $\bar{\alpha}$.*

In Table 3.11 and Tab. 3.12, the estimated coefficients of the indicial functions are reported, whereas in Tables 3.13 and 3.14 the mean value of the aerodynamic coefficients and the slope of the static curves extracted from the coefficients c_j^ξ are compared with those evaluated in Section 3.2.2.1. It is worth remarking that the choice of not identifying all the aeroelastic derivatives and the related indicial functions, does not allow to estimate the mean values of the lift and moment coefficient as well as the slope of the drag curve.

Φ_j^ξ	$a_{j,1}^\xi$	$b_{j,1}^\xi$	$a_{j,2}^\xi$	$b_{j,2}^\xi$	$a_{j,3}^\xi$	$b_{j,3}^\xi$	c_j^ξ
$\Phi_{\mathrm{D}}^{\dot{p}}$	-8.496	12.055	0	0	0	0	-0.1428
$\Phi_{\mathrm{L}}^{\dot{h}}$	-9.626	16.762	0.626	0.383	0	0	-4.9036
$\Phi_{\mathrm{L}}^{\alpha}$	0.416	0.346	-3.821	8.239	0	0	-4.8322
$\Phi_{\mathrm{M}}^{\dot{h}}$	-19.664	0.390	19.848	0.385	0	0	1.0952
$\Phi_{\mathrm{M}}^{\alpha}$	-102.832	11.720	0.262	0.1615	131.159	14.749	1.0952

Table 3.11: *GBB section: indicial functions coefficients for $\bar{\alpha} = 0°$.*

Φ_j^ξ	$a_{j,1}^\xi$	$b_{j,1}^\xi$	$a_{j,2}^\xi$	$b_{j,2}^\xi$	$a_{j,3}^\xi$	$b_{j,3}^\xi$	c_j^ξ
$\Phi_{\mathrm{D}}^{\dot{p}}$	-6.982	9.696	0	0	0	0	-0.140
$\Phi_{\mathrm{L}}^{\dot{h}}$	-9.635	16.972	0.635	0.425	0	0	-4.670
$\Phi_{\mathrm{L}}^{\alpha}$	0.393	0.235	-14.211	33.975	0	0	-5.335
$\Phi_{\mathrm{M}}^{\dot{h}}$	0.501	0.274	-0.312	0.565	0	0	1.107
$\Phi_{\mathrm{M}}^{\alpha}$	0.256	0.181	-10859.3	12.161	10884.9	12.187	1.075

Table 3.12: *GBB section: indicial functions coefficients for $\bar{\alpha} = 0°$, all c_j^ξ assumed independent.*

	Drag		Lift		Moment	
	AD	*Stat.*	*AD*	*Stat.*	*AD*	*Stat.*
$\bar{C}_j(\bar{\alpha})$	0.0714	0.0714	–	0.0529	–	0.0329
$\partial_\alpha C_j\vert_{\bar{\alpha}}$	–	0	4.8322	4.6372	1.0952	1.1089

Table 3.13: *GBB section: indicial functions coefficients for $\bar{\alpha} = 0°$.*

	Drag		Lift		Moment	
	AD	*Stat.*	*AD*	*Stat.*	*AD*	*Stat.*
$\bar{C}_j(\bar{\alpha})$	0.0700	0.0714	–	0.0529	–	0.0329
$\partial_\alpha C_j\vert_{\bar{\alpha}}$	–	0	5.3352	4.6372	1.0747	1.1089

Table 3.14: *GBB section: indicial functions coefficients for $\bar{\alpha} = 0°$, all c_j^ξ assumed independent.*

The variation of the coefficients of the indicial functions with the angle of attack $\bar{\alpha}$ is proposed in Figs. 3.15-3.19 where the dashed curve is the approximating polynomial law evaluated by a least square minimization of the data obtained by the procedure previously described in this section and summarized in Tabs. 3.15-3.20.
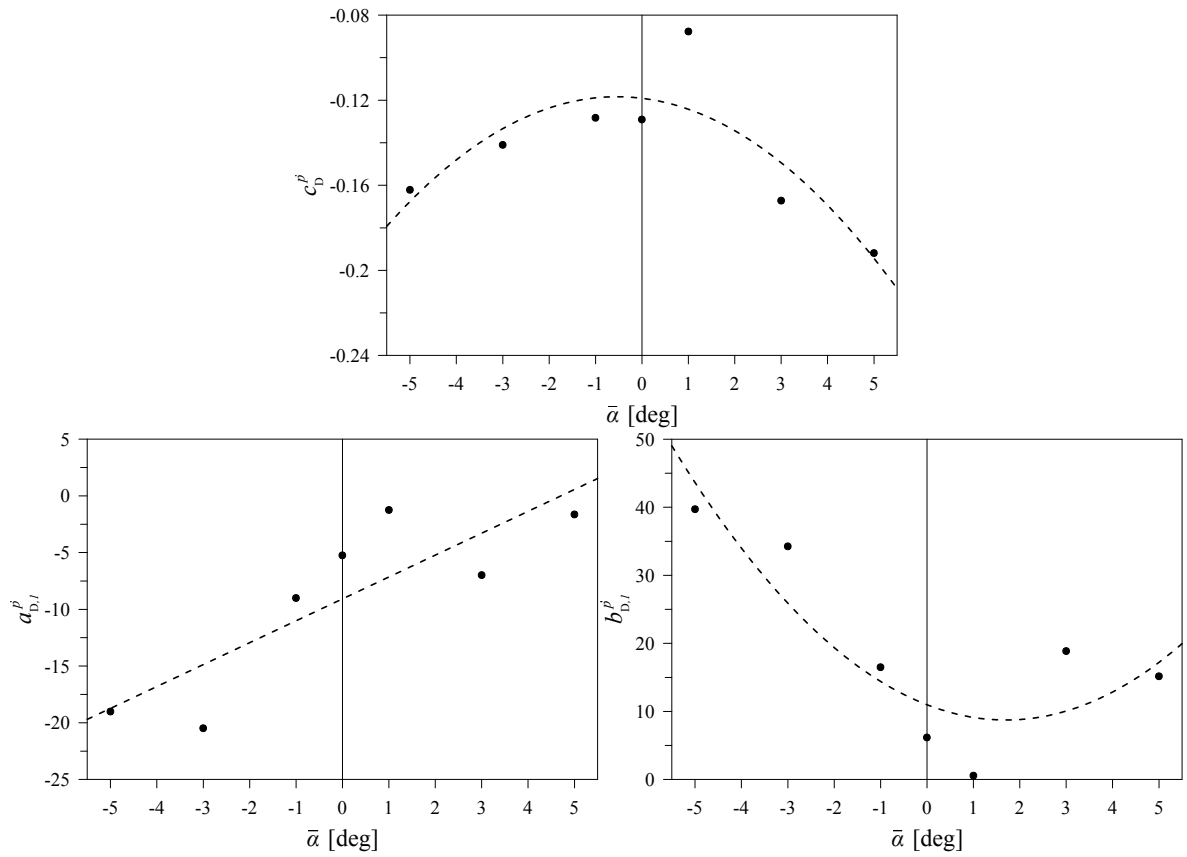
Fig. 3.15: *GBB deck section: indicial function coefficients at different values of $\bar{\alpha}$ (Drag due to a step change in $\dot{p}/U$).*
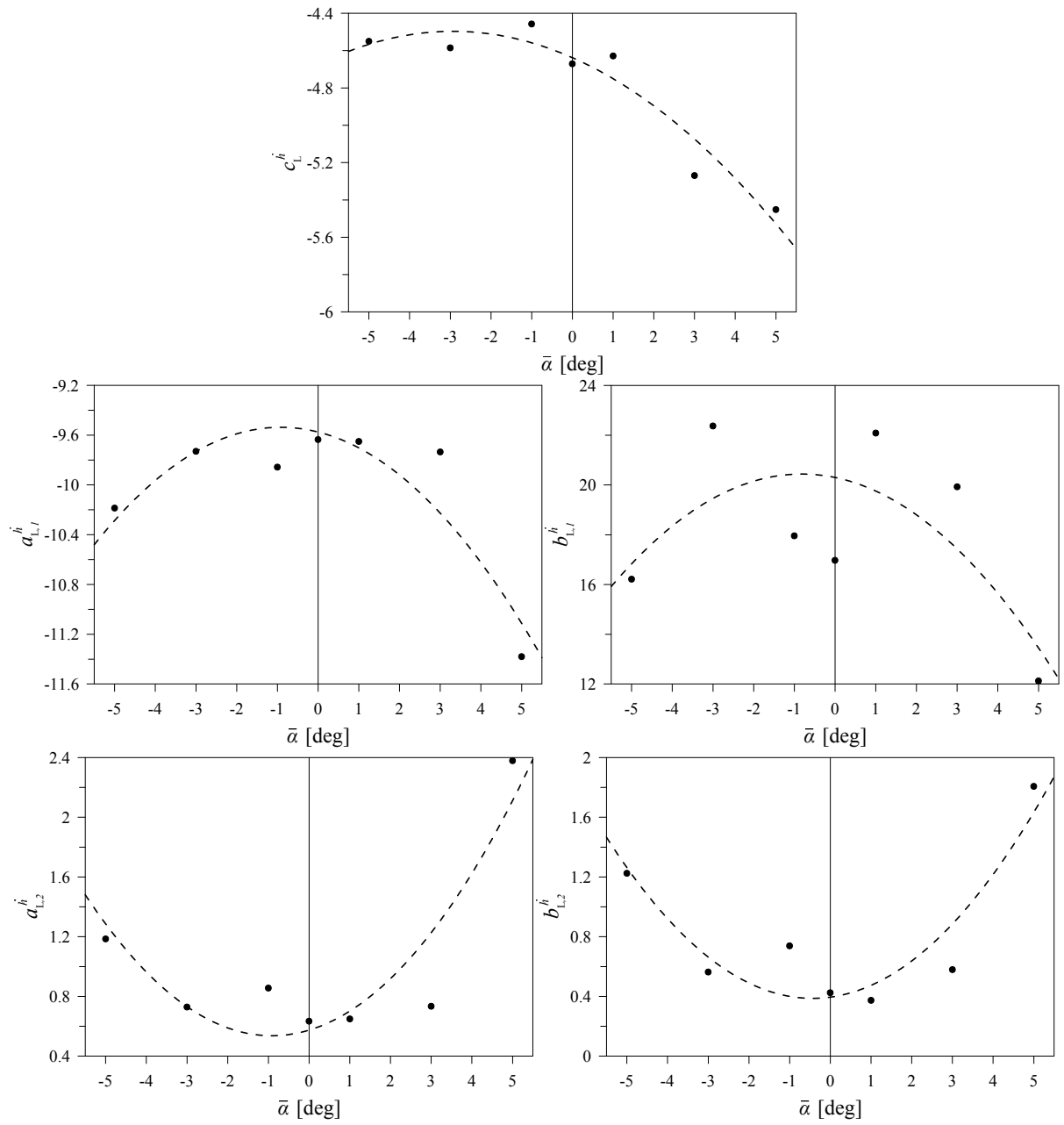
Fig. 3.16: *GBB deck section: indicial function coefficients at different values of $\bar{\alpha}$ (Lift due to a step change in $\dot{h}/U$).*
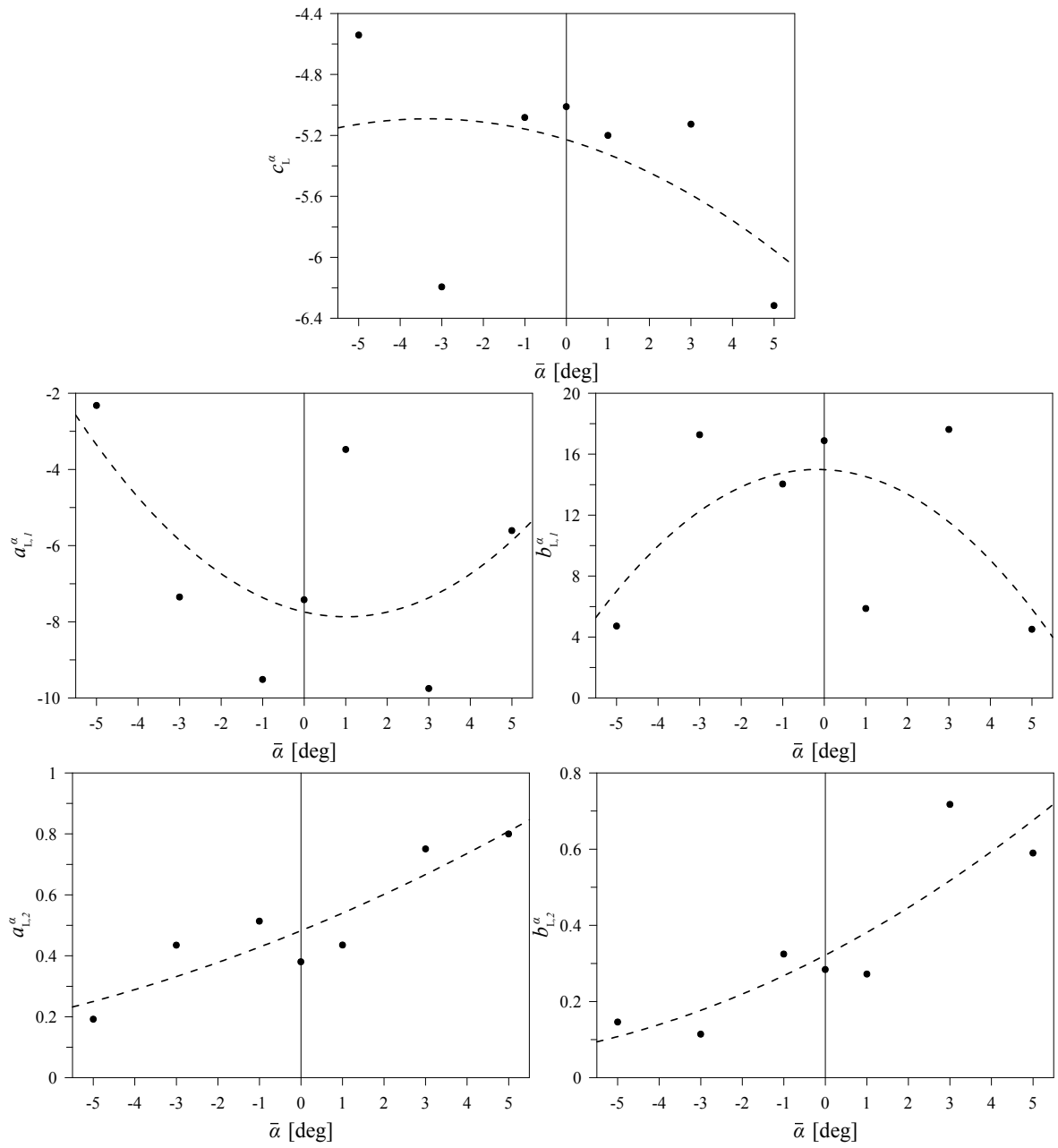
Fig. 3.17: *GBB deck section: indicial function coefficients at different values of $\bar{\alpha}$ (Lift due to a step change in α).*
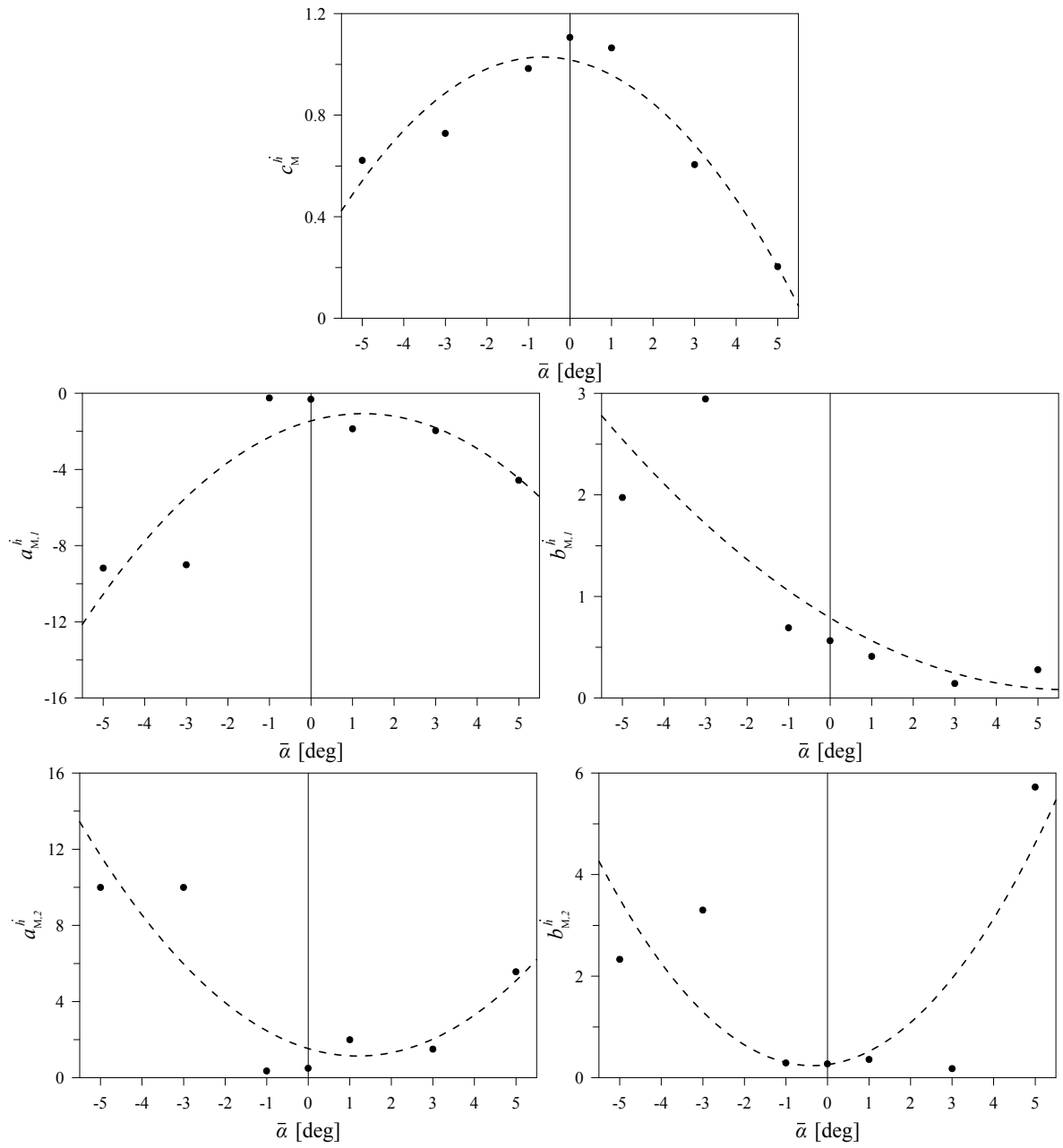
Fig. 3.18: *GBB deck section: indicial function coefficients at different values of $\bar{\alpha}$ (Aerodynamic Moment due to a step change in $\dot{h}/U$).*
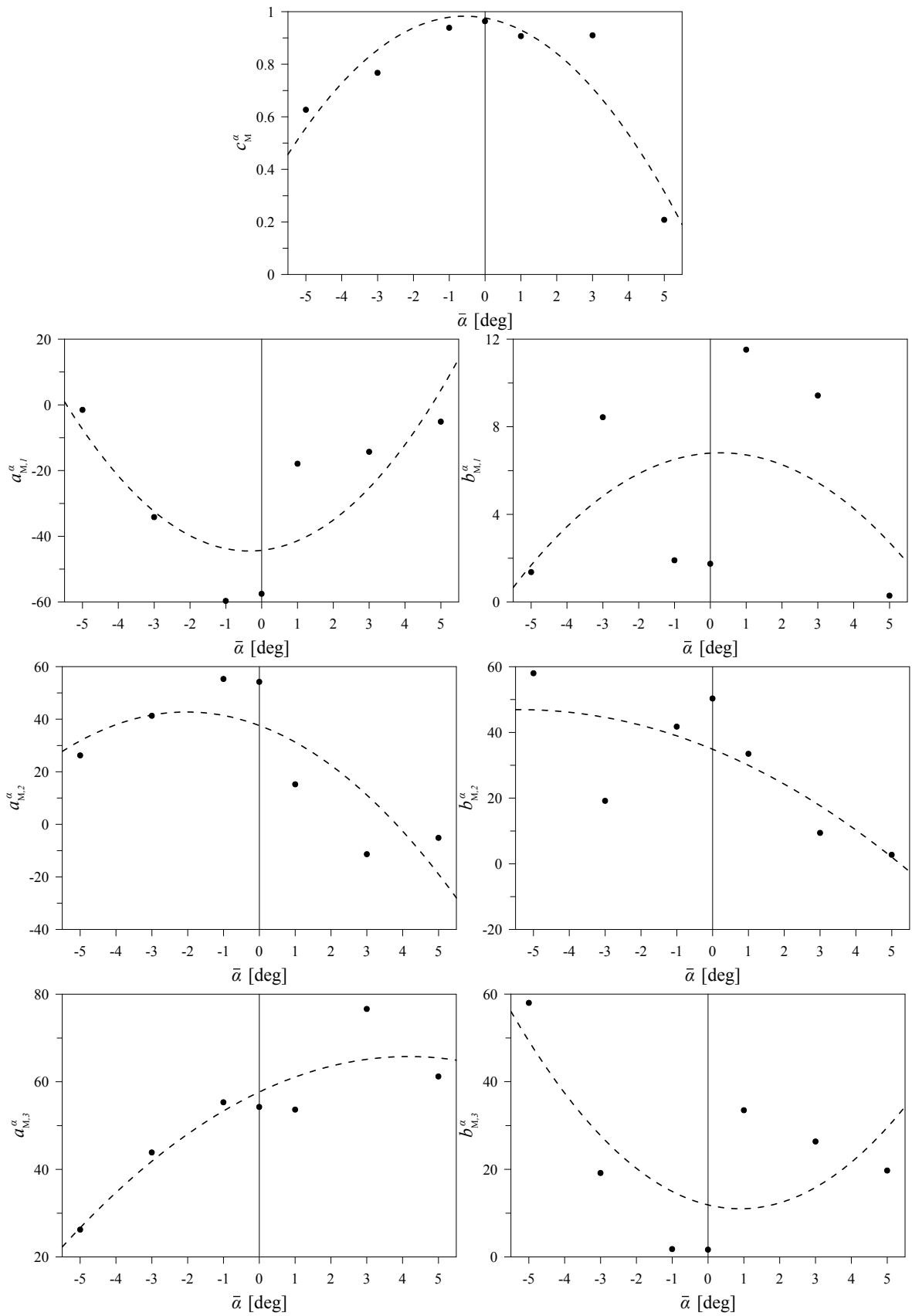
Fig. 3.19: *GBB deck section: indicial function coefficients at different values of $\bar{\alpha}$ (Aerodynamic Moment due to a step change in α).*

Φ_j^ξ	$a_{j,1}^\xi$	$b_{j,1}^\xi$	$a_{j,2}^\xi$	$b_{j,2}^\xi$	$a_{j,3}^\xi$	$b_{j,3}^\xi$	c_j^ξ
Φ_D^p	-11.643	26.447	-0.472	0.741	0	0	-0.111
Φ_L^h	0.650	0.374	-9.650	22.091	0	0	-4.628
Φ_L^α	-3.474	5.873	0.436	0.273	0	0	-5.199
Φ_M^h	760.053	0.397	-759.929	0.397	0	0	1.065
Φ_M^α	-358.858	12.568	375.903	13.046	0.229	0.055	1.170

Table 3.15: *GBB section: indicial functions coefficients for $\bar{\alpha} = +1°$.*

Φ_j^ξ	$a_{j,1}^\xi$	$b_{j,1}^\xi$	$a_{j,2}^\xi$	$b_{j,2}^\xi$	$a_{j,3}^\xi$	$b_{j,3}^\xi$	c_j^ξ
Φ_D^p	0.940	0.016	-3.673	48.767	0	0	-2.711
$\Phi_L^{\dot{h}}$	8240.85	0.204	-8241.28	0.203	-18.566	8.383	-0.946
Φ_L^α	0.771	0.732	-5.158	7.809	0	0	-5.160
$\Phi_M^{\dot{h}}$	-0.296	3.797	-0.040	0.261	0	0	0.858
Φ_M^α	1.781×10^6	5.707	-3.572×10^6	5.721	1.791×10^6	5.734	0.923

Table 3.16: *GBB section: indicial functions coefficients for $\bar{\alpha} = +3°$.*

Φ_j^ξ	$a_{j,1}^\xi$	$b_{j,1}^\xi$	$a_{j,2}^\xi$	$b_{j,2}^\xi$	$a_{j,3}^\xi$	$b_{j,3}^\xi$	c_j^ξ
Φ_D^p	0.593	0.463	-3.038	6.010	0	0	-0.252
$\Phi_L^{\dot{h}}$	7.418	0.333	-7.113	0.186	-12.674	21.764	-1.898
Φ_L^α	-2.584	0.248	-18.002	3.162	11.586	1.079	-3.294
$\Phi_M^{\dot{h}}$	-4.705	0.298	17106.7	14.735	-17131.6	14.773	0.207
Φ_M^α	-4.842	0.273	900.455	6.644	-864.612	6.426	0.209

Table 3.17: *GBB section: indicial functions coefficients for $\bar{\alpha} = +5°$.*

Φ_j^ξ	$a_{j,1}^\xi$	$b_{j,1}^\xi$	$a_{j,2}^\xi$	$b_{j,2}^\xi$	$a_{j,3}^\xi$	$b_{j,3}^\xi$	c_j^ξ
Φ_D^p	-16.875	19.395	0.354	0.504	0	0	-0.146
$\Phi_L^{\dot{h}}$	-9.651	17.879	0.651	0.477	0	0	-4.787
Φ_L^α	-9.514	14.042	0.514	0.325	0	0	-5.082
Φ_M^h	-582.972	0.479	583.065	0.479	0	0	0.966
Φ_M^α	-16919.8	14.287	0.327	0.286	16950.5	14.312	1.030

Table 3.18: *GBB section: indicial functions coefficients for $\bar{\alpha} = -1°$.*

Φ_j^ξ	$a_{j,1}^\xi$	$b_{j,1}^\xi$	$a_{j,2}^\xi$	$b_{j,2}^\xi$	$a_{j,3}^\xi$	$b_{j,3}^\xi$	c_j^ξ
$\Phi_D^{\dot p}$	-15.345	13.053	0.869	1.860	0	0	-0.145
$\Phi_L^{\dot h}$	-9.570	22.963	0.571	0.339	0	0	-5.061
Φ_L^α	-9.491	29.155	0.491	0.072	0	0	-7.127
$\Phi_M^{\dot h}$	-1416.99	0.183	1417.3	0.183	0	0	1.243
Φ_M^α	-13.201	5.564	8.078	16.045	36.123	16.045	0.768

Table 3.19: *GBB section: indicial functions coefficients for $\bar\alpha = -3°$.*

Φ_j^ξ	$a_{j,1}^\xi$	$b_{j,1}^\xi$	$a_{j,2}^\xi$	$b_{j,2}^\xi$	$a_{j,3}^\xi$	$b_{j,3}^\xi$	c_j^ξ
$\Phi_D^{\dot p}$	-19.388	33.516	0.388	0.379	0	0	-0.211
$\Phi_L^{\dot h}$	-10.153	24.542	0.561	0.043	0.592	1.807	-9.454
Φ_L^α	-3.382	8.834	-3.382	0.508	3.352	0.467	-4.316
$\Phi_M^{\dot h}$	-10.687	0.194	10.844	0.181	10.844	435.431	1.047
Φ_M^α	-2.363	1.485	5.070	21.721	28.293	21.721	0.589

Table 3.20: *GBB section: indicial functions coefficients for $\bar\alpha = -5°$.*

Finally, in Eqs. (3.2.29)-(3.2.33) are reported the nonlinear expressions of the indicial functions coefficients in terms of the effective angle of attack.

- Drag due to an instantaneous change in $\dot p/U$

$$c_D^{\dot p} = -0.119093 - 0.152922\,\alpha^E - 8.12684\,\alpha^{E2}$$
$$a_{D,1}^{\dot p} = -9.08144 + 110.593\,\alpha^E \tag{3.2.29}$$
$$b_{D,1}^{\dot p} = 10.9893 - 151.374\,\alpha^E + 2551.63\,\alpha^{E2}$$

- Lift due to an instantaneous change in $\dot h/U$

$$c_L^{\dot h} = -4.63784 - 5.50893\,\alpha^E - 53.7433\,\alpha^{E2}$$
$$a_{L,1}^{\dot h} = -9.57469 - 4.72776\,\alpha^E - 147.569\,\alpha^{E2}$$
$$b_{L,1}^{\dot h} = 20.3016 - 19.3603\,\alpha^E - 677.453\,\alpha^{E2} \tag{3.2.30}$$
$$a_{L,2}^{\dot h} = 0.57469 + 4.72792\,\alpha^E + 147.572\,\alpha^{E2}$$
$$b_{L,2}^{\dot h} = 0.395365 + 2.12066\,\alpha^E + 138.258\,\alpha^{E2}$$

- Lift due to an instantaneous change in α

$$c_L^{\alpha^E} = -5.22785 - 4.74107\,\alpha^E - 40.9614\,\alpha^{E2}$$
$$a_{L,1}^{\alpha^E} = -7.74122 - 14.3973\,\alpha^E + 410.761\,\alpha^{E2}$$
$$b_{L,1}^{\alpha^E} = 14.989 - 6.70829\,\alpha^E - 1123.96\,\alpha^{E2} \tag{3.2.31}$$
$$a_{L,2}^{\alpha^E} = 0.482501 + 3.1992\,\alpha^E + 6.15893\,\alpha^{E2}$$
$$b_{L,2}^{\alpha^E} = 0.321943 + 3.25265\,\alpha^E + 9.1801\,\alpha^{E2}$$

- Aerodynamic Moment due to an instantaneous change in $\dot h/U$

$$c_{\mathrm{M}}^{\dot{h}} = 1.01784 - 1.94729\,\alpha^{\mathrm{E}} - 84.8161\,\alpha^{\mathrm{E}2}$$

$$a_{\mathrm{M},1}^{\dot{h}} = -1.45159 + 34.8321\,\alpha^{\mathrm{E}} - 795.574\,\alpha^{\mathrm{E}2}$$

$$b_{\mathrm{M},1}^{\dot{h}} = 0.788939 - 14.0458\,\alpha^{\mathrm{E}} + 69.7451\,\alpha^{\mathrm{E}2} \qquad (3.2.32)$$

$$a_{\mathrm{M},2}^{\dot{h}} = 1.53358 - 37.6714\,\alpha^{\mathrm{E}} + 900.035\,\alpha^{\mathrm{E}2}$$

$$b_{\mathrm{M},2}^{\dot{h}} = 0.258172 + 6.28261\,\alpha^{\mathrm{E}} + 499.934\,\alpha^{\mathrm{E}2}$$

- Aerodynamic Moment due to an instantaneous change in α

$$c_{\mathrm{M}}^{\alpha^{\mathrm{E}}} = 0.976116 - 1.38887\,\alpha^{\mathrm{E}} - 70.8025\,\alpha^{\mathrm{E}2}$$

$$a_{\mathrm{M},1}^{\alpha^{\mathrm{E}}} = -44.2767 + 68.3032\,\alpha^{\mathrm{E}} + 5619.12\,\alpha^{\mathrm{E}2}$$

$$b_{\mathrm{M},1}^{\alpha^{\mathrm{E}}} = 6.79692 + 5.90456\,\alpha^{\mathrm{E}} - 603.964\,\alpha^{\mathrm{E}2}$$

$$a_{\mathrm{M},2}^{\alpha^{\mathrm{E}}} = 37.602 - 290.482\,\alpha^{\mathrm{E}} - 4094.04\,\alpha^{\mathrm{E}2} \qquad (3.2.33)$$

$$b_{\mathrm{M},2}^{\alpha^{\mathrm{E}}} = 34.8833 - 256.841\,\alpha^{\mathrm{E}} - 1369.1\,\alpha^{\mathrm{E}2}$$

$$a_{\mathrm{M},3}^{\alpha^{\mathrm{E}}} = 57.6747 + 222.179\,\alpha^{\mathrm{E}} - 1525.08\,\alpha^{\mathrm{E}2}$$

$$b_{\mathrm{M},3}^{\alpha^{\mathrm{E}}} = 11.8829 - 113.017\,\alpha^{\mathrm{E}} + 3615.91\,\alpha^{\mathrm{E}2}$$

The goal here was to find a minimal set of coefficients, producing an approximation that is as simple as possible. In this respect up to the quadratic term in the effective angle of attack was considered. These representations will be useful in future development of nonlinear unsteady aerodynamic loading and associated aeroelastic simulations, guaranteeing a good balance between accuracy in fitting the indicial response behavior and also in minimizing computational efforts when the indicial response functions are used in the practical evaluation of the unsteady loading. In the fully nonlinear representation of the aerodynamic loading with functional integral terms, one can be satisfied with an approximate solution if provides accuracy. Although non explored here, a recurrence algorithm, such as the mid-point rule, estimating the relative error incurred in the integral terms, can be employed for this purpose. This is left as a future development to be carried out elsewhere.

Chapter 4
Structural Modeling

In the following sections, the finite kinematics and the nonlinear equations governing the equilibrium and the dynamics of suspension bridges are derived and illustrated. A finite element (FE) computational approach is employed to solve the nonlinear partial differential equations (PDE) governing the dynamics of two long-span suspension bridges, the Runyang and the Hu Men suspension bridges, whose mean structural characteristics are reported in the body of the text. In the last section, a first aeroelastic application of the model is proposed and the torsional divergence phenomenon is studied for the two suspension bridges.

4.1 Fully Nonlinear Parametric Model

A three-dimensional geometrically exact approach [72, 73] is employed to obtain the equations of motion according to a Total and an Updated Lagrangian formulation. The bridge undeformed (stress-free) configuration is considered as the reference configuration. The fixed Cartesian reference frame $\{\boldsymbol{e}_1, \boldsymbol{e}_2, \boldsymbol{e}_3\}$ has the origin in the center of mass of the left deck terminal section (see Fig. 4.1). For the two suspension cables under their own weight, the catenary equilibrium states, taken as reference configuration, are given by:

$$y^{\mathrm{c}}(x) = \frac{H^{\mathrm{c}}}{\rho A^{\mathrm{c}} g} \left\{ \cosh \left[\frac{\rho A^{\mathrm{c}} g}{H^{\mathrm{c}}} \left(\frac{l}{2} - x \right) \right] - \cosh \frac{\rho A^{\mathrm{c}} g \, l}{2 \, H^{\mathrm{c}}} \right\} \tag{4.1.1}$$

where x is the horizontal coordinate along the base line of the deck in the reference configuration (here, it is taken to coincide with the centerline), ρA^{c} is the cable mass per unit length, g is the gravitational constant, l is the span of the bridge, and H^{c} is the horizontal component of the tension N^{c} in each cable. To identify the two suspension cables and the associated variables, the superscripts $''+''$ and $''-''$ are introduced with the convention that the plus sign refers to the cable undergoing incremental tension, the minus indicates the cable undergoing tension loosening, respectively, when the deck is subject to a counterclockwise rotation. The orientation of the deck cross section in the reference configuration is given by the unit vectors $\{\boldsymbol{b}_1(x), \boldsymbol{b}_2(x)\}$ collinear with the principal inertia directions. The local frame is completed by the unit vector $\boldsymbol{b}_3 = \boldsymbol{b}_1 \times \boldsymbol{b}_2$ orthogonal to the cross section. For the suspension cables in the reference configuration, the unit vectors $\boldsymbol{a}_3^{\pm}(x)$ represent the local tangent to the cable base lines (i.e., the cables centerlines). To complete the local frame for the cables, a pair of orthogonal unit vectors $\{\boldsymbol{a}_1^{\pm}(x), \boldsymbol{a}_2^{\pm}(x)\}$ lying in the plane orthogonal to $\boldsymbol{a}_3^{\pm}(x)$ is considered.

4.1.1 Kinematic and Dynamic Formulation

In the orthonormal basis of the fixed inertial reference frame $\{\boldsymbol{e}_1, \boldsymbol{e}_2, \boldsymbol{e}_3\}$, the reference (stress-free) configuration of the deck is described by the position vector of the centerline, $\boldsymbol{x}(x) = x\boldsymbol{e}_3$, where x is the coordinate along the bridge span (see Fig. 4.1); on the other hand, the reference configurations of the two cables are given by the vectors $\boldsymbol{y}^{\pm}(x)$. The equilibrium configurations of the deck-girder and cables under the static loads, respectively denoted by $\mathcal{B}_\circ$ and $\mathcal{C}_\circ$, are described by:

$$\boldsymbol{p}_\circ = \boldsymbol{x}(x) + \boldsymbol{u}_\circ(x) , \quad \boldsymbol{q}_\circ^{\pm} = \boldsymbol{y}^{\pm}(x) + \boldsymbol{v}_\circ^{\pm}(x). \tag{4.1.2}$$
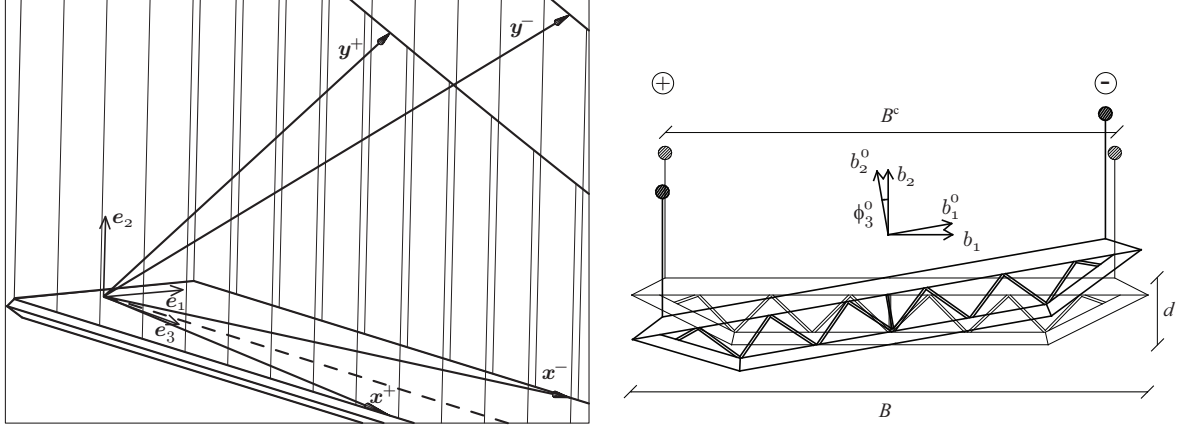

Fig. 4.1: *three-dimensional view (left) and deck section reference frames (right) of the suspension bridge model.*

The orientation of the deck cross sections is given by the unit vectors $\{\boldsymbol{b}_1^\circ(x), \boldsymbol{b}_2^\circ(x), \boldsymbol{b}_3^\circ(x)\}$, whereas the cables tangent unit vectors are $\boldsymbol{a}_\circ^{\pm}(x)$, where the subscript 3 is omitted for ease of notation. In terms of the fixed basis $\{\boldsymbol{e}_1, \boldsymbol{e}_2, \boldsymbol{e}_3\}$, they are expressed as

$$\boldsymbol{b}_i^\circ(x) = \sum_{j=1}^{3} R_{j,i}^\circ(x)\boldsymbol{e}_j ,$$

$$\boldsymbol{a}_\circ^{\pm}(x,t) = \frac{\cos\theta^c}{\nu_\circ^{\pm}}\left[v_{\circ 1,x}^{\pm}\boldsymbol{e}_1 + \left(y_x^c + v_{\circ 2,x}^{\pm}\right)\boldsymbol{e}_2 + \left(1 + v_{\circ 3,x}^{\pm}\right)\boldsymbol{e}_3\right] \tag{4.1.3}$$

where $\cos\theta^c$ is the horizontal projection of the tangent unit vector to the catenary cable configuration $y^c(x)$, $\theta^c = \arctan\left(y_x^c\right)$, the subscript x indicates differentiation with respect to x and $R_{j,i}^\circ(x)$ represents the (i,j)th component of the orthogonal matrix $\mathbf{R}^\circ$ obtained through the following sequence of finite rotations (see Fig. 4.2): flexural rotation about axis $\boldsymbol{e}_1$, flexural rotation about $\boldsymbol{b}_2^{(1)}$ and torsional rotation about axis $\boldsymbol{b}_3^{(2)}$ where $\{\boldsymbol{b}_1^{(k)}, \boldsymbol{b}_2^{(k)}, \boldsymbol{b}_3^{(k)}\}$ is the basis resulting from the kth rotation. The nine components of the rotation matrix $\mathbf{R}^\circ$ are given by

$$R_{11}^\circ = \cos\phi_2^\circ \cos\phi_3^\circ, \; R_{12}^\circ = -\cos\phi_2^\circ \sin\phi_3^\circ, \; R_{13}^\circ = \sin\phi_2^\circ ,$$

$$R_{21}^\circ = \sin\phi_1^\circ \sin\phi_2^\circ \cos\phi_3^\circ + \cos\phi_1^\circ \sin\phi_3^\circ, R_{22}^\circ = \cos\phi_1^\circ \cos\phi_3^\circ - \sin\phi_1^\circ \sin\phi_2^\circ \sin\phi_3^\circ,$$

$$R_{23}^\circ = -\sin\phi_1^\circ \cos\phi_2^\circ, \quad R_{3,1}^\circ = \sin\phi_1^\circ \sin\phi_3^\circ - \cos\phi_1^\circ \sin\phi_2^\circ \cos\phi_3^\circ,$$

$$R_{32}^\circ = \cos\phi_1^\circ \sin\phi_2^\circ \sin\phi_3^\circ + \sin\phi_1^\circ \cos\phi_3^\circ, \quad R_{33}^\circ = \cos\phi_1^\circ \cos\phi_2^\circ. \tag{4.1.4}$$
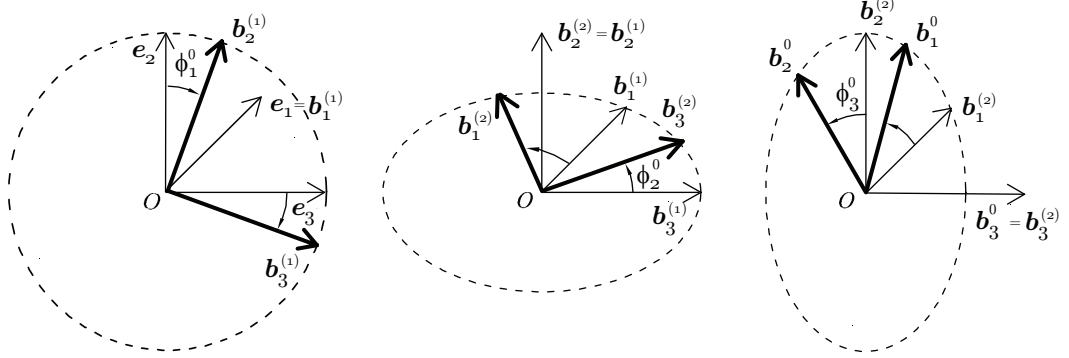
Fig. 4.2: *Sequence of finite rotations experienced by the deck local bases.*

The motions of the deck-girder and the cables baselines are described by $\breve{\boldsymbol{p}}(x,t)$ and $\breve{\boldsymbol{q}}^{\pm}(x,t)$:

$$\breve{\boldsymbol{p}}(x,t) = \boldsymbol{p}_{\circ}(x) + \boldsymbol{u}(x,t)\,, \quad \breve{\boldsymbol{q}}^{\pm}(x,t) = \boldsymbol{q}_{\circ}^{\pm}(x) + \boldsymbol{v}^{\pm}(x,t)\,. \tag{4.1.5}$$

The deck intrinsic frame $\{\breve{\boldsymbol{b}}_1(x,t), \breve{\boldsymbol{b}}_2(x,t), \breve{\boldsymbol{b}}_3(x,t)\}$ and the cables tangent unit vectors $\breve{\boldsymbol{a}}_3^{\pm}(x,t)$ can be expressed in terms of the fixed basis $\{\boldsymbol{e}_1, \boldsymbol{e}_2, \boldsymbol{e}_3\}$ as

$$\breve{\boldsymbol{b}}_i(x,t) = \sum_{j=1}^{3} \breve{R}_{j,i}(x,t)\boldsymbol{e}_j\,,$$

$$\breve{\boldsymbol{a}}^{\pm}(x,t) = \frac{\cos\theta^c}{\breve{\nu}^{\pm}} \Big[\left(v_{\circ 1,x}^{\pm} + v_{1,x}^{\pm}\right)\boldsymbol{e}_1 + \left(y_x^c + v_{\circ 2,x}^{\pm} + v_{2,x}^{\pm}\right)\boldsymbol{e}_2 + \left(1 + v_{\circ 3,x}^{\pm} + v_{3,x}^{\pm}\right)\boldsymbol{e}_3 \Big] \tag{4.1.6}$$

where $\breve{R}_{j,i}(x,t)$ is the component of the total rotation matrix $\breve{\mathbf{R}}(x,t)$ obtained as

$$\breve{\mathbf{R}}(x,t) := \mathbf{R}^{\circ}(x) \cdot \mathbf{R}(x,t). \tag{4.1.7}$$

In Eq. (4.1.7), $\mathbf{R}(x,t)$ represents the sequence of incremental finite rotations $\phi_i(x,t)$ from the static configuration $\mathcal{B}_{\circ}$ to the dynamic configuration $\breve{\mathcal{B}}$ and its components are formally the same as those shown in (4.1.4).

The generalized total strain parameters are defined in the local basis of each structural element. For the cables, the static stretch and the total dynamic stretch are given by

$$\nu_{\circ}^{\pm} = \partial_s \boldsymbol{q}_{\circ}^{\pm} \cdot \boldsymbol{a}_{\circ}^{\pm}\,, \quad \breve{\nu}^{\pm} = \partial_s \breve{\boldsymbol{q}}^{\pm} \cdot \breve{\boldsymbol{a}}^{\pm} \tag{4.1.8}$$

where $\partial_s(\cdot)$ indicates the derivative with respect to the cable arc length coordinate s, $\partial_s(\cdot) = \cos\theta^c \, \partial_x(\cdot)$ and $\partial_x(\cdot)$ indicates differentiation with respect to the bridge span coordinate x. The deck generalized strains comprise the stretch, the two shear strains, the two bending curvatures, and the twist curvature defined as:

$$\partial_x \boldsymbol{p}_{\circ} = \eta_1^{\circ}\boldsymbol{b}_1^{\circ} + \eta_2^{\circ}\boldsymbol{b}_2^{\circ} + \nu^{\circ}\boldsymbol{b}_3^{\circ}\,, \quad \partial_x \boldsymbol{b}_k^{\circ} = \boldsymbol{\mu}^{\circ} \times \boldsymbol{b}_k^{\circ}\,,$$
$$\partial_x \breve{\boldsymbol{p}} = \breve{\eta}_1 \breve{\boldsymbol{b}}_1 + \breve{\eta}_2 \breve{\boldsymbol{b}}_2 + \breve{\nu}\breve{\boldsymbol{b}}_3\,, \quad \partial_x \breve{\boldsymbol{b}}_k = \breve{\boldsymbol{\mu}} \times \breve{\boldsymbol{b}}_k. \tag{4.1.9}$$

For the sake of brevity, only the nonlinear expressions of the static shear strains, stretch, and curvatures are reported, in particular:

$$\eta_1^{\circ} = \cos\phi_2^{\circ}\cos\phi_3^{\circ}\,\partial_x u_{\mathrm{o}1} + \left(\sin\phi_1^{\circ}\sin\phi_2^{\circ}\cos\phi_3^{\circ} + \cos\phi_1^{\circ}\sin\phi_3^{\circ}\right)\partial_x u_{\mathrm{o}2} +$$
$$+ \left(\sin\phi_1^{\circ}\sin\phi_3^{\circ} - \cos\phi_1^{\circ}\sin\phi_2^{\circ}\cos\phi_3^{\circ}\right)\left(1 + \partial_x u_{\mathrm{o}3}\right),$$

$$\eta_2^{\circ} = -\cos\phi_2^{\circ}\sin\phi_3^{\circ}\,\partial_x u_{\mathrm{o}1} + \left(\cos\phi_1^{\circ}\cos\phi_3^{\circ} - \sin\phi_1^{\circ}\sin\phi_2^{\circ}\sin\phi_3^{\circ}\right)\partial_x u_{\mathrm{o}2} +$$
$$+ \left(\sin\phi_1^{\circ}\cos\phi_3^{\circ} + \cos\phi_1^{\circ}\sin\phi_2^{\circ}\sin\phi_3^{\circ}\right)\left(1 + \partial_x u_{\mathrm{o}3}\right),$$

$$\nu^{\circ} = \sin\phi_2^{\circ}\,\partial_x u_{\mathrm{o}1} - \sin\phi_1^{\circ}\cos\phi_2^{\circ}\,\partial_x u_{\mathrm{o}2} + \cos\phi_1^{\circ}\cos\phi_2^{\circ}\left(1 + \partial_x u_{\mathrm{o}3}\right).$$

$$(4.1.10)$$

and

$$\mu_1^{\circ} = \cos\phi_2^{\circ}\cos\phi_3^{\circ}\,\partial_x\phi_1^{\circ} + \sin\phi_3^{\circ}\,\partial_x\phi_2^{\circ},$$
$$\mu_2^{\circ} = \cos\phi_3^{\circ}\,\partial_x\phi_2^{\circ} - \cos\phi_2^{\circ}\sin\phi_3^{\circ}\,\partial_x\phi_1^{\circ},$$
$$\mu_3^{\circ} = \partial_x\phi_3^{\circ} + \sin\phi_2^{\circ}\,\partial_x\phi_1^{\circ}.$$

$$(4.1.11)$$

For the equilibrium and dynamic configurations $\mathcal{B}^{\circ}$ and $\breve{\mathcal{B}}$, ν° and $\breve{\nu}$ represent the deck stretches, $(\eta_1^{\circ}, \eta_2^{\circ})$ and $(\breve{\eta}_1, \breve{\eta}_2)$ are the shear strains along the $\boldsymbol{b}_1^{\circ}$ and $\breve{\boldsymbol{b}}_1$ and $\boldsymbol{b}_2^{\circ}$ and $\breve{\boldsymbol{b}}_2$ directions, respectively. The components of the curvature vector in the static and dynamic local basis ($\boldsymbol{\mu}^{\circ} = \mu_1^{\circ}\boldsymbol{b}_1^{\circ} + \mu_2^{\circ}\boldsymbol{b}_2^{\circ} + \mu_3^{\circ}\boldsymbol{b}_3^{\circ}$ and $\breve{\boldsymbol{\mu}} = \breve{\mu}_1\breve{\boldsymbol{b}}_1 + \breve{\mu}_2\breve{\boldsymbol{b}}_2 + \breve{\mu}_3\breve{\boldsymbol{b}}_3$) denote the torsional curvatures $(\mu_3^{\circ}, \breve{\mu}_3)$ and the bending curvatures $(\mu_1^{\circ}, \breve{\mu}_1)$ and $(\mu_2^{\circ}, \breve{\mu}_2)$, respectively.

To describe the cables equilibrium and dynamic generalized stress resultants, the vectors $\boldsymbol{n}_{\circ}^{\pm}$ and $\breve{\boldsymbol{n}}^{\pm}$ are introduced as:

$$\boldsymbol{n}_{\circ}^{\pm}(x) = N_{\circ}^{\pm}(x)\boldsymbol{a}_{\circ}^{\pm}, \quad \breve{\boldsymbol{n}}^{\pm}(x,t) = \breve{N}^{\pm}(x,t)\breve{\boldsymbol{a}}^{\pm}. \tag{4.1.12}$$

The generalized stress resultants and stress moment resultants of the deck-girder are given by $(\boldsymbol{n}^{\circ}, \boldsymbol{m}^{\circ})$ in $\mathcal{B}^{\circ}$ and by $(\breve{\boldsymbol{n}}, \breve{\boldsymbol{m}})$ in $\breve{\mathcal{B}}$. The component form of the deck contact forces and couples is given by:

$$\boldsymbol{n}^{\circ}(x) = Q_1^{\circ}(x)\boldsymbol{b}_1^{\circ} + Q_2^{\circ}(x)\boldsymbol{b}_2^{\circ} + N^{\circ}(x)\boldsymbol{b}_3^{\circ},$$
$$\breve{\boldsymbol{n}}(x,t) = \breve{Q}_1(x,t)\breve{\boldsymbol{b}}_1 + \breve{Q}_2(x,t)\breve{\boldsymbol{b}}_2 + \breve{N}(x,t)\breve{\boldsymbol{b}}_3,$$
$$\boldsymbol{m}^{\circ}(x) = M_1^{\circ}(x)\boldsymbol{b}_1^{\circ} + M_2^{\circ}(x)\boldsymbol{b}_2^{\circ} + T^{\circ}(x)\boldsymbol{b}_3^{\circ},$$
$$\breve{\boldsymbol{m}}(x,t) = \breve{M}_1(x,t)\breve{\boldsymbol{b}}_1 + \breve{M}_2(x,t)\breve{\boldsymbol{b}}_2 + \breve{T}(x,t)\breve{\boldsymbol{b}}_3$$

$$(4.1.13)$$

where the components have the meaning of tensions $(N^{\circ}, \breve{N})$, shear forces $(Q_1^{\circ}, \breve{Q}_1)$ and $(Q_2^{\circ}, \breve{Q}_2)$ for the contact force vectors $(\boldsymbol{n}^{\circ}, \breve{\boldsymbol{n}})$ while, for the contact couples $(\boldsymbol{m}^{\circ}, \breve{\boldsymbol{m}})$, they represent the torques $(T^{\circ}, \breve{T})$ and the bending moments $(M_1^{\circ}, \breve{M}_1)$ and $(M_2^{\circ}, \breve{M}_2)$. The equilibrium equations can thus be written as

$$\partial_x\boldsymbol{n}_{\circ}^{\pm} + \boldsymbol{f}_{\circ}^{\pm} - \boldsymbol{r}_{\circ}^{\pm} = \boldsymbol{o},$$
$$\partial_x\boldsymbol{n}^{\circ} + \boldsymbol{f}^{\circ} + \boldsymbol{r}_{\circ}^{+} + \boldsymbol{r}_{\circ}^{-} = \boldsymbol{o},$$
$$\partial_x\boldsymbol{m}^{\circ} + \partial_x\boldsymbol{p}_{\circ} \times \boldsymbol{n}^{\circ} + \tfrac{B^{\mathrm{c}}}{2}\,\boldsymbol{b}_1^{\circ} \times (\boldsymbol{r}_{\circ}^{-} - \boldsymbol{r}_{\circ}^{+}) + \boldsymbol{c}^{\circ} = \boldsymbol{o}.$$

$$(4.1.14)$$

where the forces $\boldsymbol{f}_{\circ}^{\pm}(x)$, $\boldsymbol{f}^{\circ}(x)$ and couples $\boldsymbol{c}^{\circ}(x)$ include the cables and deck weights and B^{c} represents the distance between the two suspension cables (see Fig. 4.1).

The equations of motion are obtained by enforcing the balance of linear and angular momentum for the cable-deck system. The equations of motion read

$$\partial_x\breve{\boldsymbol{n}}^{\pm} + \breve{\boldsymbol{f}}^{\pm} - \breve{\boldsymbol{r}}^{\pm} = \rho A^{\mathrm{c}}\sec\theta_{\circ}^{\pm}(x)\,\partial_{tt}\boldsymbol{v}^{\pm} + D_j^{\mathrm{c}}\,\partial_t\boldsymbol{v}^{\pm},$$
$$\partial_x\breve{\boldsymbol{n}} + \breve{\boldsymbol{f}} + \breve{\boldsymbol{r}}^{+} + \breve{\boldsymbol{r}}^{-} = \rho A^{\mathrm{d}}\partial_{tt}\boldsymbol{u} + D_j^{\mathrm{d}}\,\partial_t\boldsymbol{u},$$
$$\partial_x\breve{\boldsymbol{m}} + \partial_x\breve{\boldsymbol{p}} \times \breve{\boldsymbol{n}} + \breve{\boldsymbol{c}} + \tfrac{B^{\mathrm{c}}}{2}\,\breve{\boldsymbol{b}}_1 \times (\breve{\boldsymbol{r}}^{-} - \breve{\boldsymbol{r}}^{+}) = \rho\boldsymbol{J}^{\mathrm{C}} \cdot \partial_t\boldsymbol{\omega} + \boldsymbol{\omega} \times (\rho\boldsymbol{J}^{\mathrm{C}} \cdot \boldsymbol{\omega}) + D_j^{\mathrm{T}}\,\boldsymbol{\omega}.$$

$$(4.1.15)$$

where $\partial_t(\cdot)$ indicates partial differentiation with respect to time t and $\sec\theta_{\rm o}^\pm(x) = \nu_{\rm o}^\pm / [\cos\theta^{\rm c}(1+\partial_x v_{{\rm o}3}^\pm)]$; $\rho A^{\rm c}$ and $\rho A^{\rm d}$ are the cables and deck mass per unit length, respectively, $\boldsymbol{\rho J}^{\rm C}$ is the tensor of the inertia mass moments of the deck cross sections referred to the center of mass; $\boldsymbol\omega(x,t)$ is the incremental angular velocity vector of the cross sections defined in the local reference frame such that $\partial_t \breve{\boldsymbol b}_k = \boldsymbol\omega \times \breve{\boldsymbol b}_k$. In addition, $\breve{\boldsymbol f}(x,t)$ and $\breve c(x,t)$ denote the total forces and couples per unit length, respectively, acting in the deck current dynamic configuration; finally, the damping forces are assumed proportional, through the coefficients D_{v_j}, D_{u_j} and D_{ϕ_j}, to the velocity $\partial_t \boldsymbol u$ and the angular velocity $\boldsymbol\omega(x,t)$. Linearly elastic constitutive laws are assumed in order to describe the relations between the generalized stress resultant forces and couples and the generalized strain parameters.

The hangers strain and the tension $\boldsymbol r_{\rm o}^\pm$ and $\breve{\boldsymbol r}^\pm$ can be defined assuming an equivalent continuous hangers distribution along the bridge span; accordingly $l_{\rm h}(x) := h + y^{\rm c}(x)$ is a function that defines the hangers undeformed length along the bridge span and h is the height of the bridge towers measured from the deck. The cables catenaries can be described in the fixed frame by $\boldsymbol y^\pm(x) = \mp (B^{\rm c}/2)\,\boldsymbol e_1 + l_{\rm h}(x)\,\boldsymbol e_2 + x\,\boldsymbol e_3$. The expressions of the static and dynamic hanger stretches $\nu_{\rm h}^{{\rm o}\pm}(x)$ and $\breve\nu_{\rm h}^\pm(x,t)$ are obtained as

$$\nu_{\rm h}^{{\rm o}\pm}(x) = \frac{\|\boldsymbol q_{\rm o}^\pm - \boldsymbol p_{\rm o}^\pm\|}{l_{\rm h}(x)}\ , \quad \breve\nu_{\rm h}^\pm(x,t) = \frac{\|\breve{\boldsymbol q}^\pm - \breve{\boldsymbol p}^\pm\|}{l_{\rm h}(x)}\ . \tag{4.1.16}$$

The vectors $\boldsymbol p_{\rm o}^\pm$ and $\breve{\boldsymbol p}^\pm$ indicate the position vectors of the hanger points of attachment onto the deck in the static and dynamic configurations, respectively, and their expressions are given by

$$\boldsymbol p_{\rm o}^\pm(x) = \boldsymbol x(x) + \boldsymbol u_{\rm o}^\pm(x)\,, \quad \breve{\boldsymbol p}^\pm(x,t) = \boldsymbol x(x) + \breve{\boldsymbol u}^\pm(x,t)\,,$$
$$\boldsymbol u_{\rm o}^\pm(x) = \boldsymbol u_{\rm o}(x) \mp \tfrac{B^{\rm c}}{2}\left(\boldsymbol b_1^{\rm o}(x) - \boldsymbol e_1\right)\,, \quad \breve{\boldsymbol u}^\pm(x,t) = \breve{\boldsymbol u}(x,t) \mp \tfrac{B^{\rm c}}{2}\left(\breve{\boldsymbol b}_1(x,t) - \boldsymbol e_1\right)\,. \tag{4.1.17}$$

where the total displacements of the deck and cable base lines, $\breve{\boldsymbol u}(x,t)$ and $\breve{\boldsymbol v}^\pm(x,t)$, respectively, are defined as

$$\breve{\boldsymbol u}(x,t) := \boldsymbol u_{\rm o}(x) + \boldsymbol u(x,t)\,, \quad \breve{\boldsymbol v}^\pm(x,t) := \boldsymbol v_{\rm o}^\pm(x) + \boldsymbol v^\pm(x,t). \tag{4.1.18}$$

The elastic constitutive law for the hangers can be written as

$$\boldsymbol r_{\rm o}^\pm(x) = \frac{E^{\rm h} A^{\rm h}}{l_{\rm h}(x)}\left(\nu_{\rm h}^{{\rm o}\pm}(x) - 1\right)\boldsymbol e_{\rm oh}^\pm\,, \quad \breve{\boldsymbol r}^\pm(x,t) = \frac{E^{\rm h} A^{\rm h}}{\nu_{\rm h}^{{\rm o}\pm}(x)\, l_{\rm h}(x)}\left(\breve\nu_{\rm h}^\pm(x,t) - 1\right)\breve{\boldsymbol e}_{\rm h}^\pm\,,$$
$$\boldsymbol e_{\rm oh}^\pm = \frac{\boldsymbol q_{\rm o}^\pm - \boldsymbol p_{\rm o}^\pm}{\|\boldsymbol q_{\rm o}^\pm - \boldsymbol p_{\rm o}^\pm\|}\ , \quad \breve{\boldsymbol e}_{\rm h}^\pm = \frac{\breve{\boldsymbol q}^\pm - \breve{\boldsymbol p}^\pm}{\|\breve{\boldsymbol q}^\pm - \breve{\boldsymbol p}^\pm\|}. \tag{4.1.19}$$

Finally, the kinematic and mechanical boundary conditions are referred to a simply-supported scheme for the deck while the two suspension cables ends are fixed atop the towers. They can be written in the global reference frame $\{\boldsymbol e_1, \boldsymbol e_2, \boldsymbol e_3\}$ as

$$\boldsymbol u_{\rm o}(0) = \boldsymbol o,\ \boldsymbol m^{\rm o}(0)\cdot\boldsymbol e_1 = 0,\ \psi_2^{\rm o}(0) = 0,\ \psi_3^{\rm o}(0) = 0$$
$$\boldsymbol u_{\rm o}(l)\cdot\boldsymbol e_1 = 0,\ \boldsymbol u_{\rm o}(l)\cdot\boldsymbol e_2 = 0,\ \boldsymbol n^{\rm o}(l)\cdot\boldsymbol e_3 = 0,\ \boldsymbol m^{\rm o}(l)\cdot\boldsymbol e_1 = 0,\ \psi_2^{\rm o}(l) = 0,\ \psi_3^{\rm o}(l) = 0$$
$$\boldsymbol v_{\rm o}^\pm(0) = \boldsymbol o,\ \boldsymbol v_{\rm o}^\pm(l) = \boldsymbol o$$
$$\breve{\boldsymbol u}(0,t) = \boldsymbol o,\ \breve{\boldsymbol m}(0,t)\cdot\boldsymbol e_1 = 0,\ \breve\psi_2(0,t) = 0,\ \breve\psi_3(0,t) = 0 \tag{4.1.20}$$
$$\breve{\boldsymbol u}(l,t)\cdot\boldsymbol e_1 = 0,\ \breve{\boldsymbol u}(l,t)\cdot\boldsymbol e_2 = 0,\ \breve{\boldsymbol n}(l,t)\cdot\boldsymbol e_3 = 0,$$
$$\breve{\boldsymbol m}(l,t)\cdot\boldsymbol e_1 = 0,\ \breve\psi_2(l,t) = 0,\ \breve\psi_3(l,t) = 0$$

where $\psi_i^{\rm o}(x)$ and $\breve\psi_i(x,t)$, $i = 1, 2, 3$, represent the static and dynamic rotations of the deck cross section and their expressions in the fixed frame $\{\boldsymbol e_1, \boldsymbol e_2, \boldsymbol e_3\}$ can be defined as:

$$\boldsymbol{\Psi}^{\circ} = \begin{bmatrix} \psi_1^{\circ} & \psi_2^{\circ} & \psi_3^{\circ} \end{bmatrix}^{\top}, \quad \breve{\boldsymbol{\Psi}} = \begin{bmatrix} \breve{\psi}_1, & \breve{\psi}_2, & \breve{\psi}_3 \end{bmatrix}^{\top},$$

$$\psi_1^{\circ} = \phi_1^{\circ} + \phi_3^{\circ} \sin \phi_2^{\circ}, \quad \psi_2^{\circ} = \phi_2^{\circ} \cos \phi_1^{\circ} - \phi_3^{\circ} \sin \phi_1^{\circ} \cos \phi_2^{\circ}, \quad (4.1.21)$$

$$\psi_3^{\circ} = \phi_2^{\circ} \sin \phi_1^{\circ} + \phi_3^{\circ} \cos \phi_1^{\circ} \cos \phi_2^{\circ}.$$

$$\begin{aligned}
\breve{\psi}_1 =& \phi_1 \cos \phi_2^{\circ} \cos \phi_3^{\circ} + \phi_2 \big(\sin \phi_2^{\circ} \sin \phi_1 - \cos \phi_2^{\circ} \sin \phi_3^{\circ} \cos \phi_1 \big) \\
& + \phi_3 \big(\sin \phi_2^{\circ} \cos \phi_1 \cos \phi_2 + \cos \phi_2^{\circ} \sin \phi_3^{\circ} \sin \phi_1 \cos \phi_2 + \cos \phi_2^{\circ} \cos \phi_3^{\circ} \sin \phi_2 \big), \\
\breve{\psi}_2 =& \phi_1 \big(\sin \phi_1^{\circ} \sin \phi_2^{\circ} \cos \phi_3^{\circ} + \cos \phi_1^{\circ} \sin \phi_3^{\circ} \big) + \phi_2 \big[\cos \phi_1 \big(\cos \phi_1^{\circ} \cos \phi_3^{\circ} \\
& - \sin \phi_1^{\circ} \sin \phi_2^{\circ} \sin \phi_3^{\circ} \big) - \sin \phi_1^{\circ} \cos \phi_2^{\circ} \sin \phi_1 \big] \\
& + \phi_3 \big[- \sin \phi_1^{\circ} \cos \phi_2^{\circ} \cos \phi_1 \cos \phi_2 - \sin \phi_1 \cos \phi_2 \big(\cos \phi_1^{\circ} \cos \phi_3^{\circ} \\
& - \sin \phi_1^{\circ} \sin \phi_2^{\circ} \sin \phi_3^{\circ} \big) + \sin \phi_2 \big(\sin \phi_1^{\circ} \sin \phi_2^{\circ} \cos \phi_3^{\circ} + \cos \phi_1^{\circ} \sin \phi_3^{\circ} \big) \big], \\
\breve{\psi}_3 =& \phi_1 \big(\sin \phi_1^{\circ} \sin \phi_3^{\circ} - \cos \phi_1^{\circ} \sin \phi_2^{\circ} \cos \phi_3^{\circ} \big) + \phi_2 \big[\cos \phi_1 \big(\sin \phi_1^{\circ} \cos \phi_3^{\circ} \\
& + \cos \phi_1^{\circ} \sin \phi_2^{\circ} \sin \phi_3^{\circ} \big) + \cos \phi_1^{\circ} \cos \phi_2^{\circ} \sin \phi_1 \big] \\
& + \phi_3 \big[\cos \phi_1^{\circ} \cos \phi_2^{\circ} \cos \phi_1 \cos \phi_2 - \sin \phi_1 \cos \phi_2 \big(\sin \phi_1^{\circ} \cos \phi_3^{\circ} \\
& + \cos \phi_1^{\circ} \sin \phi_2^{\circ} \sin \phi_3^{\circ} \big) + \sin \phi_2 \big(\sin \phi_1^{\circ} \sin \phi_3^{\circ} - \cos \phi_1^{\circ} \sin \phi_2^{\circ} \cos \phi_3^{\circ} \big) \big].
\end{aligned} \qquad (4.1.22)$$

4.1.2 Nondimensional Form

The governing static and dynamic equations (4.1.14) and (4.1.15), together with the associated boundary conditions (4.1.20), are cast in nondimensional form by using the deck span l as characteristic length and $\sqrt{\rho A^{\mathrm{d}} l^4 / E^{\mathrm{d}} J_1}$ as characteristic time, where ρA^{d} is the deck mass per unit length, E^{d} is the deck Young modulus and J_1 the moment of inertia about the local axis $\boldsymbol{b}_1$. The deck nondimensional mass per unit length turns out to be $\varrho^{\mathrm{d}} = 1$ whereas the cables mass in nondimensional form can be written as $\varrho^{\mathrm{c}} = \rho A^{\mathrm{c}} / \rho A^{\mathrm{d}}$. Moreover, the nondimensional structural damping coefficients are expressed as

$$\bar{D} v_j = 2 \zeta \omega_{v_j} \varrho^{\mathrm{c}}, \quad \bar{D} u_j = 2 \zeta \omega_{u_j}, \quad \bar{D} \phi_3 = 2 \zeta \omega_{\phi_3} \bar{J}^{\,\mathrm{m}}, \quad (j = 1, 2, 3). \qquad (4.1.23)$$

With this notation it is assumed that the nondimensional damping coefficients are proportional through a damping factor ζ to the nondimensional first lower natural frequencies ω_{v_j}, ω_{u_j} and ω_{ϕ_3} evaluated for the linear representation of the bridge under the self-weight; $\bar{J}^{\,\mathrm{m}} = \big(\rho J_3^{\mathrm{c}} + \frac{1}{2} \rho A^{\mathrm{c}} B^{\mathrm{c}2} \big) / \big(\rho A^{\mathrm{d}} l^2 \big)$ is the nondimensional mass moment along the direction $\breve{\boldsymbol{b}}_3$ of the deck accounting for the cables mass contribution. The contribution of the flexural angular rates on the structural damping as well as their inertial contribution is neglected in the modeling. The independent nondimensional stiffness parameters are defined as ratios to the flexural deck stiffness $E^{\mathrm{d}} J_1 / l^3$.

The nondimensionalized equations (4.1.14) and (4.1.15), projected into the fixed basis $\{\boldsymbol{e}_1, \boldsymbol{e}_2, \boldsymbol{e}_3\}$, yield twelve nonlinear partial-differential equations in twelve independent kinematic unknowns. The obtained equations govern the elastostatic and elastodynamic problems, respectively, and the following independent parameters are introduced to cast the model in nondimensional form:

$$\alpha^{\mathrm{c}} = \frac{H^{\mathrm{c}} l^2}{E^{\mathrm{d}} J_1}, \quad \kappa^{\mathrm{c}} = \frac{E^{\mathrm{c}} A^{\mathrm{c}} l^2}{E^{\mathrm{d}} J_1}, \quad \kappa^{\mathrm{h}} = \frac{E^{\mathrm{h}} A^{\mathrm{h}} l^2}{E^{\mathrm{d}} J_1}, \quad \kappa^{\mathrm{d}} = \frac{A^{\mathrm{d}} l^2}{J_1}$$

$$\gamma_j = \frac{G^{\mathrm{d}} A_j^{*\mathrm{d}} l^2}{E^{\mathrm{d}} J_1}, \quad \chi = \frac{J_2}{J_1}, \quad \tau = \frac{G^{\mathrm{d}} J_3}{E^{\mathrm{d}} J_1} \qquad (4.1.24)$$

where A^c and A^h are the cables and hangers cross section area, E^c and E^h their Young's modulus, A^d and A^{*d} are the deck cross section area and shear area in direction $\boldsymbol{b}_j$, $j = 1, 2,$, G^d is the shear modulus; J_2 and J_3 are the flexural moment of inertia and the torsional moment of inertia. The space and time nondimensional coordinates are then defined as $\bar{x} = x/l$, $\bar{y}^c(\bar{x}) = y^c(x)/l$, $\bar{y}^{\pm}(\bar{x}) = y^{\pm}(x)/l$, $\bar{t} = t\bar{\omega}$, $\bar{\omega} = \sqrt{E^d J_1/(\rho A^d l^4)}$ and the displacement vectors as $\bar{\boldsymbol{u}} = \boldsymbol{u}/l$, $\bar{\boldsymbol{v}}^{\pm} = \boldsymbol{v}^{\pm}/l$. Accordingly, by considering the definitions in (4.1.24), the elastic constitutive laws can be expressed in the nondimensional form:

$$N_o^{\pm} = N^c + \kappa^c \left(\nu_o^{\pm} - 1\right) , \; N^o = \kappa^d \left(\nu^o - 1\right) , \; Q_1^o = \gamma_1 \, \eta_1^o , \; Q_2^o = \gamma_2 \, \eta_2^o ,$$
$$M_1^o = \mu_1^o , \; M_2^o = \chi \, \mu_2^o , \; T^o = \tau \, \mu_3^o ,$$
$$\check{N}^{\pm} = N^c + \kappa^c \left(\check{\nu}^{\pm} - 1\right) , \; \check{N} = \kappa^d \left(\check{\nu} - 1\right) , \; \check{Q}_1 = \gamma_1 \, \check{\eta}_1 , \; \check{Q}_2 = \gamma_2 \, \check{\eta}_2 ,$$
$$\check{M}_1 = \check{\mu}_1 , \; \check{M}_2 = \chi \, \check{\mu}_2 , \; \check{T} = \tau \, \check{\mu}_3 ,$$
$$\boldsymbol{r}_o^{\pm}(x) = \frac{\kappa^h}{\bar{l}_h(x)} \left(\nu_h^{o\pm}(x) - 1\right) \boldsymbol{e}_{oh}^{\pm} , \; \check{\boldsymbol{r}}^{\pm}(x,t) = \frac{\kappa^h}{\nu_h^{o\pm}(x)\,\bar{l}_h(x)} \left(\check{\nu}_h^{\pm}(x,t) - 1\right) \check{\boldsymbol{e}}_h^{\pm}$$

(4.1.25)

where $N^c = \alpha^c/\cos\theta^c$ is the catenary cable tension and $\bar{l}_h = l_h/l$.

4.2 Computational Approach and Model Validation

The coupled nonlinear partial-differential equations of motion (4.1.15), cast in a nondimensional form, are implemented in the finite element computational platform [56] using the PDE-mode feature. The space-time integration is numerically performed by using the FE method. The mesh of the one-dimensional domain $[0, 1]$, representing the bridge span, was adapted to optimize the accuracy and evaluation time of the solution, and fourth-order Lagrangian polynomials were used to approximate each of the 12 kinematic independent variables of the system. The generalized-α method, a one step implicit, second-order method present in the FE code employed, was adopted for solving the transient problem when integrating equations (4.1.14) and (4.1.15).

A preliminary validation of the equations of motion is performed evaluating the modal properties of two existing suspension bridges: the Runyang Suspension Bridge with a span of 1490 m and the Hu Men Suspension Bridge having a span of about 888 m. These two bridges have more or less the same shape and cross sectional size, but a very different span since the Runyang span is about 70% greater than the Hu Men span. This implies significantly different nonlinear behaviors as highlighted by the investigations carried out in this work about the static aeroelastic stability. The following analyses are based on the reference mechanical parameters and the obtained results are compared with those proposed in [14, 36, 37] for the Runyang bridge and [15, 18] for the Hu Men bridge, respectively.

The elastogeometric properties of the girder-deck of the Runyang and Hu Men bridges can be summarized as follows: $l = 1490/888$ m, $B = 35.9/35.6$ m, $D = 3/3.012$ m, $A^d = 1.2481/1.2443$ m^2, $\rho A^d = 18387/18330$ kg/m, $\rho J_3^e = 1.852 \cdot 10^6/1.743 \cdot 10^6$ kg m^2/m, $E = 210/210$ GPa, $G = 80.77/80.77$ GPa, $J_1 = 1.9842/1.98$ m^4, $J_2 = 137.754/124.39$ m^4, $J_3^e = 5.034/5.1$ m^4. Here and henceforth, the slash separates quantities referred to the Runyang bridge (left) from those referred to the Hu Men bridge (right). On the other hand, the suspension cables exhibit the following properties: $E^c = 200/200$ GPa, $d^c = 0.776/0.623$ m, $A^c = 0.47347/0.305$ m^2, $\rho A^c = 3817/2397$ kg/m. The sag of the cables under their own weight is $149/84.6$ m and the horizontal force is $H^c = 7.096/2.792 \cdot 10^7$ N. The hangers have the following properties: $E^h = 210/160$ GPa, $d^h = 0.0522/0.0529$ m, $A^h = 2.14/2.198 \cdot 10^{-3}$ m^2, and the distance between the hangers is $B^c = 34.3/33$ m. The height of the towers is $h = 154/90$ m. The damping factor is 0.5% for both bridges.

4.3 Modal Analysis

The eigenvalue problem is solved considering the bridge deformed configuration under dead load so as to account for the pre-stressed state. The study is performed in two steps: in the first step, the equilibrium equations (4.1.14) are solved to obtain the equilibrium state and the generalized stresses are evaluated across the structure. In the second step, the lowest natural frequencies and mode shapes of the bridge are evaluated solving the eigenvalue problem associated with equations (4.1.15) including the computed equilibrium configuration.

In Tab. 4.1 the lowest few frequencies of the bridge modes are illustrated and compared with the literature results obtained via a linear FE model of the structure. Slightly higher values obtained by the proposed model are due to the adopted continuum formulation in which the stiffness parameters are average values and the real discrete hanger distribution is replaced by a continuum equivalent distribution. The kinematic unknowns, which govern such a rich mechanical problem in the present continuum formulation, are only 12.

Proposed parametric nonlinear model						
f_1[Hz]	f_2[Hz]	f_3[Hz]	f_4[Hz]	f_5[Hz]	f_6[Hz]	f_7[Hz]
F-1 sym	*F-2 skew*	*F-2 sym*	*F-1 skew*	*F-2 skew*	*T skew*	*T sym*
$v_1^\pm\vert u_1$	$v_2^\pm,u_2$	$v_2^\pm,u_2$	$v_1^\pm\vert u_1$	$v_2^\pm,u_2$	$v_2^\pm,\phi_3$	$v_2^\pm,\phi_3$
SF 0.045|0.064	0.050	0.074	0.09|0.175	0.108	0.211	0.253
$v_1^\pm,u_1$	$v_2^\pm,u_2$	$v_2^\pm,u_2$	$v_1^\pm,u_1$	$v_2^\pm,u_2$	$v_2^\pm,\phi_3$	$\breve{v}_2^\pm,\breve{\phi}_3$
PS 0.070	0.096	0.128	0.1707	0.1797	0.229	0.277
Literature results [36]						
–	–	0.126	–	0.172	–	0.241

Table 4.1: *Frequencies of the lowest six modes of the Runyang suspension bridge about the stress-free and pre-stressed configurations.* SF *stands for stress-free and* PS *refers to pre-stresses condition, whereas* F-1, F-2 *and* T *identify the flexural modes in directions* $\boldsymbol{e}_2$ *and* $\boldsymbol{e}_3$ *and the torsional mode, respectively.*

Proposed parametric nonlinear model						
f_1[Hz]	f_2[Hz]	f_3[Hz]	f_4[Hz]	f_5[Hz]	f_6[Hz]	f_7[Hz]
F-1sym	*F-2 skew*	*F-2 sym*	*F-1 skew*	*F-2 skew*	*T skew*	*T sym*
$v_1^\pm\vert u_1$	$v_2^\pm,u_2$	$v_2^\pm,u_2$	$v_1^\pm\vert u_1$	$v_2^\pm,u_2$	$v_2^\pm,\phi_3$	$v_2^\pm,\phi_3$
SF 0.06|0.170	0.065	0.106	0.119|0.469	0.174	0.402	0.409
F-2 skew	*F-1 sym*	*F-2 sym*	*F-2 skew*	*F-1 skew*	*T skew*	*T sym*
$v_2^\pm,u_2$	$v_1^\pm,u_1$	$v_2^\pm,u_2$	$v_2^\pm,u_2$	$v_1^\pm,u_1$	$v_2^\pm,\phi_3$	$v_2^\pm,\phi_3$
PS 0.129	0.161	0.181	0.269	0.319	0.434	0.439
Literature results [35]						
–	–	0.172	–	–	0.426	0.361

Table 4.2: *Frequencies of the lowest six modes of the Hu Men suspension bridge about the stress-free and pre-stressed configurations.* SF *stands for stress-free and* PS *refers to pre-stresses condition, whereas* F-1, F-2 *and* T *identify the flexural modes in directions* $\boldsymbol{e}_2$ *and* $\boldsymbol{e}_3$ *and the torsional mode, respectively.*

The first row gives the frequencies calculated considering the stress-free configuration of the bridge. The first mode is a symmetric local mode affecting the cables alone moving in the out-of-plane direction in a pendulum-like mode. The second mode is the first symmetric lateral bending mode for the deck involving also the cables. The modes that follow in the sequence are the lowest skew–symmetric and
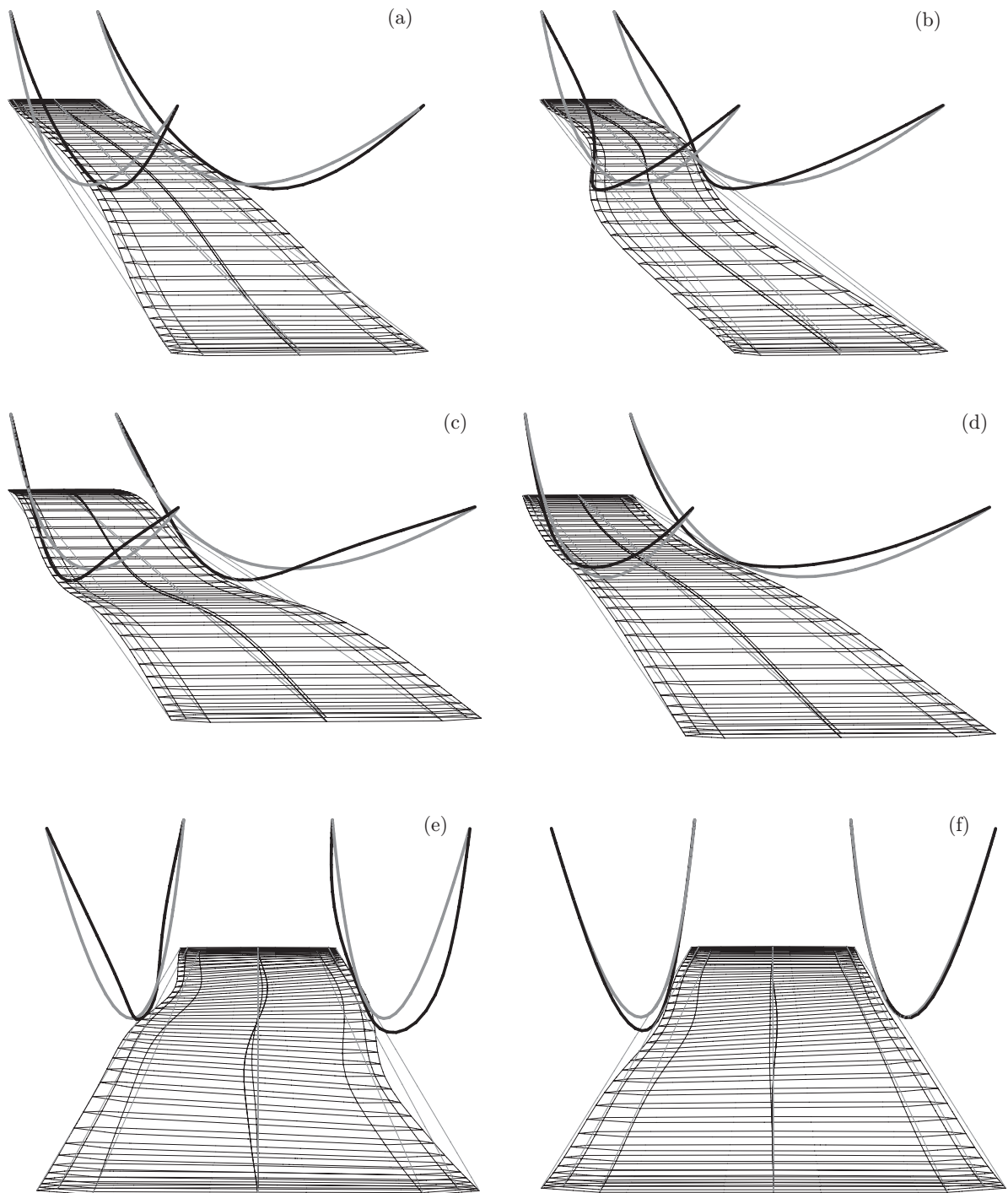
Fig. 4.3: *The lowest six mode shapes of the Runyang suspension bridge.*

lowest symmetric bending modes in the vertical direction. Thereafter, the bridge exhibits the lowest skew-symmetric lateral mode and the second skew-symmetric mode in the vertical direction. The sixth and the seventh modes are the lowest skew-symmetric and symmetric torsional modes.

On the other hand, if the prestressed condition is taken into account, the local cable mode disappears but the sequence of global modes is preserved. The difference is the higher values of the frequencies of all modes due to the positive geometric stiffness of the cables. A good correlation is found with the frequencies reported in the literature [36]. The lowest six modal configurations of the Runyang suspension bridge are portrayed in Fig. 4.3. The aspect ratio of the reference geometry of the bridge as well as the scaling of the modal displacement components have been optimized for visualization purposes of the modal patterns.

For the Hu Men Suspension Bridge, the modal sequence for the stress-free bridge is the same as the Runyang bridge although the frequencies are higher due to the shorter span of the Hu Men. For the prestressed condition, the only difference is that the fourth mode is the second skew-symmetric vertical mode while the fifth mode is the lowest skew-symmetric lateral mode. The frequencies are all higher for this bridge.

4.4 Nonlinear Precritical Equilibrium Paths

The theoretical predictions based on the present nonlinear formulation have been first tested in the context of a static stability analysis since suspension bridges exhibit a substantial nonlinear precritical behavior due to the geometric nonlinearities of the cables. The aim of the analysis is to evaluate the nonlinear equilibrium paths of the bridge subject to vertical downward loads of increasing magnitude (quantified by the multiplier λ of the dead loads) and estimate the increase of stiffness suffered by the cables. On the other hand, path following analyses for increasing upward loads are performed to show the softening effect induced by the loss of tension in the cables. The geometric nonlinearities accounted for in the deck modeling are expected to give a marginal contribution to the increase of the overall stiffness of the bridge because of the assumed typical boundary conditions for the deck. The simply supported scheme does not allow the stretching effect to appear with the associated funicular-type load-bearing capacity so that the only nonlinear (geometric) contribution to the deck stiffness comes from nonlinear curvature effects.

Figures 4.4a and 4.4b show the nonlinear equilibrium paths obtained for the vertical displacement component of the deck and the maximum stretch of the cables compared with the paths obtained by linear theory. The increment of stiffness due to the geometric nonlinearity is appreciable; the difference in the structural response becomes discernible already at low values of the dead load multiplier λ. Otherwise, very small increments of upward loads induce a pronounced softening behavior, which can be appreciated in Figs. 4.4c and 4.4d, due to the loss of tension suffered by the cables.

The equilibrium paths, shown in Figs. 4.5a and 4.5b, were obtained considering the bridge prestressed under the dead load f_2°, subsequently subject to an incremental horizontal load f_1° (Fig. 4.5-a) and twisting couple c_3° (Fig. 4.5-b) proportional to the load f_2°. These uniform loads are considered collinear with the directions of the aeroelastic forces so as to show that the geometric nonlinearities accounted for in the cables and deck-girder induce coupling between forces and displacements along different directions contrary to the predictions of linear theory. In fact such effects vanish in the context of a linear model as suggested by the tangent lines to the curves at the origin of the plots in Figs. 4.5. Moreover, Figs. 4.6a and 4.6b show that the main consequence is the nontrivial, nonsymmetric stretch variations in the cables.
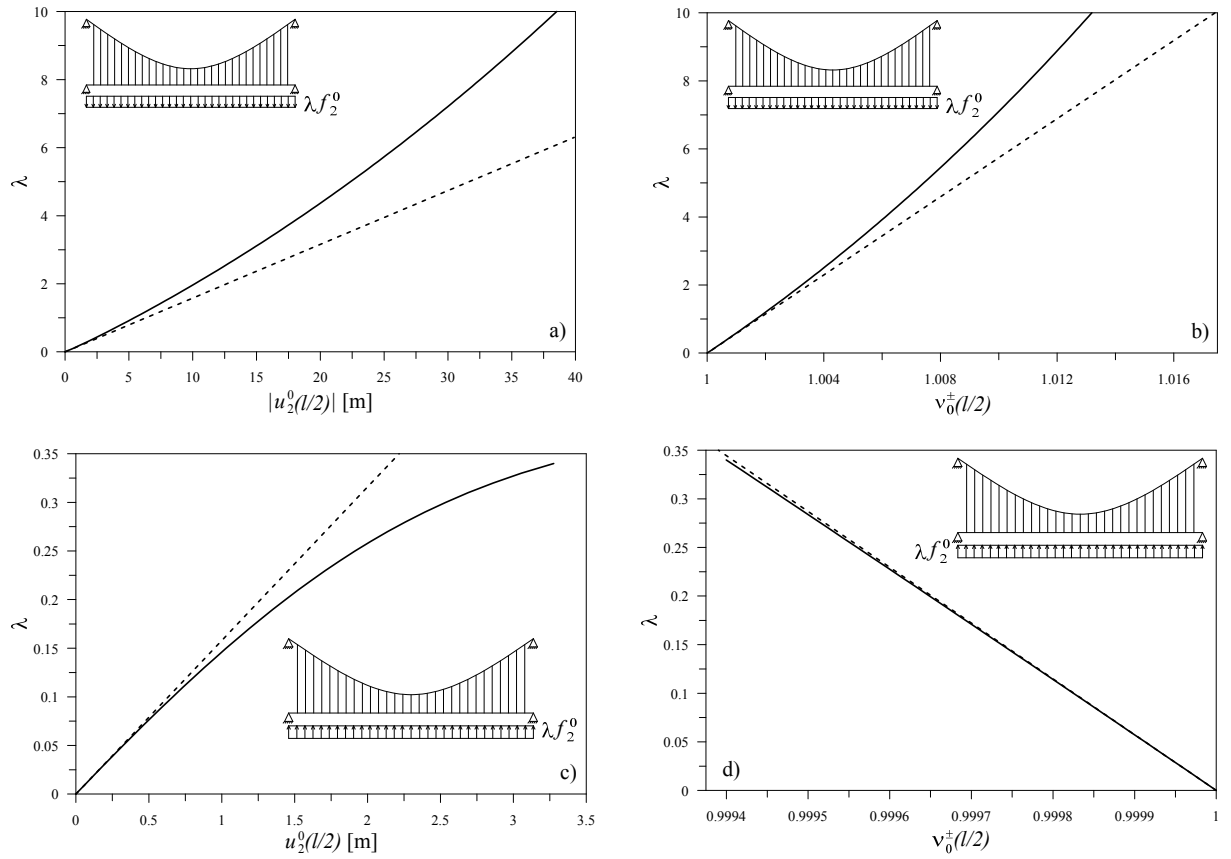
Fig. 4.4: *Nonlinear equilibrium paths under vertical loads: (a) vertical (absolute) deck displacement and (b) cables stretch at the mid-span for increasing load, (c) vertical deck displacement and (d) cables stretch at the mid-span for decreasing load.*
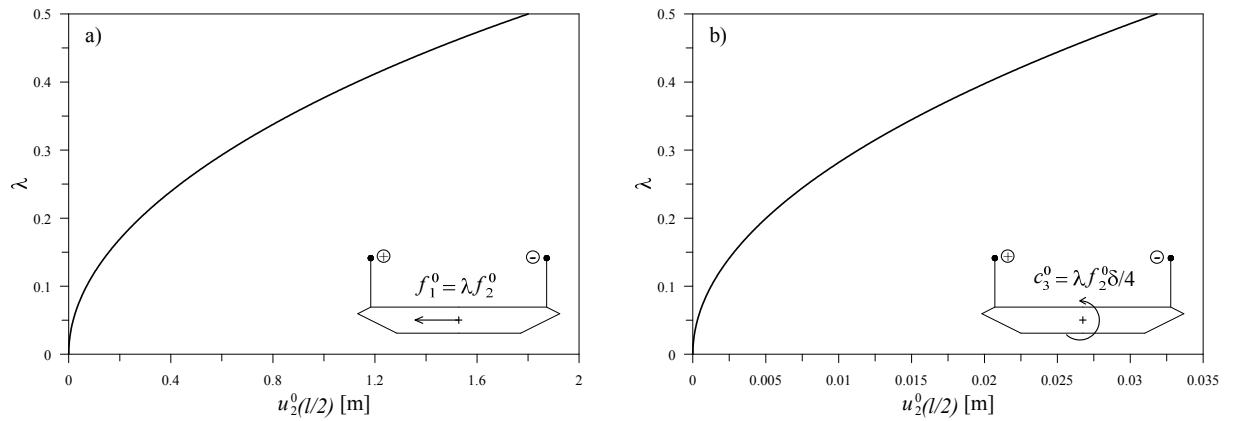

Fig. 4.5: *Nonlinear equilibrium paths: vertical displacement of the mid-span deck section for (a) increasing uniform horizontal load and (b) uniform torque.*
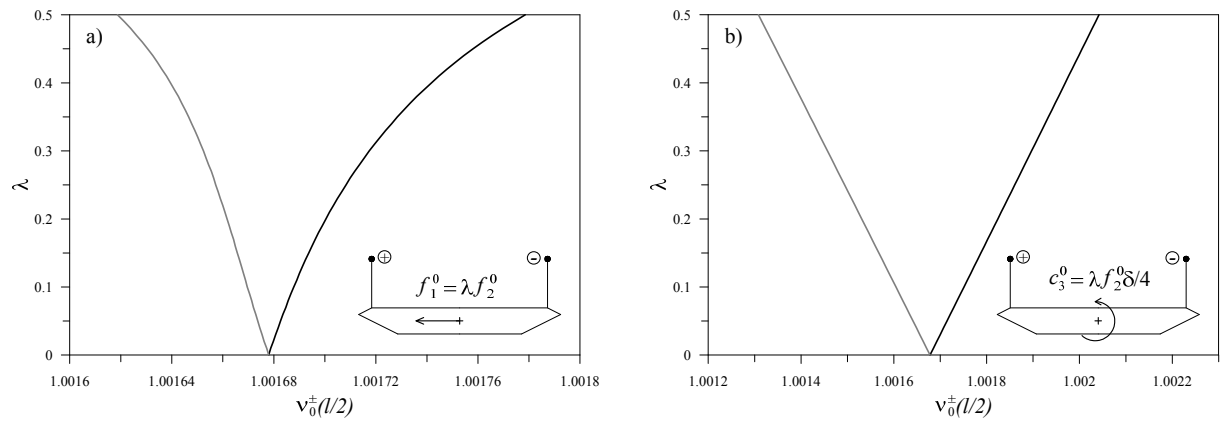
Fig. 4.6: *Cables stretch at the mid-span: (a) for increasing uniform horizontal load and (b) for increasing uniform torque. The gray lines refer to the cable " − ", the black lines refer to the cable " + ".*

Chapter 5
Aeroelastic Stability Analysis

The proper evaluation of the bridge tangent stiffness in the pre-stressed configuration induced by the in-service loads, accounting also for the torsional and out-of-plane components, is a necessary step within the context of an accurate study of the limit states arising from wind-structure interaction. In bridge design, aeroelastic phenomena are usually investigated in the context of cumbersome FE models where sensitivity parametric analyses are computationally demanding because the regeneration of the mesh for the whole geometry of the bridge must be carried out for each individual analysis. On the other hand, the proposed geometrically exact continuum model of suspension bridges represents a suitable parametric framework for investigating limit states and conducting rapid structural optimization studies.

In the following chapter, a nonlinear coupled fluid-structure model for suspension bridges is assembled and static and dynamic aeroelastic instabilities phenomena are investigated. The aerodynamic properties available in the literature for the two case study bridges presented in Section 4.2 are first adopted in the calculations in order to validate the proposed nonlinear modeling; thus, the torsional divergence phenomenon is investigated both by a static parametric analysis and via a modal approach by studying the associated eigenvalue problem, whereas the flutter critical condition is evaluated in the frequency-domain through the use of the aeroelastic derivatives available in the literature. Finally, the frequency- and time-domain descriptions of the aerodynamics of the GBB deck cross section derived in Chapter 3 are then assumed and parametric flutter analyses are performed in both domains and the results compared.

5.1 Static Aeroelastic Instability: Torsional Divergence

The torsional divergence represents the bifurcation of the equilibrium state occurring when the bridge torsional stiffness becomes zero under the static aerodynamic wind loads. This condition is studied by computing the nonlinear precritical equilibrium path under increasing aerodynamic forces until the critical condition is flagged by the singularity of the stiffness matrix. Moreover, an eigenvalue analysis linearized about the configuration induced by the static aerodynamic load is performed, and the critical condition is identified when one of the eigenvalues goes through zero on the real axis.

The static aerodynamic coefficients experimentally determined in wind tunnel tests for the sectional models of the Runyang bridge and the Hu Men bridge are shown in Fig. 5.1. The data obtained by digitalization of the original figures are used to determine by polynomial fitting the following expressions for the lift, drag, and aerodynamic moment coefficients:

i) Runyang bridge:

$$C_{\mathrm{L}}^{\mathrm{R}}\left(\alpha^{\mathrm{E}}\right) = -0.0864 + 0.0744\,\alpha^{\mathrm{E}} - 0.00195\,\alpha^{\mathrm{E}\,2},$$

$$C_{\mathrm{D}}^{\mathrm{R}}\left(\alpha^{\mathrm{E}}\right) = 0.7510 + 0.05867\,\alpha^{\mathrm{E}} - 0.0066\,\alpha^{\mathrm{E}\,2},$$

$$C_{\mathrm{M}}^{\mathrm{R}}\left(\alpha^{\mathrm{E}}\right) = 0.0153 + 0.01654\,\alpha^{\mathrm{E}}.$$

ii) Hu Men bridge:

$$C_{\mathrm{L}}^{\mathrm{HM}}\left(\alpha^{\mathrm{E}}\right) = -0.024 + 0.0789\,\alpha^{\mathrm{E}},$$

$$C_{\mathrm{D}}^{\mathrm{HM}}\left(\alpha^{\mathrm{E}}\right) = 0.8276 + 0.0242535\,\alpha^{\mathrm{E}} - 0.00815\,\alpha^{\mathrm{E}\,2},$$

$$C_{\mathrm{M}}^{\mathrm{HM}}\left(\alpha^{\mathrm{E}}\right) = 0.0153 + 0.0181\,\alpha^{\mathrm{E}}.$$
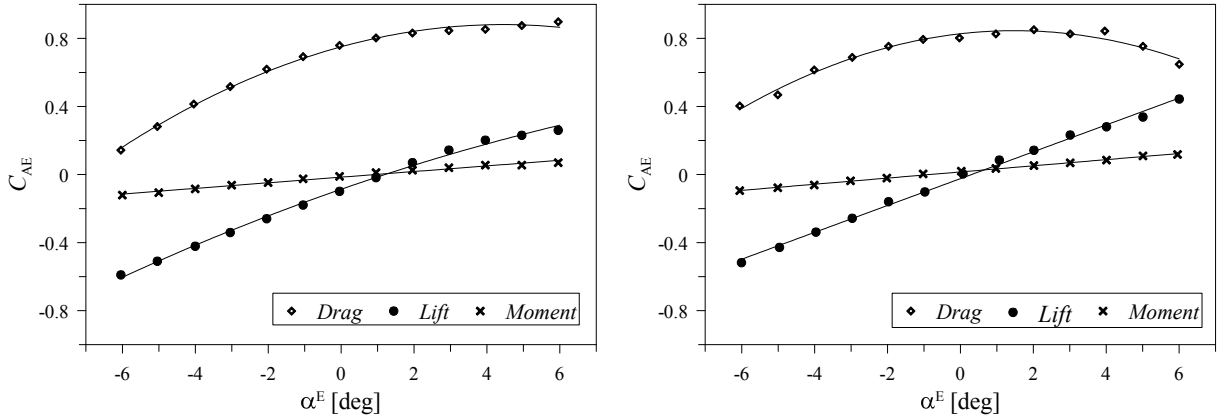
Fig. 5.1: *Lift, drag and moment coefficients obtained in previous experiments and by polynomial fitting for (left) the Runyang bridge and (right) the Hu Men bridge.*

The interaction between the cables and the wind is accounted for by considering the drag force alone having the drag coefficient set to $C_{\mathrm{D}} = 0.7$ as suggested in [74].
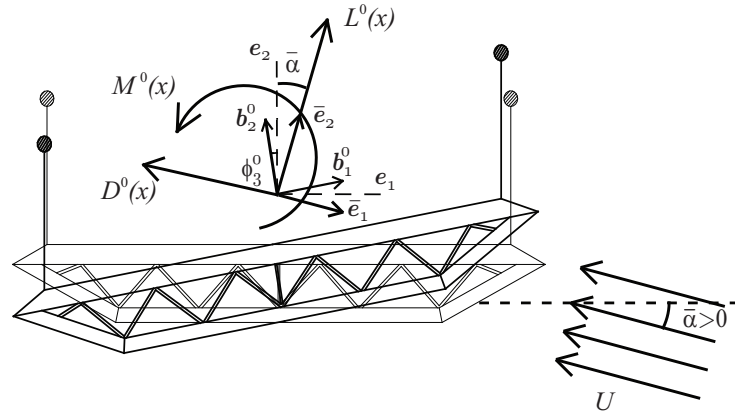
Fig. 5.2: *Positive convention of the aerodynamic forces.*

In the orthonormal frame $\{\bar{e}_1, \bar{e}_2, \bar{e}_3\}$, where $\bar{e}_1$ identifies the direction of the wind speed $\boldsymbol{U} = -U\,\bar{e}_1$ (see Fig. 5.2), such that $\bar{\alpha} = \arccos\left(\boldsymbol{e}_1 \cdot \bar{e}_1\right)$, the nondimensional expressions of the forces per unit length of the deck generated by the static component U of the wind speed are expressed as

$$\boldsymbol{f}^{\mathrm{o}}_{\mathrm{AE}} = -D^{\mathrm{o}}(x)\bar{\boldsymbol{e}}_1 + L^{\mathrm{o}}(x)\bar{\boldsymbol{e}}_2 \, , \; \boldsymbol{c}^{\mathrm{o}}_{\mathrm{AE}} = M^{\mathrm{o}}(x)\bar{\boldsymbol{e}}_3$$

$$L^{\mathrm{o}}(x) = \mathcal{F}\,\delta\,C_{\mathrm{L}}(\alpha^{\mathrm{E}}) \, , \; D^{\mathrm{o}}(x) = \mathcal{F}\,\delta\,\bar{d}\,C_{\mathrm{D}}(\alpha^{\mathrm{E}}) \, , \; M^{\mathrm{o}}(x) = \mathcal{F}\,\delta^2\,C_{\mathrm{M}}(\alpha^{\mathrm{E}}) \tag{5.1.1}$$

$$\boldsymbol{f}^{\pm}_{\mathrm{o,AE}} = -D^{\mathrm{o}}_{\mathrm{c}}(x)\bar{\boldsymbol{e}}^{\pm}_1 = -0.7\,\mathcal{F}\,\frac{d^{\mathrm{c}}}{B}\bar{\boldsymbol{e}}^{\pm}_1$$

where d^{c} is the cable diameter, $\alpha^{\mathrm{E}} = \bar{\alpha} + \phi^{\mathrm{o}}_3$ is the static effective angle of attack, B and d are the deck width and height, respectively, (see Fig. 4.1) and

$$\mathcal{F} = \frac{1}{2}\frac{\rho\,U^2}{\rho A^{\mathrm{d}}\bar{\omega}^2} \, , \; \delta = \frac{B}{l} \, , \; \bar{d} = \frac{d}{B} \tag{5.1.2}$$

where, consistently with the definition given in Chapter 4, the term ρA^{d} represents the mass per unit length of the bridge deck. Finally, the static aerodynamic forces (5.1.1) enter the equilibrium equations (4.1.14) through $\boldsymbol{f}^{\mathrm{o}}(x)$, $\boldsymbol{c}^{\mathrm{o}}(x)$ and $\boldsymbol{f}^{\pm}_0(x)$.

A parametric nonlinear calculation is performed by increasing the static aerodynamic forces through the wind velocity U. The pre-critical equilibrium paths are evaluated for three initial wind angles of attack $\bar{\alpha}$. The evolution of all kinematic variables for the Runyang suspension bridge including the vertical and horizontal deck displacements u^{o}_2 and u^{o}_1 and the twisting rotation ϕ^{o}_3 can be observed in Figs. 5.3a and 5.3b. Torsional divergence is found to occur around 100 m/s when $\bar{\alpha} = +3°$, as shown in Fig. 5.3b. For $\bar{\alpha} = 0°$ or for negative values of the angle of attack, the static lift and moments are negative thus inducing a tensioning of the cables which, in turn, causes an increase of the bridge torsional stiffness.
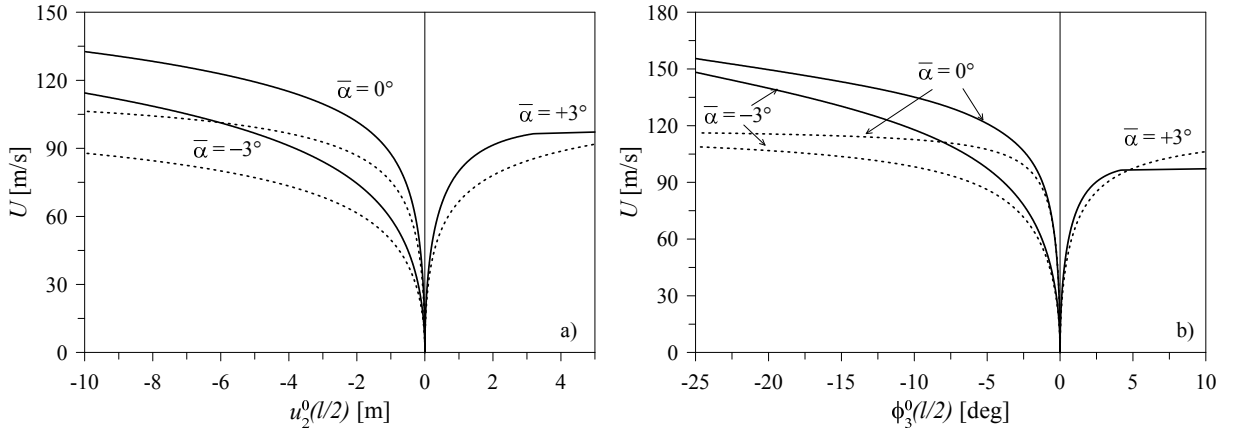
Fig. 5.3: *Equilibrium paths of the Runyang bridge for increasing aeroelastic loads at different wind angles of attack $\bar{\alpha}$: (a) vertical displacement and (b) torsional rotation vs. wind velocity U. The dashed lines refer to a linearized model, the solid lines refer to the proposed fully nonlinear model.*

The same analyses are conducted for the Hu Men suspension bridge for which a torsional divergence analysis is provided in [15]. Figure 5.4 shows the equilibrium paths obtained by the nonlinear model and compared with the typical path constructed by a linear model that neglects flexural-torsional coupling. A lower critical wind velocity is obtained by the proposed nonlinear model. The results are in good agreement with those of [15, 37]. It shows how the coupling of the static aerodynamic forces leads to a decrease of the critical wind velocity.

Figure 5.5 shows the nonlinear precritical paths for different initial wind angles of attack $\bar{\alpha}$, it can be noticed how the initial angle $\bar{\alpha}$ affects the aeroelastic response in determining the critical condition. Lower U^{cr} is estimated by assuming $\bar{\alpha} > 0$ whereas for negative values of $\bar{\alpha}$ the divergence condition is not reached in the considered range of wind speed U. This is related to the expressions of the static
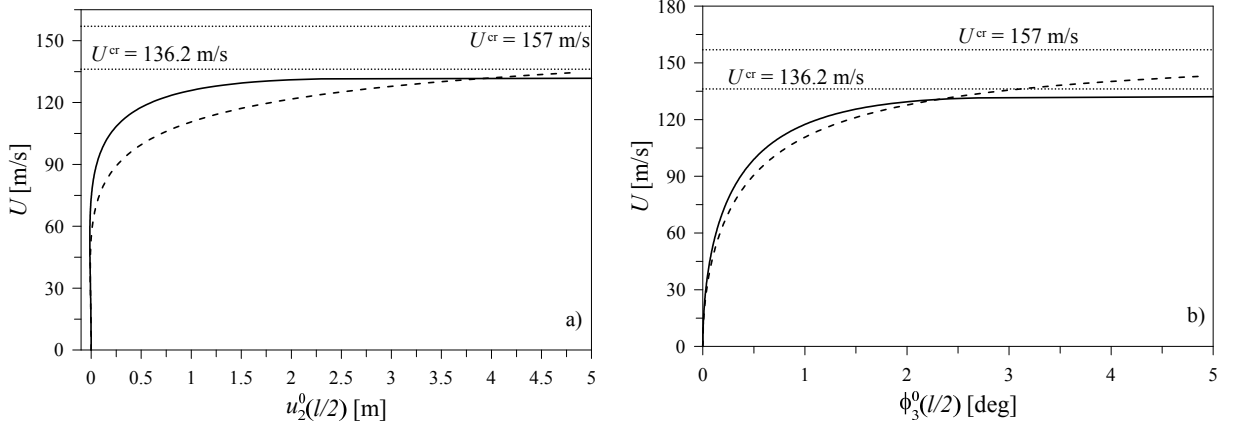
Fig. 5.4: *Linear (dashed) and nonlinear (solid) equilibrium paths of the Hu Men suspension bridge for increasing aeroelastic loads for $\bar{\alpha} = 0°$: (a) vertical displacement and (b) torsional rotation vs. wind velocity U.*
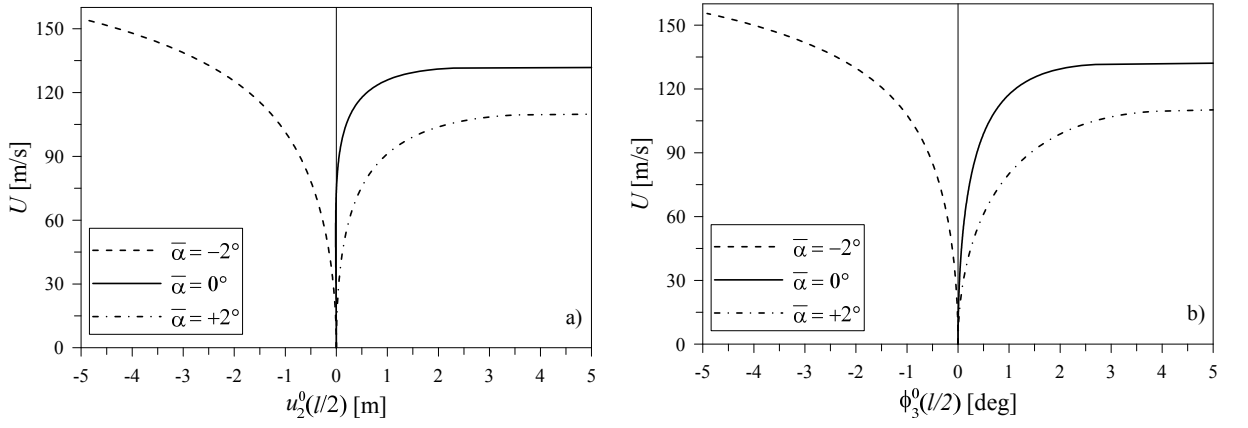

Fig. 5.5: *Equilibrium paths of the Hu Men suspension bridge for increasing aeroelastic loads for different $\bar{\alpha}$: (a) vertical displacement and (b) torsional rotation vs. wind velocity U.*

aerodynamic coefficients characterizing the considered cross section (see Figure 5.1, left), for which an initial value of the wind angle of attack $\bar{\alpha} = -2°$ generates a negative lift and moment and the increasing wind speed U leads to a negative increase of the effective angle $\alpha^{E} = \bar{\alpha} + \phi_3^{o}$. Such negative angle generates a downward lift that increases the tension in the bridge cables, and consequently their geometric stiffness, thus increasing the bridge global torsional stiffness, entailing the shift of the critical wind speed to higher values.

The path traced by the eigenvalues as the wind speed is varied in the vicinity of the divergence bifurcation for the Runyang bridge confirms that two complex conjugate eigenvalues move on the imaginary axis toward the origin and coalesce to zero when the bifurcation occurs; this is shown in Fig. 5.6 (left). On the other hand, the sensitivity of the frequency of the mode that undergoes divergence (imaginary part of the eigenvalue) with respect to the wind speed is appreciable, see Fig. 5.6 (right) where the three angles of attack $\bar{\alpha} = (+3°, +2°, +1°)$ are considered. Similar behaviors are observed in the vicinity of the divergence bifurcation of the Hu Men suspension bridge in Fig. 5.7. The flexural/torsional modes that undergo divergence for the Runyang and Hu Men bridges in the critical state are shown in Fig. 5.8.
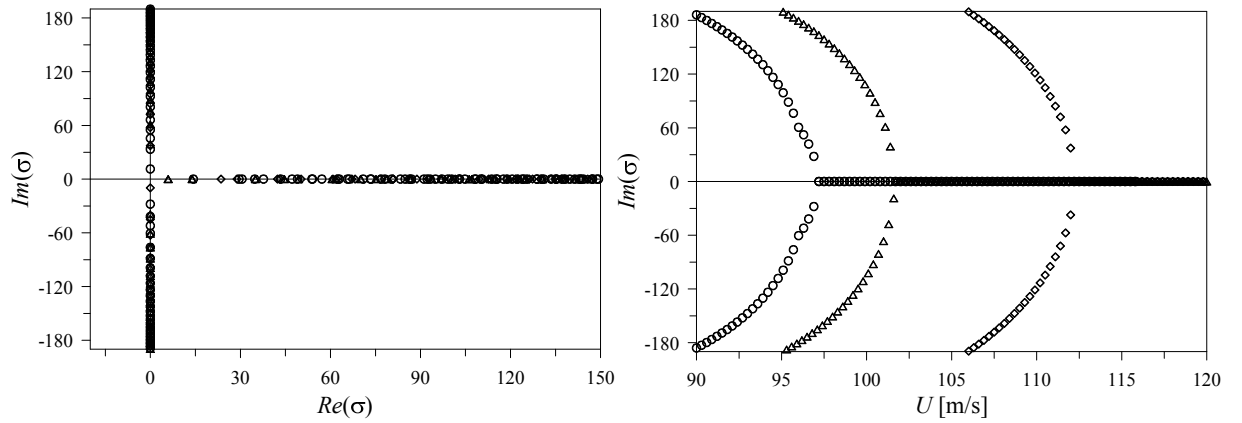
Fig. 5.6: *The path of the lowest eigenvalue of the Runyang suspension bridge in the vicinity of the divergence bifurcation (left) and imaginary part vs. wind speed (right): circles stand for $\bar{\alpha} = +3°$, triangles stand for $\bar{\alpha} = +2°$, and diamonds stand for $\bar{\alpha} = +1°$.*
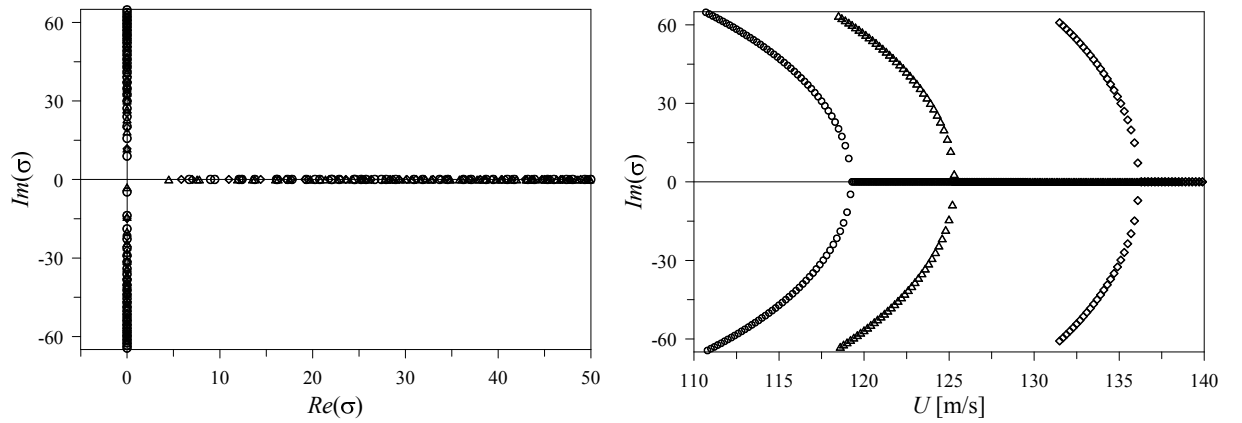
Fig. 5.7: *The paths of the lowest eigenvalue of the Hu Men suspension bridge in the vicinity of the divergence bifurcation: circles stand for $\bar{\alpha} = +2°$, triangles stand for $\bar{\alpha} = +1°$, and diamonds stand for $\bar{\alpha} = 0°$.*
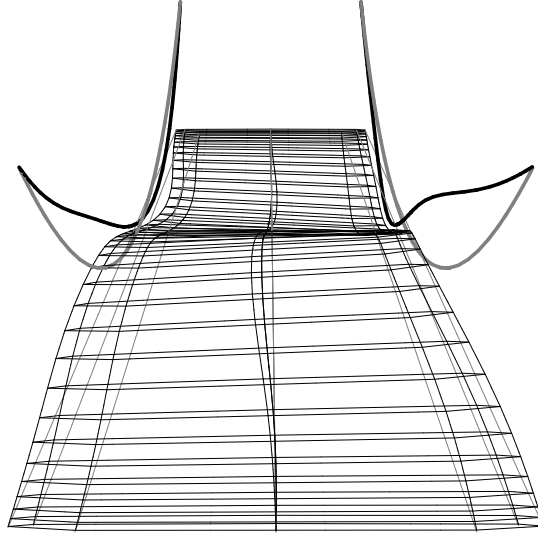
Fig. 5.8: *Mode undergoing divergence for the Runyang suspension bridge (left) when $\bar{\alpha} = +1°$ and $U^{\mathrm{cr}} = 111.2$ m/s and for the Hu Men suspension bridge (right) when $\bar{\alpha} = 0°$ and $U^{\mathrm{cr}} = 136.2$ m/s.*

The continuum formulation is also used for sensitivity analyses whose main results are shown in Fig. 5.9. Here the geometric and constitutive characteristics of the Runyang and Hu Men Suspension Bridge, indicated respectively by subscripts "R" and "HM", are taken as reference values about which some suitable variations are considered. As expected, the results highlight the high sensitivity of the aeroelastic response of the bridge to the parameters governing the global elastogeometric (nonlinear) stiffness of the bridge. In particular, not only the cables axial stiffness k^{c}, supposedly the most relevant source of geometric nonlinearity, but also the deck torsional stiffness τ strongly influence the value of the torsional divergence speed U^{cr}. Moreover, the nonlinear dependence of the critical velocity to the variation of these two parameters seems to be more emphasized only in the vicinity of the design values of the bridges analyzed. It also appears that the critical speed is less sensitive to variations in the hangers stiffness ratio κ^{h} and clearly this is due to the fact that its design value is already very high, condition that justify the assumption of undeformability of the hangers, usually made in the classical modeling. Finally, the presence of a very slight contribution of the parameter χ governing the flexural bending in the plane $\{\boldsymbol{b}_3, \boldsymbol{b}_1\}$ is due to the nonlinear expression of the torsional curvature containing a term related to the flexural finite rotation ϕ_2^{o}.
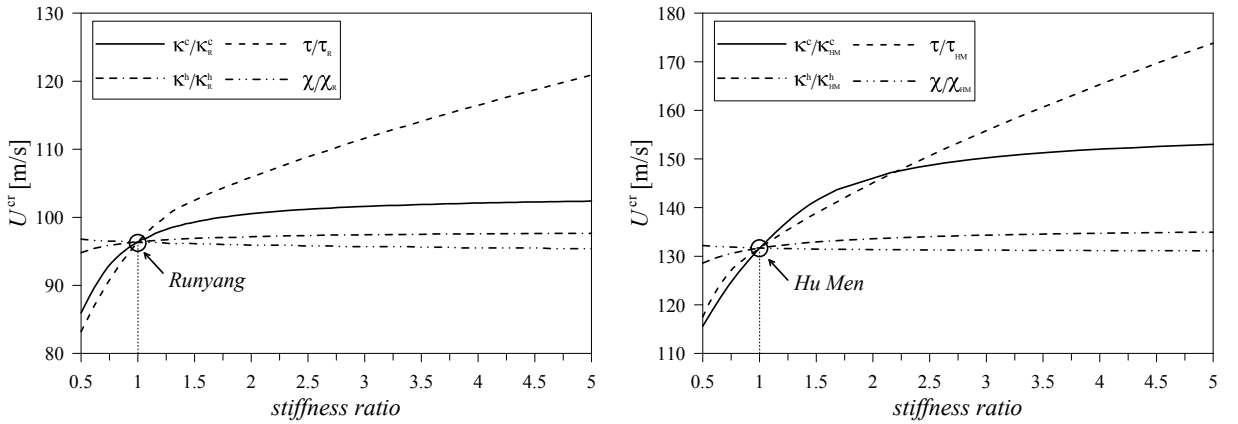
Fig. 5.9: *Sensitivity analyses to the stiffness parameters ratios vs. the critical divergence wind speed. Subscripts "R" and "HM" refer to the Runyang bridge and Hu Men bridge parameters, respectively.*

5.1.1 The Great Belt Bridge Aerodynamics

In the following section, the critical speed at the onset of the torsional divergence condition is evaluated assuming the aerodynamic properties of the GBB section. While the numerically calculated curves of the static lift, drag, and aerodynamic moment coefficients proposed in Chapter 3 are here adopted in order to define the static aeroelastic loads, the structural characteristics of the bridge model and the boundary conditions are those of the Runyang suspension bridge. The reference values employed in the evaluation of the aerodynamic loads are those reported in Chapter 3: $B = 31$ m and $d = 4.4$ m.

Only the eigenvalue procedure described in the previous section was adopted to evaluate the wind speed at the onset of torsional divergence. The paths of the real and imaginary parts of the lowest eigenvalue are shown in Fig. 5.10 (left) for different values of the initial angle of attack $\bar{\alpha}$ whereas Fig. 5.10 (right) shows the critical velocities as the values where the imaginary part of the lowest eigenvalue becomes zero. A sensitivity analysis on the effect of $\bar{\alpha}$ in the evaluation of the torsional divergence condition is then shown in Figure 5.11 where the asymmetric behavior of the section is highlighted. In particular, it is shown how the minimal critical torsional divergence value occurs at small positive mean angles of attack, and it is associated with the lower stabilizing effect due to the minimal values of the aerodynamic loads at those angles. By contrary, as the angles of attack increases toward lower negative or higher positive values a relatively large increase in the divergence speed is obtained. In this case the aerodynamic loads effect coupled with the structural characteristics of the bridge are such that a stabilizing behavior is experienced leading to a higher values of the divergence speed.
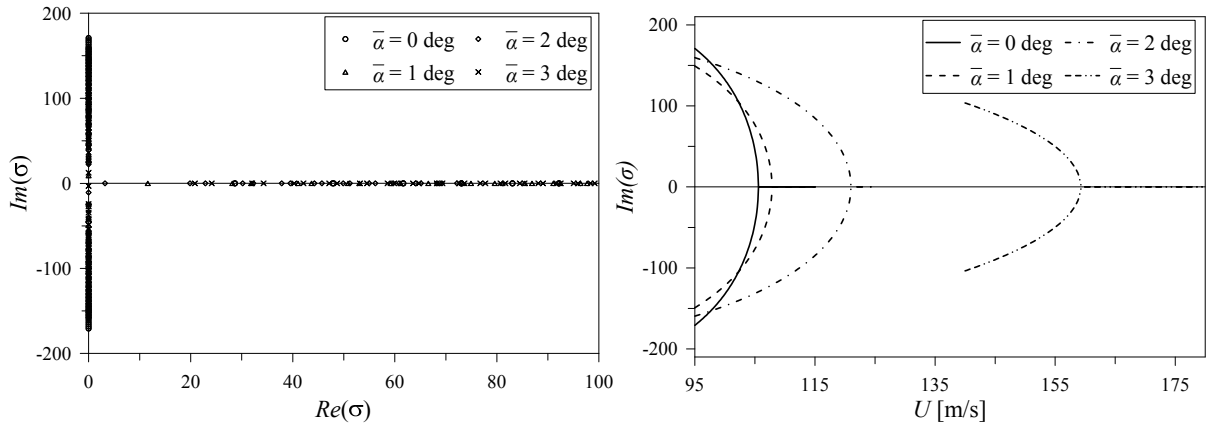
Fig. 5.10: *Lowest eigenvalue path for the Runyang suspension bridge, assuming the aerodynamics of the GBB section, in the vicinity of the divergence speed (left) and imaginary part vs. wind speed (right).*
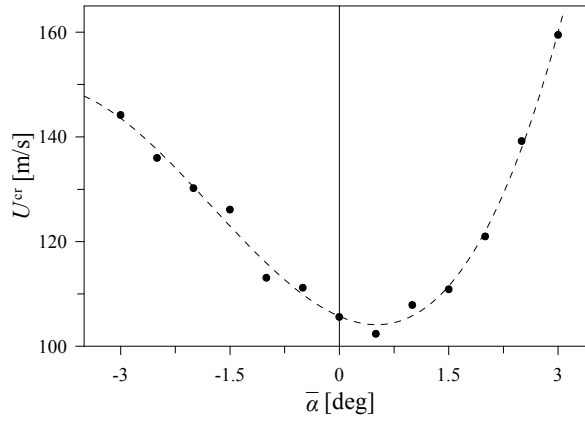
Fig. 5.11: *Critical velocity U^{cr} at the onset of the torsional divergence condition for selected values of the mean angle of attack $\bar{\alpha}$.*

5.2 Dynamic Aeroelastic Instability: Flutter

As previously described in Chapter 2, the flutter condition can be studied by performing time-dependent simulations or by evaluating the solution of a linear (or nonlinear) eigenvalue problem. Aerodynamic, geometric and constitutive nonlinearities, characterizing the aeroelastic model can be accounted for employing the first approach. In this case the flutter condition is evaluated by analyzing the time histories of aeroelastic vibrational response at different wind speeds, thus, by estimating the critical velocity when a periodic oscillation is reached. On the other hand, in the eigenvalue approach only the prestress condition induced by the static component of the wind-induced loads and by the dead loads is taken into account by studying the eigenvalue problem arising from the linearization of the balance equations around the static aeroelastic configuration.

The definition of the flutter condition is straightforward; according to Bisplinghoff et al. [75], flutter can be defined as the dynamic instability of an elastic body in an air stream. As indicated in [76] a more pertinent definition of the flutter condition and the properties of an aeroelastic system can be proposed by studying the stability of the infinitesimal motions about that condition [21]. It is then sufficient to analyze the aeroelastic vibration with a complex exponential time dependence function, since all other motions can be defined by superposition. However the air loads due to the deflections of the elastic structure from

the undeformed state are affecting the flutter condition. If the dynamic aeroelastic characteristics of the perturbed system are the same, whatever reference point is assumed, then it is possible to investigate the flutter behavior of the system; this correspond to the classical flutter speed, e.g. the flutter velocity in linear equilibrium condition, or *linear flutter speed*. On the other hand, the perturbed motion dynamics can be influenced by the chosen equilibrium point. Therefore, the reduced linear perturbation system leads to a linear approximation of the behavior of the system in the neighborhood of the static equilibrium point, implying that there is going to be a flutter speed associated with each condition. In this case the flutter speed is the one obtained from the nonlinear equilibrium condition, or *nonlinear flutter speed*. Clearly, when the structure is highly flexible, as in the case of long-span suspension bridges, the classical approach is no longer suitable to correctly identify the flutter speed.Moderate to large deflections under loads strongly modify the equilibrium point.

5.2.1 Flutter via Eigenvalue Approach

This approach, is based on the knowledge of the *flutter derivatives*, experimentally or numerically obtained for each bridge section. The critical condition is obtained at the wind speed where a complex-conjugate pair of eigenvalues crosses the imaginary axis. Figure 5.2 shows the aerodynamic (non-classical) convention assumed in this work: the lift force along with the vertical displacement are assumed positive upward, the drag force is oriented in the direction of the air flow and the moment is assumed positive if the section rotates in the counter-clockwise direction.

To compute the onset of flutter, the classical complex eigenvalue analysis is performed by expressing the aerodynamic forces in terms of the flutter derivatives. Herein, two approaches are implemented; the first approach, proposed by [24], consists of defining a complex nonlinear eigenvalue problem solved by increasing the wind speed U about the static aeroelastic equilibrium until the condition of purely imaginary eigenvalues is found. On the other hand, several linear eigenvalue problems can be solved for each value of U to obtain the actual eigenvalues in the vicinity of the flutter condition. The first approach can be easily adopted for a two-DOF sectional model, as in [25], although it is a nonclassical procedure for multi-dof systems. The results obtained by the two approaches are discussed next.

The expressions of the aerodynamic forces per unit length, in terms of the aeroelastic derivatives $(P_i,\ H_i,\ A_i,\ i=1,...6)$, are given in (5.2.1). The latter are then introduced in the aeroelastic governing equations (4.1.15) through $\breve{f}(x,t)$ and $\breve{c}(x,t)$ as follows:

$$\breve{f}_{\mathrm{AE}} = f_{\mathrm{AE}}^{\mathrm{o}} - D(x,t)\bar{e}_1 + L(x,t)\bar{e}_2\,,\ \breve{c}_{\mathrm{AE}} = c_{\mathrm{AE}}^{\mathrm{o}} + M(x,t)\bar{e}_3\,,$$

$$D(x,K) = \tfrac{1}{2}\rho B\,U^2\Big(\frac{K}{U}P_1\partial_t u_2 + \frac{KB}{U}P_2\partial_t\phi_3 + K^2 P_3\phi_3 + \frac{K^2}{B}P_4 u_2 - \frac{K}{U}P_5\partial_t u_1 - \frac{K^2}{B}P_6 u_1\Big)$$

$$L(x,K) = \tfrac{1}{2}\rho B\,U^2\Big(\frac{K}{U}H_1\partial_t u_2 + \frac{KB}{U}H_2\partial_t\phi_3 + K^2 H_3\phi_3 + \frac{K^2}{B}H_4 u_2 - \frac{K}{U}H_5\partial_t u_1 - \frac{K^2}{B}H_6 u_1\Big)$$

$$M(x,K) = \tfrac{1}{2}\rho B^2 U^2\Big(\frac{K}{U}A_1\partial_t u_2 + \frac{KB}{U}A_2\partial_t\phi_3 + K^2 A_3\phi_3 + \frac{K^2}{B}A_4 u_2 - \frac{K}{U}A_5\partial_t u_1 - \frac{K^2}{B}A_6 u_1\Big)$$

$$(5.2.1)$$

Consistently with the classical notations, ρ denotes the air density, B is the deck depth, U is the dimensional wind velocity, and K is the reduced frequency defined as $K := 2\pi f B/U$, where f is the frequency of oscillation of the bridge (see Chapter 2).

5.2.1.1 Complex Eigenvalue Problem

The expressions of the aerodynamic forces are first cast in a suitable nondimensional form. By assuming the reduced frequency K as function of the circular frequency ω_{f} at the onset of flutter

$$K := \frac{\omega_{\mathrm{f}}\, B}{U} \tag{5.2.2}$$

and by introducing the dimensionless parameters

$$\mathcal{F}_{\mathrm{f}} = \frac{1}{2}\frac{\rho\,B\,l}{\rho A^{\mathrm{d}}}\,,\quad \delta = \frac{B}{l} \tag{5.2.3}$$

the nondimensional form of Eq. (5.2.1) becomes

$$D(x,\sigma) = \mathcal{F}_{\mathrm{f}}\,\delta\Big[\sigma\,P_1\,\partial_t u_2(x,t) + \sigma\,\delta\,P_2\,\partial_t\phi_3(x,t) + \sigma^2\,\delta\,P_3\,\phi_3(x,t) + \sigma^2\,P_4\,u_2(x,t) +$$
$$-\sigma\,P_5\,\partial_t u_1(x,t) - \sigma^2\,P_6\,u_1(x,t)\Big]$$

$$L(x,\sigma) = \mathcal{F}_{\mathrm{f}}\,\delta\Big[\sigma\,H_1\,\partial_t u_2(x,t) + \sigma\,\delta\,H_2\,\partial_t\phi_3(x,t) + \sigma^2\,\delta\,H_3\,\phi_3(x,t) + \sigma^2\,H_4\,u_2(x,t) +$$
$$-\sigma\,H_5\,\partial_t u_1(x,t) - \sigma^2\,H_6\,u_1(x,t)\Big] \tag{5.2.4}$$

$$M(x,\sigma) = \mathcal{F}_{\mathrm{f}}\,\delta^2\Big[\sigma\,A_1\,\partial_t u_2(x,t) + \sigma\,\delta\,A_2\,\partial_t\phi_3(x,t) + \sigma^2\,\delta\,A_3\,\phi_3(x,t) + \sigma^2\,A_4\,u_2(x,t) +$$
$$-\sigma\,A_5\,\partial_t u_1(x,t) - \sigma^2\,A_6\,u_1(x,t)\Big]$$

where σ is the nondimensional circular flutter frequency $\sigma = \omega_{\mathrm{f}}/\bar\omega$. By assuming the solution of the dynamic problem in the form $\big[\boldsymbol{u}(x,t),\phi_j(x,t),\boldsymbol{v}^{\pm}(x,t)\big] = \big[\bar{\boldsymbol{u}}(x),\bar\phi_j(x),\bar{\boldsymbol{v}}^{\pm}(x)\big]e^{i\sigma t}$ with $j = 1,2,3$, the flutter condition is found when a pair of eigenvalues $\sigma = \sigma_{\mathrm{R}} + i\,\sigma_{\mathrm{I}}$ becomes *purely real*.

In terms of the eigenvalue σ, the aerodynamic nondimensional loads can be written as

$$\bar{D}(x,\sigma) = \mathcal{F}_{\mathrm{f}}\,\delta\,\sigma^2\Big(i\,P_1\bar{u}_2 + i\,\delta P_2\bar\phi_3 + \delta P_3\bar\phi_3 + P_4\bar{u}_2 - i\,P_5\bar{u}_1 - P_6\bar{u}_1\Big)e^{i\sigma t}$$

$$\bar{L}(x,\sigma) = \mathcal{F}_{\mathrm{f}}\,\delta\,\sigma^2\Big(i\,H_1\bar{u}_2 + i\,\delta H_2\bar\phi_3 + \delta H_3\bar\phi_3 + H_4\bar{u}_2 - i\,H_5\bar{u}_1 - H_6\bar{u}_1\Big)e^{i\sigma t} \tag{5.2.5}$$

$$\bar{M}(x,\sigma) = \mathcal{F}_{\mathrm{f}}\,\delta^2\,\sigma^2\Big(i\,A_1\bar{u}_2 + i\,\delta A_2\bar\phi_3 + \delta A_3\bar\phi_3 + A_4\bar{u}_2 - i\,A_5\bar{u}_1 - A_6\bar{u}_1\Big)e^{i\sigma t}$$

Accordingly, the nondimensional inertia and damping forces, by neglecting the contributions of the rotatory inertia and damping about axes $\check{\boldsymbol{b}}_1$ and $\check{\boldsymbol{b}}_2$, can be expressed as

$$\bar{\boldsymbol{f}}_{\mathrm{M}}^{\pm} + \bar{\boldsymbol{f}}_{\mathrm{D}}^{\pm} = \Big[-\sigma^2\varrho^{\mathrm{c}}\sec\theta_{\mathrm{o}}^{\pm}(x)\,\bar{\boldsymbol{v}}^{\pm}(x) + i\,\sigma D_j^{\mathrm{c}}\,\bar{\boldsymbol{v}}^{\pm}(x)\Big]e^{i\sigma t}\,,$$

$$\bar{\boldsymbol{f}}_{\mathrm{M}} + \bar{\boldsymbol{f}}_{\mathrm{D}} = \Big[-\sigma^2\bar{\boldsymbol{u}}(x) + i\,\sigma D_j^{\mathrm{d}}\,\bar{\boldsymbol{u}}(x)\Big]e^{i\sigma t}\,, \tag{5.2.6}$$

$$\bar{\boldsymbol{c}}_{\mathrm{M}} + \bar{\boldsymbol{c}}_{\mathrm{D}} = \Big[-\sigma^2 J^{\mathrm{m}}\bar\phi_3(x) + i\,\sigma D_j^{\mathrm{T}}\,\bar\phi_3(x)\Big]e^{i\sigma t}\,\boldsymbol{b}_3\,.$$

5.2.1.2 Classical Eigenvalue Problem

The solution of the dynamic problem is here assumed in the form $\big[\boldsymbol{u}(x,t),\phi_j(x,t),\boldsymbol{v}^{\pm}(x,t)\big] = \big[\bar{\boldsymbol{u}}(x),\bar\phi_j(x),\bar{\boldsymbol{v}}^{\pm}(x)\big]e^{\sigma t}$ with $j = 1,2,3$. It is worth noticing that now σ does not represent the frequency of oscillation of the structure at the onset of flutter, as in the Scanlan formulation described in Section 5.2.1.1, but it is the nondimensional circular frequency $\sigma = \omega/\bar\omega$ of the system. Accordingly,

the flutter condition is obtained when a pair of eigenvalues $\sigma = \sigma_{\mathrm{R}} + i\,\sigma_{\mathrm{I}}$ becomes *purely imaginary*. By introducing the parameter $\bar{U} := U/(\bar{\omega}\,l)$, the aerodynamic nondimensional loads can be written in terms of the eigenvalue σ as

$$\bar{D}(x,K,\sigma) = \mathcal{F}_{\mathrm{f}}\,\bar{U}^2 \Big(\frac{KP_1}{\bar{U}}\,\sigma\,\bar{u}_2 + \delta \frac{KP_2}{\bar{U}}\,\sigma\,\bar{\phi}_3 + K^2 P_3\,\bar{\phi}_3 + \frac{K^2 P_4}{\delta}\,\bar{u}_2 - \frac{KP_5}{\bar{U}}\,\sigma\,\bar{u}_1 - \frac{K^2 P_6}{\delta}\,\bar{u}_1 \Big) e^{\sigma t}$$

$$\bar{L}(x,K,\sigma) = \mathcal{F}_{\mathrm{f}}\,\bar{U}^2 \Big(\frac{KH_1}{\bar{U}}\,\sigma\,\bar{u}_2 + \delta \frac{KH_2}{\bar{U}}\,\sigma\,\bar{\phi}_3 + K^2 H_3\,\bar{\phi}_3 + \frac{K^2 H_4}{\delta}\,\bar{u}_2 - \frac{KH_5}{\bar{U}}\,\sigma\,\bar{u}_1 - \frac{K^2 H_6}{\delta}\,\bar{u}_1 \Big) e^{\sigma t}$$

$$\bar{M}(x,K,\sigma) = \mathcal{F}_{\mathrm{f}}\,\delta\,\bar{U}^2 \Big(\frac{KA_1}{\bar{U}}\,\sigma\,\bar{u}_2 + \delta \frac{KA_2}{\bar{U}}\,\sigma\,\bar{\phi}_3 + K^2 A_3\,\bar{\phi}_3 + \frac{K^2 A_4}{\delta}\,\bar{u}_2 - \frac{KA_5}{\bar{U}}\,\sigma\,\bar{u}_1 - \frac{K^2 A_6}{\delta}\,\bar{u}_1 \Big) e^{\sigma t}$$

$$(5.2.7)$$

On the other hand, the nondimensional inertia and damping forces can be written as

$$\bar{\boldsymbol{f}}_{\mathrm{M}}^{\pm} + \bar{\boldsymbol{f}}_{\mathrm{D}}^{\pm} = \Big[\sigma^2 \varrho^{\mathrm{c}} \sec\theta_{\mathrm{o}}^{\pm}(x)\,\bar{\boldsymbol{v}}^{\pm}(x) + \sigma D_j^{\mathrm{c}}\,\bar{\boldsymbol{v}}^{\pm}(x) \Big] e^{\sigma t}\,,$$

$$\bar{\boldsymbol{f}}_{\mathrm{M}} + \bar{\boldsymbol{f}}_{\mathrm{D}} = \Big[\sigma^2 \bar{\boldsymbol{u}}(x) + \sigma D_j^{\mathrm{d}}\,\bar{\boldsymbol{u}}(x) \Big] e^{\sigma t}\,,$$

$$(5.2.8)$$

$$\bar{\boldsymbol{c}}_{\mathrm{M}} + \bar{\boldsymbol{c}}_{\mathrm{D}} = \Big[\sigma^2 J^{\mathrm{m}} \bar{\phi}_3(x) + \sigma D_j^{\mathrm{T}}\,\bar{\phi}_3(x) \Big] e^{\sigma t}\,\boldsymbol{b}_3\,.$$

For the sake of clarity, the relation between the nondimensional parameters $\mathcal{F}_{\mathrm{f}}$ and $\mathcal{F}$, employed in the static and dynamic aeroelastic analyses, is given in the follow

$$\mathcal{F}_{\mathrm{f}} = \mathcal{F}\,\frac{\delta}{\bar{U}^2} \tag{5.2.9}$$

5.2.2 Numerical Results

A first set of simulations is carried out in order to evaluate the flutter velocity for the Runyang suspension bridge by adopting the experimental values of the flutter derivatives calculated for its deck cross section [14]. For that case study, only the aeroelastic derivatives H_i and A_i, $i = 1,...4$ were available. The analyses are performed employing both the eigenvalue approaches described in Section 5.2 and according to the following procedure:

1. An initial lower value than the critical free-stream wind speed U is assumed and the aeroelastic configuration induced by the static components of the aerodynamic loads is calculated by solving the nonlinear PDEs system (4.1.14) accounting for the expressions (5.1.1).
2. The first torsional mode is tentatively assumed to be the expected flutter mode and its frequency $\tilde{f}_1^T$ is used as trial value to evaluate the reduced velocity $U_{\mathrm{r}} := U/(Bf)$.
3. The aeroelastic derivatives are evaluated at the calculated value of U_{r} and the eigenvalue problem (Scanlan or *classical* approach) is solved by linearizing the balance equations (4.1.15), accounting for the aerodynamic loads given by the expressions (5.2.4) or (5.2.7), around the static aeroelastic configuration.
4. The frequency f_1^T of the lowest torsional mode is evaluated and compared with the trial value $\tilde{f}_1^T$ and steps 2. and 3. are iterated until $|f_1^T - \tilde{f}_1^T| \leq \epsilon_{tol}$, where ϵ_{tol} is the chosen tolerance. At each iteration, the value of $\tilde{f}_1^T$ is updated to the last evaluated value of f_1^T.
5. The wind velocity U is increased and the procedure is performed until the critical condition is reached (i.e. until the damping of the lowest torsional mode becomes zero).

The numerical simulations were carried out by the FE solver Comsol Multiphysics® [56] by coupling this software with the computational platform Matlab® in order to perform the iterative procedure described

above. Figure 5.12 shows the variation of the torsional and flexural bending frequencies f and logarithmic decrement Δ with the wind velocity U and the results obtained for the two eigenvalue problems are compared. As expected the two procedures lead to the same result only at the flutter speed where the Scanlan assumption (see Eq. (5.2.2)), which defines K as function of the flutter circular frequency ω_{f}, is valid.
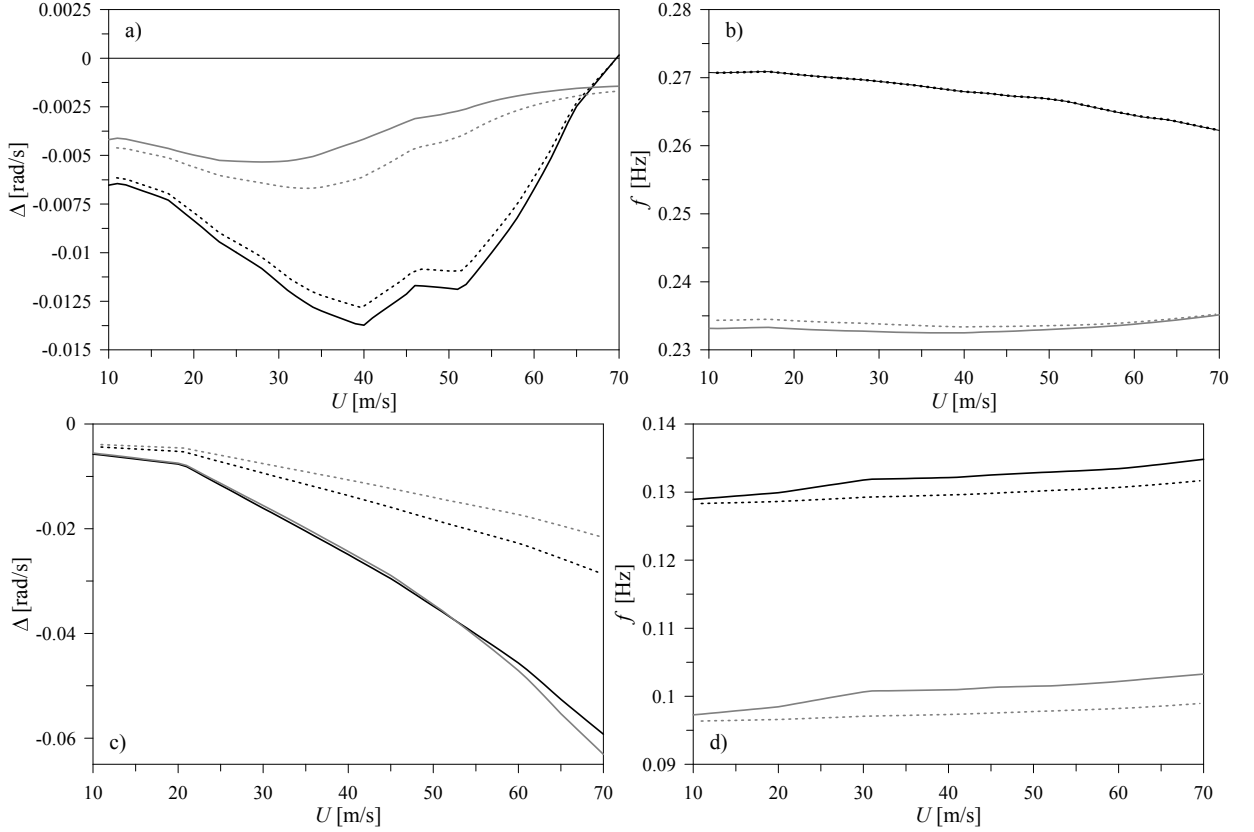

Fig. 5.12: *Flutter investigation for the Runyang bridge using the experimental aeroelastic derivatives for $\bar{\alpha} = 0°$: (a) and (b) torsional modes, (c) and (d) vertical bending modes. The dashed lines indicate the Scanlan procedure, the solid lines represent the iterative procedure. The black lines refer to the symmetric modes, the gray lines refer to the skew-symmetric modes.*

In Fig. 5.13 a three-dimensional view of the flutter mode shape at $U \approx 70$ m/s is shown, it is evident that is due to the coupling between bending and torsional modes.

Figure 5.14 shows the expected high sensitivity of the flutter speed with respect to the damping ratio and the multiplier of the dead loads. In particular, the figure highlights the nonlinear trend, with a 40% increase in the dead load leading to a 10% increase in the flutter speed, due to the positive geometric stiffness induced in the structure, mostly in the cables, by the pre-stress static loads. These studies are possible only in the context of a fully nonlinear parametric model formulation since the prestress condition is properly accounted for and the tangent stiffness at the prestressed state is correctly evaluated.
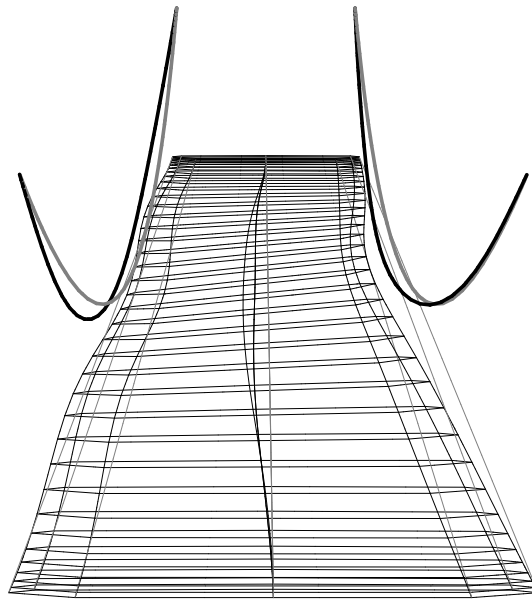
Fig. 5.13: *Flutter mode shape of the Runyang suspension bridge for $\bar{\alpha} = 0°$.*
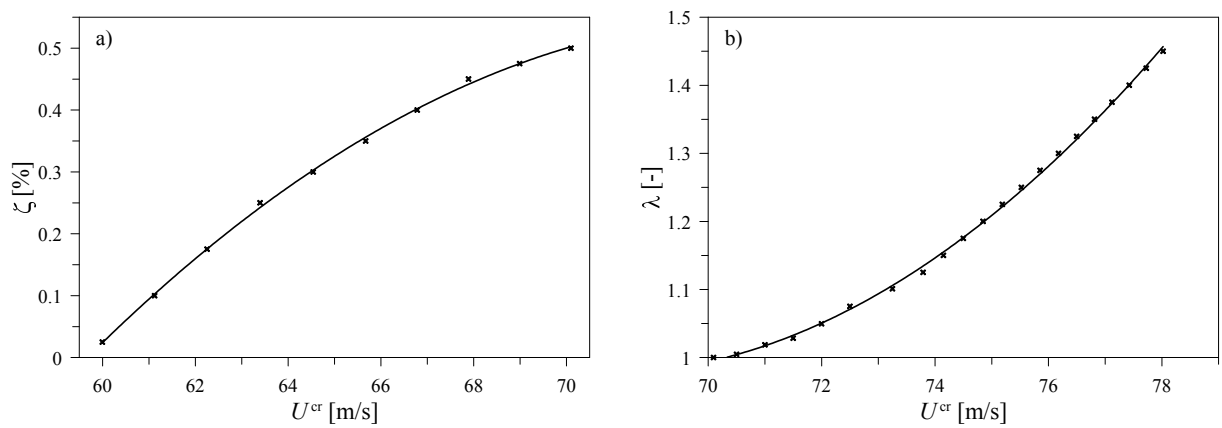
Fig. 5.14: *Sensitivity of the flutter speed to: (a) the structural damping ratio ζ, (b) the dead load multiplier λ for $\bar{\alpha} = 0°$.*

5.2.2.1 The Great Belt Bridge Aerodynamics

The computational fluid dynamic studies conducted in Chapter 3 that allowed to determine the flutter derivatives for the GBB suspension bridge cross section at different values of the mean angle $\bar{\alpha}$, are in this section employed in order to study the influence of the wind angle of attack in the evaluation of the critical flutter condition. In Fig. 5.15, the numerical values of the flutter derivatives for the deck cross section of the GBB suspension bridge evaluated via CFD calculations, and discussed in Chapter 3, are proposed. Data are calculated for increasing values of the reduced velocity $U_r = 2\pi/K$.
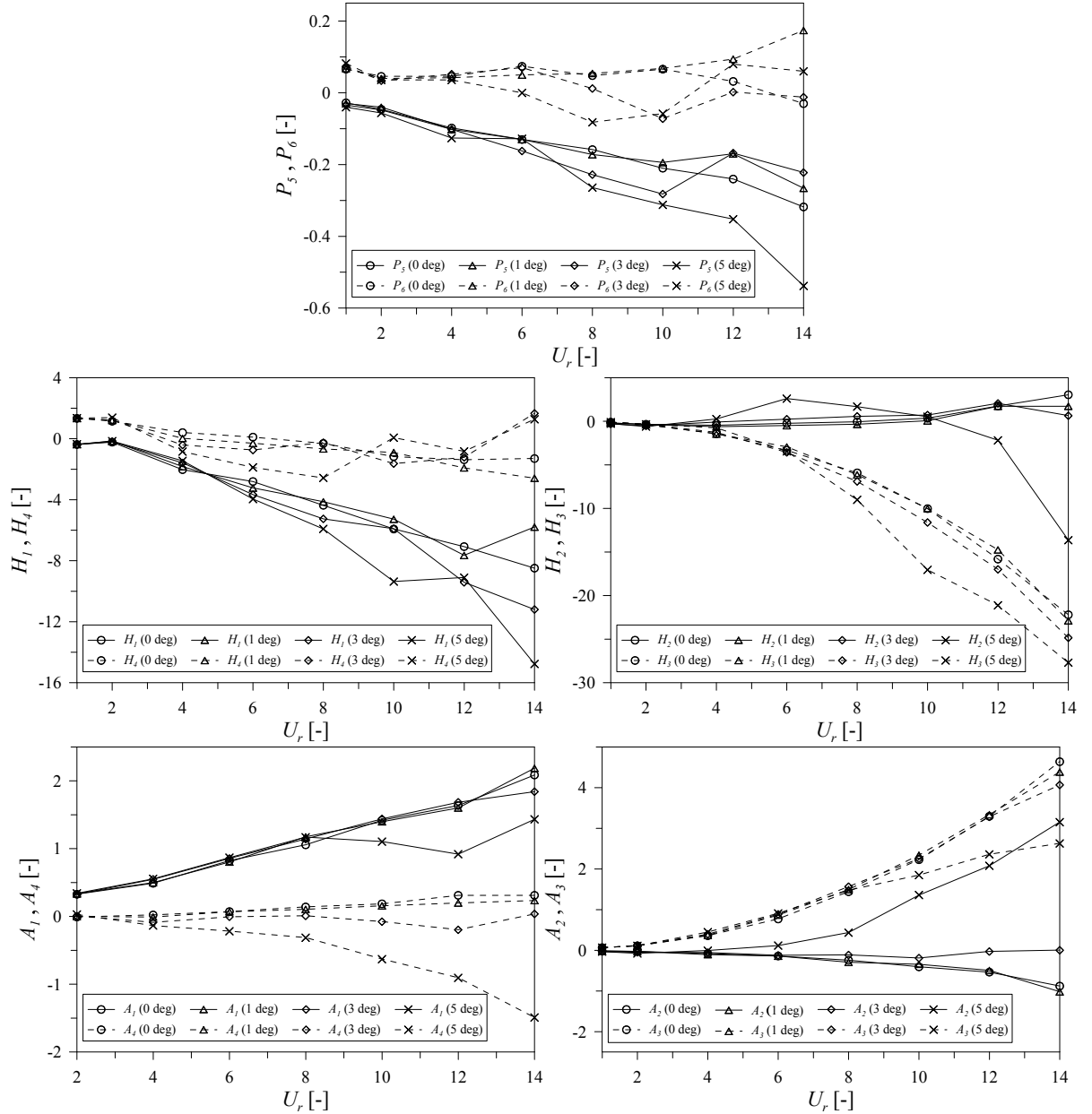
Fig. 5.15: *GBB deck section: aeroelastic derivatives calculated at different mean angles $\bar{\alpha}$.*

Figure 5.16 shows the path of the first symmetric torsional mode, in terms of its damping and frequency, obtained for the set of flutter derivatives evaluated at different values of $\bar{\alpha}$. Figure 5.18 shows the sensitivity of the value of the critical flutter velocity U^{cr} to the mean angle of attack and in Fig. 5.17 the comparison is proposed between the aeroelastic responses obtained assuming linear and nonlinear structural models. In the nonlinear model the eigenvalue problem is defined by linearizing the bridge equations of motions about the aeroelastic equilibrium, thus, the pre-stress effect induced by the static aerodynamic loads turns out to reduce the global torsional stiffness of the bridge, as evident comparing the frequencies in Fig. 5.17 (right), situation that implies the decrease of the critical speed U^{cr} with respect to the linear model, in this case of about 5.9%.
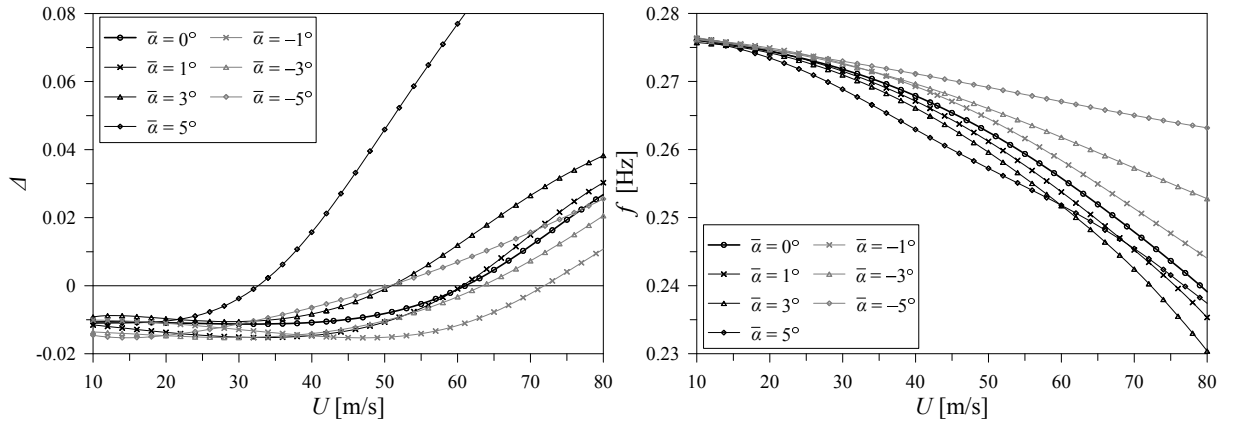
Fig. 5.16: *Flutter investigation for the Runyang bridge using the aeroelastic derivatives of the GBB cross section. Fully nonlinear structural model.*
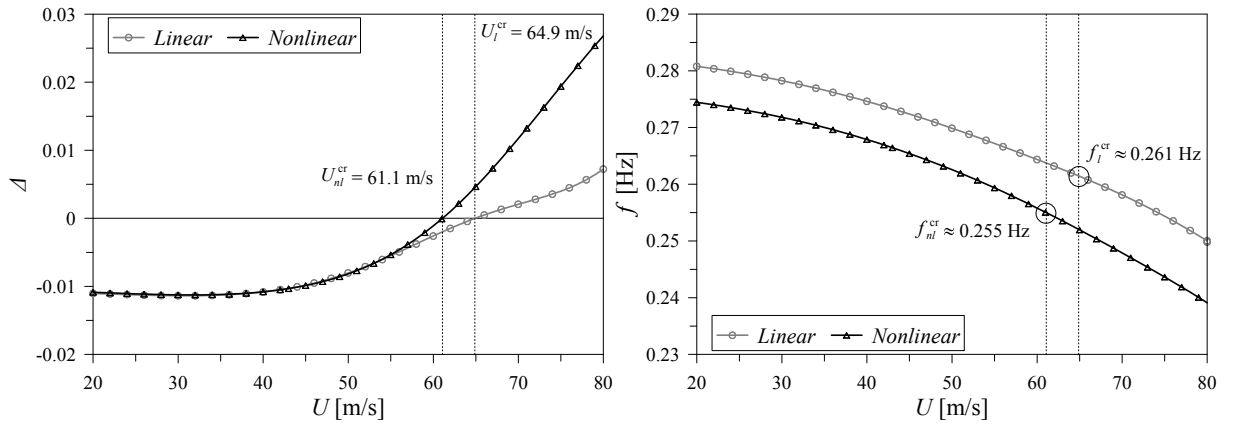
Fig. 5.17: *Flutter investigation for the Runyang bridge using the aeroelastic derivatives of the GBB cross section: comparison between linear and nonlinear structural model results for $\bar{\alpha} = 0°$.*

Figure 5.18 shows the variation of the flutter speed U^{cr} and frequency f^{cr} at selected values of the initial angle of attack $\bar{\alpha}$, and assuming the corresponding *flutter derivatives*, for the linear and nonlinear structural models.

The behavior highlighted in Fig.5.18 is typical of bluff-bodies with non-symmetrical cross section with positive camber. In this sense, the flutter speed reaches its maximum for a negative value of the mean
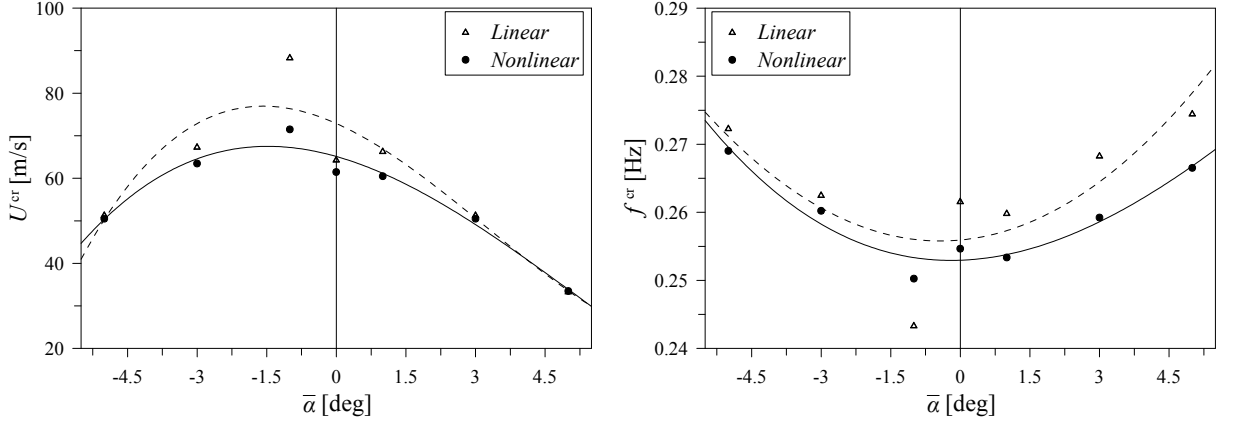
Fig. 5.18: *Critical flutter velocity (left) and flutter speed (right) for selected values of the mean angle of attack $\bar{\alpha}$. Least square minimizations by cubic polynomial functions: nonlinear structural model (solid line), linear structural model (dashed line).*

angle of attack highlighting the effect of the static lift coefficient at those angles. The smaller aerodynamic loads generated at negative assets positive affect the flutter speed which increases proportionally.

5.2.3 Flutter Analysis via Indicial Functions

To perform aeroelastic stability studies, an alternative strategy is the analysis in the time domain where the bridge response is carried out within a given range of wind speeds that is expected to bracket the flutter speed [77] and the critical condition is found when the bridge dynamic response shows a periodic oscillation. The time domain analysis has a significant advantage respect to the eigenvalue approach, as it allows to study the pre- and post-critical flutter response accounting for structural and aerodynamic nonlinearities [78, 79]. The drawbacks are the high computational burden and complexity necessary to obtain appropriate analytical functions describing the unsteady aerodynamics of the typical cross sections of a deck bridge. Once these are available, the computations can be carried out in a relatively straight forward manner.

This section concerns the evaluation of the flutter response of a suspension bridge having structural characteristics of the Runyang bridge, illustrated in Section 4.2, and assuming the aerodynamics of the GBB cross section, developed and studied in Chapter 3. It is worth mentioning that the cross sections of the two bridges, Runyang and GBB, are very similar in terms of shape (boxed section) and absolute dimensions ($B = [35.9,\ 31]$ m and $d = [3,\ 4.4]$ m). Nevertheless, since the Runyang deck cross section ($B/d = 11.97$) is more streamlined with respect to that of the GBB ($B/d = 7.04$), lower values of the critical wind velocities are expected with respect to the cases analyzed in Chapter 5. The aeroelastic equilibrium is first solved accounting for the static components of the wind loads referred to the nonlinear coefficients curves calculated by the CFD analyses illustrated in Section 3.2; in particular, the nonlinear expressions of the lift, drag, and aerodynamic moment coefficients (3.2.15) in terms of the effective angle of attack α^{E} are reported below:

$$C_D(\alpha^{\mathrm{E}}) = 0.0695 + 0.1332\,\alpha^{\mathrm{E}} + 4.7033\,\alpha^{\mathrm{E}2} - 1.1667\,\alpha^{\mathrm{E}3} - 24.1297\,\alpha^{\mathrm{E}4},$$

$$C_L(\alpha^{\mathrm{E}}) = 0.0496 + 6.3567\,\alpha^{\mathrm{E}} - 2.5893\,\alpha^{\mathrm{E}2} - 109.3908\,\alpha^{\mathrm{E}3} - 2.6756\,\alpha^{\mathrm{E}4} + 786.1796\,\alpha^{\mathrm{E}5}, \qquad (5.2.10)$$

$$C_M(\alpha^{\mathrm{E}}) = 0.0330 + 1.1379\,\alpha^{\mathrm{E}} - 0.7673\,\alpha^{\mathrm{E}2} - 27.0033\,\alpha^{\mathrm{E}3} + 4.5606\,\alpha^{\mathrm{E}4} + 249.0324\,\alpha^{\mathrm{E}5}.$$

where the expression of α^{E} was proposed in Chapter 2 in the form $\alpha^{\mathrm{E}}(x) = \bar{\alpha} + \phi_3^{\mathrm{o}}(x)$. The nonlinear coefficients, whose expressions are given in Eq. (5.2.10), are shown in Fig. 5.19 where the nonlinearities arising at high angles of attack are appreciable.
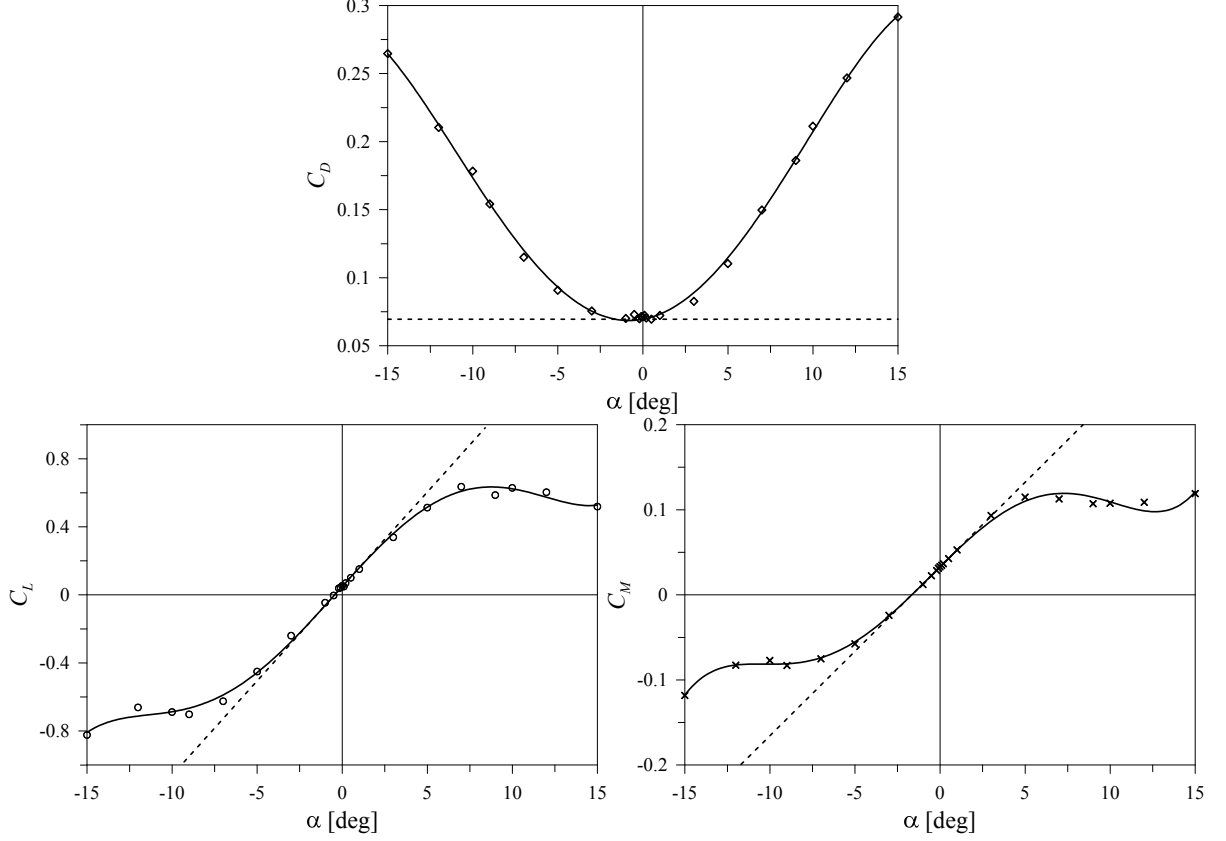

Fig. 5.19: *Drag, lift, and moment coefficients: DVM numerical results (symbols), polynomial fitting (solid line) and linear approximation (dashed line).*

The aeroelastostatic governing equations are reported below

$$\partial_x \boldsymbol{n}_{\mathrm{o}}^{\pm} + \boldsymbol{f}_{\mathrm{o}}^{\pm} + \boldsymbol{f}_{\mathrm{o},\mathrm{AE}}^{\pm} - \boldsymbol{r}_{\mathrm{o}}^{\pm} = \boldsymbol{o} \,,$$
$$\partial_x \boldsymbol{n}^{\mathrm{o}} + \boldsymbol{f}^{\mathrm{o}} + \boldsymbol{f}_{\mathrm{AE}}^{\mathrm{o}} + \boldsymbol{r}_{\mathrm{o}}^{+} + \boldsymbol{r}_{\mathrm{o}}^{-} = \boldsymbol{o} \,, \tag{5.2.11}$$
$$\partial_x \boldsymbol{m}^{\mathrm{o}} + \partial_x \boldsymbol{p}_{\mathrm{o}} \times \boldsymbol{n}^{\mathrm{o}} + \tfrac{B^{\mathrm{c}}}{2} \, \boldsymbol{b}_1^{\mathrm{o}} \times (\boldsymbol{r}_{\mathrm{o}}^{-} - \boldsymbol{r}_{\mathrm{o}}^{+}) + \boldsymbol{c}^{\mathrm{o}} + \boldsymbol{c}_{\mathrm{AE}}^{\mathrm{o}} = \boldsymbol{o} \,.$$

where, according to expressions (5.1.1) and the signs convention in Figure 5.2

$$\boldsymbol{f}_{\mathrm{AE}}^{\mathrm{o}}(x) = -\mathcal{F}\,\delta\,C_{\mathrm{D}}(\alpha^{\mathrm{E}})\bar{\boldsymbol{e}}_1 + \mathcal{F}\,\delta\,C_{\mathrm{L}}(\alpha^{\mathrm{E}})\bar{\boldsymbol{e}}_2 \,, \ \ \boldsymbol{c}_{\mathrm{AE}}^{\mathrm{o}}(x) = \mathcal{F}\,\delta^2\,C_{\mathrm{M}}(\alpha^{\mathrm{E}})\bar{\boldsymbol{e}}_3 \tag{5.2.12}$$

The nondimensional drag force per unit length is here expressed in terms of the bridge deck width B instead of the depth d according to the definition of the coefficient C_D; furthermore, the contribution of the drag force on the cables was neglected in the simulations. At an assigned value of the free-stream wind speed U, the solution of equations (5.2.11), representing the prestress effect induced by the static aeroelastic configuration, is then substituted into the equations of motion (4.1.15) and the response to the unsteady aerodynamics loads given in the indicial form (see Section 2.3.2) is studied by solving the following PDEs-ODEs system of equations given by equations (5.2.13) and (5.2.15), respectively.

$$\partial_x \breve{\boldsymbol{n}}^\pm + \breve{\boldsymbol{f}}^\pm - \breve{\boldsymbol{r}}^\pm = \rho A^{\mathrm{c}} \sec \theta_{\mathrm{o}}^\pm(x) \, \partial_{tt} \boldsymbol{v}^\pm + D_j^{\mathrm{c}} \, \partial_t \boldsymbol{v}^\pm,$$

$$\partial_x \breve{\boldsymbol{n}} + \breve{\boldsymbol{f}} + \breve{\boldsymbol{f}}_{\mathrm{AE}} + \breve{\boldsymbol{r}}^+ + \breve{\boldsymbol{r}}^- = \rho A^{\mathrm{d}} \partial_{tt} \boldsymbol{u} + D_j^{\mathrm{d}} \, \partial_t \boldsymbol{u}, \tag{5.2.13}$$

$$\partial_x \breve{\boldsymbol{m}} + \partial_x \breve{\boldsymbol{p}} \times \breve{\boldsymbol{n}} + \breve{\boldsymbol{c}} + \breve{\boldsymbol{c}}_{\mathrm{AE}} + \tfrac{B^{\mathrm{c}}}{2} \, \breve{\boldsymbol{b}}_1 \times (\breve{\boldsymbol{r}}^- - \breve{\boldsymbol{r}}^+) = \boldsymbol{\rho J}^{\mathrm{C}} \cdot \partial_t \boldsymbol{\omega} + \boldsymbol{\omega} \times (\boldsymbol{\rho J}^{\mathrm{C}} \cdot \boldsymbol{\omega}) + D_j^{\mathrm{T}} \, \boldsymbol{\omega}$$

In Eq. (5.2.13), the total aerodynamic forces $\breve{\boldsymbol{f}}_{\mathrm{AE}} = \breve{D}(x,t)\bar{\boldsymbol{e}}_1 + \breve{L}(x,t)\bar{\boldsymbol{e}}_2$ and moment $\breve{\boldsymbol{c}}_{\mathrm{AE}} = \breve{M}(x,t)\bar{\boldsymbol{e}}_3$, accounting for the static components of the wind loads, $\breve{D}(x,t) = D^{\mathrm{o}}(x) + D(x,t)$, $\breve{L}(x,t) = L^{\mathrm{o}}(x) + L(x,t)$, and $\breve{M}(x,t) = M^{\mathrm{o}}(x) + M(x,t)$, are defined in terms of the indicial functions and the added aerodynamic states and

$$D(x,t) = \mathcal{F} \delta \sum_\xi c_{\mathrm{D}}^\xi \left[\varPhi_{\mathrm{D}}^\xi(0)\xi(x,t) + \sum_{k=1}^N \hat{b}_{\mathrm{D,k}}^\xi a_{\mathrm{D,k}}^\xi W_{\mathrm{D,k}}^\xi(x,t) \right] ,$$

$$L(x,t) = \mathcal{F} \delta \sum_\xi c_{\mathrm{L}}^\xi \left[\varPhi_{\mathrm{L}}^\xi(0)\xi(x,t) + \sum_{k=1}^N \hat{b}_{\mathrm{L,k}}^\xi a_{\mathrm{L,k}}^\xi W_{\mathrm{L,k}}^\xi(x,t) \right] , \tag{5.2.14}$$

$$M(x,t) = \mathcal{F} \delta^2 \sum_\xi c_{\mathrm{M}}^\xi \left[\varPhi_{\mathrm{M}}^\xi(0)\xi(x,t) + \sum_{k=1}^N \hat{b}_{\mathrm{M,k}}^\xi a_{\mathrm{M,k}}^\xi W_{\mathrm{M,k}}^\xi(x,t) \right] .$$

where, as previously defined, $\mathcal{F} = \frac{1}{2}\frac{\rho U^2}{\rho A^{\mathrm{d}} \bar{\omega}^2}$, $\delta = \frac{B}{l}$ and

$$\xi(x,t) = \left\{ \frac{\partial_t u_1(x,t)}{\bar{U}}, \frac{\partial_t u_2(x,t)}{\bar{U}}, \phi_3(x,t) \right\}, \quad \text{with} \quad \bar{U} = \frac{U}{\bar{\omega} \, l}$$

The linear differential equations governing the time-evolution of the added aerodynamic states $W_{j,k}^\xi$ coupled with the system of nonlinear partial differential equations (5.2.13) can be written as

$$\partial_t W_{\mathrm{D,k}}^\xi(x,t) = \xi(x,t) - \hat{b}_{\mathrm{D,k}}^\xi W_{\mathrm{D,k}}^\xi(x,t)$$

$$\partial_t W_{\mathrm{L,k}}^\xi(x,t) = \xi(x,t) - \hat{b}_{\mathrm{L,k}}^\xi W_{\mathrm{L,k}}^\xi(x,t) \tag{5.2.15}$$

$$\partial_t W_{\mathrm{M,k}}^\xi(x,t) = \xi(x,t) - \hat{b}_{\mathrm{M,k}}^\xi W_{\mathrm{M,k}}^\xi(x,t)$$

where equations (5.2.15) represent a system of $\sum_{j=1}^3 \sum_\xi N_j^\xi = 10$ (see Section 2.3.4) first-order ordinary differential equations.

The values of the coefficients c_j^ξ, $\hat{b}_{\mathrm{j,k}}^\xi$, and $a_{\mathrm{j,k}}^\xi$ adopted in the analyses, were determined by CFD calculations as discussed in Section 3.2.2 and in Tab. 5.1 are reported the coefficients evaluated for an initial wind angles of attack $\bar{\alpha} = 0°$.

$\varPhi_j^\xi$	$a_{j,1}^\xi$	$b_{j,1}^\xi$	$a_{j,2}^\xi$	$b_{j,2}^\xi$	$a_{j,3}^\xi$	$b_{j,3}^\xi$	c_j^ξ
$\varPhi_{\mathrm{D}}^{\dot{u}_1}$	-6.982	9.696	0	0	0	0	-0.140
$\varPhi_{\mathrm{L}}^{\dot{u}_2}$	-9.635	16.972	0.635	0.425	0	0	-4.670
$\varPhi_{\mathrm{L}}^{\phi_3}$	0.393	0.235	-14.211	33.975	0	0	-5.335
$\varPhi_{\mathrm{M}}^{\dot{u}_2}$	0.501	0.274	-0.312	0.565	0	0	1.107
$\varPhi_{\mathrm{M}}^{\phi_3}$	0.256	0.181	-10859.3	12.161	10884.9	12.187	1.075

Table 5.1: *GBB section: indicial functions coefficients for $\bar{\alpha} = 0°$.*

Once evaluated the nonlinear aeroelastic equilibrium at a selected value of the free-stream speed U by integrating equations (5.2.11), the time dependent simulations presented in the follow are carried out

by solving simultaneously equations (5.2.13) and (5.2.15) for an assigned initial condition perturbing the aeroelastic equilibrium state. The indicial model here considered is linear, as the evolution of the unsteady loads is described adopting the added states formulation, used to convert the integral form of the aerodynamic loads into a differential form, that can straightforwardly be treated numerically. However, these indicial functions have been computed in Chapter 3 by taking into account flow separation and boundary layer thickness, typical viscous flow phenomena. In addition, as indicated in Eq. (5.2.10), the nonlinear form of the aerodynamic loads is considered to evaluate the static equilibrium condition therefore the procedure uses a nonlinear unsteady aerodynamic description.
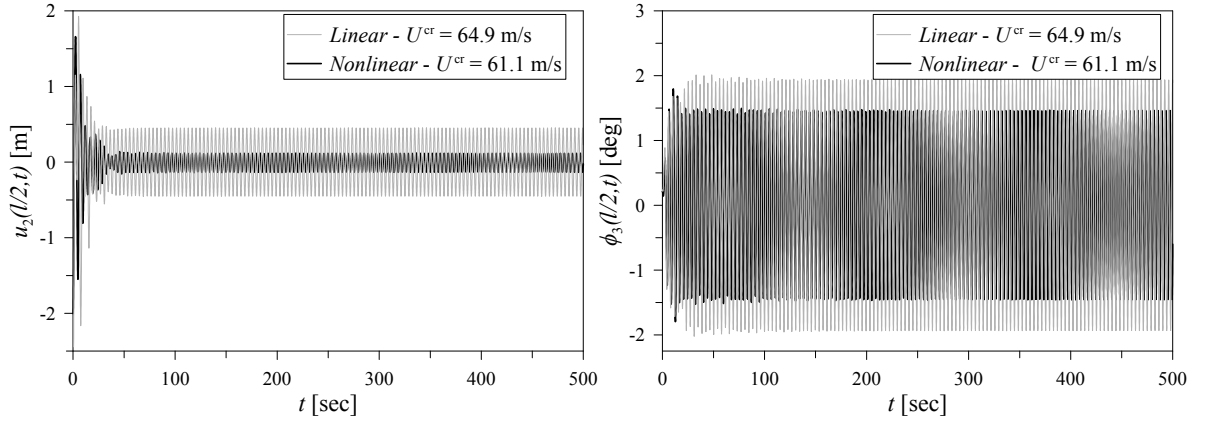
Fig. 5.20: *Time histories of the incremental vertical displacement u_2 and torsional rotation ϕ_3 at the mid-span. Response at the onset of flutter for an initial angle of attack $\bar{\alpha} = 0°$.*
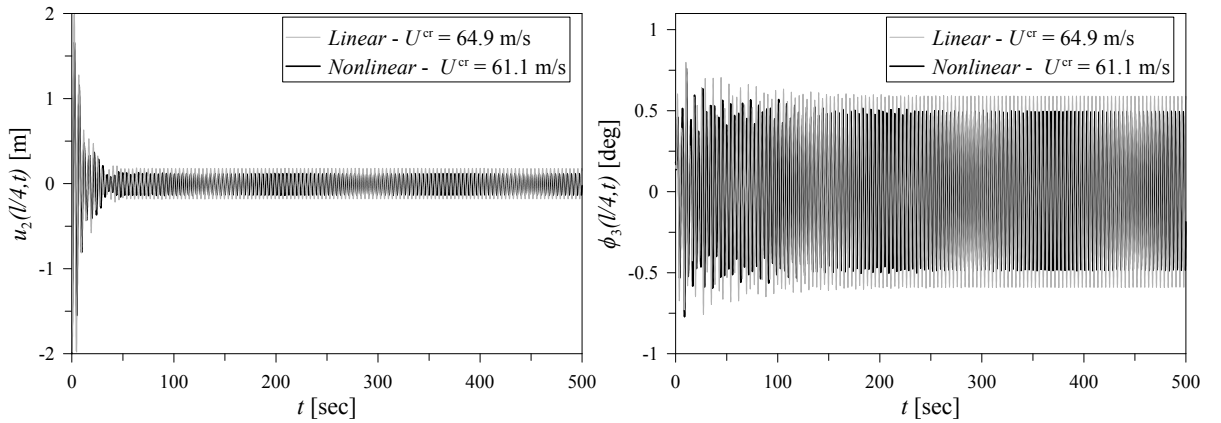
Fig. 5.21: *Time histories of the incremental vertical displacement u_2 and torsional rotation ϕ_3 at the quarter-span. Response at the onset of flutter for an initial angle of attack $\bar{\alpha} = 0°$.*

The numerical simulations revealed that the eigenvalue analyses carried out by employing both, the linear and the fully nonlinear structural models, and accounting for the aerostatic configuration in the nonlinear case, produce the same results obtained from the time dependent simulations performed by adopting the indicial functions derived from the aerodynamic derivatives. That is expected since both the frequency- and time-domain representation of the aerodynamics of the bridge cross section (bluff-body with sharp edges) are identical but in different spaces.

By performing time-domain analyses the critical flutter condition is attained when periodic oscillations are reached. Figures 5.20 and 5.21 show the time histories of the response at the onset of flutter in terms of the deck maximum deflection u_2 and torsional rotation ϕ_3 at the mid-span and highlight the vertical flexural-torsional modal coupling typical of the flutter mode in long-span suspension bridges. The frequency spectrum of the flutter oscillation is shown in Fig. 5.22 where one can appreciate the expected correspondence of the results experienced in the frequency domain analyses and shown in Fig. 5.17.
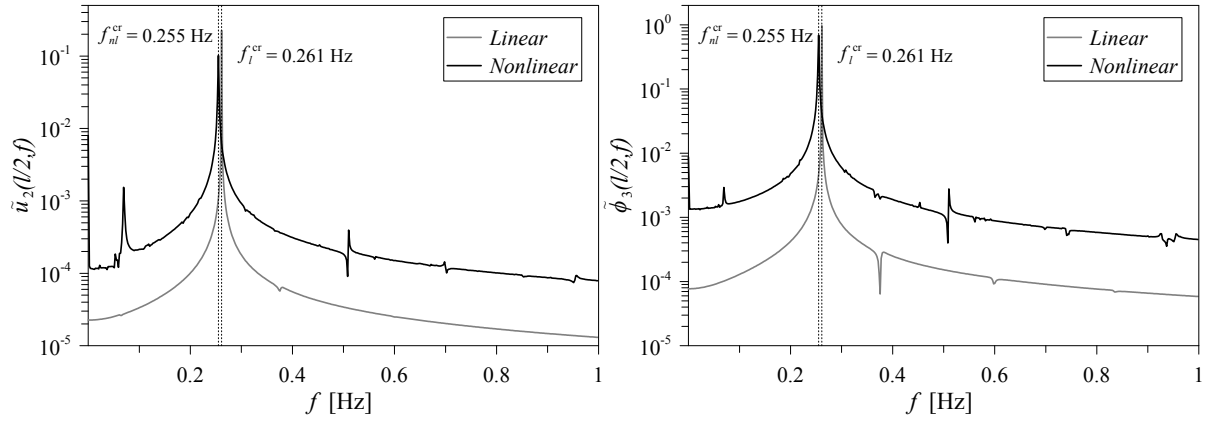
Fig. 5.22: *FFT of the flutter response for the linear and nonlinear structural models. Response at the onset of flutter for an initial angle of attack $\bar{\alpha} = 0°$.*

The two suspension bridge models assume the same aerodynamics, thus the differences shown in the responses are due to the geometric nonlinearities retained in the proposed fully nonlinear structural model and derived in Chapter 4. As previously discussed in Section 4.4 and shown in Figs 4.4, 4.5 and 4.6, the large deformations induced in the cables and the deck may give hardening or softening behavior, depending on the direction of the load forcing the bridge. As highlighted in Figs 5.20 and 5.21, in the flutter motion the structural nonlinear modeling shows smaller amplitudes of oscillation with respect to the response of the linear model. At the mid-span, where the cables stiffness contribution is more relevant, these differences have been quantified in $\approx 24\%$ for the maximum torsional rotation ϕ_3 and $\approx 49\%$ for the vertical bending displacement u_2, whereas lower gaps, $\approx 14\%$ and 24.5% for ϕ_3 and u_2, respectively, have been estimated at the quarter-span.

Chapter 6
Aeroelastic Response

In this chapter, the aeroelastic response in the post-flutter regime is investigated by coupling the unsteady nonlinear aerodynamics of the GBB developed in Section 3.2.2.1 and Section 3.2.2.3 with the nonlinear parametric structural model presented in Chapter 4. Both quasi-steady (QS) and unsteady (US) nonlinear aerodynamics are adopted and the influence of the modeled nonlinearities on the flutter boundary is determined. The Limit Cycle Oscillations (LCOs) occurring in the post-critical wind speed regimes are compared and the differences between the two modeling approaches are highlighted.

The continuation of the LCOs is then performed through numerical FE simulations and the stable bifurcation branch, showing the evolution of the maximum amplitude of the LCO with the free-stream velocity U, is determined assuming the fully nonlinear structural model and the nonlinear quasi-steady and unsteady aerodynamics. A reduced-order linearized model of suspension bridge is then coupled with the quasi-steady aerodynamics and path following of the stable and unstable branches is performed.

Finally, in the last Section, the effects of nonuniform spatial wind distributions on the critical flutter condition are estimated together with the aeroelastic response to a nonuniform (in time and space) gust load.

6.1 Quasi-Steady Nonlinear Aerodynamic Loading

Analysis of the post-critical flutter response of suspension bridges is performed by adopting nonlinear quasi-steady aerodynamics, and the limit cycle oscillations occurring in the post-flutter range are then investigated. The quasi-steady theory is used primarily in the time domain but it is worth noticing that such a theory is only applicable at high values of reduced velocities $U_{\rm r}$, that is when a low-frequency dynamics are involved in the aeroelastic response and no added mass effects are induced. This formulation can be referred to as the case of unsteady aerodynamics when $K \to 0$.

Within the quasi-steady formulation, the dimensionless aerodynamic loads are expressed as

$$\breve{D}(x,t) = \mathcal{F}\,\delta\,C_{\rm D}\left(\alpha^{\rm E}\right) \,,\;\; \breve{L}(x,t) = \mathcal{F}\,\delta\,C_{\rm L}\left(\alpha^{\rm E}\right) \,,\;\; \breve{M}(x,t) = \mathcal{F}\,\delta^2\,C_{\rm M}\left(\alpha^{\rm E}\right) \,. \tag{6.1.1}$$

where, as discussed in Chapter 2, the effective dynamic total angle of attack $\alpha^{\rm E}(x,t)$ is defined as

$$\alpha^{\rm E}(x,t) = \bar{\alpha} + \phi_3^{\rm o}(x) + \phi_3(x,t) - \frac{\partial_t u_2(x,t) + \frac{B}{4}\,\partial_t \phi_3(x,t)}{U + \partial_t u_1(x,t)} \tag{6.1.2}$$

and the nonlinear expressions (5.2.10) of the aerodynamic coefficients of the GBB deck cross section are adopted.

The analysis of the nonlinear aeroelastic response was performed for selected values of the wind speed U and iterated until the condition leading to a stable LCO was detected. In particular, according to the ULF approach described in Chapter 4, the nonlinear equilibrium under the action of the static aerodynamic loads was first calculated by solving the system of PDEs (5.2.11) and assuming the expression (5.2.12) of the static aeroelastic loads. By introducing the vector of the dynamic total aeroelastic loads as

$$\check{\boldsymbol{f}}_{\mathrm{AE}}(x,t) = -\check{D}(x,t)\bar{\boldsymbol{e}}_1 + \check{L}(x,t)\bar{\boldsymbol{e}}_2 \,, \ \check{\boldsymbol{c}}_{\mathrm{AE}}(x,t) = \check{M}(x,t)\bar{\boldsymbol{e}}_3 \qquad (6.1.3)$$

the dynamic aeroelastic equations (5.2.13) are adopted and the response to a perturbation (initial condition) of the aeroelastic equilibrium is then evaluated in terms of the time evolution of the incremental states $v_i^{\pm}(x,t)$, $u_i(x,t)$, $\phi_i(x,t)$, $\partial_t v_i^{\pm}(x,t)$, $\partial_t u_i(x,t)$, $\partial_t \phi_i(x,t)$ with $i = 1, 2, 3$.

In Figures 6.1 the time histories of the pre-critical response in terms of the deck vertical and horizontal displacements and the rotation at the mid-span are shown. The aerodynamic loads in the pre-critical flutter regime are such that the vertical and torsional oscillations die out rapidly whereas the nonlinear drag does not seem to give a significative contribution to the dynamics of the system.
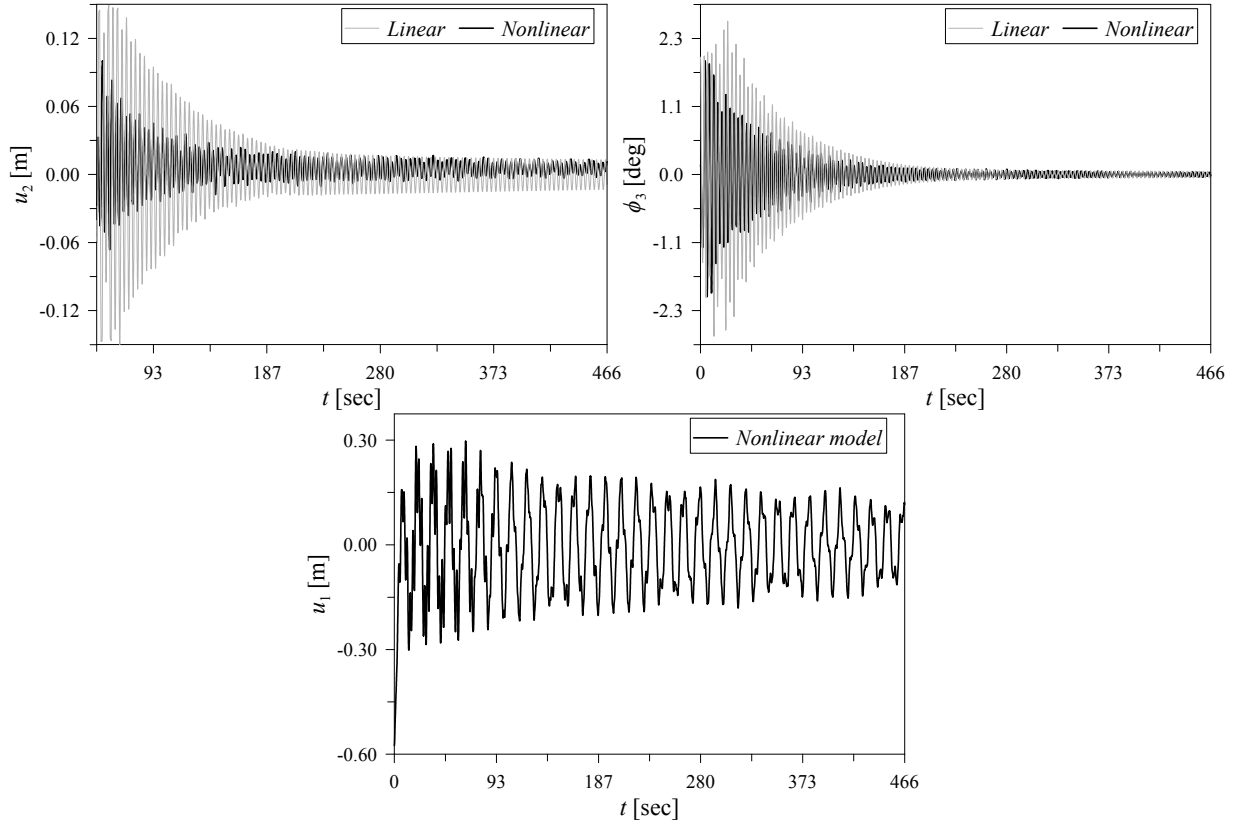

Fig. 6.1: *Time histories of the incremental vertical u_2 and horizontal u_1 displacements and torsional rotation ϕ_3 at the mid-span. pre-critical response at $U = 40$ m/s and for an initial angle of attack $\bar{\alpha} = 0°$.*

The first LCO is found at a critical wind speed of $U_l^{\mathrm{cr}} \approx 56.5$ m/s for the linearized structural model and $U_{nl}^{\mathrm{cr}} \approx 52.8$ m/s by adopting the fully nonlinear structural model, implying that the quasi-steady nonlinear aerodynamics modeling predicts a loss of aeroelastic stability of the bridge at a value about

12.9% and 13.6%, for the two structural models respectively, lower than the critical velocity estimated by adopting linear unsteady aerodynamics.

The results of the post-critical flutter response of the bridge are presented in Fig. 6.2 and Fig. 6.3 where the vertical and torsional limit cycles are shown. The main effect of the structural nonlinearities is to bring forward the rise of LCO. In 6.4 the LCO frequencies are compared for the cases of linear and nonlinear structural models. As shown in the figures, the amplitudes of the maximum torsional rotation ϕ_3 during the post-critical LCO are larger than $10°$ and rise up as the wind velocity increases. Therefore the geometrically exact structural modeling and the nonlinear aerodynamic characterization at high angles of attack carried out in the present work are fully justified.
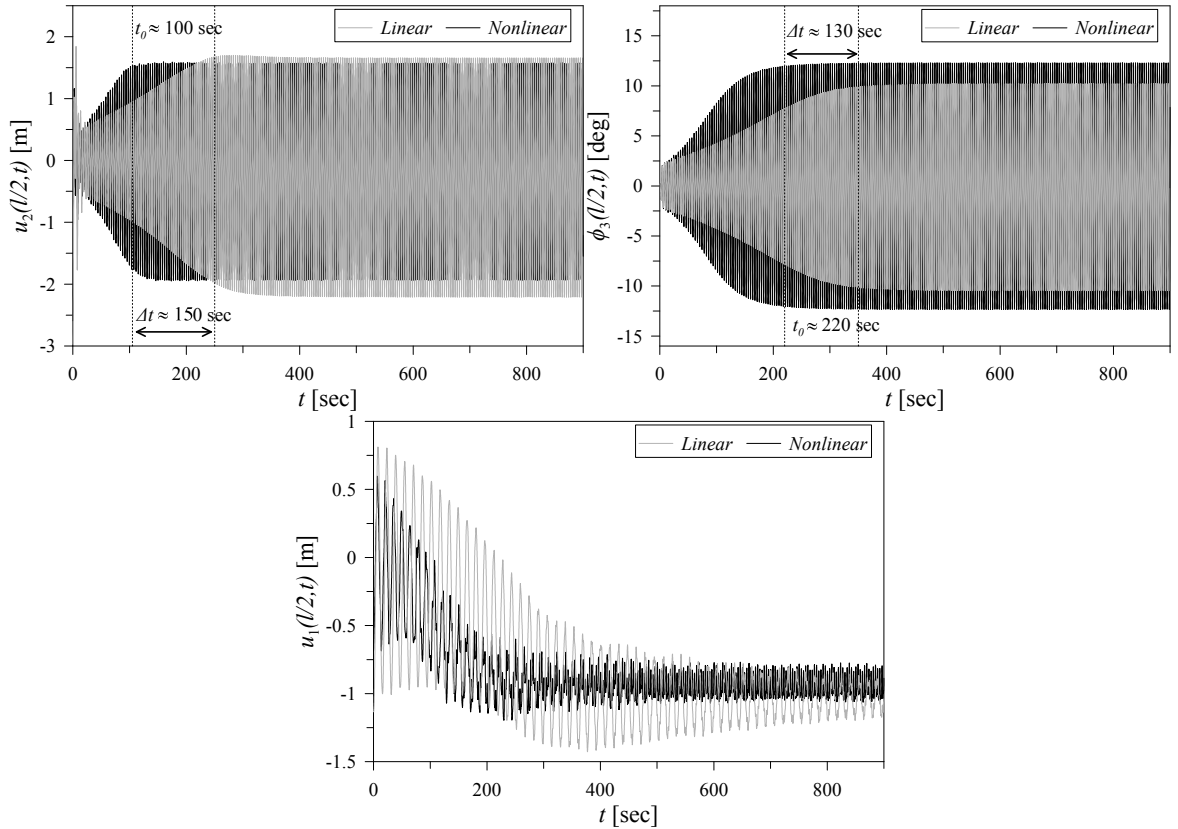
Fig. 6.2: *Time histories of the incremental vertical u_2 and horizontal u_1 displacements and torsional rotation ϕ_3 at the mid-span. LCO at $U = 62$ m/s and for an initial angle of attack $\bar{\alpha} = 0°$.*

Quasi-periodic responses, characterized by low-frequency amplitude modulation, are found at higher values of the post-critical wind speed. In Fig. 6.5 the time history and the frequency spectrum of the nonlinear quasi-periodic response are shown for $U = 70$ m/s where the modulation frequency of $f_1 = 0.042$ Hz superimposed on the carrier frequency of $f_2 = 0.216$ Hz.

The time-dependent response of the bridge, assuming the proposed nonlinear structural model, is evaluated at the post-flutter wind speed of $U = 60$ m/s and the stress-state induced by large-amplitude LCO is reported in Figs. 6.6 and 6.7 where the components of the total stress resultants in the cables and the deck are given in their dimensional form. In particular, notice that the maximum axial force in the cables, is registered at the anchorages ($x = 0, l$), is of $\breve{N}^+ \approx 3.75 \times 10^8$ N; since the area of the cables cross section, for the case study, is $A^c = 0.47347 \times 10^6$ mm^2, an estimation of the maximum tension induced in a the cables in post-critical oscillation can be then $f \approx 790$ N/mm^2. This value is still lower
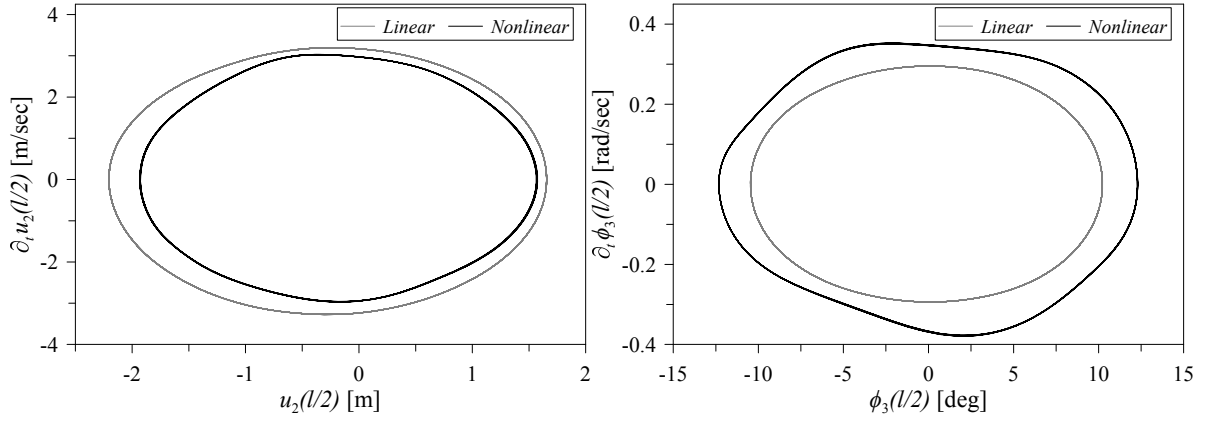
Fig. 6.3: *Phase portrait of the incremental vertical displacement u_2 and velocity $\partial_t u_2$ and torsional rotation ϕ_3 and angular velocity $\partial_t \phi_3$ at the mid-span. LCO at $U = 62$ m/s and for an initial angle of attack $\bar{\alpha} = 0°$.*
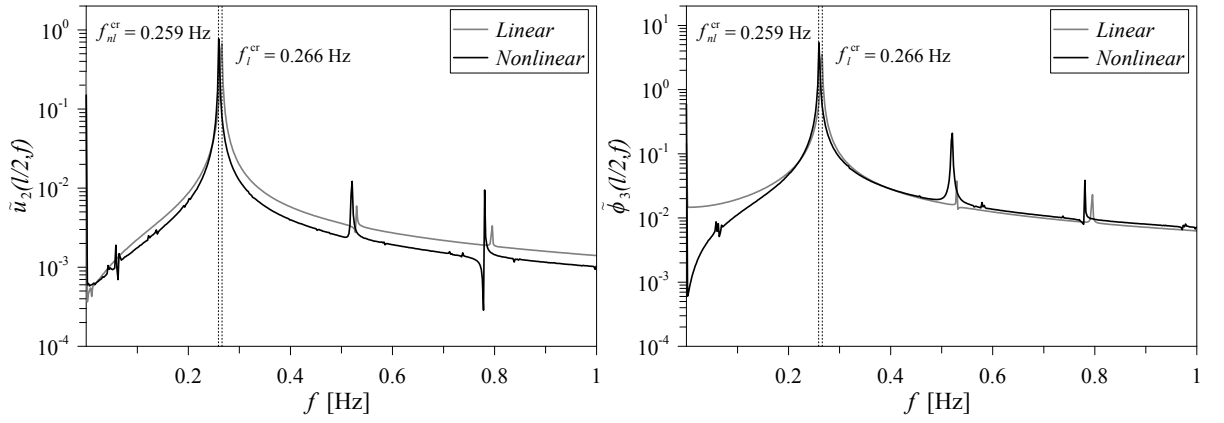

Fig. 6.4: *FFT of the flutter response for the linear and nonlinear structural models. LCO at $U = 62$ m/s and for an initial angle of attack $\bar{\alpha} = 0°$.*

than the characteristic tensions of the steel usually employed in suspensions cables design, i.e. at the yield strength $f_{0.2} \geq 1180$ N/mm^2 and the ultimate value $f_u \geq 1570$ N/mm^2, the linear elastic constitutive laws assumed in the modeling are still valid also in the post-flutter oscillation regime.
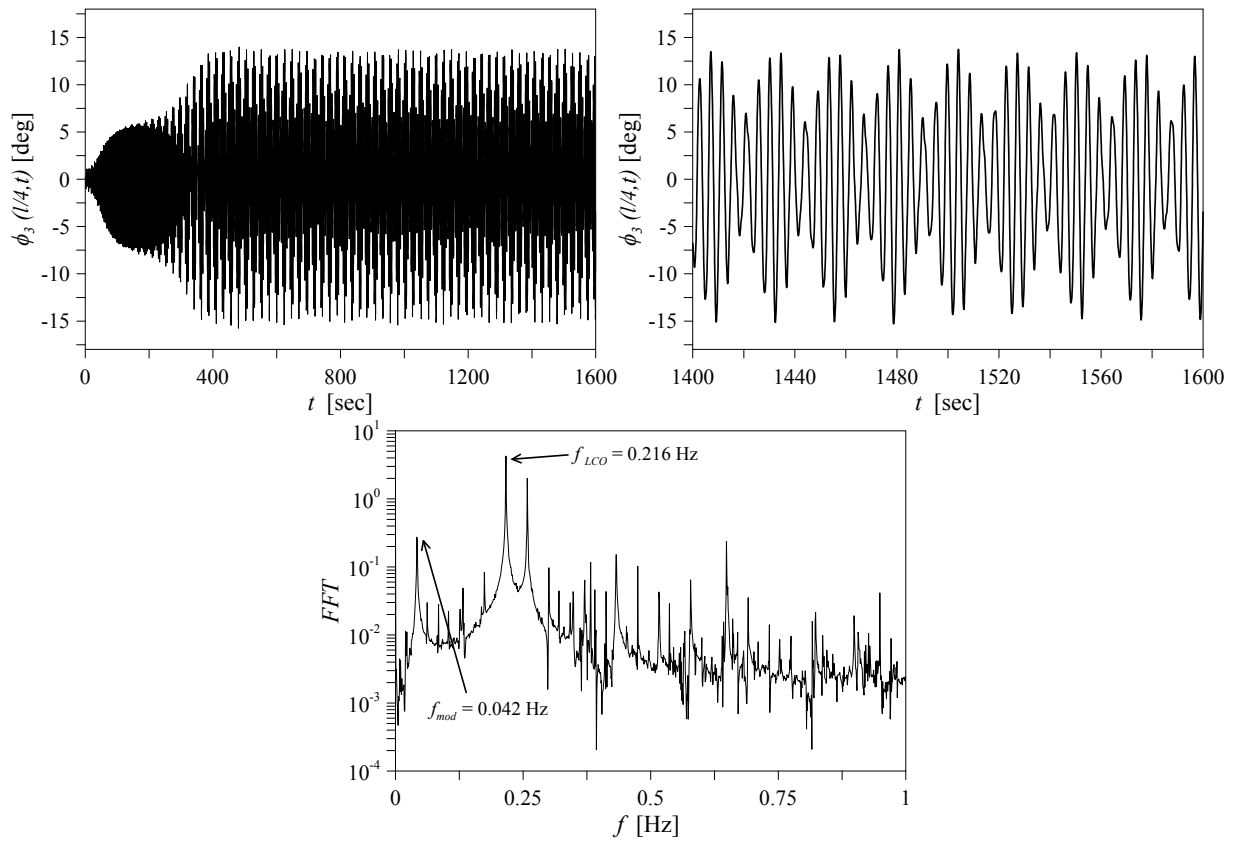
Fig. 6.5: *Post-flutter quasi-periodic response (U = 70 m/s), time histories of the torsional rotation ϕ_3 of the bridge deck quarter-span and frequency spectrum.*
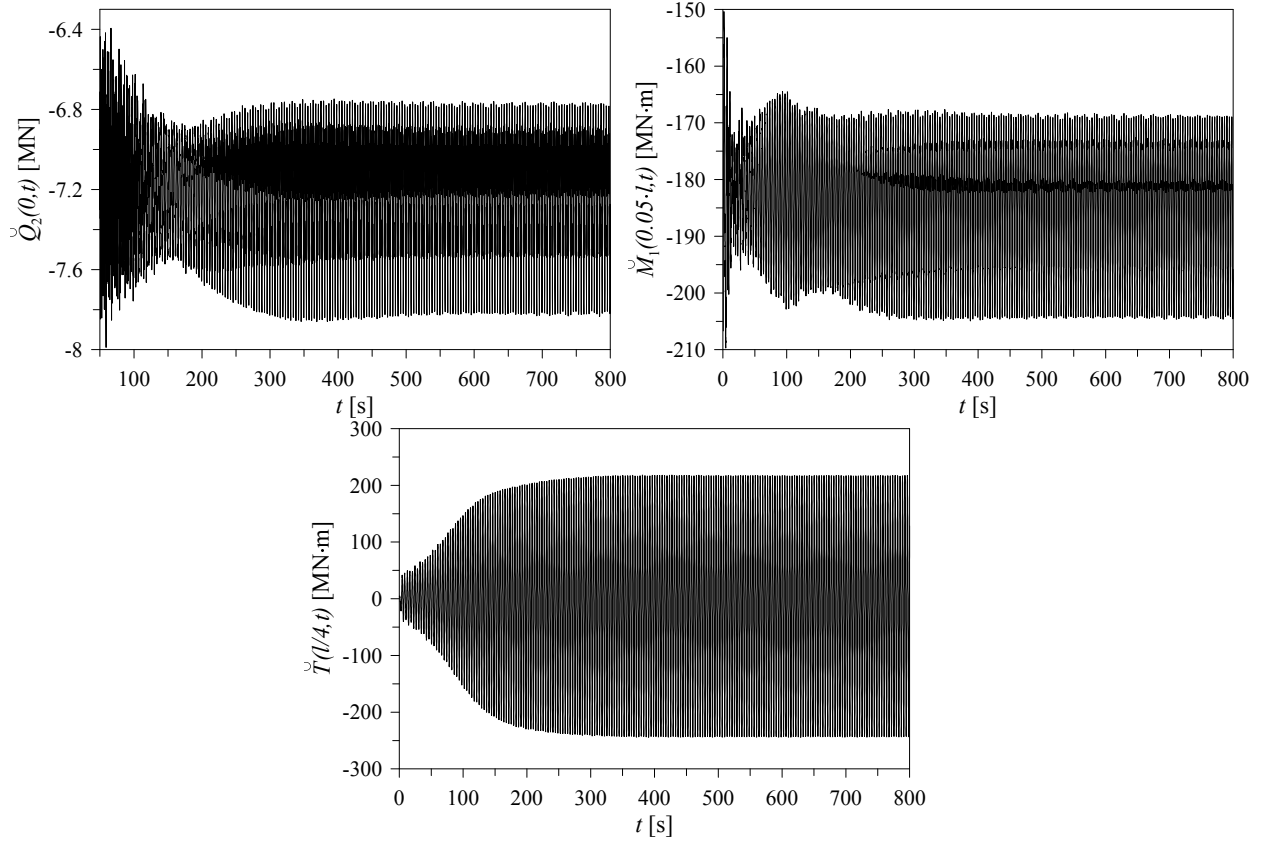
Fig. 6.6: *Time histories of the maximum values of the total shear $\breve{Q}_2(0,t)$, bending moment $\breve{M}_1(0.04\,l,t)$, and torque $\breve{T}(0.25\,l,t)$ in the bridge deck at $U = 62$ m/s and for an initial angle of attack $\bar{\alpha} = 0°$ during a LCO.*
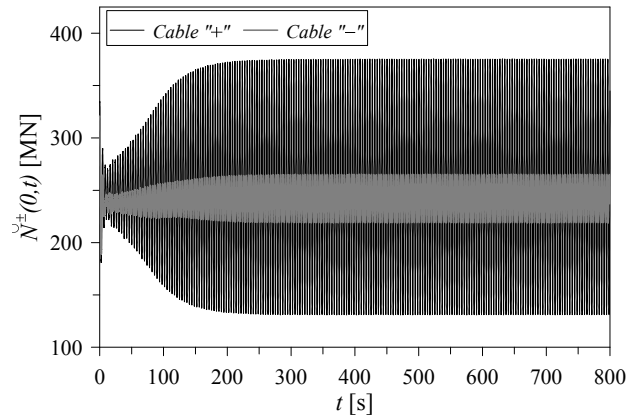
Fig. 6.7: *Time histories of the maximum values of the total stress resultants $\breve{N}_2^{\pm}(0,t)$ in the cables computed at the cables anchorages at $U = 62$ m/s and for an initial angle of attack $\bar{\alpha} = 0°$ during a LCO.*

6.2 Unsteady Nonlinear Aerodynamic Loading

An important step in the nonlinear aeroelastic modeling of suspension bridges is to account also for the unsteady effects, due to the instantaneous variation of the wind angle of attack, in the aerodynamic description of the self-excited aeroelastic loads as discussed in Sections 2.3.3 and 2.3.5. The natural extension of this process is to consider unsteady aerodynamic loads based on a nonlinear functional form of the indicial functions described in Section 2.3.5. However, such a formulation implies the evaluation of convolutional integrals that are nonlinearly dependent on the aerodynamic states ξ and cannot be treated by the same added-states approach used for the linear case.

Nevertheless, the first step towards the fully nonlinear aerodynamic formulation is that of considering the nonlinearities due to flow separation at high angles of attack by assuming the nonlinear expressions of the static coefficients and their slope rather than their value at the mean angle of attack $\bar{\alpha}$. Thus, the aeroelastic equilibrium is evaluated at the effective angle of attack

$$\alpha^{\mathrm{E}}(x,t) = \bar{\alpha} + \phi_3^{\mathrm{o}}(x) + \phi_3(x,t) - \frac{\partial_t u_2(x,t) + \frac{B}{4}\,\partial_t \phi_3(x,t)}{U + \partial_t u_1(x,t)} \tag{6.2.1}$$

whereas only the instantaneous variation from such equilibrium is assumed to be linear thus the Duhamel convolution integral is still valid and the added state formulation described in Section 2.3.4 can be adopted. The equations governing the aeroelastic equilibrium as well as the motion of the bridge together with the added state equations giving the unsteady aerodynamics are those summarized in Section 5.2.3. The indicial formulation of the unsteady drag, lift, and moment is briefly reported here

$$\begin{aligned}
D(x,t) &= \mathcal{F}\,\delta \sum_\xi c_{\mathrm{D}}^\xi \left[\Phi_{\mathrm{D}}^\xi(0)\xi(x,t) + \sum_{k=1}^N \hat{b}_{\mathrm{D,k}}^\xi a_{\mathrm{D,k}}^\xi W_{\mathrm{D,k}}^\xi(x,t) \right], \\
L(x,t) &= \mathcal{F}\,\delta \sum_\xi c_{\mathrm{L}}^\xi \left[\Phi_{\mathrm{L}}^\xi(0)\xi(x,t) + \sum_{k=1}^N \hat{b}_{\mathrm{L,k}}^\xi a_{\mathrm{L,k}}^\xi W_{\mathrm{L,k}}^\xi(x,t) \right], \\
M(x,t) &= \mathcal{F}\,\delta^2 \sum_\xi c_{\mathrm{M}}^\xi \left[\Phi_{\mathrm{M}}^\xi(0)\xi(x,t) + \sum_{k=1}^N \hat{b}_{\mathrm{M,k}}^\xi a_{\mathrm{M,k}}^\xi W_{\mathrm{M,k}}^\xi(x,t) \right].
\end{aligned} \tag{6.2.2}$$

As detailed in Section 3.2.2.3, only the contribution of the flutter derivatives covering an important role in the aeroelastic behavior of suspension bridges, that is, H_i, A_i $(i=1,2,3,4)$, P_5 and P_6 was retained. Thus, by recalling the relations between the coefficients c_j^ξ of the indicial formulation and the values of the aerodynamic coefficients C_j (Eq. (3.2.23)) and the slopes $\partial_\alpha C_j$ (Eq. (3.2.24)) of the static curves at the mean value of the angle of attack α_{w}, it turns out that only 3 of the 5 coefficients c_j^ξ are independent; in particular, the following relationships hold

$$c_L^{\dot{u}_2} = c_L^{\phi_3} + \frac{c_D^{\dot{u}_1}}{2}\,, \ \ c_M^{\dot{u}_2} = c_M^{\phi_3}\,. \tag{6.2.3}$$

Therefore, the expressions of the indicial coefficients c_j^ξ depending on the nonlinear curves of the static coefficients and their slopes, read

$$c_D^{\dot{u}_1} = -2\,C_D\left(\alpha^{\mathrm{E}}\right),\ \ c_L^{\phi_3} = -\partial_\alpha C_L|_{\alpha^{\mathrm{E}}},\ \ c_L^{\dot{u}_2} = -\partial_\alpha C_L|_{\alpha^{\mathrm{E}}} - C_D\left(\alpha^{\mathrm{E}}\right),\ \ c_M^{\dot{u}_2} = c_M^{\phi_3} = \partial_\alpha C_M|_{\alpha^{\mathrm{E}}}, \tag{6.2.4}$$

where, from the expressions of the static coefficients curves given by 5.2.10, their slopes, as a function of the effective angle of attack α^{E}, can be written as

$$\partial_\alpha C_L|_{\alpha^E} = 6.357 - 5.179\,\alpha^E - 328.172\,\alpha^{E2} - 10.703\,\alpha^{E3} + 3930.9\,\alpha^{E4}\,,$$
$$\partial_\alpha C_M|_{\alpha^E} = 1.138 - 1.535\,\alpha^E - 81.01\,\alpha^{E2} + 18.242\,\alpha^{E3} + 1245.16\,\alpha^{E4}\,,$$
(6.2.5)

while the considered nonlinear expression of the drag coefficient reads

$$C_D(\alpha^E) = 0.0695 + 0.1332\,\alpha^E + 4.7033\,\alpha^{E2} - 1.1667\,\alpha^{E3} - 24.1297\,\alpha^{E4}\,.$$
(6.2.6)

According to the updated Lagrangian formulation adopted in this work, the simulations are performed by first evaluating the nonlinear aeroelastic equilibrium at a selected value of the free-stream speed U, then the time-dependent simulations are carried out by solving simultaneously equations (5.2.13) and (5.2.15) for an assigned initial condition perturbing the aeroelastic equilibrium state. Only the fully nonlinear structural model is employed in the calculations.

The first periodic oscillation, leading the bridge to a LCO, is found at a wind speed $U_{cr} = 58.2$ m/s, slightly lower ($\approx 4.8\%$) of that estimated assuming linear unsteady aerodynamic loads. In Fig. 6.8 the LCOs at a post-critical speed $U = 62$ m/s obtained assuming the unsteady and the quasi-steady (discussed in Section 6.1) nonlinear aerodynamics are compared. In the same figure, the post-flutter divergent response obtained assuming a linear unsteady modeling is superposed. While the nonlinear representation of the aerodynamic loading is capable of capturing the limit cycle, adopting a linearized form of the loading a linear flutter-like behavior is predicted with an unboundedly growing oscillating response. Figure 6.8 also shows the frequency spectrum during the post-critical oscillation, it appears that the dynamics of the bridge described by the linear unsteady aerodynamics is dominated by one main frequency ($f = 0.254$ Hz) while using the nonlinear representation of the aerodynamic loading, the presence of the super-harmonics is very distinct. The three-dimensional configuration of the suspension bridge during the LCO at $U = 62$ m/s is then shown in Fig. 6.9.

Quasi-periodic responses, characterized by a low-frequency amplitude modulation, are found at higher values of the post-critical wind speed. In Fig. 6.10 the time history and the frequency spectrum of the modulated LCO are shown for $U = 80$ m/s.

From Fig. 6.11 one can observe that the two dynamics - those of the unsteady and quasi-steady loading - occur at slightly different frequencies ($f^{US} = 0.272$ Hz and $f^{QS} = 0.261$ Hz) as shown in Fig. 6.8, with the dynamic effective angle of attack in phase with the corresponding loading. Obviously the frequency of the drag coefficient is twice the frequency of the oscillating lift and aerodynamic moment coefficients.

In Figure 6.12 the cyclic variation of the aeroelastic loads with the effective angle of attack α^E, normalized with respect to the wind dynamic pressure ($\frac{1}{2}\rho U^2 B$ for drag and lift, and $\frac{1}{2}\rho U^2 B^2$ for the aerodynamic moment), shows the aerodynamic hysteresis occurring during the post-critical LCO. The power spent by the aerodynamic loads during a stable LCO and shown in Fig. 6.13 can be calculated as

$$P_{AE}(t) = \int_0^l \left[D(x,t)u_1(x,t) + L(x,t)u_2(x,t) + M(x,t)\phi_3(x,t) \right] dx$$
(6.2.7)

and the work performed during one period is

$$\mathcal{W}_{AE} = \int_0^{T_{LCO}} P_{AE}(t)\,dt\,.$$
(6.2.8)

Thus, at post-flutter speed at $U = 62$ m/s, for which the corresponding LCO (shown in Fig. 6.8) has frequency $f_{LCO}^{US} = 0.272$ Hz, the work of the aerodynamic loads during one period $T_{LCO} = 3.68$ s turns out to be $\mathcal{W}_{AE} \approx 1.463 \times 10^6$ J.

This parameter represents an important indicator of the amount of energy extracted from the airstream by the structure in the elastic deformation process. During one cycle of vibration, the aerodynamic forces
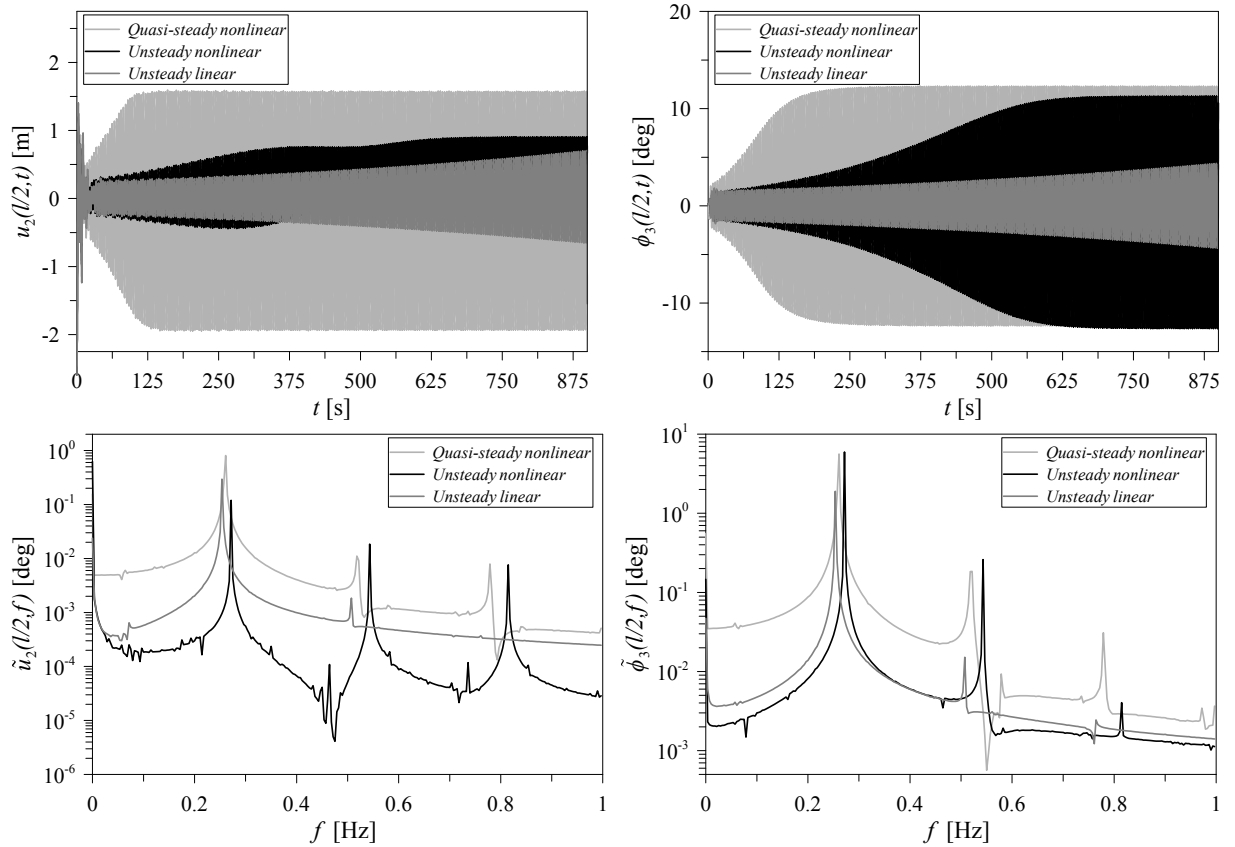
Fig. 6.8: *Post-flutter LCO (U = 62 m/s), time histories of the vertical incremental displacement u_2 and torsional rotation ϕ_3 of the bridge deck and frequency spectrum.*
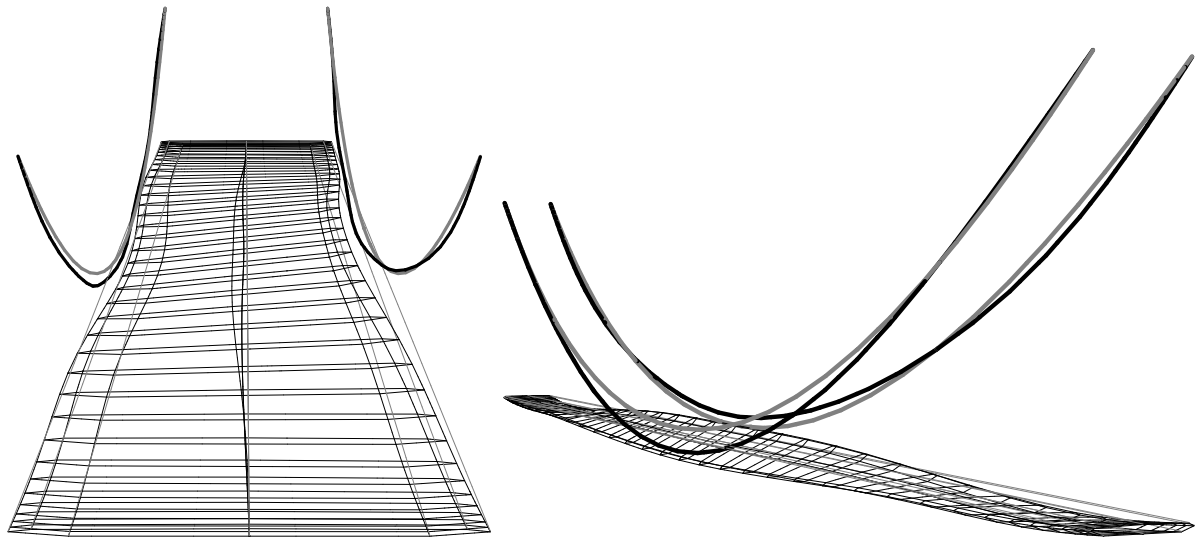

Fig. 6.9: *Three-dimensional views of the aeroelastic configuration during the post-flutter LCO at U = 62 m/s.*
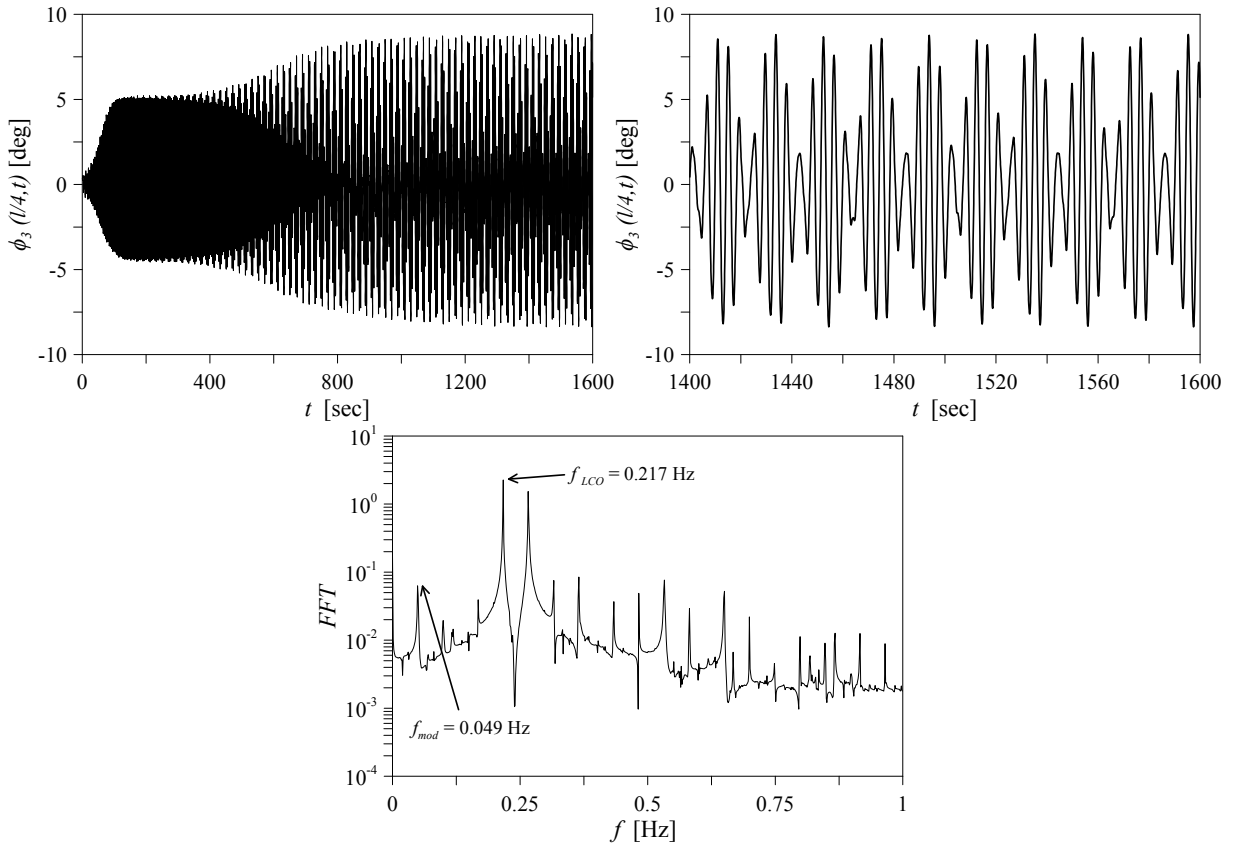
Fig. 6.10: *Post-flutter quasi-periodic response (U = 80 m/s), time histories of the torsional rotation ϕ_3 of the bridge deck quarter-span and frequency spectrum.*

perform work on the bridge, converting aerodynamic energy into kinetic and strain energy. The system is oscillating in a stable LCO, therefore, the interaction between structural deflections and aerodynamic forces is such that the oscillating bridge absorbs energy from the airstream, and releases to the airstream an equivalent amount. Therefore, the kinetic and strain energies are traded so that the total energy in the system is invariant. This is different from the linear post-flutter condition where the airstream energy is such that creates a situation in which a disturbance can grow unbounded with time. One could use this information to evaluate the possibility of controlling the bridge deformation during its oscillations by means of active controls, as the excess energy from the airstream, that could lead into an aeroelastic instability, need to be absorbed and dissipated.

Considerations on the Aeroelastic Modeling

From the analyses performed in the previous sections, one can conclude that the structural geometric nonlinearities influence the aeroelastic stability of suspension bridges such that flutter occurs at lower values of the free-stream speed U (a reduction of about 6%) when compared to the linearized structural model. On the other hand, a quasi-steady nonlinear aerodynamics, leading the bridge to LCOs in post-flutter regime, implies a further reduction of the critical wind speed of about 13% with respect to the flutter speed calculated in the context of linear aerodynamics. Furthermore, the results illustrate that the unsteady nonlinear aerodynamic modeling, is less conservative than the quasi-steady formulation with an higher critical speeds (about 10% more than QS nonlinear model) and smaller LCO amplitudes.
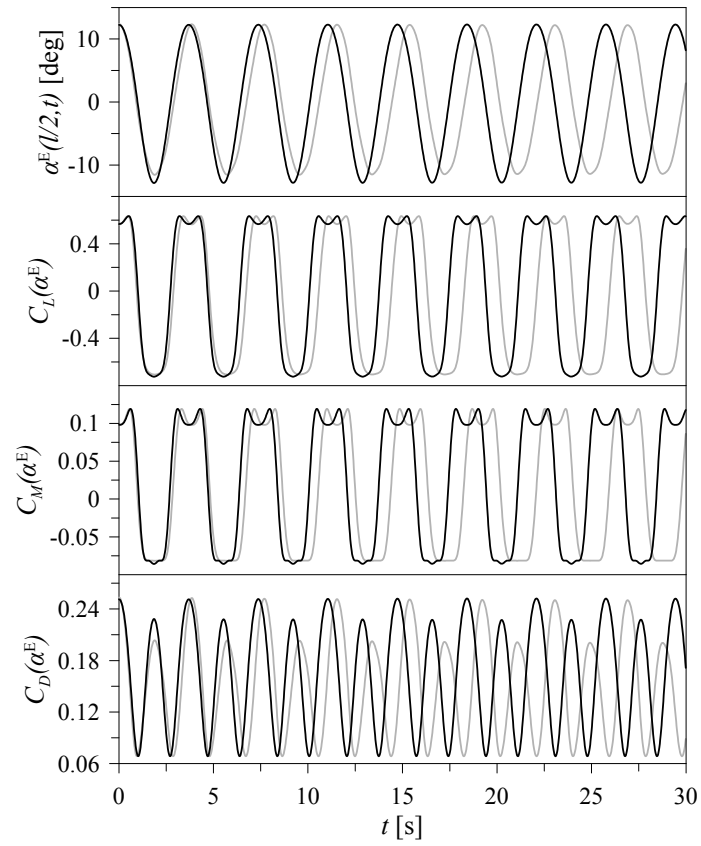
Fig. 6.11: *Effective angle of attack and quasi-steady (grey line) and unsteady (black line) lift, moment, and drag coefficients in a post-flutter LCO.*
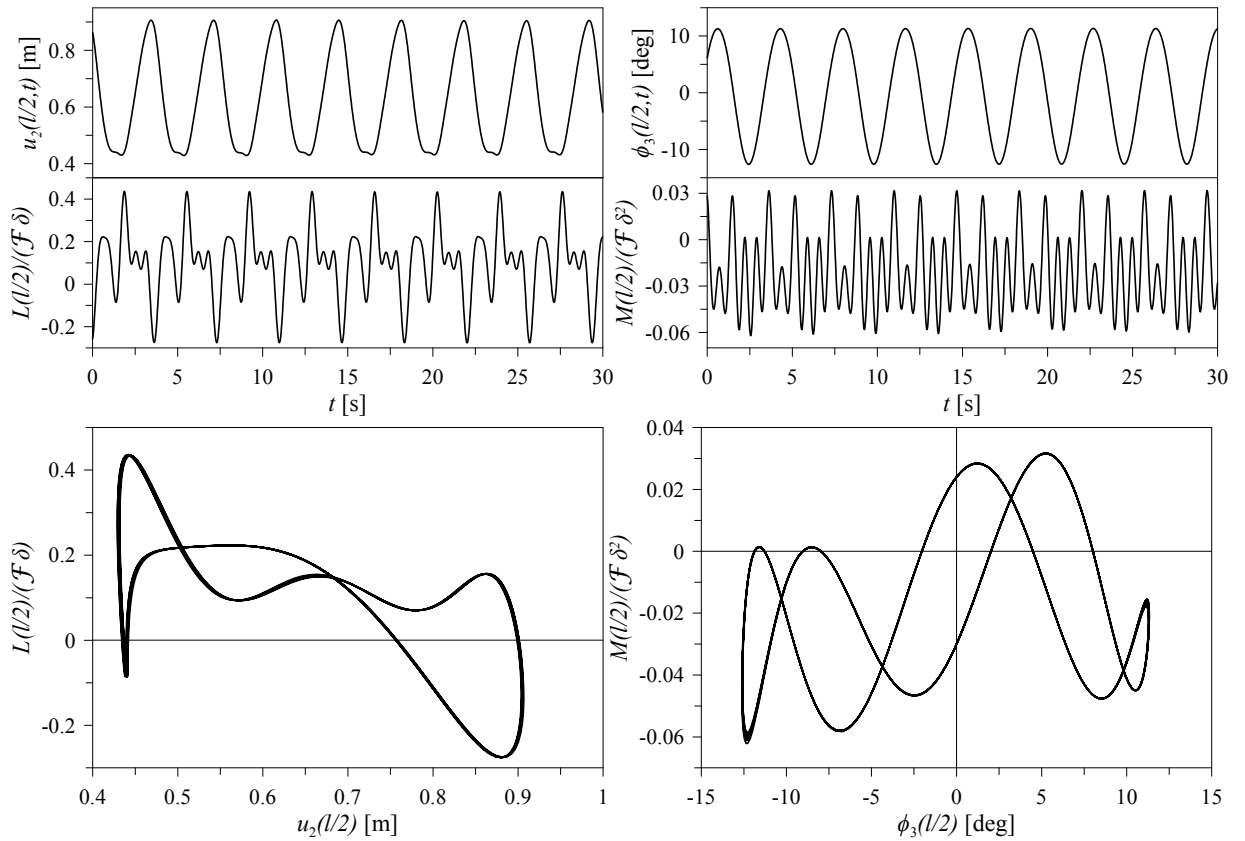
Fig. 6.12: *Vertical deck displacement and torsional rotation and normalized unsteady lift and moment during the post-critical LCO at $U = 62$ m/s.*
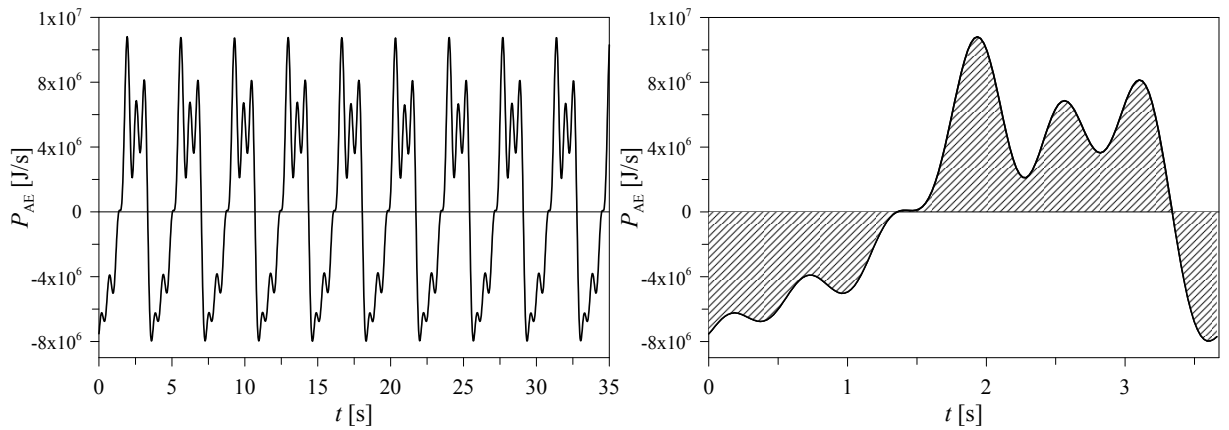

Fig. 6.13: *Power of the aerodynamic loads during a LCO at $U = 62$ m/s; power over one period T_{LCO} (right).*

6.3 Continuation of the LCO

The investigation of the post-flutter scenario is performed in the context of a quasi-steady nonlinear aerodynamic modeling and the post-critical analysis has been carried out according to various strategies. By considering the geometrically exact structural model, a straightforward brute-force approach has been adopted and it consists of considering a speed past the Hopf bifurcation point at which the stable LCO is found by time integration of the aeroelastic governing equations. The speed is varied and the initial conditions are considered as the values reached by the state variables at the steady-state LCO at the previous speed. Furthermore, the one-parameter continuation of these LCOs is performed and the bifurcation diagrams, featuring both the stable and unstable branches, are obtained with a reduced-order linearized model of suspension bridge. The approach to the computation of the LCOs and the bifurcation behavior of the nonlinear aeroelastic response here pursued is based on a pseudo-arclength continuation strategy. A Matlab-based continuation toolbox (COCO) [80, 81] has been employed. Figure 6.14 describes the flow-chart of the continuation procedure performed by the toolbox in order to path follow the periodic orbits representing the LCO attained by the wing in the post-flutter regime.
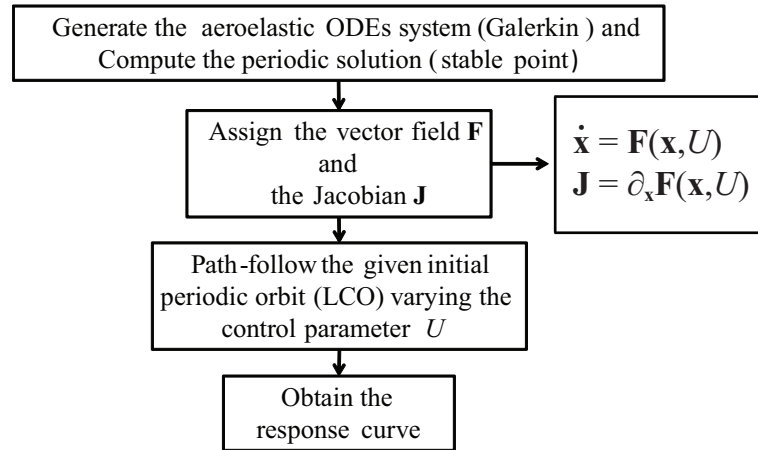

Fig. 6.14: Flow chart of the continuation procedure performed by COCO [80].

In Fig. 6.15 the results of the time-marching (TM) simulations in the context of finite element (FE) discretization (COMSOL Multiphysics® [56]) are superimposed to the full continuation of the LCO adopting a linearized structural model. The dots representing the stable bifurcation branch determined with the fully nonlinear model were obtained by evaluating the maximum LCO amplitude at several values of the post-critical wind speed U. The resolution of the points extracted by TM simulations for wind speeds U close to the critical value is strongly affected by the step size chosen to discretize the range of variation of U. In fact, in the neighborhood of the Hopf bifurcation point where the tangent to the stable branch curve becomes vertical, a tiny variation in velocity is required moving backward from a stable LCO at higher values of U in order to continue on the stable LCO solution.

Figures 6.16 and 6.17 display the post-critical stable and unstable flutter behavior, represented for selected values of the structural damping ratio ζ and the initial wind angle of attack $\bar{\alpha}$. The damping ratio contributes significantly to increase the flutter speed, i.e. the Hopf bifurcation point shifts toward higher speeds and affects also the position of the fold points. Interestingly the value of the displacement at the folds are similar independently of the value of the structural damping. Similar conclusions can be reached for the cases displayed in Figure 6.17 where the bifurcation diagrams are proposed for three values of the initial angle of attack $\bar{\alpha}$. The numerical results in the neighborhood of the folds should be
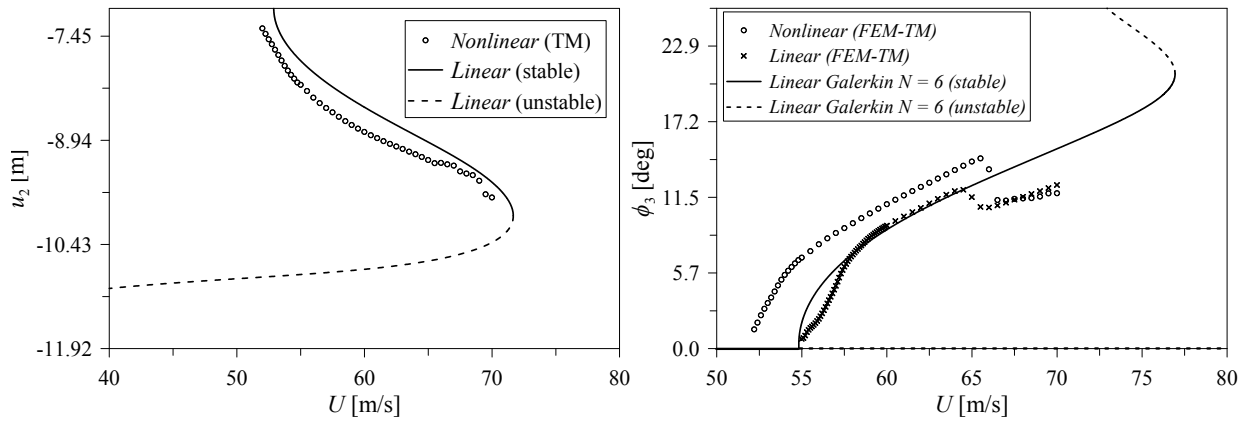
Fig. 6.15: *Bifurcation diagram for $\zeta = 0.5\%$. Stable branch (solid line) and unstable branch (dashed line).*

carefully considered since the bifurcations occur at very high torsional angles, where the aerodynamic characteristics of the bridge section turn out to be quite uncertain.
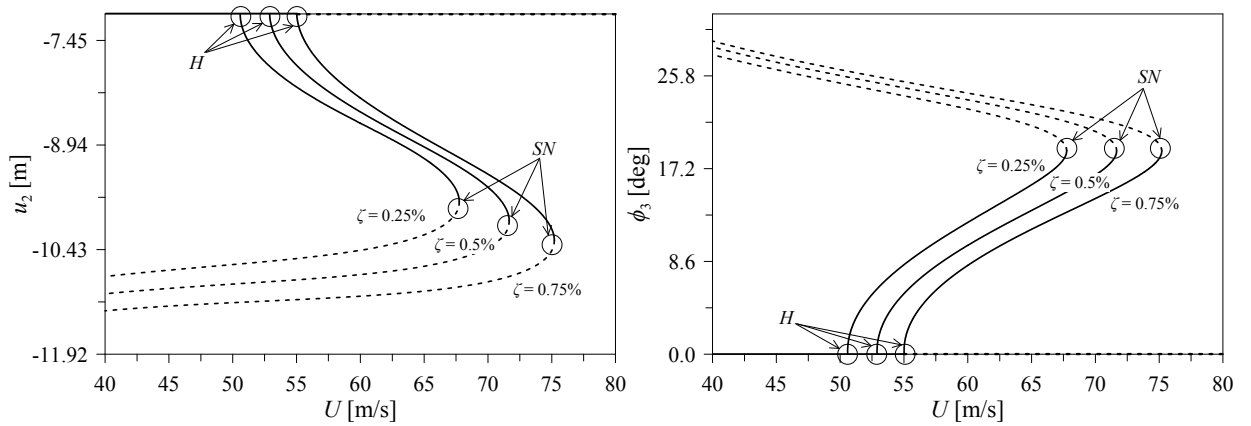

Fig. 6.16: *Bifurcation diagrams for selected values of the damping ratio ζ. Stable branches (solid lines) and unstable branches (dashed lines).*

The continuation results here obtained show a full sensitivity of the flutter and post-flutter behavior with respect to significant parameters such as structural damping and initial angle of attack. The uncertainties inherent in these parameters are such that these types of sensitivity studies should be a necessary part of the aerodynamic stability assessment of a new bridge design.
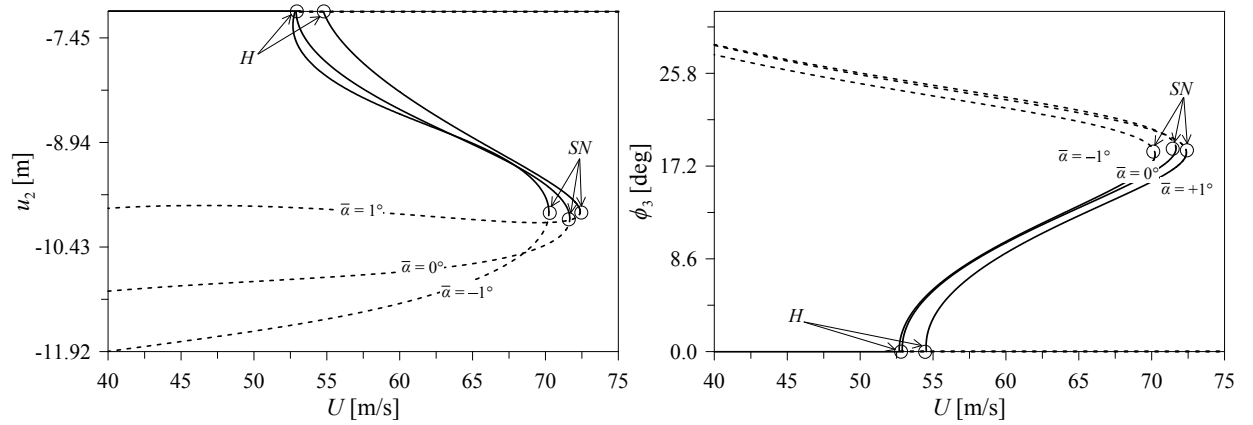
Fig. 6.17: *Bifurcation diagrams for selected values of the angle of attack $\bar{\alpha}$. Stable branches (solid lines) and unstable branches (dashed lines).*

6.4 Nonuniform Wind Distributions

A formulation for the study of the aeroelastic response of suspension bridges to distributed wind gusts is presented in this section. The wind gust loads can be treated as a random (spectral turbulence) or discrete event. For random gusts, typical spectral models include the von Kármán and Dryden turbulence models [82]. While spectral-type gusts are determined by a random process having a wide range of wavelengths, those belonging to t he group of discrete gusts feature a single gust of predetermined magnitude and shape. In the present investigation the bridge response to gusts is calculated based on various gust models, albeit they are all discrete. On the other hand, the procedure presented herewith is general and spectral gust distributions can be adopted in conjunction with the presented aeroelastic model.

The gust loading signature adopted for the analysis is the *1-COSINE* gust distribution in time and with a Gaussian spatial distribution along the bridge span (see Fig. 6.18) represented through the function $\Upsilon_{\mathrm{g}}(x) = \vartheta \exp\left[-\frac{(x-\mu\, l)^2}{2(\sigma\, l)^2}\right]$, where ϑ, μ and σ are the characteristic parameters of the Gaussian-type function and $H(t)$ is the Heaviside function. The study of the response to the gust is conducted in a speed range in which no dynamic aeroelastic instability is encountered, hence the dynamic response of the bridge does not affect its flutter characteristics. As discussed in Section 2.1, the wind gust can be defined as a time-dependent component $\boldsymbol{u}_{\mathrm{g}}(x,t)$ of the wind velocity (see Eq. (2.1.1)). In the plane orthogonal to the bridge span direction $\boldsymbol{e}_3$, the dimensionless gust speed vector $\boldsymbol{u}_{\mathrm{g}}(x,t)$ is defined as

$$\boldsymbol{u}_{\mathrm{g}}(x,t) = u_{\mathrm{g}}(x,t)\boldsymbol{e}_1 + w_{\mathrm{g}}(x,t)\boldsymbol{e}_2 \tag{6.4.1}$$

which can be written in terms of the assumed Gaussian spatial distribution as $\boldsymbol{u}_{\mathrm{g}}(x,t) = \Upsilon_{\mathrm{g}}(x)\widetilde{\boldsymbol{u}}_{\mathrm{g}}(t)$ and the time-dependent part $\widetilde{\boldsymbol{u}}_g$ of the gust function is then expressed by the following 1-COSINE function

$$\widetilde{\boldsymbol{u}}_{\mathrm{g}}(t) = \tfrac{1}{2}\boldsymbol{u}_{\mathrm{g}}^{\mathrm{o}}\left(1 - \cos\frac{\pi t}{t_{\mathrm{g}}}\right)\left(H\left(t\right) - H\left(t - 2t_{\mathrm{g}}\right)\right) \tag{6.4.2}$$

The parameter t_{g} represents the gust traveling time, that is, the time employed by the gust to transit through the deck width B and can be evaluated as $t_{\mathrm{g}} := B/u_{\mathrm{g}}^{\mathrm{o}}$. By defining the maximum intensity u_g^{o} of the horizontal component $u_{\mathrm{g}}(x,t)$ of the gust speed as proportional to the intensity U of the free-stream velocity through the coefficient c_{g}, ($u_{\mathrm{g}}^{\mathrm{o}} := c_{\mathrm{g}}\, U$), and by identifying the direction of $\boldsymbol{u}_{\mathrm{g}}(x,t)$ through the angle of attack α_{g}, the dimensionless peak value $\bar{w}_{\mathrm{g}}^{\mathrm{o}} = w_{\mathrm{g}}^{\mathrm{o}}/(l\,\bar{\omega})$ of the gust speed vertical component $w_{\mathrm{g}}(x,t)$ can be evaluated as

$$\bar{w}_{\mathrm{g}}^{\mathrm{o}} = c_{\mathrm{g}}\,\bar{U}\tan\alpha_{\mathrm{g}}\,. \tag{6.4.3}$$

The unsteady aerodynamic loads for the considered incompressible flow regime are expressed in terms of the indicial function derived from the aerodynamic admittances produced for the GBB deck cross section and already discussed in the previous sections. In addition, in order to evaluate the aeroelastic response to gusts of arbitrary distribution and shape, the concept of another indicial function, commonly referred to as the Küssner function [46] associated with the gust penetration effects, is used. Likewise the Wagner function, also this function is expressed in terms of Bessel's functions. The approximation derived by von Kármán and Sears [47] can be also used effectively. This function expresses the corresponding variation of the lift coefficient induced by a change in the angle of attack due to the penetration in a unit-speed gust [75]. Following [75], the contribution in the aerodynamic lift force due to the effect of a vertical component of the wind gust $w_{\mathrm{g}}(x,t)$ is defined by the function $\breve{L}_{\mathrm{g}}$ and can be expressed as

$$\breve{L}_g(x,t) = \mathcal{F}_{\mathrm{f}}\,\bar{U}\,\frac{\partial C_{\mathrm{L}}}{\partial\alpha^{\mathrm{E}}}\int_0^t \partial_t\Psi(t-\tau)w_{\mathrm{g}}(x,\tau)d\tau \tag{6.4.4}$$
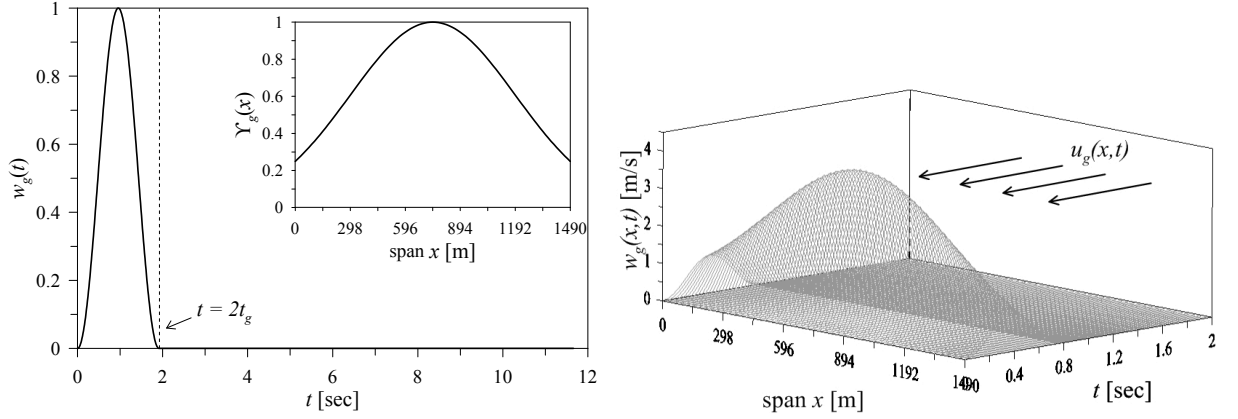
Fig. 6.18: *Normalized 1-COSINE gust time and Gaussian spatial distribution, assuming $\vartheta = 1$ $\sigma = 0.3$, $\mu = 0.5$, $\alpha_{\mathrm{g}} = 2.5°$, $c_{\mathrm{g}} = 1.25$.*
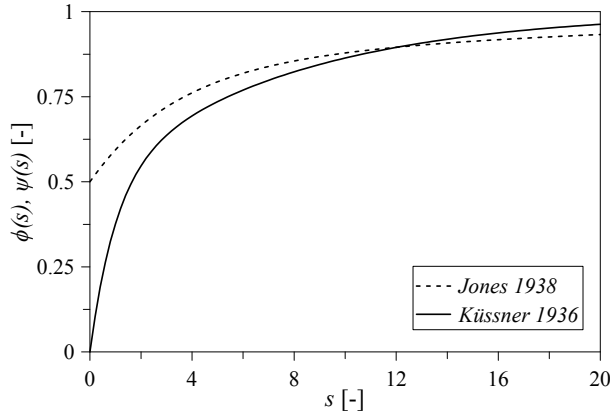

Fig. 6.19: *Küssner function and Wagner function approximation given by Jones [59].*

where $\mathcal{F}_{\mathrm{f}} = \frac{1}{2}\rho\,B\,l/\rho A^{\mathrm{d}}$, $\delta = B/l$ and $\partial C_{\mathrm{L}}/\partial\alpha^{\mathrm{E}}$ is the static lift curve slope coefficient [rad^{-1}] whose expression, derived from (5.2.10), is

$$\frac{\partial C_{\mathrm{L}}}{\partial\alpha^{\mathrm{E}}} = 6.357 - 5.179\,\alpha^{\mathrm{E}} - 328.172\,\alpha^{\mathrm{E}2} - 10.703\,\alpha^{\mathrm{E}3} + 3930.898\,\alpha^{\mathrm{E}4} \tag{6.4.5}$$

evaluated at $\alpha^{\mathrm{E}}(x) = \bar{\alpha} + \phi_3^{\mathrm{o}}(x)$. In Eq. (6.4.4), $\Psi(t) = 1 - \sum_{k=1}^{2} A_k e^{-\hat{B}_k t}$ is the Küssner function where $\hat{B}_k = 2(\bar{U}/\delta)B_k$ and $A_1 = 0.5$, $A_2 = 0.5$, $B_1 = 0.13$, $B_2 = 1$. Since the gust load $\breve{L}_{\mathrm{g}}(x,t)$ is of circulatory nature, in the case of incompressible flow, it acts on the quarter chord point of the deck section and the moment generated with respect to the elastic center can be written in nondimensional form as:

$$\breve{M}_{\mathrm{g}}(x,t) = \frac{\delta}{4}\,\breve{L}_{\mathrm{g}}(x,t)\,. \tag{6.4.6}$$

The contribution of the unsteady aerodynamic loads (6.4.4) and (6.4.6) related to the gust effect is then introduced in the bridge aeroelastic governing equations (5.2.13) by the vectors $\breve{\boldsymbol{f}}_{\mathrm{AE}} = -\breve{D}(x,t)\bar{\boldsymbol{e}}_1 + \left(\breve{L}(x,t) + \breve{L}_g(x,t)\right)\bar{\boldsymbol{e}}_2$ and $\breve{\boldsymbol{c}}_{\mathrm{AE}} = \left(\breve{M}(x,t) + \breve{M}_g(x,t)\right)\bar{\boldsymbol{e}}_3$.

To overcome the calculation of the convolution integral by which the gust load is expressed, according to the formulation described in Section 2.3.2, the added aerodynamic state $G_k(t)$ is introduced and (6.4.4)

can be written as

$$\breve{L}_g(x,t) = \mathcal{F}_\mathrm{f}\,\bar{U}\,\frac{\partial C_\mathrm{L}}{\partial \alpha^\mathrm{E}}\,\Upsilon_\mathrm{g}(x)\sum_{k=1}^{2} A_k \hat{B}_k\,G_k(t)\,. \tag{6.4.7}$$

The system of ODEs governing the evolution in time of the added aerodynamic states $G_k(t)$ is given by

$$\begin{aligned} \partial_t G_1(t) &= \widetilde{w}_\mathrm{g}(t) - \hat{B}_1 G_1(t)\,, \\ \partial_t G_2(t) &= \widetilde{w}_\mathrm{g}(t) - \hat{B}_2 G_2(t)\,. \end{aligned} \tag{6.4.8}$$

which, unlike the case of the self-excited aerodynamic loads (see Eqs. (5.2.15)) are not coupled with the aeroelastic governing equations (5.2.13).

6.4.1 Numerical Results

Parametric studies are carried out to investigate the aeroelastic behavior of a typical long-span bridge to a traveling *1-COSINE* gust load. The numerical investigation shows also the capability of the parametric model to enable sensitivity analyses suitable for structural optimizations. The elastogeometric properties of the deck-girder of the Runyang bridge reported in the [14] are summarized in Section 4.2.

6.4.1.1 Energy Equivalence of the Wind Speed Spatial Distributions

The wind spatial distribution effects the critical flutter speed are studied next. Consistently with the assumption made for the gust modeling, a Gaussian distribution $\Upsilon(x) = \vartheta\exp\left[-\frac{(x-\mu\,l)^2}{2(\sigma\,l)^2}\right]$ of the wind speed is considered. By assuming $U_\mathrm{G}(x) = \bar{U}\,\Upsilon(x)$, the wind profiles are defined so as to have the same energy content as the uniform distribution. Therefore, to perform parametric analyses by varying μ and σ in the Gaussian function, the amplitude ϑ is calculated according to the condition

$$\int_0^l \Upsilon(x)^2\,dx = 1 \tag{6.4.9}$$

where the two sides of equation (6.4.9) represent the normalized kinetic energy of the Gaussian and the uniform wind distribution, respectively.

6.4.1.2 Flutter Assuming Uniform and Nonuniform Wind Speed

Time-dependent simulations were then performed by assuming the Gaussian distribution of the wind field across the bridge span. Two main velocity profiles were investigated, a symmetric shape centered about the bridge mid-span, that is $\mu = 0.5$, and a nonsymmetric shape with maximum speed value at the quarter-span, $\mu = 0.25$. From these two spatial distributions, the critical flutter speed U^cr was evaluated by varying the parameter σ that regulates the amplitude of the Gaussian bell-shape. In particular, for each set of parameters (μ,σ) adopted, the amplitude ϑ was evaluated accordingly to the energy equivalence relationship (6.4.9). In Fig. 6.20, the ratio between the flutter speed of the nonuniform and uniform wind $U^\mathrm{cr}/U^\mathrm{cr}_{uni}$ is reported for increasing values of σ and the spatial distributions at selected values of σ are included in the insets.

Flutter resulted from a coupled flexural-torsional skew-symmetric mode, thus, as shown in Fig. 6.20, the way the energy is transferred to the structural system can lead to an increase of about 10% with
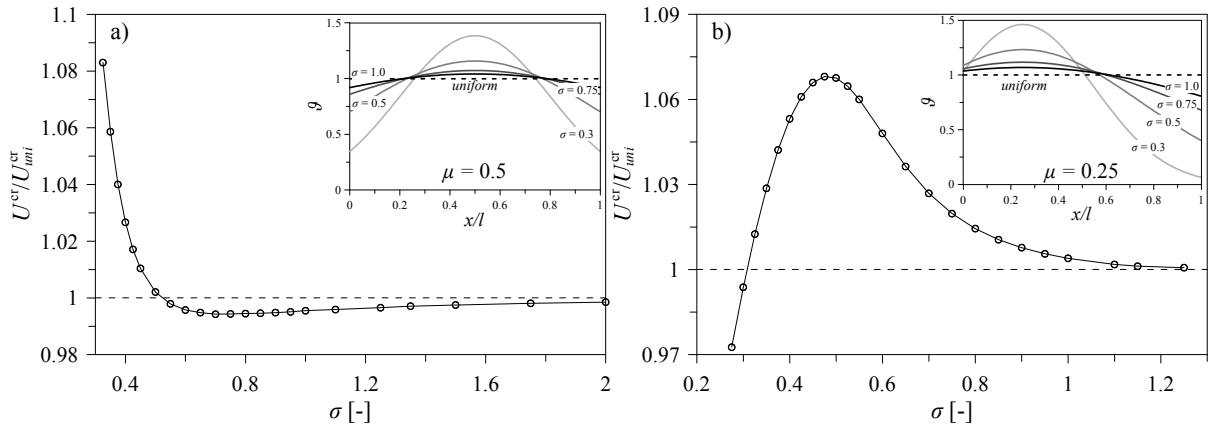
Fig. 6.20: *Flutter speed versus the parameter σ of the Gaussian function for a symmetric ($\mu = 0.5$) and non symmetric ($\mu = 0.25$) wind spatial distribution.*

respect to the case when the bridge is under uniform flow conditions. The analyses were performed considering the same amount of energy, and while for a restricted range of wind distribution conservative results are obtained by using a uniform flow spatial distribution, the analysis shows that there is a wide range of σ for which non-conservative predictions are expected. Indeed, it is shown that aerodynamic loads having a peak where the flutter (skew-symmetric) mode has its crest, can be less conservative than the uniform case. One can see that, a symmetric spatial distribution of the aerodynamic loads implies a higher critical flutter speed, which occurs when the energy is transferred to the structure from a Gaussian load concentrated at the mid-span (low values of σ), and slightly lower critical speed ($< 1\%$) for a more uniform distribution, $\sigma > 0.45$.

6.4.1.3 Aeroelastic Response to a Nonuniform Gust

Further analyses were carried out to study the behavior of the bridge to an incoming vertical gust. The response in the transient part of the time histories of the motion induced in the bridge was analyzed. In order to focus the study only on the effects of the spatial distribution of the load induced by the gust, the free-stream speed U is assumed uniformly distributed across the bridge span. U is adopted as unique reference speed in the analyses since the vertical component w_g of the gust speed is directly dependent on it (i.e., $\bar{w}_g^o = c_g \bar{U} \tan \alpha_g$). A gust angle of attack $\alpha_g = 2.5°$ is assumed in the calculations and a 25% increase of the free-stream speed U is considered for the evaluation of the gust speed intensity, $c_g = 1.25$.

Also in this case, a Gaussian function is chosen to describe the spatial distribution of the gust loads; in particular, according to the criterion expressed in (6.4.9), the same content in energy of the uniform counterpart is assumed.

The incremental vertical displacement u_2 and torsional rotation ϕ_3 induced by the gust load at the deck mid-span are shown in Fig. 6.21 for a wide range of wind speeds. The figures represent the maximum amplitudes of the kinematic variables during the transient response assuming symmetric Gaussian ($\mu = 0.5$) and nonsymmetric Gaussian ($\mu = 0.25$) gusts compared with the response to a uniform gust. As expected, at the mid-span, the major differences (indicated in the figure insets with $\Delta[\%]$) occur for the symmetric case, 40-50\% for ϕ_3 and higher than 100\% for the vertical displacement u_2. Such a behavior strongly depends on the speed regime as shown in the insets of Fig. 6.21. From results not displayed here, similar behavior occurs for the response at the quarter-span to a nonsymmetric gust load.
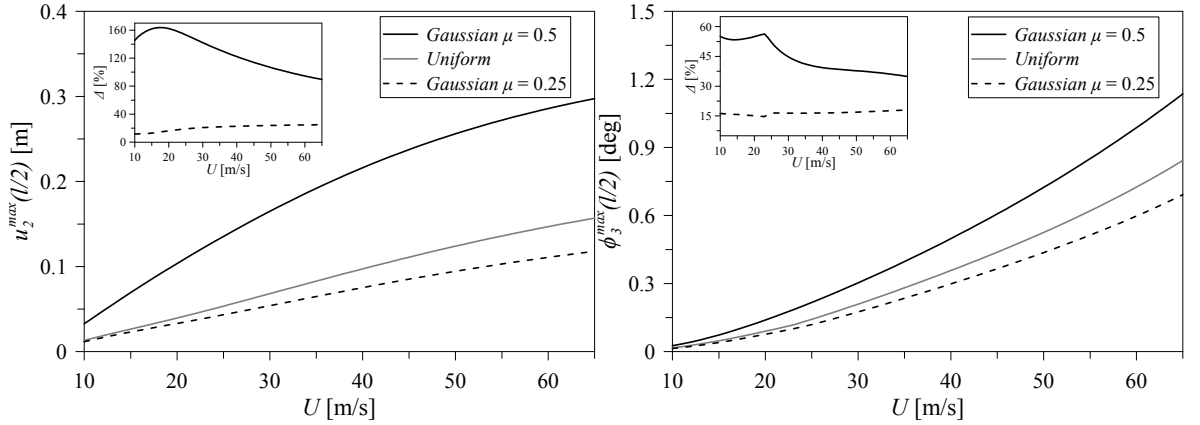
Fig. 6.21: *Maximum vertical displacement and torsional rotation at the deck mid-span for increasing free-stream wind speed U, σ = 0.2.*
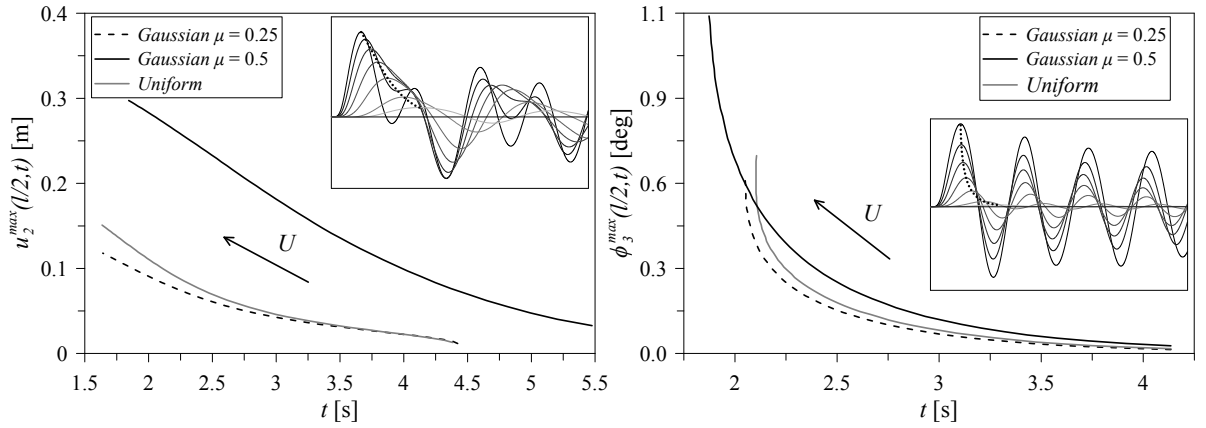

Fig. 6.22: *Maximum vertical displacement and torsional rotation at the deck mid-span versus time for increasing wind speeds U, σ = 0.2*

The evolution in time of the maximum response shown in Fig. 6.21 is reported in Fig. 6.22. The observed anticipation of the peak at the increase of the wind speed is related to the definition itself of the gust traveling time t_{g} that governs the dynamics of the induced aerodynamic loads, inversely proportional to U, $t_{\mathrm{g}} = B/\left(c_{\mathrm{g}}U\right)$.

Figure 6.23 shows the position of the amplitude of ϕ_3^{max} along the bridge nondimensional span sweeping the parameter μ at a selected wind speed and value of σ. The analysis shows the capability of the proposed parametric aeroelastic model to investigate the maximum effect of the gust while varying its peak position across the bridge span and allows to predict where the maximum response is attained.

In Fig. 6.24 the increment of the maximum torsional rotation ϕ_3 with respect to the value attained for a uniform gust ϕ_3^{uni} is evaluated for several values of σ, parameter that regulates the width of the bell-shape Gaussian distribution. The results refer to the bridge mid-span for a gust with $\mu = 0.5$ and to the quarter-span for $\mu = 0.25$, more precisely, where the maximum effect of the gust speed distribution is expected. The curves depend nonlinearly on σ, showing a peak at $\sigma \approx 0.15$ and a convergence to the response for the uniform case for $\sigma > 1$. The maximum amplitudes ϑ of the Gaussian energy-equivalent distributions for the assumed σ are depicted in the insets.

The effect of the gust traveling time in the transient response of the bridge is also studied. The amount of energy contained in the gust is kept constant by uncorrelating the wind speed and t_{g}. This implies
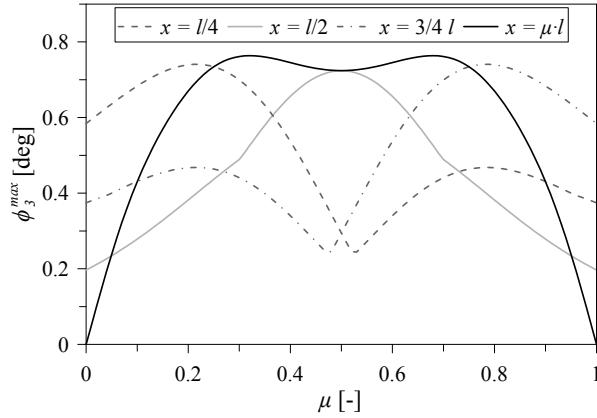
Fig. 6.23: *Torsional rotation at mid-span (solid grey), quarter-span (dashed) and at three-quarters of the span (dash-dotted) versus the dimensionless position μ of the gust peak, $U = 50$ m/s and $\sigma = 0.2$. The solid black line shows the value at $x = \mu l$.*
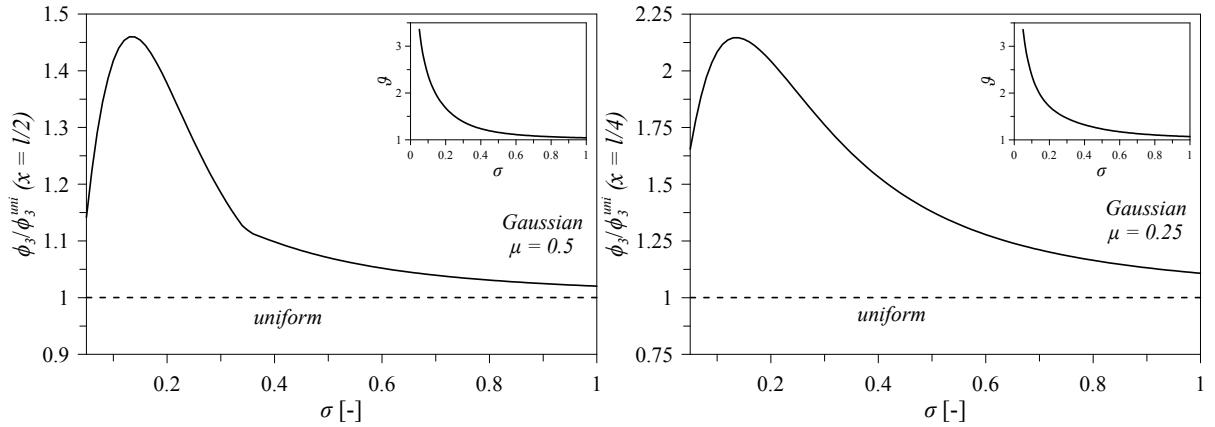

Fig. 6.24: Torsional rotation at mid-span and quarter-span versus the width σ of the gust spatial distribution: symmetric, $\mu = 0.5$, and nonsymmetric, $\mu = 0.25$. Dashed line indicates the value assuming a uniform gust; $U = 50$ m/s

that a reduction of traveling time corresponds to a higher power content of the gust. For a fixed value of the free-stream speed U, the variation of the maximum amplitude of the kinematic reference parameters is investigated when increasing the value of t_g. Figure 6.25 shows that the maximum deformation occurs for a particular selected value of t_g, representing the time that the gust takes to transit through the bridge deck. While the energy content is the same in all cases, for different Gaussian distributions, the time t_g affects the way the flow transfers its energy to the structure. The maximum deformation occurs when the energy is transferred quite rapidly, however, lower deformation occurs if the gust transition on the bridge is either too fast or too slow, as indicated in Fig. 6.26. Figure 6.25 also illustrates that a symmetric Gaussian distribution is capable of exciting the bridge structural modes more effectively than an asymmetric or a uniform gust. Indeed, in this case an overall higher deformation in the vertical and torsional degrees of freedom is obtained.
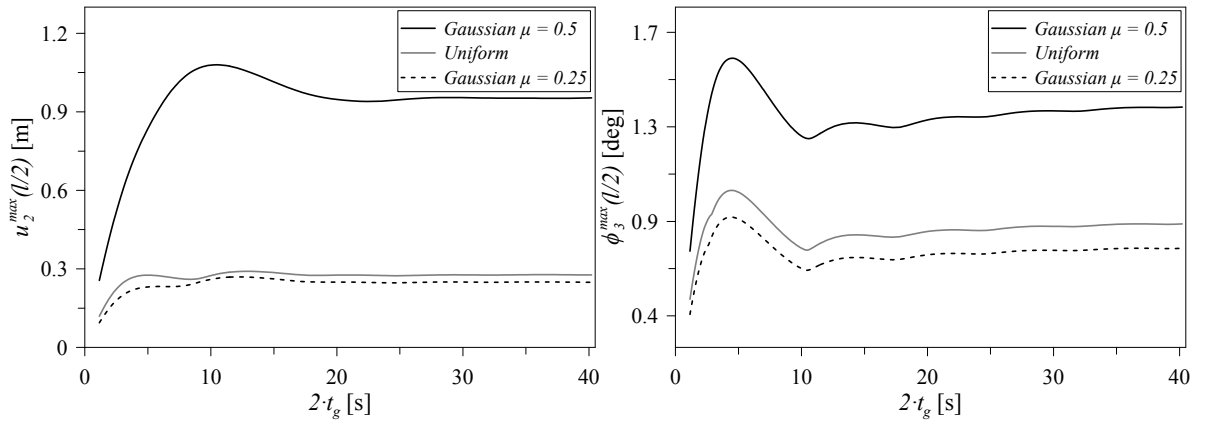
Fig. 6.25: *Maximum vertical displacement and torsional rotation at the deck mid-span varying the gust traveling time t_g for $U = 50$ m/s when $\sigma = 0.2$ for the nonuniform gust spatial distributions.*
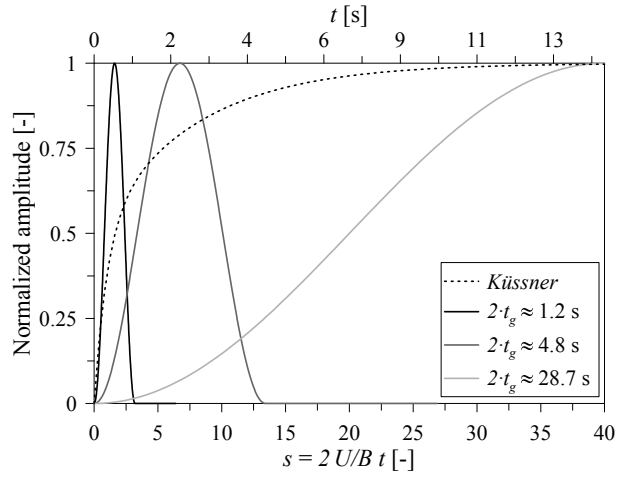

Fig. 6.26: *1-COSINE gust time distributions assuming different t_g (solid lines) and Küssner function (dashed line)*

Chapter 7
Conclusions

The proposed work is devoted to the development of advanced analytical and numerical tools enabling investigations into the nonlinear static and dynamic aeroelastic response of suspension bridges. Two disciplines are integrated within this interdisciplinary work. Computational fluid-dynamic-based evaluations of viscous aerodynamic loads around bluff-bodies are coupled with a geometrically exact nonlinear structural model of long-span suspension bridges so as to construct fluid-structure interaction reduced-order models.

The nonlinear aerodynamic characteristics of the boxed sharp-edge cross section of the Danish Great Belt Bridge were investigated by using two state-of-the-art computational tools. FLUENT® by ANSYS, a CFD tool enabling to determine the approximate solution of the unsteady RANS equations accounting for turbulence effects by the k-ϵ method, and the discrete-vortex method employed in DVMFLOW®, a Navier-Stokes solver specifically developed for external flows past two-dimensional bodies of arbitrary shape. The grid-free nature of the computational method employed by DVMFLOW® enables computationally efficient simulations around stationary and moving bodies. DVMFLOW® was then selected as the primary candidate to evaluate the nonlinear indicial functions needed to perform dynamic aeroelastic investigations of the bridges within a reduced-order framework.

Frequency-domain representation of the aerodynamic loads in terms of flutter derivatives were computed for selected values of the initial angle of attack. Consequently, indicial functions were derived for these angles and incorporated into the proposed ROM model. The two formulations, in the frequency and time domains, inherently consider viscous effects including flow separation and boundary layer thickening, whose contribution to the dynamic behavior of the bridges can be remarkable.

A geometrically exact parametric model of suspension bridges was formulated and the nonlinear equations of motion were obtained via a Lagrangian formulation. The nonlinear system of partial differential equations governing the equilibrium and dynamic aeroelastic response of suspension bridges was solved via a FE discretization considering the structural and aerodynamic characteristics of two case-study bridges, the Runyang and the Hu Men suspension bridges. An initial modal analysis was carried out to compare the natural frequencies evaluated by the proposed model with literature results. A good agreement was found for both case studies. Parametric analyses were performed to highlight the influence of the cable geometric stiffness in the nonlinear equilibrium and dynamic response of the bridge. The characteristic mechanical asymmetry is exhibited as a softening or a hardening behavior depending on whether the loads are upward or downward. This is due to loss of tension or to increase of tension in the suspension cables. This nonlinear mechanical feature due to the suspension cables turns out to affect significantly the aeroelastic limit states.

The developed reduced-order models of the nonlinear aerodynamic loads for the GBB section, both in the frequency and time domains, were integrated in the fully nonlinear parametric structural model. Static (divergence) and dynamic (Hopf) bifurcation analyses were carried out to investigate the occurrence of

torsional divergence and flutter. The eigenvalue problem, obtained by linearization about the prestressed configuration, induced by dead and aeroelastic loads, was solved. The determined bifurcation diagrams showed the high sensitivity of the bridge flexural-torsional frequency in the neighborhood of the critical condition. These studies have also shown the sensitivity of the critical condition with respect to the stiffness bridge properties (namely, the elastic torsional and bending stiffness, the elastogeometric stiffness of the suspension cables) and the initial wind angle of attack. The complete parametric model here developed has demonstrated high flexibility, since it can be used to perform sensitivity analyses for inherently nonlinear nonconservative problems.

The development of the frequency- and time-domain representations of the aerodynamic loads enables the solution of the coupled fluid-flow and structural problems, and the characterization of the static and dynamic behavior of the selected bridges. The formulation proposed in this Dissertation has a general value. For example, steady, quasi-steady and unsteady aerodynamic models can be integrated within the same approach. In addition time- and space-dependent loading due to disturbances, such as gust loads, are accounted for. This is straightforward using a similar framework adopted to implement the unsteady aerodynamic loads through the indicial formulation.

Finally, the proposed mixed PDE-ODE aeroelastic governing equations are expressed in a form that is amenable to further nonlinear dynamic investigations. The model was used to construct bifurcation diagrams, Hopf and fold bifurcations were found for the long-span bridges under investigation. The Hopf bifurcations were found to be supercritical and the branches of limit cycles characterizing the post-flutter response terminate at fold bifurcations where the loss of local attractors occurs.

To the best of the author's knowledge the currently available instruments used in the design phases of these structures are relatively simplified and ignore the complexities inherently present in suspension bridges and their dynamic interactions with self-excited forces. Neglecting the nonlinear characteristics, either of the structural or aerodynamic nature, can lead to erroneous solutions. When predictions are not conservatives, catastrophic failures might occur with significant losses.

The following points offer the major highlights of this research.

- The aerodynamics of typical deck cross sections have been fully described through CFD simulations by the use of a mesh-free discrete-vortex method implemented in the software DVMFLOW. The viscous effects and the flow separation characterizing such a sharped-edge boxed sections have been captured and included in the time- and frequency-domain description of the aeroelastic loads.
- The static curves of the aerodynamic coefficients have been evaluated for a wide range of angles of attack where the nonlinear effects turned out to be indeed relevant. The dynamic aeroelastic loads have been described in the frequency domain through the use of the flutter derivatives evaluated in the present work at several angles of attack. The unsteady aerodynamic loads have been then derived in the time domain through an indicial approach by determining the indicial functions obtained from the aeroelastic derivatives.
- A fully nonlinear parametric model of suspension bridges has been derived and first validated by preliminary analyses characterizing the static and modal characteristics of two existing bridges. *Torsional divergence* and *flutter* phenomena have been investigated through the proposed model assuming the aerodynamic characteristics available in the literature for these bridges and showing the capability of the model to carry out sensitivity analyses to investigate the influence of the structural and aerodynamic parameters on the critical condition.
- The nonlinear aerodynamics derived in the present work for the considered bridge deck cross section have been coupled with the structural model and critical and post-critical responses have been determined. Post-critical LCOs have been investigated accounting for both nonlinear quasi-steady and nonlinear unsteady aerodynamics and the differences highlighted.
- Nonuniform spatial wind distributions have been modeled and the effects of the flow nonuniformity on the critical flutter condition have been highlighted. Time and spatial nonuniform gusts have been studied and the transient part of the dynamic response to the loads induced by them has been investigated through parametric analyses.
- Path following of the LCOs has been carried out by determining the stable supercritical bifurcation branches for the fully nonlinear model whereas both stable and unstable branches have been explored in the context of a reduced-order model of suspension bridges through the use of an *ad hoc* continuation code.

Major findings of this research are also summarized.

- The aerodynamics of suspension bridges deck sections are to be described in a wide range of wind angles of attack in order to capture the characteristic nonlinearities arising from flow separation in the post-stall flow regime. The nonlinear dependence of the aerodynamic loads from the mean angle of attack has been demonstrated to be of fourth- and fifth-order for the drag and the lift and aerodynamic moment, respectively.

- The static and dynamic response of suspension bridges are strongly affected by the geometric nonlinearities induced by the cables stiffness contribution, showing hardening or softening behaviors depending on the direction of the loads. A fully nonlinear modeling is required for the correct description of the aeroelastic response of these structures and, consequently, for the evaluation of the aerostatic and aerodynamic stability limit states.

- The complete aeroelastic model obtained by coupling the structural and aerodynamic models in the form of the nonlinear partial-differential equations and the added states ordinary-differential equations. These equations, cast in nondimensional form and in first-order formulation in terms of time derivatives, are implemented in the computational platform COMSOL [56] using the PDE-mode feature and the space-time integration is numerically performed by using the finite element method.

- The structural and aerodynamic main parameters, such as the damping ratio, stiffness ratios, pre-stressed configurations (given by gravitational or aeroelastic loads), and mean wind angle of attack, may influence the critical condition and the proposed parametric model, allowing for sensitivity non-linear analyses, straightforward tool for the investigation of these phenomena.

- The aerodynamic nonlinearities govern the post-flutter aeroelastic response, thus the only way to investigate the post-critical dynamics of the bridge is through a nonlinear aerodynamic modeling of the aeroelastic loads represented in the time domain. The present work proposed both a quasi-steady and an unsteady nonlinear aerodynamic formulation for suspension bridges and highlighted the importance and main differences using the two formulations.

  - The structural geometric nonlinearities influence the aeroelastic stability of suspension bridges and flutter might occur at lower values of the free-stream speed when compared with the case assuming a linearized structural model. This reduction amounts to about 10%.
  - A quasi-steady nonlinear aerodynamic formulation can predict LCOs in the post-flutter regime. Such a formulation also leads to further reduction of the critical wind speed of about 15% with respect to the flutter speed calculated in the context of linear aerodynamics.
  - Unsteady nonlinear aerodynamic modeling is less conservative than the quasi-steady formulation entailing slightly higher critical speeds (about 10% more than the QS nonlinear model) and smaller LCO amplitudes.

- The modeled nonuniform spatial wind distributions have proved effects of the flow nonuniformity on the critical flutter condition. Simulations with uniform and nonuniform flow spatial distributions with equivalent energy showed that one should cautiously consider a uniform flow distribution when examining the flutter behavior of these large structures since there is a large range of nonuniform distributions leading to lower flutter speed predictions. Thus the practitioner should investigate the flutter boundary for free-stream velocities that are impacting the bridge span nonuniformly.

- The behavior of the bridge to a traveling vertical gust with time and spatial nonuniform distributions has been also investigated with the objective of evaluating the maximum structural deformations occurring during the dynamic transient responses. Also in this case the analysis revealed that asymmetric loading can induce vertical and torsional deformations significantly different that those associated with uniform gust loading. As such, the bridge can reach earlier its ultimate limit states under transient loading with catastrophic consequences. It is imperative to add considerations of nonuniformity of

the flow and gust during the aeroelastic design of long-span structures, particularly in the design of suspension bridges.

- Path following of the LCOs has been instrumental for determining the stable supercritical bifurcation branch for the fully nonlinear model whereas both stable and unstable branches have been explored in the context of a reduced-order model of suspension bridges through the use of an *ad hoc* continuation code; the role of uncertain parameters such as the structural damping ratio and the initial wind angle of attack have been studied.

Acknowledgements

References

1. H. M. Irvine, *Cable structures*, Cambridge, Mass: MIT Press, 1981.
2. A. M. Abdel-Ghaffar, "Free lateral vibrations of suspension bridges," *Journal of the Structural Division of ASCE*, vol. 104, no. 3, pp. 503 − 525, 1978.
3. A. M. Abdel-Ghaffar, "Free torsional vibrations of suspension bridges," *Journal of the Structural Division of ASCE*, vol. 105, no. 4, pp. 767 − 788, 1979.
4. A. M. Abdel-Ghaffar, "Vertical vibration analysis of suspension bridges," *Journal of the Structural Division of ASCE*, vol. 106, no. 10, pp. 2053 − 2075, 1980.
5. A. M. Abdel-Ghaffar, "Suspension bridge vibration: Continuum formulation," *Journal of the Engineering Mechanics Division of ASCE*, vol. 108, no. 6, pp. 1215 − 1232, 1982.
6. A. M. Abdel-Ghaffar and L. I. Rubin, "Nonlinear free vibrations of suspension bridges: theory," *Journal of the Engineering Mechanics Division of ASCE*, vol. 109, pp. 313 − 329, 1983.
7. A. M. Abdel-Ghaffar and L. I. Rubin, "Nonlinear free vibrations of suspension bridges: application," *Journal of the Engineering Mechanics Division of ASCE*, vol. 109, pp. 330 − 345, 1983.
8. M. Abdel-Rohman and A. H. Nayfeh, "Passive control of nonlinear oscillations in bridges," *Journal of the Engineering Mechanics Division of ASCE*, vol. 113, pp. 1694 − 1708, 1987.
9. M. Abdel-Rohman and A. H. Nayfeh, "Active control of nonlinear oscillations in bridges," *Journal of the Engineering Mechanics Division of ASCE*, vol. 113, pp. 335 − 349, 1987.
10. M. Çevika and M. Pakdemirlib, "Non-linear vibrations of suspension bridges with external excitation," *International Journal of Non-Linear Mechanics*, vol. 40, pp. 901 − 923, 2005.
11. J. Malík, "Nonlinear models of suspension bridges," *J. Math. Anal. Appl.*, vol. 321, pp. 828 − 850, 2006.
12. J. Malík, "Generalized nonlinear models of suspension bridges," *J. Math. Anal. Appl.*, vol. 324, pp. 1288 − 1296, 2006.
13. V. Boonyapinyo, H. Yamada, and T. Miyata, "Wind-induced nonlinear lateraltorsional buckling of cable-stayed bridges," *Journal of structural engineering-ASCE*, vol. 120, no. 2, pp. 486 − 506, 1994.
14. X. Zhang, H. Xiang, and B. Sun, "Nonlinear aerostatic and aerodynamic analysis of long-span suspension bridges considering wind-structure interactions," *Journal of Wind Engineering and Industrial Aerodynamics*, vol. 90, pp. 1065 − 1080, 2002.
15. J. Cheng, J. Jiang, and R. Xiao, "Aerostatic stability analysis of suspension bridges under parametric uncertainty," *Engineering Structures*, vol. 25, pp. 1675 − 1684, 2003.
16. J. Cheng, J. Jiang, R. Xiao, and H. Xiang, "Series method for analyzing 3d nonlinear torsional divergence of suspension bridges," *Computers and Structures*, vol. 81, pp. 299 − 308, 2003.
17. V. Boonyapinyo, Y. Lauhatanon, and P. Lukkunaprasit, "Nonlinear aerostatic stability analysis of suspension bridges," *Engineering Structures*, vol. 28, pp. 793 − 803, 2006.
18. J. Cheng and R. Xiao, "A simplified method for lateral response analysis of suspension bridges under wind loads," *Communications in Numerical Methods in Engineering*, vol. 22, pp. 861 − 874, 2006.
19. W. Lacarbonara and A. Arena, "Aerostatic torsional divergence of suspension bridges via a fully nonlinear continuum formulation," in *10*th *National Congress of Wind Engineering IN-VENTO 2008, Cefalù (Italy), Jun. 8–11, 2008*, 2008.
20. W. Lacarbonara and A. Arena, "3-dimensional model of suspension bridges via a fully nonlinear continuum formulation," in *GIMC 2008, XVII Convegno Italiano di Meccanica Computazionale, Alghero, Sept. 10–12, 2008*, 2008.
21. T. Theodorsen, "General theory of aerodynamic instability and the mechanism of flutter," Tech. Rep. 496, NACA, 1935.
22. L. Salvatori and C. Borri, "Frequency- and time-domain methods for the numerical modeling of full-bridge aeroelasticity," *Computers and Structures*, vol. 85, pp. 675 − 687, 2007.

23. L. Salvatori and P. Spinelli, "Effects of structural nonlinearity and along-span wind coherence on suspension bridge aerodynamics: Some numerical simulation results," *Journal of Wind Engineering and Industrial Aerodynamics*, vol. 94, pp. 415 – 430, 2006.

24. R. H. Scanlan and J. J. Tomko, "Airfoil and bridge deck flutter derivates," *Journal of the Engineering Mechanics Division of ASCE*, vol. 97, pp. 1717 – 1737, 1971.

25. E. Simiu and R. H. Scanlan, *Wind effects on structures-Fundamentals and Applications to Design, Third Edition*, Wiley-Interscience Publication, 1996.

26. R. H. Scanlan, "Reexamination of sectional aerodynamic force functions for bridges," *Journal of Wind Engineering and Industrial Aerodynamics*, vol. 89, pp. 1257 – 1266, 2001.

27. T. J. A. Agar, "Aerodynamic flutter analysis of suspension bridges by a modal technique," *Engineering Structures*, vol. 11, no. 2, pp. 75 – 82, 1989.

28. A. H. Namini, "Analytical modeling of flutter derivatives as finite elements," *Computers and Structures*, vol. 41, no. 5, pp. 1055 – 1064, 1991.

29. A. H. Namini, "Finite element-based flutter analysis of cable-suspended bridge," *Journal of Structural Engineering-ASCE*, vol. 118, no. 6, pp. 1509 – 1526, 1992.

30. X. G. Hua and Z. Q. Chen, "Full-order and multimode flutter analysis using ansys," *Finite Elements in Analysis and Design*, vol. 44, pp. 537 – 551, 2008.

31. S. S. Mishra, K. Kumar, and P. Krishna, "Multimode flutter of long-span cable-stayed bridge based on 18 experimental aeroelastic derivatives," *Journal of Wind Engineering and Industrial Aerodynamics*, vol. 96, pp. 83 – 102, 2008.

32. S. Preidikman and D. T. Mook, "Numerical simulation of flutter of suspension bridges," *Applied Mechanics Reviews*, vol. 50, pp. 174 – 179, 1997.

33. W. Lacarbonara and A. Arena, "Flutter of an arch bridge via a fully nonlinear continuum formulation," *Journal of Aerospace Engineering*, vol. 24, no. 1, pp. 112 – 123, 2011.

34. A. Arena and W. Lacarbonara, "Static and aeroelastic limit states of ponte della musica via a fully nonlinear continuum model," in *19mo Congresso dell'Associazione Italiana di Meccanica Teorica e Applicata, Ancona, Sept. 14–17, 2009*, 2009.

35. S. R. Chen and C. S. Cai, "Evolution of long-span bridge response to wind-numerical simulation and discussion," *Computers and Structures*, vol. 81, pp. 2055 – 2066, 2003.

36. X. Zhang and B. Sun, "Parametric study on the aerodynamic stability of a long-span suspension bridge," *Journal of Wind Engineering and Industrial Aerodynamics*, vol. 92, pp. 431 – 439, 2004.

37. X. Zhang, "Influence of some factors on the aerodynamic behavior of long-span suspension bridges," *Journal of Wind Engineering and Industrial Aerodynamics*, vol. 95, pp. 149 – 164, 2007.

38. M. S. Pfeil and R. C. Batista, "Aerodynamic stability analysis of cable-stayed bridges," *Journal of Structural Engineering-ASCE*, vol. 121, pp. 1748 – 1788, 1995.

39. Q. Ding, A. Chen, and H. Xiang, "Coupled flutter analysis of long-span bridges by multimode and full-order approaches," *Journal of Wind Engineering and Industrial Aerodynamics*, vol. 90, pp. 1981 – 1993, 2002.

40. Y. K. Cheung, "The finite strip method in the analysis of elastic plates with two opposite simply supported ends," in *Instn. Civ. Engrg. London*, 1968.

41. D. T. Lau, M. S. Cheung, and S. H. Cheng, "3d flutter analysis of bridges by spline finite-strip method," *Journal of Structural Engineering-ASCE*, vol. 126, pp. 1246 – 1254, 2000.

42. D. Karmakar, S. Ray-Chaudhuri, and M. Shinozuka, "Conditional simulation of non-gaussian wind velocity profiles: Application to buffeting response of vincent thomas suspension bridge," *Probabilistic Engineering Mechanics*, vol. 29, pp. 167–175, July 2012.

43. L. Singh, N. P. Jones, R. H. Scanlan, and O. Lorendeaux, "Identification of lateral flutter derivatives of bridge decks," *Journal of Wind Engineering and Industrial Aerodynamics*, vol. 60, pp. 81 – 89, 1996.

44. P. P. Sarkar, L. Caracoglia, F. K. Jr Haan, H. Sato, and J. Murakoshid, "Comparative and sensitivity study of flutter derivatives of selected bridge deck sections, part 1: Analysis of inter-laboratory experimental data," *Engineering Structures*, vol. 31, pp. 158 – 169, 2009.

45. H. Wagner, "Über die entstehung des dynamischen auftriebes von tragflügeln," *Z.f.a.M.M.*, vol. 5, pp. 17–35, 1925.

46. H. G. Küssner, "Zusammenfassender bericht über den instationaren auftrieb von flügeln," *Luftfahrtforschung*, vol. 12, pp. 410–424, 1936.

47. Th. von Kármán and W. R. Sears, "Airfoil theory for non-uniform motion," *Journal of the Aeronautical Sciences*, vol. 5 (10), pp. 379–390, 1938.

48. I. E. Garrick, "On some reciprocal relations in the theory of nonstationary flows," Tech. Rep. 629, National Advisory Committee for Aeronautics, 1938.

49. I. E. Garrick, "On some fourier transforms in the theory of non-stationary flows," in *Proceedings of the Fifth International Congress for Applied Mechanics*, New York, 1939, pp. 590–593.

50. A. Larsen, "Aerodynamic aspects of the final design of the 1624-m suspension bridge across the great belt," *Journal of Wind Engineering and Industrial Aerodynamics*, vol. 48, pp. 261–285, 1993.

51. J. H. Walther, *DVM for 2-D Flow Past Bodies of Arbitrary Shape Undergoing Prescribed Rotary and Translational Motion*, Ph.D. thesis, Techincal University of Denmark, 1994.

52. A. Larsen and J. H. Walther, "Aeroelastic analysis of bridge girder sections based on discrete vortex simulations," *Journal of Wind Engineering and Industrial Aerodynamics*, pp. 253 – 265, 1997.

53. J. B. Frandsen, "Numerical bridge deck studies using finite elements. part i: flutter," *Journal of Fluids and Structures*, vol. 19, no. 2, pp. 171 – 191, 2004.

54. A. L. Braun and A. M. Awruch, "Numerical simulation of the wind action on a long-span bridge deck," *Journal of the Brazilian Society of Mechanical Sciences and Engineering*, vol. 25, pp. 352 – 383, 2003.

55. L. Bruno and S. Khris, "The validity of 2d numerical simulations of vortical structures around a bridge deck," *Mathematical and Computer Modelling*, vol. 37, pp. 795–828, 2003.

56. COMSOL Multiphysics, *User's Guide Version 3.5*, COMSOL AB, Stockholm, 2008.

57. T. Miyata, H. Yamada, V. Boonyapinyo, and J. C. Stantos, "analytical investigation on the response of a very long suspension bridge under gusty wind. proc., 9th int. conf. on wind engineering, new delhi, india, 10061017.," in *Proceedings of 9th Int. Conf. on Wind Engineering*, 1995.

58. X. Chen and A. Kareem, "Advances in modeling of aerodynamic forces on bridge decks," *Journal of Engineering Mechanics*, vol. 128, no. 11, pp. 1193 – 1205, November 2002.

59. R. T. Jones, "Operational treatment of the non-uniform lift theory in airplane dynamics," Tech. Rep. 667, NASA, 1938.

60. M. Tobak, G. T. Chapman, and L. B. Schiff, "Mathematical modeling of the aerodynamic characteristics in flight dynamics," Tech. Rep. TM 85880, NASA, 1984.

61. M. Tobak and G. T. Chapman, "Nonlinear problems in flight dynamics involving aerodynamic bifurcations," Tech. Rep. TM 86706, NASA, 1985.

62. P. H. Reisenthel, M. T. Bettencourt, and D. S. Grismer, "A nonlinear indicial prediction tool for unsteady aerodynamic modeling," *AIAA Paper*, vol. 98, pp. 43–50, 1998.

63. J. Gordon Leishman, *Principles of Helicopter Aerodynamics*, Cambridge Aerospace Series, 2002.

64. P. Marzocca, L. Librescu, D.-H. Kim I., and Lee, "Linear/nonlinear unsteady aerodynamic modeling of 2-d lifting surfaces via a combined cfd/analytical approach," in *AIAA Paper 2003-1925*, April 2003.

65. D. Lee, J.G. Leishman, and J.D. Baeder, "A nonlinear indicial method for calculation of unsteady airloads," in *59th Annual Forum and Technology Display of the American Helicopter*, 2003.

66. F. M. White, *Viscous Fluid Flow*, Second edition, 1991.

67. Inc. ANSYS, *ANSYS FLUENT, Release 12.1. User's Guide*, ANSYS, Inc., 2009.

68. B. E. Launder and D. B. Spalding, "The numerical computation of turbulent flows," *Computer Methods in Applied Mechanics and Engineering*, vol. 3, pp. 269 – 289,, 1974.

69. C. Costa and C. Borri, "Application of indicial functions in bridge deck aeroelasticity," *Journal of Wind Engineering and Industrial Aerodynamics*, vol. 94, pp. 859 – 881, 2006.

70. Inc. Wolfram Research, *Mathematica*, Wolfram Research, Inc., Champaign, Illinois, version 7.0 edition, 2008.

71. R. H. Scanlan, "Interpreting aeroelastic models of cable-stayed bridges," *Journal of the Engineering Mechanics*, vol. 113, pp. 555 – 575, 1987.

72. S. S. Antman, *Nonlinear problems of elasticity, 2nd Ed.*, Springer, 2005.

73. W. Lacarbonara, *Nonlinear Structural Mechanics. Theory, Phenomena and Modeling*, Springer, New York, 2012.

74. H. F. Xiang, "Wind-resistant design guidebook for highway bridges," *China Communication Press*, 1996, in Chinese.

75. R.L. Bisplinghoff, H. Ashley, and R.L Halfman, *Aeroelasticity*, Dover Publication, New York, 1955.

76. G. Frulla, E. Cestino, and P. Marzocca, "Critical behavior of slender wing configurations," *Proceedings of the Institution of Mechanical Engineers, Part G: Journal of Aerospace Engineering*, vol. 224, 2009.

77. T.J.A. Agar, "The analysis of aerodynamic flutter of suspension bridges," *Computers & Structures*, vol. 30, no. 3, pp. 593 – 600, 1988.

78. X. Chen, M. Matsumoto, and A. Kareem, "A. time domain flutter and buffeting response analysis of bridges," *Journal of Engineering Mechanics*, vol. 126, pp. 7 – 16, 2000.

79. F. Petrini, F. Giuliano, and F. Bontempi, "Comparison of time domain techniques for the evaluation of the response and the stability in long span suspension bridges," *Computers and Structures*, vol. 85, pp. 1032 – 1048, 2007.

80. Harry Dankowicz and Frank Schilder, "An extended continuation problem for bifurcation analysis in the presence of constraints," *Journal of Computational and Nonlinear Dynamics*, vol. 6, no. 3, pp. 031003, 2011.

81. G. Formica, A. Arena, W. Lacarbonara, and H. Dankowicz, "Coupling fem with parameter continuation for analysis of bifurcations of periodic responses in nonlinear structures," *Journal of Computational and Nonlinear Dynamics*, vol. 8, pp. 021013–1 – 021013–8, April 2013.

82. NASA, *Terrestrial Environment and (Climatic) Criteria Handbook for Use in Aerospace Vehicle Development*, August 2000, HDBK-1001.